LA-12896

C.3

LA-12896
C. 3

Computational and Experimental Studies of Hydrodynamic Instabilities and Turbulent Mixing

(Review of NVIIEF Efforts)

Los Alamos
NATIONAL LABORATORY

Los Alamos National Laboratory is operated by the University of California for the United States Department of Energy under contract W-7405-ENG-36.

This work was performed under contract number 0002P0004-95 (008) between Russian Federal Nuclear Center (VNIIEF), Russia and Los Alamos National Laboratory, USA.

LA-12896

UC-700
Issued: February 1995

Computational and Experimental Studies of Hydrodynamic Instabilities and Turbulent Mixing

(Review of NVIIEF Efforts)

*V. A. Andronov**
*I. G. Zhidov**
*E. E. Meskov**
*N. V. Nevmerzhitskii**
*V. V. Nikiforov**
*A. N. Razin**
*V. G. Rogatchev**
*A. I. Tolshmyakov**
*Yu. V. Yanilkin**

**Russian Federal Nuclear Center (VNIIEF), RUSSIA*

Los Alamos
NATIONAL LABORATORY
Los Alamos, New Mexico 87545

FOREWORD

The work on material instability, turbulence, and mixing carried out at Arzamas-16, in the former Soviet Union, has been largely unavailable in the English language. Occasional publications in the open literature have provided intriguing fragments of information, indicating that the program of investigation has been extensive and very impressive, combining strongly interactive activities that are experimental, theoretical, and computational. With recent changes in international relationships, the interactions among scientists and engineers of many countries have now become much more open. This report is a superb manifestation of the changes.

Preparation of the report was funded by a subcontract from the Los Alamos National Laboratory. A group of distinguished scientists from Arzamas-16 visited Los Alamos to discuss the content; Los Alamos scientists have likewise traveled to Russia for this purpose. The final report is a scientific triumph with much international significance.

Francis H. Harlow

COMPUTATIONAL AND EXPERIMENTAL STUDIES OF HYDRODYNAMIC INSTABILITIES AND TURBULENT MIXING

(Review of NVIIEF Efforts)

by

V. A. Andronov, I. G. Zhidov, E. E. Meskov,
N. V. Nevmerzhitskii, V. V. Nikiforov, A. N. Razin,
V. G. Rogatchev, A. I. Tolshmyakov,
and Yu. V. Yanilkin

ABSTRACT

This report describes an extensive program of investigations conducted at Arzamas-16 in Russia over the past several decades. The focus of the work is on material interface instability and the mixing of two materials. Part I of the report discusses analytical and computational studies of hydrodynamic instabilities and turbulent mixing. The EGAK codes are described and results are illustrated for several types of unstable flow. Semiempirical turbulence transport equations are derived for the mixing of two materials, and their capabilities are illustrated for several examples. Part II discusses the experimental studies that have been performed to investigate instabilities and turbulent mixing. Shock-tube and jelly techniques are described in considerable detail. Results are presented for many circumstances and configurations.

Francis H. Harlow

I. COMPUTATIONAL STUDIES OF HYDRODYNAMIC INSTABILITIES AND TURBULENT MIXING

CONTENTS

INTRODUCTION

The report presents the basic results of some calculations, theoretical and experimental efforts in the study of Rayleigh-Taylor, Kelvin-Helmholtz, Richtmyer-Meshkov instabilities and the turbulent mixing which is caused by their evolution.

Since the late forties the VNIIEF has been conducting these investigations. This report is based on the data which were published in different times in Russian and foreign journals.

The first part of the report deals with calculations and theoretical techniques for the description of hydrodynamic instabilities applied currently, as well as with the results of several individual problems and their comparison with the experiment.

These methods can be divided into two types: direct numerical simulation methods and phenomenological methods. The first type includes the regular 2D and 3D gasdynamical techniques as well as the techniques based on small perturbation approximation and on incompressible liquid approximation. The second type comprises the techniques based on various phenomenological turbulence models.

The second part of the report describes the experimental methods and cites the experimental results of Rayleigh-Taylor and Richtmyer-Meskov instability studies as well as of turbulent mixing.

The applied methods were based on thin-film gaseous models, on jelly models and liquid layer models. The research was done for plane and cylindrical geometries. As drivers, the shock tubes of different designs were used as well as gaseous explosive mixtures, compressed air and electric wire explosions.

The experimental results were applied in calculational-theoretical technique calibrations.

The authors did not aim at covering all VNIIEF research done in this field of science. To a great extent the choice of the material depended on the personal contribution of the author in these studies.

The authors express deep gratitude to F.Harlow for the useful discussions of a wide spectrum of problems in hydrodynamic instabilities and turbulent mixing and for American-Russian workshop on these issues arranged in Los Alamos.

1. HYDRODYNAMIC INSTABILITY

1.1. NUMERICAL METHODS FOR HYDRODYNAMIC INSTABILITIES INVESTIGATION

1.1.1. SMALL PERTURBATION METHOD IN GAS DYNAMICS.

The studies of turbulent mixing processes must be preceded by the stability analysis of the gas-dynamic flow of interest which is to define the space regions where the flow is unstable and to estimate the growth rate of small perturbations. This can be done analytically only for some applications demonstrating a highly simplified formulation. Generally when unperturbed flow depends on coordinates and time in complicated manner, strict analytical study of its stability is impossible. Therefore it is interesting to develop numerical methods for stability studies.

References [2,3,4] present the numerical method called "MV" allowing simultaneous computations of 1-D gas-dynamic flows including those with contact and shock discontinuities as well as the growth rate of small 3-D perturbations of this flow in the linear approximation.

The main principles serving the base for "MV" method are presented below.

Numerical studies of gas-dynamic flows in terms of stability relative to small perturbations use the small parameter method and Lagrangian approach to the flow description. The solution is assumed to exist for basic hydrodynamic problem (without perturbations) in the class of discontinuous functions.

Denote by **Π** the vector function of initial-boundary conditions and **R**- the generalized vector of the problem solution. Attaching **Π** conditions to the system of gas-dynamic differential equations ensures the unique solution of this system that is uniquely defines **R** (particle trajectories and hydrodynamic quantities)

$$\vec{r}(\vec{\alpha},t)=\vec{r}(\Pi),\quad \left\{f_i\left(\vec{r},\rho,T\right)\right\}=f(\vec{\alpha},t),$$

where $\vec{\alpha}=\left(\alpha_1,\alpha_2,\alpha_3\right)$- are Lagrangian coordinates fixing the initial position of the particle in space for basic solution, $\vec{r}$- is the vector radius of the particle ρ, T- are independent thermodynamic variables, f_i - are dependent thermodynamic variables, $i=1,2\ldots$.

Small perturbations are applied to initial-boundary conditions of the basic problem.. **Π** is represented as follows.

$$\Pi(\vec{\alpha},t,\sigma)=\Pi^{(0)}_{(\vec{\alpha},t)}+\sigma\,\Pi^{(1)}_{(\vec{\alpha},t)},\quad 0\le\sigma\le 1, \tag{1}$$

where $\Pi^{(0)}$- is the specified vector function of the basic problem, $\Pi^{(1)}$- is the applied perturbation of initial-boundary conditions.

The method applicability condition is to meet the smallness requirement for the perturbation norm $\left\|\Pi^{(1)}\right\| << \left\|\Pi^{(0)}\right\|$.

The family of trajectories for each particle $\vec{r}(\Pi)$for fixed time forms the curve of variations relating two particle positions depending on Π ($\Pi=\Pi^{(0)}$or $\Pi=\Pi^{(0)}\div\Pi^{(1)}$) as σ changes from 0 to 1. Thus for each point of the basic trajectory $\vec{r}\left(\Pi^{(0)}\right)=f(t)$ two directions are specified and hence two differencing operators for these directions

$$\frac{d}{dt}=\frac{\partial}{\partial t}+\left(\vec{u}\vec{\nabla}\right),\quad \vec{u}=\left.\frac{d\,\vec{r}(\Pi)}{d\,t}\right|_{\Pi^{(0)}};$$

$$\frac{d}{d\sigma}=\frac{\partial}{\partial\sigma}+\left(\delta\vec{r}\,\vec{\nabla}\right),\quad \delta\vec{r}=\left.\frac{d\,\vec{r}(\Pi)}{d\sigma}\right|_{\Pi^{(0)},\ \Pi^{(1)}} \tag{2}$$

$$\frac{d}{dt}\frac{d}{d\sigma}=\frac{d}{d\sigma}\frac{d}{dt}.$$

Represent the solution vector $\mathbf{R}(\alpha,t)$ as Taylor series with varying Π

$$f(\vec{\alpha},t;\Pi)=f^{0}(\vec{\alpha},t)\big|_{\Pi^{(0)}}+\sum_{k=1}^{N}\delta^{k}f(\vec{\alpha},t)\frac{\sigma^{k}}{k!}, \tag{3}$$

where $\delta^{k}R=\left.\frac{d^{k}R}{d\sigma^{k}}\right|_{\sigma=0}$.

The equations for $\delta^{k}R$ are generated by sequentially applying the operator (2) to the vector form of gas-dynamic equations. In general case, for example, in the presence of contact boundaries and shock discontinuities when the problem has a multiregion solution structure, the region boundaries and boundary conditions are also differentiated over σ..

Using the small parameter method implies the time and space evolution requirement for the family $R(\Pi)$. The smooth region splitting of the solution should be retained. The boundary shapes and boundary conditions must be differentiable within the smoothness order in adjacent regions.

All equations for the perturbation of any order over k are linear relative to $\delta^{k}R$. The r.h.s. of these equations depends on lower order variations and is not linear relative to these variations.

This approach can be used to study the stability of any flows that are described by hydrodynamic model including various physical processes. The flow under study and applied perturbations may be of any dimension.

One of the methods for perturbation equations is represented by through-out computations using artificial computational viscosity leading to spatial smearing of the unperturbed solution and perturbation features.

NUMERICAL MV METHOD

The numerical MV method [2,3,4] is a technique for through-out computations of the first variation (k=1) for the perturbation of 1-D symmetric flows. The system of equations for variation is uniform. The variation coefficients depend on the solution of 1-D basic problem. Therefore the variables are separated when the computational algorithm is developed,

$$\delta^{1}R(\vec{\alpha},t)=\sum_{n=1}^{\infty}\delta R_{n}(\alpha_{1},t)\,\Phi_{n}(\alpha_{2},\alpha_{3}), \tag{4}$$

where α_1- is Lagrangian coordinate of basic $R^{0}(\alpha_{1},t,\Pi^{0})$, $\Pi^{(0)}=\Pi^{(0)}(\alpha_{1},t)$. In MV method, the basic solution may have plane, cylindrical or spherical symmetry. The functions $\Phi_{n}(\alpha_{2},\alpha_{3})$ form the specified basis for the perturbation expansion over the variables α_2, α_3, with its form depending on the basic problem symmetry type. For example,. $\Phi_n(\alpha_2,\alpha_3)$ are harmonic functions in the case of plane symmetry.

The equations for basic solution $R^0(\alpha_1,t)$ and for harmonic amplitudes $\delta R_n(\alpha_1,t)$ are integrated together using the difference scheme called "pseudoviscosity cross" [1]. The heat transfer is accounted by the implicit first order accurate difference scheme.

The difference grid is generated from the basic problem conditions and spatial size smallness requirement for the cell Δr as compared to the perturbation wavelength. The timestep is chosen from Courant condition: $\Delta t=K\Delta r/c$ where c - is the sound speed, $K\approx0.5$- is the redundancy coefficient. Pseudoviscosity required for δR_n evaluation is obtained by differentiating Rychtmyer type viscosity for 3-D flows over σ. This viscosity is important not only in R^0 discontinuity zones where it smears the delta function of δR_n solution but also where the derivations of R^0 are not smooth that is where it smears δR_n discontinuities.

For external boundaries, the time variation law is specified for R^0 and δR_n functions. Their values are determined from the expansion of 2-D or 3-D boundary conditions and initial geometry into series (4).

The systems of differential equations, their difference analogs and appropriate codes are reported in [2,3,4].

The MV method is adapted to the stability investigations for shock waves and interfaces of two media [5].

The studies of gas-dynamic flow within the linear approximation allow to find when and where the flow instability occurs and to define the evolution law at earlier times.

TEST COMPUTATION EXAMPLE FOR MV CODE

Consider the shock wave motion through the plane interface of two media.

Let one of the medium ($x>0$) be a perfect gas with adiabatic index $\gamma=5/3$ and described by the equation of state $P=(\gamma-1)\rho E$, where P- is pressure, ρ- is density, E- is specific energy. The initial gas pressure is zero and the density $\rho=1$. The second medium ($x<0$) is a weightless gas with a constant pressure $P_0=100$ (ρ_0-= 0, the sound speed $\tilde{n}_0=\infty$). A strong shock wave moves along $x>0$ under the pressure impact. This wave is plane when no perturbation exists.

Introduce the perturbation of the interface

$$\delta(y)=\Delta_0\exp(iky),$$

where y- is the transversal coordinate, Δ_0 - is the initial perturbation amplitude, k- is wave number. For the linear case, all quantities will depend on in a similar way. Denote the shock front perturbation amplitude ξ -and the interface perturbation amplitude by η. For $t=0$ $\xi=\eta=\Delta_0$.

The evolution of small perturbation in the flow of interest is computed analytically with the method reported in [6], [7]. According to this solution, the expressions for shock front surface and surface perturbation amplitude, respectively, have the form

$$\xi(\tau) = \frac{1}{3k}\left(3\,J_0(\tau) + 2\,J_2(\tau)\right)$$

$$\eta(x) = \frac{1}{k}\left(-0.1 + 1.1\,J_0(x) + 0.2\,J_2(x) - 0.9\,x\left(J_1(x) - 2\sum_{m=0}^{\infty} J_{2m+1}(x)\right)\right),$$

where $\tau = \frac{k\,\Delta r_f}{\sqrt{h}}$; $x = kct$; $h = \frac{\gamma+1}{\gamma-1}$, $J_m(x)$ - is Bessel function; Δr_f - is the travel path of the shock front by the time t; c - sound speed behind the shock front in the unperturbed solution.

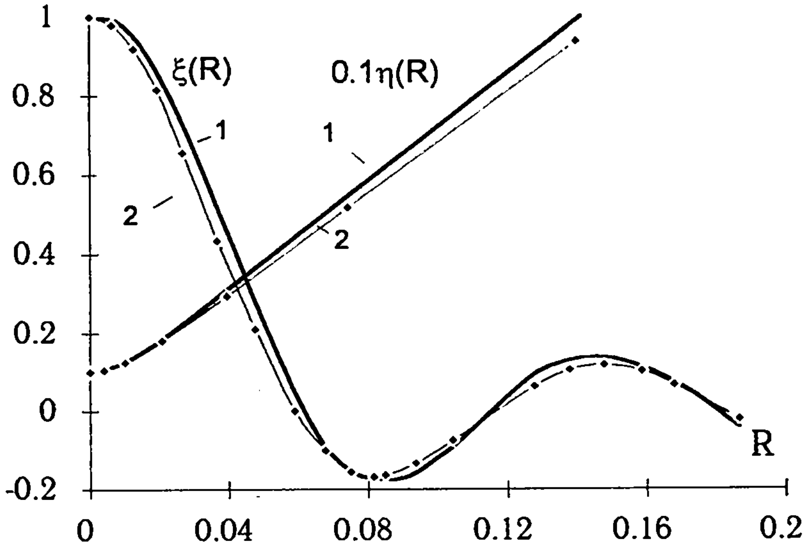

Fig 1. Plane shock front and interface perturbation amplitude versus travel paths of the shock front and interface, respectively..
1 - numerical MV data;
2 - analytical data.

This problem was computed with MV code [3] for k=100. The cell size is 2.10^{-3}. Figure 1 shows numerical and analytical results normed to the initial value of interface perturbation amplitude. The figure demonstrates a good agreement between numerical and analytical data. The shock front amplitude, ξ, depends on the front travel path, $R=\Delta r_f$, in a sign-variable manner and the modulus decreases with time. The interface amplitude η increases monotonically with the interface travel path $R=\Delta r_b$.

1.1.2. USING THE BOUNDARY INTEGRAL EQUATIONS METHOD FOR NONSTATIONARY INCOMPRESSIBLE FLUID DYNAMICS

For some hydrodynamic applications, the moving medium may be thought of as an incompressible inviscid fluid. Using this assumption allows to apply the potential theory data and to develop an efficient computational method for time-dependent potential flows with strongly distorted boundaries. The numerical method

[8] described below is one of the implementations of the technique called Boundary Integral Equations Method (BIEM).

The sense of the method as applied to hydrodynamics is the following. The parameters of vortex-free incompressible fluid flow are found from Laplace equation for the velocity potential with time-dependent boundary conditions on the moving boundary.

The velocity potential is represented as the integral of the source function specified on the fluid interface.

By solving the integral equation, we determine the source function from the boundary value of the velocity potential. There values are used to compute the normal component of the surface velocity. Cauchy-Lagrange integral is used to determine how the boundary potential depends on time. The boundary displacement is found given the cinematic relations.

This approach permits to convert the volume boundary motion problem to a surface one which reduces the number of spatial variables and the computation time.

Two code versions were implemented. The first is intended for axisymmetric problems and the second for periodic flows near the interface of two variable density fluids.

The first method - [8], is close to the methods reported in [9,10], however the version from [9] has a low accuracy and is not suitable for flows with strongly sheared boundaries. That from [10] demonstrates a high approximation accuracy but does not allow to compute the motion of fluids containing varying volume cavities

Consider the main relations serving the base for the boundary integral equations method.

The incompressible fluid hydrodynamics equations have the form:

$$\operatorname{div}\vec{u} = 0 \tag{5}$$

$$\frac{\partial \vec{u}}{\partial t} + \vec{u}\,\nabla\vec{u} = -\frac{1}{\rho}\nabla P + \vec{F} \tag{6}$$

For potential external forces $\vec{F}$ $(\vec{F} = \nabla U)$, Thompson theorem indicates that $\operatorname{rot}\vec{u} = 0$, if the flow was initially vortex-free. In this case the fluid velocity can be expressed via the potential gradient

$$\vec{u} = \nabla\varphi \tag{7}$$

and equation (1.1) converts to Laplace equation for the velocity potential

$$\Delta\varphi = 0 \tag{8}$$

Equation (6) can be written as Cauchy-Lagrange relation:

$$\frac{\partial\varphi}{\partial t} + \frac{1}{2}|\nabla\varphi|^2 + \frac{P}{\rho} + U = \Phi(t). \tag{9}$$

Consider the method implementation for axisymmetric problems where the fluid-filled region extends to infinity and contains a single-bound cavity whose volume may change with time.

The expression for φ can be represented as a simple layer potential:

$$\varphi(\vec{r}_0) = \frac{1}{4}\int_s \frac{q(\vec{r})\,dS}{|\vec{r} - \vec{r}_0|}, \tag{10}$$

where $\vec{r}, \vec{r}_0$ - are vector radii of surface and fluid volume points, respectively; $q(\vec{r})$ - is the integrable source function defined on S surface.

We use the system of cylindrical r, z coordinates. The contour L of generatrix of this surface will be specified parametrically; that is $L(\tau){:}\,\{r(\tau), z(\tau)\}$. In this case the expression (10) converts to the form:

$$\varphi(r_0, z_0) = \int_L q(\tau) \frac{r K(k) D(r)}{\sqrt{(r + r_0)^2 + (z - z)^2}} d\tau, \tag{11}$$

$$\text{where} \quad D(\tau) = \sqrt{\left(\frac{dr}{d\tau}\right)^2 + \left(\frac{dz}{d\tau}\right)^2}, \quad k = \sqrt{\frac{4 r r_0}{(r + r_0)^2 + (z - z_0)^2}},$$

$K(k)$ - is the full elliptic first kind integral.

For the velocity components of fluid points $u_r = \dfrac{\partial \varphi}{\partial r_0}$ and $u_z = \dfrac{\partial \varphi}{\partial z_0}$ we have:

$$u_r(r_0, z_0) = \frac{1}{4} \int_L q(\tau) \frac{\sqrt{r}}{r_0^{3/2}} k \left\{ \frac{E(k)}{1 - k^2} \left[1 - \frac{k^2}{2} \left(1 + \frac{r_0}{r} \right) \right] - K(k) \right\} D(\tau)\, d\tau \tag{12}$$

$$u_z(r_0, z_0) = \int_L \frac{r (z - z_0) E(k) D(\tau)\, d\tau}{(1 - k^2)\left[(r + r_0)^2 + (z - z_0)^2\right]^{3/2}}, \tag{13}$$

where $E(k)$ - is the full elliptic second kind integral. The relations (11)-(13) in the limiting sense are valid for the fluid points on the boundary. The computational scheme is discretized as follows. N reference points are specified on L contour, the values $\tau = 1$ and N correspond to the axial points (see Fig. 2), the parameter step is unity for the transition from one point to another. The time derivatives for moving boundary reference points are denoted as:

$$\frac{d}{dt} = \frac{\partial}{\partial t} + \vec{u}_b \nabla \tag{14}$$

where $\vec{u}_b$ - is the velocity of boundary points. Normal velocity components for the surface and fluid must coincide according to the continuity condition

$$\vec{u}_b \vec{n} = \left. \frac{\partial \varphi}{\partial n} \right|_S \equiv u_n. \tag{15}$$

Using Cauchy-Lagrange integral (9), the relation (14) and kinematic bounds yields the system of 3N equations (16) describing the motion of computational points and potential variations:

$$\begin{aligned} \frac{dr_i}{dt} &= u_{n_i} n_{r_i} + \tilde{u}_{\tau_i} n_{z_i} \\ \frac{dz_i}{dt} &= u_{n_i} n_{z_i} - \tilde{u}_{\tau_i} n_{r_i} \\ \frac{d\varphi_i}{dt} &= \frac{P_\infty(t) - P(t, r_i, z_i)}{\rho} - g z_i + \frac{1}{2} u_{n_i}^2 - \frac{1}{2} u_{\tau_i}^2 + \tilde{u}_{\tau_i} u_{\tau_i}, \end{aligned} \tag{16}$$

where - u_n, u_τ, - are normal and tangent fluid velocity components on the boundary; n_r, n_z - are external normal components; $P(t, r_i, z_i)$ is the pressure specified on the boundary; P_∞ is the pressure in an infinitely distant (with z=0); g -is the gravity field acceleration (vertically downward); $\tilde{u}_\tau$- tangent component of the reference point velocity. The physical problem setup does not restrict $\tilde{u}_\tau$, so various algorithms are possible for tangent displacement of reference points.

The replacement of integral relation (11) with an algebraic one is accomplished as follows: the potential at **j** point is considered to be the sum of "contributions" from the rings formed by the reference points (see Fig. 2)

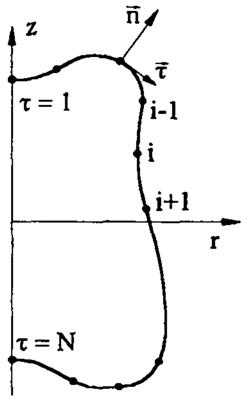

Fig.2. Contour shape description for BIE method.

The interpolation of $q(\tau)$ over the reference points allows to replace (11) with a system of algebraic equations relative to $q(\tau)$ values at reference points that is:

$$\varphi_j = \sum_{i=1}^{N} A_{ij} q_i \tag{17}$$

The expressions with structure similar to (18) and (19) replace the integral relations (12) and (13):

$$u_{r_j} = \sum_{i=1}^{N} B_{ij} q_i \tag{18}$$

$$u_{z_j} = \sum_{i=1}^{N} C_{ij} q_i . \tag{19}$$

The following numerical algorithm is adopted. By solving (17), the source function q is determined from the specified potential values. The fluid velocity components on the interface are calculated from the relations (18) and (19) with known q. The solution of equation (16) yields the new position of the boundary and updated potential values of the reference points.

The representation of $q(\tau)$ in the form of piecewise constant function adopted in [9] is insufficient to describe the flows containing considerable deformations as the practice shows; however yet the quadratic interpolation results in very cumbersome and multipleshape algorithms for matrix computations, therefore the linear interpolation of $q(\tau)$ was chosen for the implementation:

$$q(\tau) = q_i + (q_{i+1} - q_i)(\tau - i), \quad \tau \in [i, i+1] \tag{20}$$

The contour shape that is $r(\tau)$ and $z(\tau)$ interpolated by fourth degree polynomials over r_i and z_i at the nearest reference points which ensure a sufficient interpolation smoothness.

The closer is the ring with (i, i+1) boundaries to the **j** point, the greater are the contributions of the rings formed by the reference points to the boundary potential value. This is especially true for the points near the axis, so various contribution evaluation algorithms were chosen to increase the solution accuracy while approaching the **j** point.

The contribution of the **i** - ring with the boundaries $\tau \in i, i+1 \neq j$ to the potential value and the velocity component of the **j** - point was computed using quadratic interpolation of the integrands from (11), (12), (13) over their values at points τ=i, i+1/2, i+1:

$$\int_{i}^{i+1} f(\tau)\,q(\tau)\,d\tau \cong \frac{1}{6}\left[f(i)+2f\left(i+\frac{1}{2}\right)\right]q(i)+\frac{1}{6}\left[f(i+1)+2f\left(i+\frac{1}{2}\right)\right]q(i+1) \qquad (21)$$

The existence of specific features of $f(\tau)$ with $\vec{r} \to \vec{r}_0$ necessitates the computations of contributions from the rings that are the nearest to the j-point using a special technique. The contribution from the fragment of the of the ring with the boundaries $[j-\varepsilon, j+\varepsilon]$ (where $\varepsilon << 1$ is a specified parameter) is computed analytically. The contributions from the "incomplete" rings closest to **j** with $\tau \in [j-1, j-\varepsilon]$ and $\tau \in [j+\varepsilon, j+1]$ are evaluated by direct numerical integration. The sums of coefficients from various q_j, occurring during the computations of contributions from various rings form the matrix elements A_{ij}, B_{ij}, C_{ij}.

The integrals are computed with Romberg method and the algebraic equations use double orthogonalization method. Differential equations were integrated with the fourth order Runge-Kutta method.

The time required for a single integration step increases more slowly than N^2, when the number of reference points, N, grows.

The code was tested on static and dynamic problems having known analytical solutions. Particularly, the change (source function) distribution over a sphere and ellipsoid was computed with a specified potential. For dynamic tests, rigid sphere rise-up in the gravity field and Rayleigh problem of bubble collapse in fluid were used.

Test computations shows that the method is cost-efficient and accurately describes the parameters of hydrodynamic flows with a relatively low number of reference points. For example, it was shown for Rayleigh problem with 25 reference points that the relative bubble asymmetry due to the method uncertainty is 4.10^{-5}. at the time of strong compression.

Numerical computations with the above method involved a series of validation calculations varying the number of reference points, their positions and the algorithms for tangent motion of reference points.

The second method version for flows with periodic boundary conditions was generated using a scheme similar to the about mentioned given the natural simplifications resulting from the plane flows geometries.

Some computational results obtained with this method are reported in section 1.2.1.

1.1.3. EGAK CODES

PHYSICAL BACKGROUND AND BASIS

The EGAK codes [11] are designed for numerical simulation of 2-D time-dependent flows of compressible multicomponent media with strong geometry deformations with the turbulence included.

The codes implement the method allowing to compute a wide spectrum of physical processes including:

- gas (fluid) dynamics with and without physical viscosity;
- (molecular and turbulent) diffusion;
- turbulent mixing.

The components may be represented by

- real materials;
- vacuum;
- absolutely incompressible bodies;

To distinguish the components their mass and volume concentrations are used together with specific energies.

The EGAK codes use a regular proceed quadrangular grid whose nodes may move rather arbitrarily as the computations. In partial cases , the grid may follow the material (Lagrangian code) or remain fixed (Eulerian grid).

To avoid the smearing of the interfaces between the components , we use the so called method of concentrations [12]. The sense of the method is as follows: when the material flows from mixed cells (containing several components), the concentration field is analyzed and the analysis date are used to determine the amount and outgoing order of the components. The EGAK codes implement this method sequentially for all above mentioned components. It allows to localize the position of interfaces within the accuracy of a single cell.

The outer boundaries of the computational domain may contain the following conditions:

- material non-penetration (rigid wall);
- input (output);
- pressure and velocity;
- others.

In addition , the incompressible component permits to implement the nonpenetration requirement inside the computational domain. This allows to simulate the flows in domains with almost arbitrary configuration including multi-sound domains.

Finite-difference schemes used in EGAK codes are generated with integrodifferential method, have the first order approximation accuracy in time and first or second order accuracy in spatial variables.

A METHOD FOR GAS-DYNAMIC FLOWS IN LAGRANGIAN -EULERIAN VARIABLES

Several Lagrangian-Eulerian methods are implemented within the codes to compute gas-dynamic or hydrodynamic flows [13, 14, 15, 16]. These methods allow the direct simulation of unstable flows including turbulized flows for a wide range of Mach numbers.

The Lagrangian-Eulerian method is described below which now serves the base for semi-empirical turbulence models. Eulerian methods [13, 14] only slightly differ from it in terms of main principles.

ORIGINAL EQUATIONS

The original equations describing time-dependent 2-D (plane or axisymmetric) multicomponent gas flows are represented by the relations expressing the conservation laws of the moving volume V:

$$\frac{d\vec{J}}{dt}+\int_{s}\rho\vec{u}(\vec{u}-\vec{u}^{*})d\vec{S}=\int_{s}Pd\vec{S} \tag{22}$$

$$\frac{dM_i}{dt}+\int_{S_i}\rho_i(\vec{u}_i-\vec{u}_i^{*})d\vec{S}=0 \tag{23}$$

$$\frac{dV_i}{dt}+\int_{S_i}(\vec{u}_i-\vec{u}_i^{*})d\vec{S}=\int_{S_i}\vec{u}_i d\vec{S} \tag{24}$$

$$\frac{dE_i^{(f)}}{dt}+\int_{S_i}\rho_i E_i(\vec{u}_i-\vec{u}_i^{*})d\vec{S}=\int_{S_i}P_i\vec{u}_i d\vec{S}, \tag{25}$$

where

ρ_i is the density of individual components;
ρ is the total material density in volume V;
V_i is the volume occupied by individual components;
$V=\sum V_i$;
$\vec{u}(v,w)$ is the velocity (v is x velocity component, w is z velocity component);

$\vec{J}(J_x,J_y)$ is the momentum ($J_x=\int_V \rho v\,dV$, $J_z=\int_V \rho w\,dV$);

$M_i=\int_{V_i}\rho_i\,dV$ is the mass of a component in volume V;

E_i is the specific internal energy of a component in volume V;

$E_i^{(f)}=\int_{V_i}E_i\rho_i\,dV$ is the total internal material energy in volume V;

P_i is the partial pressure of components;
P- is the total material pressure energy in volume V;

$\vec{u}^*$ is the velocity of points of S surface limiting the volume V;

S_i are the surfaces limiting the volumes V_i, filled with individual components;
$i=1,2,\ldots,N$ is the order number of the component;
N is the number of components;

The system (22-25) is closed by the equations of state for the medium components

$$P_i=P_i(\rho_i,E_i). \tag{26}$$

The system (22-26) is computed with splitting method in two steps. The first (Lagrangian) step solves equations (22-26) without convective terms or gas-dynamic equations in Lagrangian variables. The second (Eulerian) step generates a new grid following the motion of its nodes relative to material and updates the values for the new grid that is approximates the terms of equations (22-25) rejected at the first step.

Vector values $\vec{u}$, $\vec{J}$ are defined at the grid nodes and scalar values $(\rho_i,\ E_i,\ P_i,\ P,\ \alpha_i=M_i/M,\ \beta_i=V_i/V)$ at the cell centers.

Further the values taken from the lower time layer will be written without time index (where no confusion occurs); the values computed at the first step are accompanied by the index $(n+1/2)$ while those from the second step have the index (n +1). In addition, the symbols have an alphanumeric index indicating the owning cell (node) as shown in Figure 3.

LAGRANGIAN STEP

The source system (22-25) computed at the first step has the form

$$\frac{d\vec{u}}{dt} = -\frac{1}{\rho}\operatorname{grad}(P+q) \tag{27}$$

$$\frac{d\rho_i}{dt} = -\rho_i \operatorname{div}\vec{u}_i \tag{28}$$

$$\frac{dE_i}{dt} = -\frac{P_i+q_i}{\rho_i}\operatorname{div}\vec{u}_i \tag{29}$$

$$\frac{d\vec{r}_i}{dt} = \vec{u}_i . \tag{30}$$

Here quadratic computational viscosities q, q_i are added to the source system.

To close the system (26-30), an additional assumption is required. This may be one of the following:

- identical material compressibility

$$\operatorname{div}\vec{u}_i = \operatorname{div}\vec{u} \tag{31}$$

- material pressures equal to the total pressure

$$P_i=P \tag{32}$$

The approximation of motion equations use precomputed pressure

$$\widetilde{P} = P^n + \left.\frac{dP}{dt}\right|_S \tau, \tag{33}$$

where S is the entropy, τ is the timestep. Explicit or implicit schemes can be obtained depending on the computational technique.

$$\widetilde{P}_i = P_i^n - \chi c_{W_i}^2 \rho_i^n \operatorname{div}\vec{u}_i^n \cdot \tau$$

$$\widetilde{P} = \sum_{i=1}^{N} \beta_i P_i^n - \chi c_W^2 \rho_i^n \operatorname{div} u^n \cdot \tau, \tag{34}$$

where $\chi = 0.6$ is the parameter, the sound speed c_W^2 is given by

$$c_W^2 = \left.\frac{\partial P}{\partial \rho}\right|_S = \sum_{i=1}^{N} \alpha_i c_{W_i}^2 .$$

Here $\rho_i = \frac{\alpha_i}{\beta_i}\rho$.

The implicit scheme results if the precomputed pressure $\widetilde{P}$ in the formula (33) is determined from the values obtained by the $t=t^{n+1/2}$

$$\widetilde{P} = P^n - \tau c_W^2 r^n \operatorname{div}\vec{u}^{n+1/2} =$$

$$= P^n - \tau c_W^2 \rho^n \operatorname{div}\vec{u}^n + \tau c_W^2 \rho^n \operatorname{div}\left(\frac{1}{\rho}\operatorname{grad}\widetilde{P}\right) \tag{35}$$

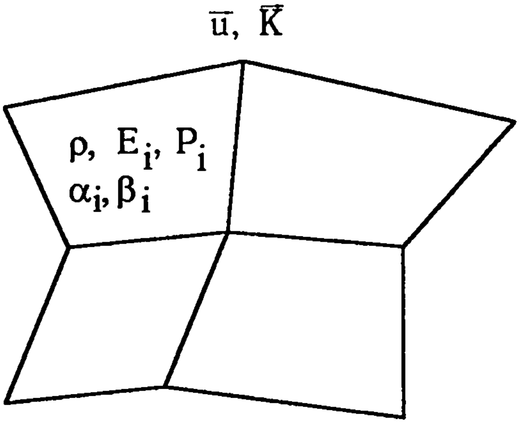

Fig.3. EGAK code counting greed fragment.

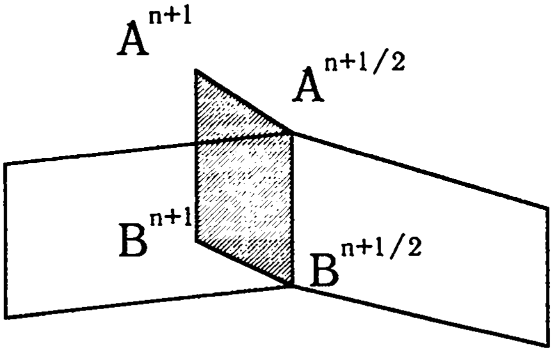

Fig.4. Volume flow through the cell surface evaluation.

To solve this equation with respect to $\widetilde{P}$, flows splitting method is used.

After the pressure is computed, the accelerations are calculated on the cell sides neighboring the node and the node acceleration is determined from the interpolation . At Lagrangian step, the grid follows the material motion..

If one of the cells surrounding the node of interest contains an incompressible element , the corresponding accelerations on the sides of such cell are set to zero. A similar procedure is accomplished on the external boundary representing a rigid wall or the boundary where the pressure is applied.

After the velocity components are computed, their spatial distribution is smoothed by the fourth order smallness operator..

Equations (28-29) can be approximated different ways depending on the assumption choice (31) and (32).

For version (31), the approximation of continuity equations (28) is easy. When approximating the energy equation, the calculation of the difference analog of $\operatorname{div}\vec{u}$ uses the velocity values:

$$\widetilde{u} = \frac{1}{2}\left(u^n + u^{n+1/2}\right).$$

This is necessary to ensure the difference scheme conservation at the first step.

When assumption (32) is used, equations (26, 28, 29, 32) must be solved together. This system has the exact solution in partial cases only, for example, for a mixture of perfect gases. For arbitrary equations of state, the system reduces to a single equation solved with iterations.

EULERIAN STEP

After a new grid is generated, it is necessary to determine the component volume, mass and energy flows from one cell to another in order to compute the convective terms from equations (22-25). These flows are assumed to be other than zero only between the cells sharing a side. Consider the computational procedure for the flows between the neighboring cells (see Figure 4), where the corresponding indices denote the position of the shared side after the first step and after the generation of a new grid.

The total volume flow equals to the rotational value (in axisymmetric case) of the quadrangle $A^{n+1/2}A^{n+1}B^{n+1}B^{n+1/2}$ shaded in Figure 4. The flow orientation depends on ΔV sign. . Figure 4 shows the case where the left cell is a donor.

When mass and energy flows from pure (single component) cells are computed, we use the first order approximation donor method and the second order donor-acceptor method. For the latter, the mass flows are given by the following formula (the energy flow formula has a similar form):

$$\Delta M = \Delta V\left[\lambda \rho_d + (1-\lambda)\rho_a\right] \tag{36}$$

where ρ_d, ρ_a are the donor and acceptor cell densities, respectively

The coefficient λ is obtained from

$$\lambda = \frac{1}{2}\left(1 - \frac{\Delta V}{V}\right) \tag{37}$$

To avoid the computational diffusion of the interfaces, the method of concentrations is used. The mass flows from a mixed cell are determined by

$$\Delta M_i = \Delta V_i \, \rho_{id} \text{ , where}$$

$$\Delta V_i = \Delta V \, \beta_i \qquad (38)$$

To evaluate β_I, the volume (or mass) concentration field is analyzed to locally reproduce the interface between the components in the vicinity of the cell of interest. Among several algorithms used, the simplest one is that using three cells for the analyses. Table 1 contains β_I values as a function of some encountered situations (digits 1 and 2 indicate the component numbers, the index "d" denotes the donor cell). In the remainder of cases $\beta_1 = \beta_{1d}$, $\beta_2 = \beta_{2d}$.

Table 1. β_i values as a function of potenial situations for three cells

Situation	β_1	β_2
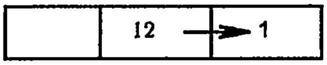	1	0
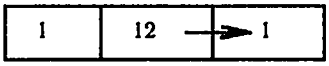	0	1
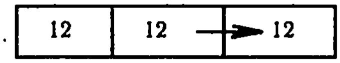	β_{1d}	β_{2d}

When the flows are determined using (38), a situation may occur where the volume of a component (for example, the first one) is greater than the volume of this component available in the donor cell or $\Delta V_1 \equiv \Delta V \beta_1 > V_{1d}$. In this case the volume of this component is decreased and that of the other is increased by the value $\Delta V_1 - V_{1d}$. Thus, we have

$$\Delta V_1 = V_{1d}; \qquad \Delta V_2 = \Delta V_2 + \left(V_{1d} - \Delta V_1\right).$$

The volume flows across other cell sides are calculated in a similar way.

When the contributions of each subsequent side are computed, the volumes of materials residing in the cell are decreased by the value of volume flows outgoing from the cell through other sides at previous computational steps. Generally, the cell sides are not equivalent for such approach. However the computations show that it influences the results only slightly.

The method implements another technique for flow computations where the sides remain equivalent. However the above method is easier to implement which motivates its application.

Thus the method for mass and energy flow computations may use both donor and donor-acceptor techniques. The former is first order accurate, the latter is second order accurate for smooth solution portions and first order accurate for the vicinity of discontinuity.

For the motion equation approximation of momentum flows consistent with the mass flows. The flow velocity is given by

$$v = \lambda v_d + (1 - \lambda) v_a,$$
$$w = \lambda w_d + (1 - \lambda) w_a,$$

where "d" and "a" indicate the donor and acceptor nodes.
The values of λ in pure cells are computed to (37).

For mixed cell nodes, $\lambda=1$.

If restriction (32) is used, the pressure are equated other the second step assuming that the internal cell energy remains unchanged and one components operates on another.

1.2 NUMERICAL CALCULATIONS OF SOME UNSTABLE FLOWS

1.2.1. NON-COMPRESSIBLE LIQUID FLOWS

NON-LINEAR STAGE OF RAYLEIGH-TAYLOR INSTABILITY

Numerous research of Rayleigh-Taylor instability (RTI) are reviewed in ref. [17], for example.

This section includes the 2-D calculation results of Rayleigh-Taylor instability for non-compressible non-viscous liquids in the plane geometry obtained with boundary integral equation method described in section 1.1.2.

The problems were solved in the following statement.

Lower semi-space is filled with liquid of ρ_1 density and upper - with liquid of ρ_2 density. Magnitude $\delta=\rho_2/\rho_1>1$. At t=0, the contact boundary shape differs slightly from the horizontal plane. Field of gravity g, is accelerated vertically downwards.

Mainly, the calculations aimed at a through description of RTI development, including the stage of small perturbations and non-linear stage where the contact boundary perturbation amplitude is comparable with the characteristic wavelength.

A calculation set was done where the initial surface perturbation was specified in the form of one harmonics

$$z(t=0,x)=a_0 \sin x.$$

Initial perturbation amplitude, a_0, varied. The calculations assumed the following parameter magnitudes: $\rho_1=1$; $g=1$; $\lambda=2\pi$; $a_0=0.05\text{-}1$. To describe the contact boundary, 30 points at λ perturbation period were used.

Figure 5.1 presents the calculated boundary shape for the ratio of densities $\delta=10$ and initial perturbation amplitude $a_0=0.05$ for t=4.83 and t=6.1. In this calculation a mushroom-shaped jet of the heavy liquid characteristic of the non-linear stage at small differences in densities appears later when the jet length is comparable with λ.

In the abovedescribed statement the RTI development calculations were done also for $\delta=2$, 5, 100, 1000. The results show that in case $\delta=2$ and 5, the boundary acquires characteristic spiral-like shapes. When density differences are large, $\delta=100$ and 1000, the instability development pattern differs qualitatively. At early moments, when perturbation amplitude $a\geq1/k$, an asymptotic flow pattern is formed. A jet area is formed where the heavy substance drops down, as well as a bubble area - where the light liquid emerges.

At the non-linear stage the flow characteristics appeared to be slightly dependent on the initial perturbation amplitude, a_0. With time, the bubble top velocity, u_z and curvature radius R in this point reach their asymptotic values. The calculation have shown that $u_z\rightarrow(0.235\pm0.005)\sqrt{\lambda g}$; $R\rightarrow0.4\lambda$, that agrees with the results in ref.[18].

At the linear stage, the surface perturbation amplitude grows exponentially with time providing that short-wave perturbations grow faster (an increment is proportional to $\frac{1}{\sqrt{\lambda}}$). The liquids interpenetrate symmetrically. At the non-linear

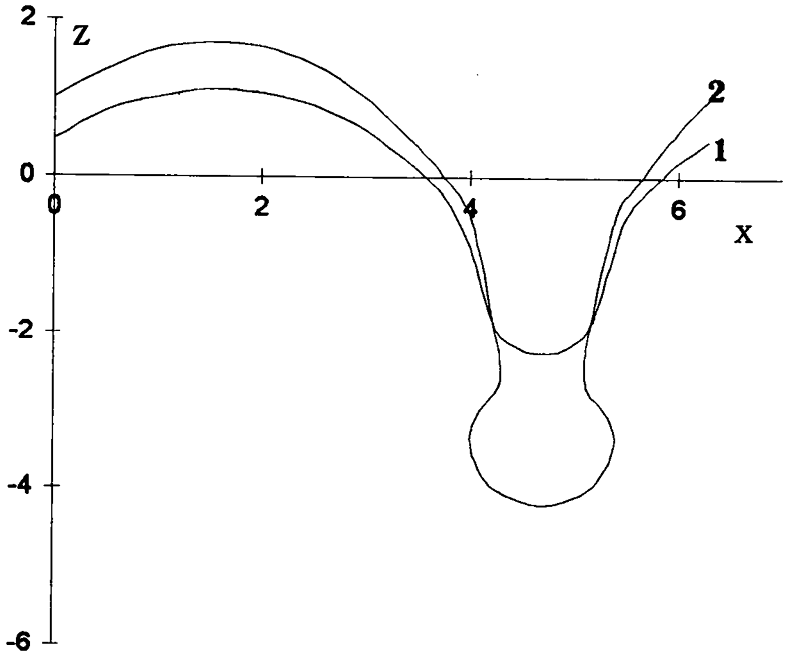

Fig.5.1 Numerical modeling of R-T instability.
Interface shape calculated for δ=10, z(t=0,x)=0.05sinx.
1 - t= 4.83, 2 - t=6.1.

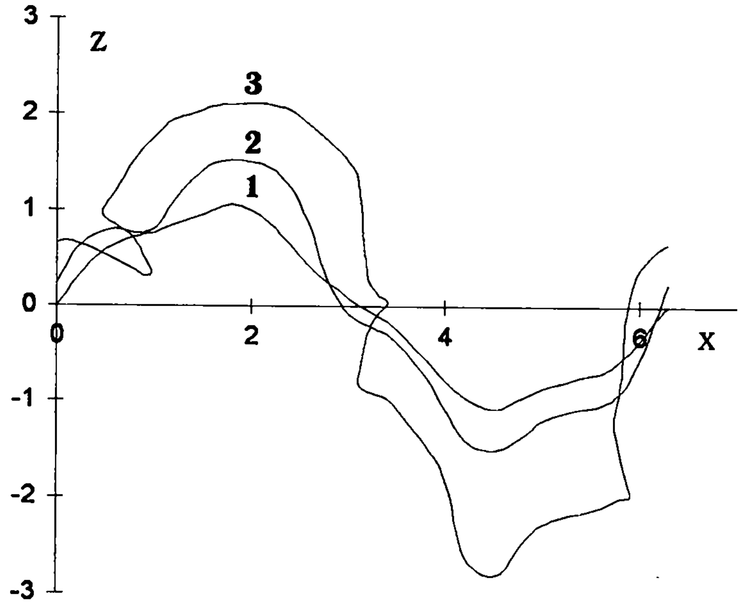

Fig.5.2. Numerical modeling of R-T instability.
Interface shape calculated for δ=10, z(t=0,x)=0.1sinx.
1 - initial shape; 2 - t=1.37; 3 - t=1.91.

stage, the picture of perturbation growth changes qualitatively. The liquids interpenetrate non-symmetrically, and the characteristic velocity for large-scale perturbation growth is higher if the wave length is bigger ($u_z = \sqrt{\lambda}$).

In general, the contact surface deformation picture obtained with BIEM technique coincides with the solution resulted from other methods [17,18]. Linear stage of perturbation growth agrees with the results of the small perturbation technique.

A calculation set was done for $\delta=10$ in the statement similar to the described above with the initial surface disturbances in the form of two harmonic superposition. Figure 5.2 gives contact surface shape for different moments, obtained in the calculation with the initial disturbances specified in the form

$$z(t = 0, x) = \sin x + 0.1 \sin 4x.$$

By $t = 1.5$, a large bubble dome emerges at $u_z=0.66$, that is close to the asymptotic value $0.235\sqrt{g2\pi}=0.59$ for long-wave component.

Several reports [17, 19, 20] mention the RTI development tendency that with time the dominant role in liquid interpenetration zone dynamics is passed to the long-wave components of initial perturbation.

RICHTMYER-MESHKOV INSTABILITY NON-LINEAR STAGE MODELING

Richtmyer-Meshkov instability (RMI) is instability of a contact gas interface of different densities under a shock wave effect.

The RMI development pattern can be qualitatively modeled via the evolution of an initially disturbed contact boundary of non-compressible liquids after the effect of the acceleration pulse short in time and large in the amplitude, g_0, or by specifying the *initial perturbations in* the velocity field.

With BIEM technique in the plane geometry, the 2-D calculations for this problem were done for magnitudes $\delta=\rho_2/\rho_1=2$, 5, 1000; $\rho_1=1$; $\lambda=2\pi$; $a_0=0.05$. The acceleration pulse, width, t_0, and its magnitude, g_0, were chosen so that the boundary perturbation amplitude change during the pulse effect was negligibly small, and the boundary velocity amplitude $u_0=1$. For example, for $\delta=1000$, - $t_0=0.001$, and $g_0=2.10^4$.

The case of small density difference was modeled with the specified the plane surface and initial sinusoidal perturbation in the velocity field, at velocity amplitude $u_0=1$. The liquid densities were assumed equal.

Of interest are the trajectories of characteristic boundary points describing the biggest depth of light liquid penetration in the heavy one - L_1 and the heavy liquid - in the light one -L_2. The problem non-linearity results in the harmonics which wave length is by 2 times less than the initial one that is coupled with available term $|\nabla\varphi^2|$ in Cauchy- Lagrange relation. Due to this, an asymmetry arises in the liquid interpenetration zone, $L_2/L_1 >1$. During the time when the amplitudes of shorter-wave perturbation are small, the width of liquid interpenetration zone, $L=L_1+L_2$ appears to be close to the magnitude predicted by the small perturbation method despite of the substantial non-linearity of the process.

The calculation results are illustrated in Fig.6-8 in dimensionless variables.

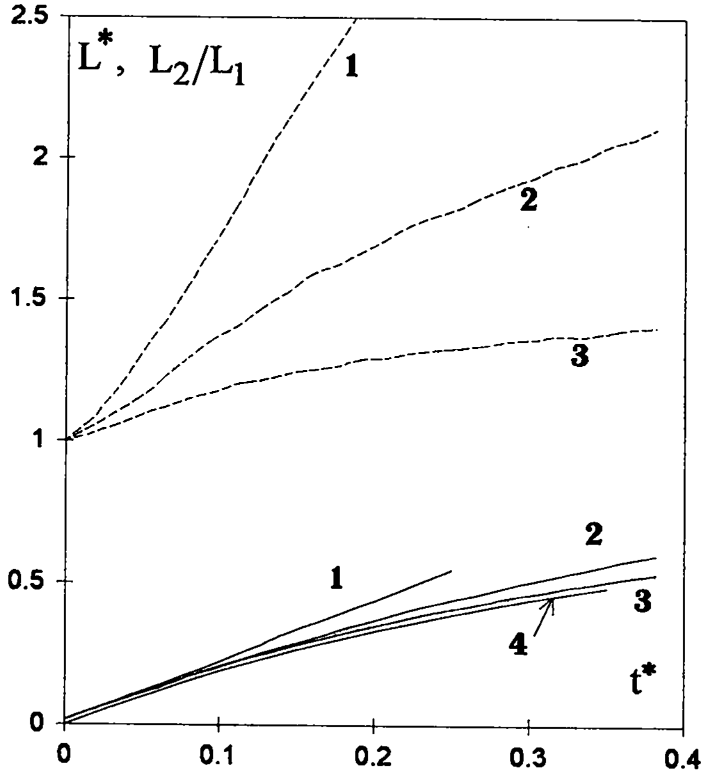

Fig.6. Numerical modeling of R-M instability.
L_2/L_1 (dashed lines) and L^* (solid lines) as functions of t^*.
1 - $\delta=1000$; 2 - $\delta=5$; 3 - $\delta=2$; 4 - $\delta=1$.

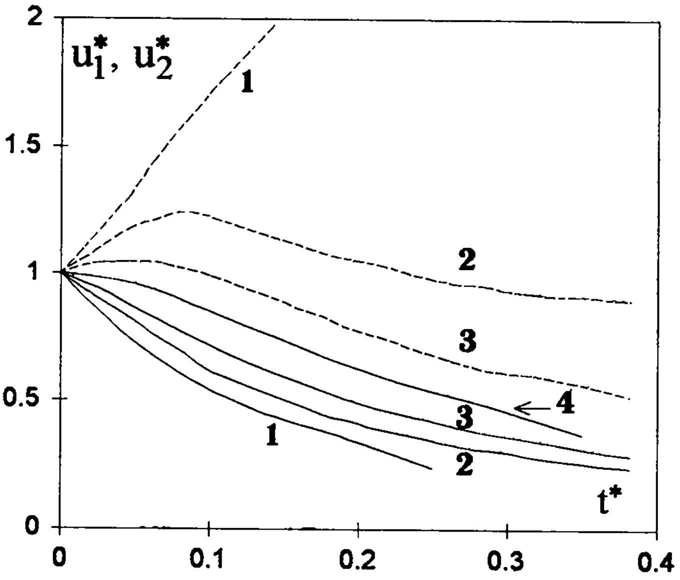

Fig.7. Numerical modeling of R-M instability.
u_1^* (dashed lines) and u_2^* (solid lines) as functions of t^*.
1 - $\delta=1000$; 2 - $\delta=5$; 3 - $\delta=2$; 4 - $\delta=1$.

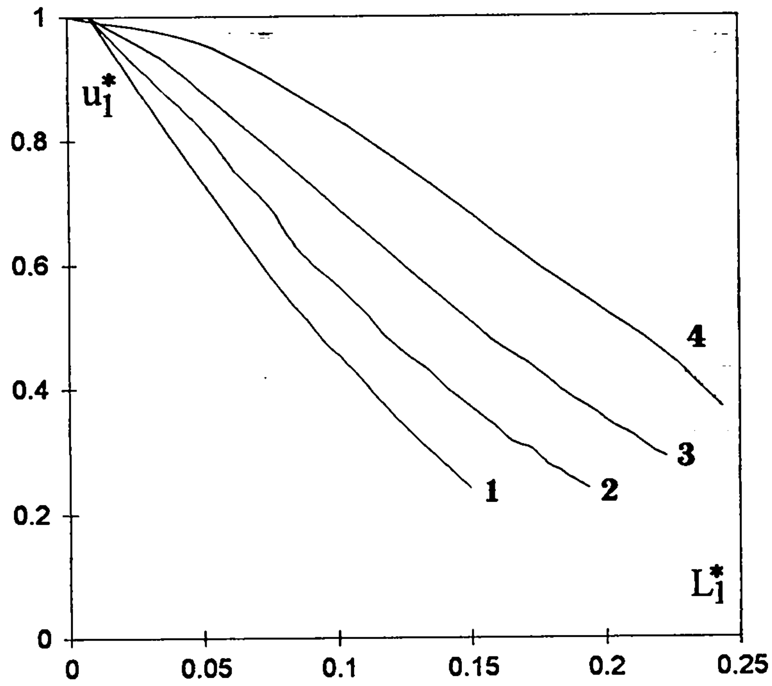

Fig.8. Numerical modeling of R-M instability.
Dimensionless velocity of light liquid interpenetrating into the heavy one as function of dimensionless interpenetrating depth.
1 - δ=1000; 2 - δ=5; 3 - δ=2; 4 - δ=1.

Figure 6 gives functions $L^*=L/\lambda$ and L_2/L_1 vs. $t^*=tu_0/\lambda$. Flow asymmetry is developed faster for large density difference, and difference in L^* obtained from small perturbations method (SPM) predictions occurs faster for small density differences.

Figure 7 presents velocity functions for light liquid penetration in the $u_1^* = \frac{dL_1}{dt}\frac{1}{u_0}$, and the heavy liquid - in the light one $u_2^* = \frac{dL_2}{dt}\frac{1}{u_0}$ vs. t^*.

Figure 8 gives the velocity function for light liquid penetration in the heavy one u_1^* vs. L_1/λ magnitude. With these function extrapolation to $u_1^*=0$, we shall get the following estimates for $\tilde{L}_1/\lambda$ - ultimate magnitudes L_1/λ at $t\to\infty$:

δ	1	2	5	1000
$\tilde{L}_1/\lambda$	0.36	0.32	0.26	0.2

Thus at the non-linear stage in $t^*\cong 0.4$, the penetration velocity of light liquid in the heavy one decreases practically to zero that allow us to conclude about the existing ultimate magnitude of penetration depth $\tilde{L}_1/\lambda\cong 0.2\text{-}0.4$.

AXISYMMETRIC PERTURBATIONS IN GAS VOID COMPRESSION BY IDEAL LIQUID

Related to the study of spherical substance compression stability is the interest in a classical problem of adiabatic compression of a inviscid unbounded liquid. Rayleigh already considered this problem for a spherically symmetrical case. The stability of spherical compression in small perturbation case (SPM) was studied in ref.[21]. This perturbation dynamics at the linear and non-linear stages of the void compression was investigated in ref.[8] with a boundary integral equation method described in section 1.1.2.

Let at the initial moment the liquid around the axisymmetric void filled with ideal weightless gas be at rest, and gas pressure P_0 be less than pressure P_∞ in the infinitely distant point. Under this pressure gradient, a potential flow appears which is characterized by gas void compression and deformation. Gas is compressed adiabatically.

As a 2-D code test, we have calculated a spherically symmetrical void compression (without initial perturbation specification). The following set of parameters was used in the calculation: initial radius $r(t=0)=1$; gas adiabatic index $\gamma=5/3$; liquid density $\rho=1$; initial pressures $P_0=0.015$; and $P_\infty=1$. According to an accurate solution of a spherically symmetrical problem these solutions correspond to the maximal bulk compression $V_0 / V_{min} = 305$ $t=0.9355$. The numerical results of BIEM code coincide with the accurate solution better than 1% in all flow characteristics.

A set of calculations was done where the initial shape of a generating surface was specified as close to spherically symmetrical with the perturbations in the form of Legendre polynomial

$$r(t = 0,\theta) = 1 + a_n P_n(\cos\theta)$$

Below, the calculation results are presented for n=2, 3, 4 and initial perturbation amplitude a_n= 0.05.

Figures 9-12 depict the gas mixture shapes at the times close to the maximal compression.

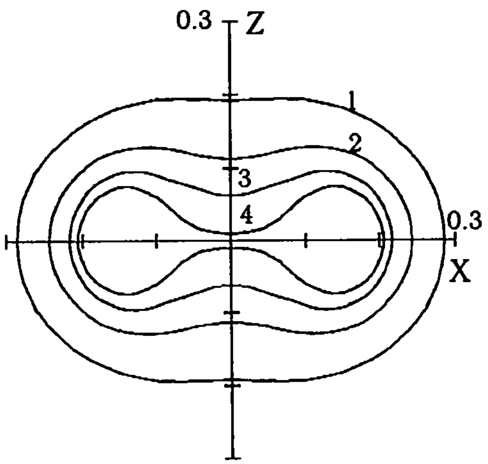

Fig. 9 The shapes of gas cavity at the end of compression stage in the case of initial perturbation: $R(t=0, \theta)=1+0.05P_2(\cos(\theta))$.

1 - $t=0.9038$; 2 - $t=0.9236$;
3 - $t=0.9294$; 4 - $t=0.9345$.

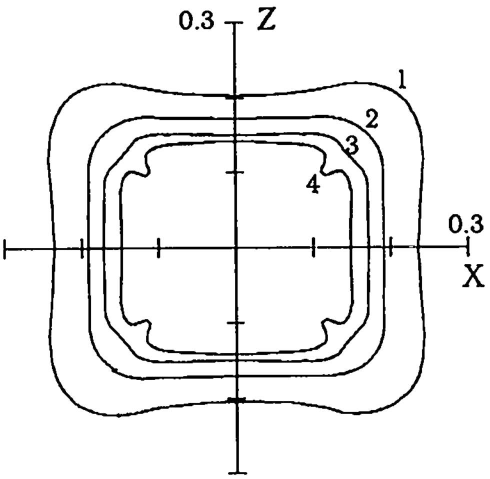

Fig. 10 The shapes of gas cavity at the end of compression stage in the case of initial perturbation: $R(t=0, \theta)=1+0.05P_4(\cos(\theta))$.

1 - $t=0.914$; 2 - $t=0.924$;
3 - $t=0.928$; 4 - $t=0.932$.

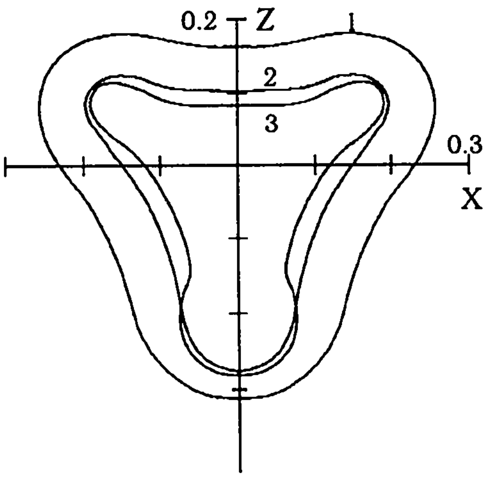

Fig. 11 The shapes of gas cavity at the end of compression stage in the case of initial perturbation: $R(t=0, \theta)=1+0.05P_3(\cos(\theta))$.

1 - $t=0.919$; 2 - $t=0.93$;
3 - $t=0.935$.

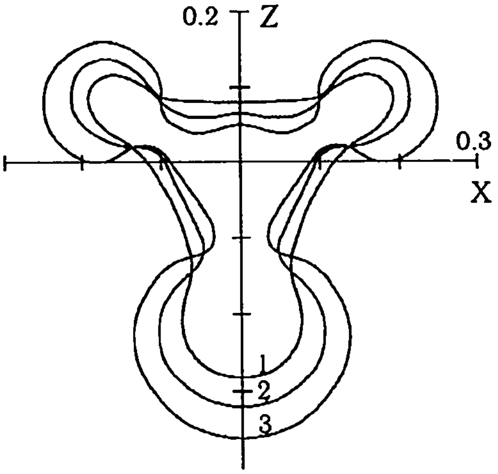

Fig. 12 The shapes of gas cavity in the beginning of expansion stage in the case of initial perturbation: $R(t=0, \theta)=1+0.05P_3(\cos(\theta))$.

1 - $t=0.935$; 2 - $t=0.94$;
3 - $t=0.9455$.

In case of n=2 perturbation, by the moment of violated simple connectedness of area (t=0.936, the void shape is almost toroidal (see Fig.9), the collapse velocity along the symmetry axis reaches magnitude approximately 10, and the gained compression is $V_0 \,/\, V(t) = 290$.

In case n=3, it appeared that at the initial perturbation amplitude, $a_3=0.05$, void simple connectedness is violated at the expansion stage after the maximal compression is achieved. In Fig.11 and Fig.12, the void shapes for n=3 at the final compression stage and initial expansion stage are shown. The time of minimal volume gain coincides with one-dimensional, and the maximal compression constituted $V_0 \,/\, V_{min} = 295$.

Figure 10 presents the void shapes for n=4 up to t=0.9332 ($V_0 \,/\, V_{min} = 280$).

Comparison of the results obtained with different number of reference contour points and at their different arrangement notifies a small error (approximately 1%).

In all cases considered, despite of high void deformation, the minimal obtained volume differs slightly from the obtained in one-dimensional compression.

At the moments when the radius vs. angle function is unambiguous, the shapes were analyzed in spectrum, i.e. the coefficients for Legendre polynomial decomposition $r(\theta)$. Values $a_n(a_0)$, where a_0- an average radius, were compared with similar SPM calculated functions.

It is easy to show that in the spherically symmetrical case for the assumed parameters the time (t) function of void radius is described with the equation

$$\frac{d^2 r}{d t^2} + \frac{3}{2}\frac{\left(\frac{d r}{d t}\right)^2}{r} = P_0 r^{-6} - \frac{1}{r}. \tag{39}$$

In case of small perturbations when the void surface shape can be presented in the form of the decomposition by Legendre polynomials:

$$r(t,\theta) = a_0(t) + \sum_{n=1} a_n(t) P_n(\cos\theta), \tag{40}$$

where $r(t)=a_0(t)$- equation (39) solution, n-harmonic amplitude growth is described [21] by the equation

$$\frac{d^2 a_l}{d x^2} + (\omega + 2)\frac{d a_l}{d x} - (l - 1)\omega a_l = 0 \ , \tag{41}$$

where $x = \ln r$, $\omega = \dfrac{d \ln \frac{d a_0}{d t}}{d x}$.

Equations (39) and (40) are the mathematical description of small perturbation method (SPM) for this particular problem.

Figure 13 gives a_n, function obtained from eq. (39), (40) for initial perturbation of n=2. These result comparison with the BIEM calculations show that SPM at 1% accuracy depicts the ground harmonics amplitude up to the loss of $r(\theta)$. function unambiguity. That means, the SPM applicability range is notably wider. (Due to a small difference, the SPM results are not shown in the Figure). However, at the non-linear stage of perturbation development, alongside with the ground harmonic, the amplitudes of harmonics which numbers differ from "n" originate, grow and become essential. First thing, the multiple harmonics of "2n" numbers appear (that is due to $|\nabla\varphi|^2$ term present in Cauchy-Lagrange relation).

INITIAL STAGE OF LOCALIZED PERTURBATION EVOLUTION

As a rule the turbulent mixing dynamics is studied in the arrangement when the unstable interface between the substances of different densities is plane. (ex. [22,23,24]). In this case, the initial perturbations are small and of a occasional nature.

To understand the mixing processes in detail, it is interesting to study the instabilities of various controlled spectra for initial perturbations. The simplest among them is a sinusoidal which evolution results in characteristic dynamic structure consisting of "bubbles" and "spikes" (ex. [25,26,27]). The results of these research appeared helpful in understanding the role of individual harmonics in a general picture of instability and turbulent mixing development and is the base for the simplest theoretical models [28, 29]. The previous sections present the results of similar research.

In ref. [30] the experimental study of substance mixing picture with the available localized perturbations evolution is described . We shall understand these perturbations as the perturbations specified on a small area as compared with the interface area. A particular example for the localized perturbations is a cavity on the media plane interface.

The BIEM method described in section 1.1.2. was applied for numerical simulation in the following statement.

In the infinite ideal liquid $\rho=1$ at rest there is an axisymmetric cavity filled with weightless gas. The cavity is a sphere of 100 radius with center coordinates $r=0$, $z=-100$, near the upper pole, for which the shape disturbance is specified in the form:

$$z = \exp\left(\frac{-r^2}{4}\right) - 0.09827 \text{ at } r \le 3 .$$

This disturbance of a secluded cavity shape is of sufficient smoothness and at small radius r coincides with the linearized problem solution. In the gas, the pressure is specified which varies according to the law which provides for the radial acceleration of a constant boundary far from a perturbation $g=1$.

Table 2 and Figure 14 illustrate the calculation results.

Table 2 presents the time functions for several magnitudes characterizing flow which were obtained in this calculation and this problem SPM solution as well as the characteristics of the bubble stationarily emerging to the surface in the tube:

u_p- emerging velocity for the perturbation dome top in coordinate system coupled with the moving non-disturbed boundary;

R^*- curvature radius of the dome top;

$u_0 = \frac{2}{3}\sqrt{gR^*}$- velocity of bubble stationary emergence which has R^* curvature [31];

R_{eff} - tube radius where a gas bubble comes to a surface at constant velocity $u_p = 0.48\sqrt{gR_{\text{eff}}}$ ([31]);

u_m- SPM rate of perturbation amplitude growth.

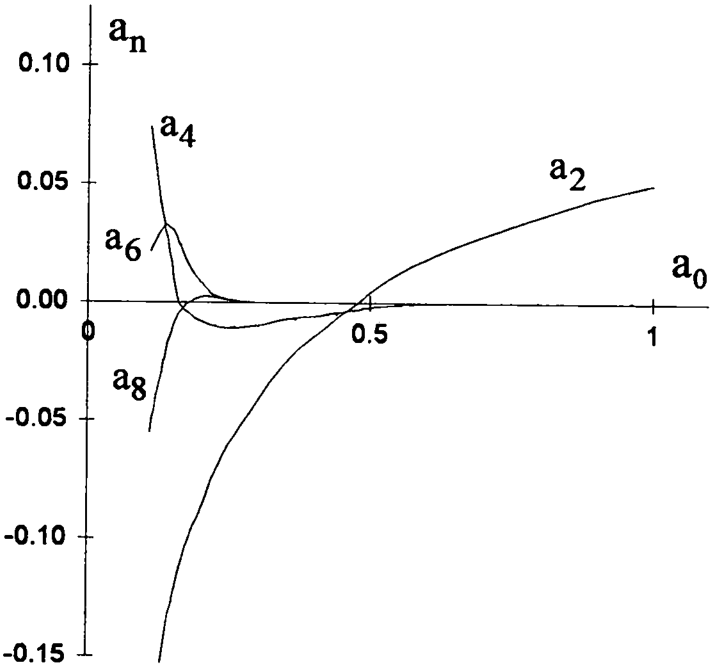

Fig.13. Harmonic amplitudes dependence on cavity radius a_0. Initial perturbation was in the form $r(t=0, \theta)=1+0.05P_2(\cos(\theta))$.

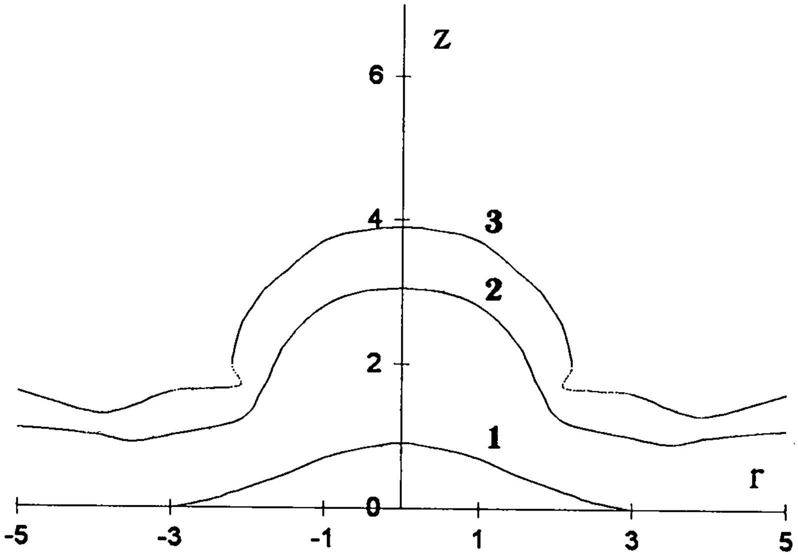

Fig.14. Local perturbation interface shapes calculated with BIE method at different moments. 1 - initial shape, 2 - t=1.5, 3 - t=1.8.

Table 2. Localized perturbation growth characteristics.

t	u_p	R^*	u_0	u_m	R_{eff}
0	0	2	0.94	0	-
0.3	0.33	1.9	0.92	0.28	0.5
0.6	0.65	1.7	0.87	0.57	1.8
0.9	0.95	1.6	0.83	0.93	3.8
1.2	1.23	1.6	0.83	1.36	5.7
1.5	1.48	1.7	0.87	1.92	7.8
1.8	1.7	1.9	0.89	2.65	11

The table 2 parameters compared, show that the cavity coming to the surface is of non-stationary character (velocity u_p differs from u_0 and does not depend on R^*). Monotous increase in R_{eff} reveals that with time the liquid father and father from the symmetry axis becomes involved in the motion.

The dome top tends to constant 0.75g that differs qualitatively from the asymptotic stage of periodic perturbation development where this acceleration equals zero.

Figure 14 depicts a contact interface area with a dotted line for t=1.8 where the small-scale vortex-like deformations occur. At these sections the solutions do not convert with the increased number of points (the more in detail the contour of this part of surface is described, the faster a vortex is formed). A notable effect of how accurate the description is, on the dome coming to the surface is not discovered.

The calculations done have revealed essential peculiarities of localized perturbation development and have stimulated the experimental research described in section 2.7.

NON-STATIONARY FLOWS IN ANGULAR POINT VICINITY IN GAS ACCELERATED LIQUID LAYER

This section is devoted to the surface interface perturbation evolution research between light and heavy substances with the angular peculiarities present there [32]. There, perturbations developing together with the natural random perturbations result in a complicated mixing picture and are characterized by the origin of special regular structure of a hydrodynamic flow.

Similar flows appear, ex., at the HE-driven acceleration of the plates and shells with fractures, a cumulative jet is formed in the oblique collision of plates.

As a natural approximation for the theoretical analysis of a regular constituent of the flows, let us consider that an accelerated plate substance is an ideal liquid. Its flow is described by Laplace equation for φ velocity potential

$$\Delta\varphi = 0. \tag{42}$$

The velocity vector depends on $\vec{u} = \vec{\nabla}\varphi$.

On the inner layer boundary p_1- pressure is specified, and on the external - p_2. Cauchy-Lagrange condition

$$\frac{d\varphi}{dt} = \frac{w^2 - u^2}{2} = q \tag{43}$$

for the surface points is an equation defining a time function of a surface potential. Here, u, w - tangential and normal components of liquid velocity on the surface; q =

0, for external layer boundary, and $q=-(P_1-P_2)/\rho$ - for inner one, time derivative is calculated for a fixed surface point, r, which velocity is always directed over normal $\vec{n}$; ρ- liquid density.

Motion equation for these points is

$$\frac{d\vec{r}}{dt}=\left(\vec{\nabla}\varphi\vec{n}\right)\vec{n}. \qquad (44)$$

If the boundary shifting is small compared to h - layer thickness (that is valid for early moments) and u and w values are small, equation (43) is integrated elementary : $\varphi=qt$.

In this case the surface deformation is found in the following way. Specifying the initial layer shape at t=0 as it is depicted in Fig.15 and using the boundary values for potential: $\varphi=qt$, we solve eq. (42) with a conformal conversion method (we present the area occupied by a liquid on the band in complex potential plane). Differentiating the discovered space distribution $\varphi(\vec{r})$, we determine the velocity vector $\vec{u}$. Finally, integrating eq.(44) over time, we find the needed shifting of inner and outer surface points. For certainty, let us consider that the inner surface fracture angle $\beta<180°$.

The boundary points are shifted to normal, and for the outer surface of the accelerated layer this shift is described by the expression

$$\left|\Delta\vec{r}_2\right|=\frac{P_1-P_2}{2\rho h}t^2\left(\frac{\lambda}{1+\lambda}\right)^{\left(\frac{\pi-\beta}{2\pi}\right)}, \qquad (45)$$

λ is found from the equation

$$r_2=\frac{h}{\pi}B_\sigma\left(\frac{\beta}{2\pi},0\right), \qquad \sigma=\frac{\lambda}{1+\lambda},$$

$B_\sigma(x,0)=\int_0^\sigma\frac{z^{x-1}}{1-z}\,dx$ - incomplete Beta function, and r_2- distance from (B) top to a specified point on the outer surface (Fig.15)

With $r_2\to\infty$ $(\lambda\to\infty)$ we obtain $\left|\Delta\vec{r}_2\right|\to\left(P_1-P_2\right)t^2/2\rho h$ that, as it should be, corresponds to the plane layer motion at $g=\left(P_1-P_2\right)/\rho h$.

In close vicinity of outer angle at $r_2\to 0$ $(\lambda\to 0)$

$$\left|\Delta\vec{r}_2\right|=\frac{P_1-P_2}{2\rho h}t^2\left(\frac{\lambda}{1+\lambda}\right)^{\left(\frac{\pi-\beta}{2\pi}\right)},$$

That is, that in the considered approximation the outer angle top does not move, that corresponds to the experimental results.

The inner surface point shifting is described by the expression

$$\left|\Delta\vec{r}_2\right|=\frac{P_1-P_2}{2\rho h}t^2\left(\frac{\lambda}{1+\lambda}\right)^{\left(\frac{\pi-\beta}{2\pi}\right)}, \qquad (46)$$

where μ is expressed via r_1- distance from top (A) to a specified surface point (Fig.15) from relation

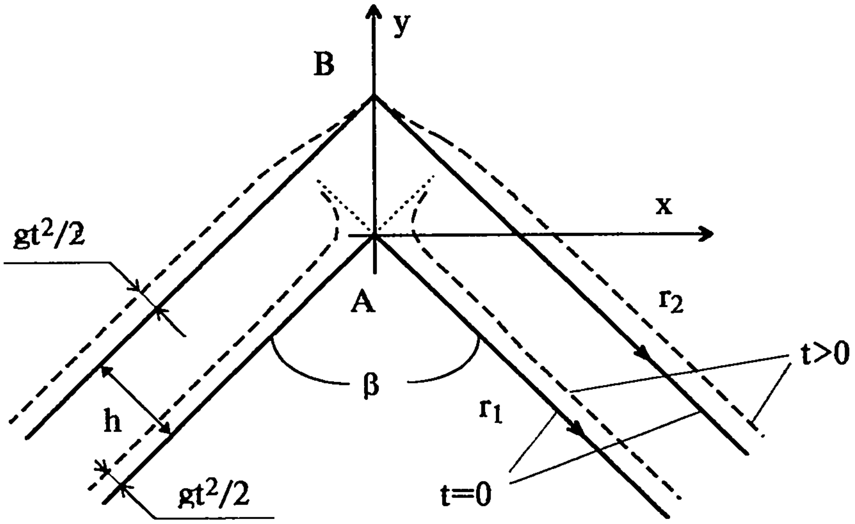

Fig.15. Liquid layer shape. Dashed lines correspond to the small perturbation method prediction.

$P_1 = 1$, $P_2 = 0$, $\rho = 1$, $h = 1$

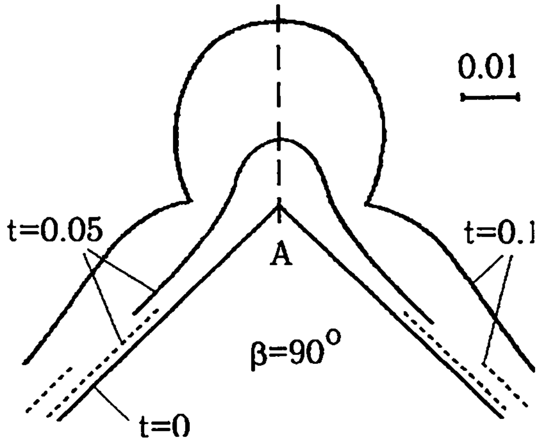

Fig.16. The inner boundary shape at the proximity of the angle vertex A. BIE code calculations

$$r_1 = \frac{h}{\pi} B_\sigma\left(1 - \frac{\beta}{2\pi}, 0\right), \qquad \sigma = \frac{\mu}{1+\mu}.$$

Like in the above considered case, at $r_1 \to \infty \ (\mu \to \infty)$ we get, $|\Delta\vec{r}_2| \to (P_1 - P_2)t^2 / 2\rho h$ In the small vicinity of top (A) at $r_1 \to 0 \ (\mu \to 0)$ the point shifting is described by the formula:

$$|\Delta\vec{r}_2| = \frac{P_1 - P_2}{2\rho h} t^2 \left(\frac{\lambda}{1+\lambda}\right)^{\left(\frac{\pi-\beta}{2\pi}\right)}, \qquad (47)$$

The limit infinity means that the above approximation are not fulfilled in the inner angle top vicinity. In relation (43) one can not neglect u^2 и w^2 magnitudes, and the surface deformation can not be considered small at any t values. The same is noted by the experiment results also.

To describe hydrodynamic flows accurately, problem (42), (43), (44) should be solved in a complete statement without simplifying suppositions. This problem was numerically solved with the boundary integral equation method [8] for $\beta=90°$. In this case, it was assumed that $P_1=1$, $P_2=0$, $\rho=1$, $h=1$.

Figure 16 illustrates the inner surface motion at small magnitude where from it is seen that in top (A) vicinity (as in the experiment) a fast growing cavity is formed which shape is almost a cylinder. On the surface two new angular peculiarities appear. The distance between the points on the cavity surface grows faster than the distance between the points on the rest inner surface. That means, the cavity is as if blown out of the point which was originally in top (A). Relation (47) being valid at $|\Delta\vec{r}_1| << r_1 << h$, reveals the present intermediate self-similarity asymptotics of 2-D problem (42), (43), (44). Providing that self-similarity index α (in expression $|\Delta r_1| \approx \mathrm{Const}\, t^\alpha$) equals $\alpha=2(2\pi-\beta)/(3\pi-2\beta)$. For $\beta=\pi/2$ $\alpha=1.5$, that approximately corresponds to the numerical results.

The analytical research of the flows in the vicinities of newly formed surface points based on self-similarity hypothesis presents the interest.

1.2.2. NONLINEAR STAGE IN KELVIN-HELMHOLTZ INSTABILITY DEVELOPMENT COMPRESSIBLE GAS CASE

Kelvin-Helmholtz (KHI), or tangential velocity discontinuity instability, is one of typical hydrodynamic instability effects.

The problem for tangential velocity in compressible gases was addressed by Landau [36] in small perturbation approximation for 2-D perturbations case.

Many typical instabilities including KHI have the linear stage characterized by increments growing with shorter wavelengths. With numerical calculation, this situation may cause short-wavelength perturbations existing in the initial distributions due to discrete computational scheme to grow, and consequently, degrade the calculation of the deterministic perturbations evolution. The above-noted difficulties set limits on the choice of computational mesh and the approximation accuracy of initial distributions.

NONLINEAR STAGE IN KHI DEVELOPMENT

Analytically, it is hardly possible to describe the evolution of perturbations with their amplitudes comparable to wavelengths, therefore the studies use numerical simulation as basic approach.

This Section describes the results of KHI studies in plane geometry for compressible gases [34,35].

Quantitative description of the nonlinear stage is limited by the time where a harmonic starts to develop substantially having wavelengths comparable to mesh size.

The calculations were made using EGAK codes [11], with the problem stated as follows.

There are two ideal gases in the upper and lower half-spaces, having the same initial pressures and adiabatic indices, equal to $P_1=P_2=0.6$ and $\gamma_1=\gamma_2=5/3$, respectively. For some initial time, there has been specified an x-periodic sinusoidal perturbation of the interface

$$z(t=0,\ x)=a_1\sin(2\pi x), \qquad (49)$$

where $a_1=0.1$ and perturbation wavelength is $\lambda=1$.

Tangential velocity discontinuity $\Delta u_x=1$ satisfied the plane flow conditions for relatively small 2-D perturbations [36]

$$\Delta u_x<(c_1{}^{2/3}+c_2{}^{2/3})^{3/2}, \qquad (50)$$

where c_1 and c_2 are the sound velocities in the upper and lower gases, respectively. Initial density was $\rho_1=1$, and ρ_2 was varied as $\rho_2=1,5,10$.

The computational field had its size in x-axis $L_n=1$. Periodic boundary conditions were used.

The interface (49) was approximated by piecewise-continuous function. This made the velocity discontinuity spread in z direction over the length $d=(1\div 2)h$, where h - is the mesh size.

The number of cells used was 50 per perturbation wave period.

As shown by the analysis of initial perturbationsspectrum, the first harmonic a_1 has its actual amplitude differing from 0.1 by no more than 1%, with the amplitudes of harmonics a_n $(1<n<10)$ not higher than $0.01a_1$. Therefore, the approximation assumed for initial perturbation was reasonable accurate.

Figures 17 through 20 illustrate some calculations.

Figure 17 shows interface shapes at different times for the case where the gases have the same initial density. What is observed is the interface spiraling. This tendency is less marked for density ratio equal to 10 (Figure 18).

Figure 20 shows the interpenetration zone thickness $L(t)=z_{max}-z_{min}$, where z_{max} and z_{min} are the maximum and minimum z-coordinates of the interface. At an earlier stage, the curves L(t) are linear, with the rise rate decreasing with larger density difference, and this is qualitatively consistent with the data from linear theory of small perturbations growing in incompressible liquids. For gases having the same densities, L is no longer observed at the level $L\approx0.7$.

While density variations in the flows of interest were within 30% the contribution of the velocity discontinuity smoothing can be estimated by making use of the data from shear flow instability studies of incompressible liquids. That the

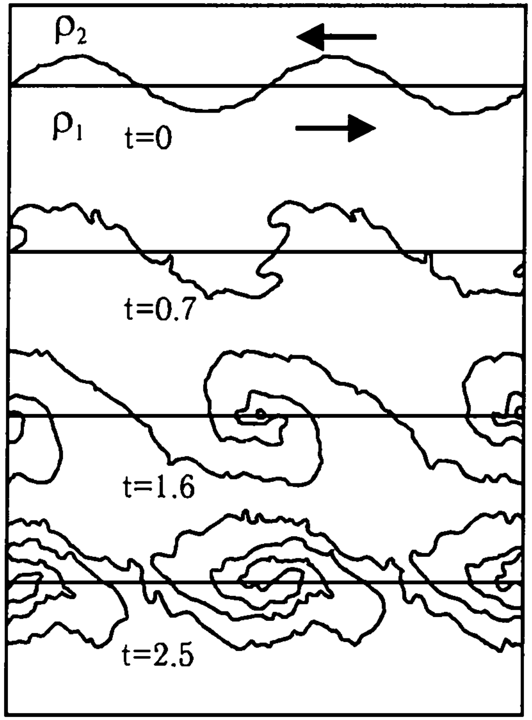

Fig. 17 Interface shape evolution. δ=1.

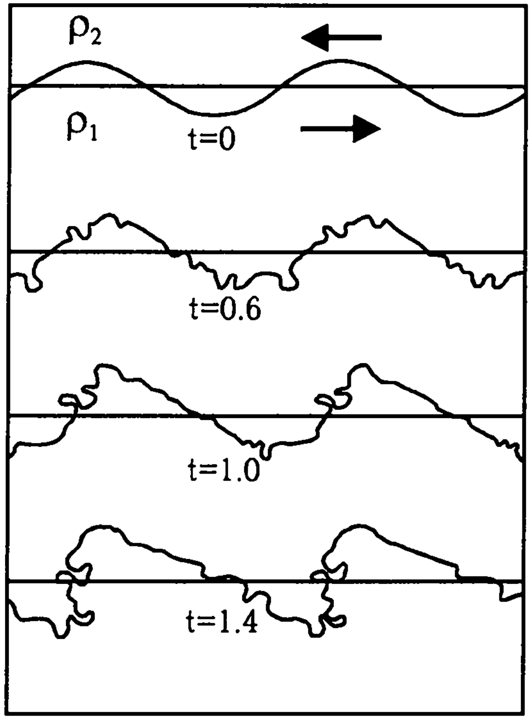

Fig. 18 Interface shape evolution. δ=10.

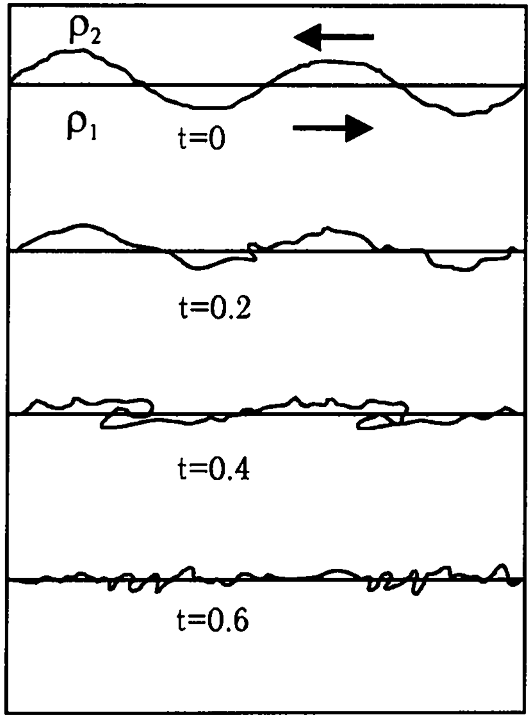

Fig. 19 Interface shape evolution in the stable case [36]. δ=1.

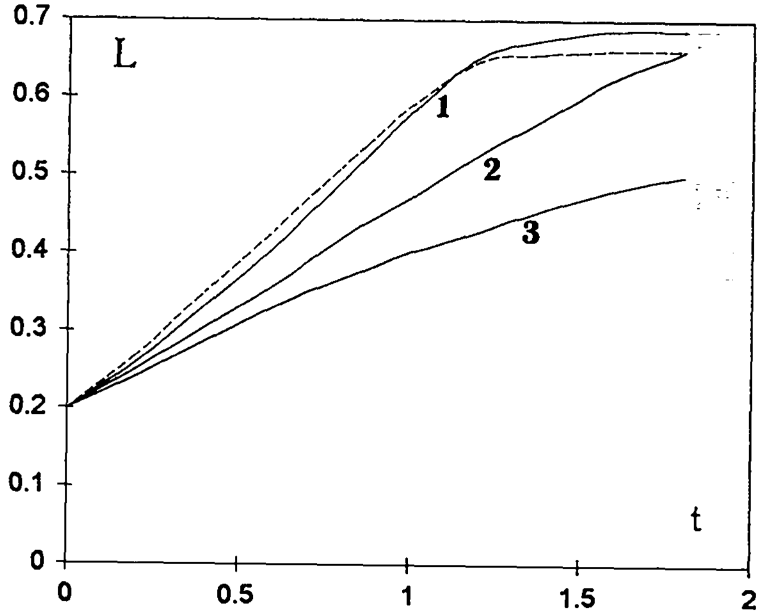

Fig.20. Numerical modeling of K-H instability with EGAK code.
1 - δ=1; 2 - δ=5; 3 - δ=10;
dashed line - the problem analogous to the problem 1 (δ=1), but sound speed was doubled.

incompressible liquid approximation is suitable for this purpose, is also supported by the similar calculations where sound velocities in gases were increased two-fold (dashed line in Figure 20). The interface shapes obtained by this calculation differ from the previous calculated data by no more than a mesh space.

When the velocity discontinuity smoothing region ($0<z<d$) has u_x linearly dependent on z, the unstable perturbations spectrum is upper limited by the wave number value $k^* \approx 1.3/d$ [37]. For $k=2\pi/\lambda<0.4k^*$, the perturbations increments differ from those in the velocity discontinuity problem by less than 10%. The calculations were performed with the spacing scale for velocity discontinuity smoothing $d=0.02$, the harmonic referring to k^* is that of the number $n^* \approx 11$. Harmonics numbered $n>11$ would not grow. But perturbations with harmonic numbers $n \approx 6$ to 11 will grow significantly slower than for velocity discontinuity case.

Small additional harmonics caused by stepwise shape. approximation of theinitial perturbation, and the above considerations both indicate reasonably accurate numerical description of the nonlinear stage of perturbations growth during a limited time. The mathematical viscosity effects analysis made using analytical assessments and by numerically solving supplementary problems, shows the calculation results for $t>2$ are more likely to be qualitative. Good accuracy of the data obtained for $t<2$ has been proved by the calculation with the mesh size taken twice as small.

The numerical solutions were verified for accuracy and representativeness using a calculation involving the velocity discontinuity $\Delta u_x=5$. From criterion (50), the flow like this should by steady with respect to comparatively small 2-D perturbations.

The interface shape as resulting from this calculation is given in Figure 19. Unlike the nonsteady case, there is no perturbations amplitude growth observed here, thus showing qualitative agreement with the conditions of reference [36].

Thus, the following may be concluded from the analyses of the calculation results.

A harmonically perturbed interface will transform with time into a periodic set of spirals. Spiraling is the more rapid, the smaller the density difference between the gases. What was to be observed, that the lateral spiral growth is limited by the value $L \cong 0.7\lambda$, this being due to the periodic nature of initial perturbations. The shear flow instability criterion referring to 2-D perturbations (50) has also proved valid for finite amplitude perturbations.

EVOLUTION OF PERTURBATIONS SPECIFIED SUPERPOSED HARMONICS

Ref. [35] used EGAK codes to continue numerical studies of shear instability problems, particularly, for more difficult initial perturbations cases. These calculations addressed harmonics interactions and the way they influence the gases interpenetrating pattern.

The calculations have been made for gases having one and the same density $\rho_0=1$ and the same pressures $P_0=0.6$. The velocity discontinuity was $\Delta u_x=1$. There were more computational cells used per unit length (60) than in the above-described calculations.

Initially, the interface perturbation was specified as

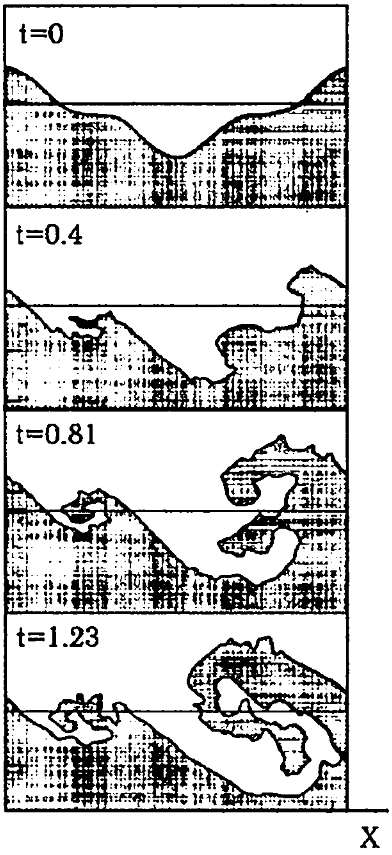

Fig.21.

Interface shape.
Problem №2.

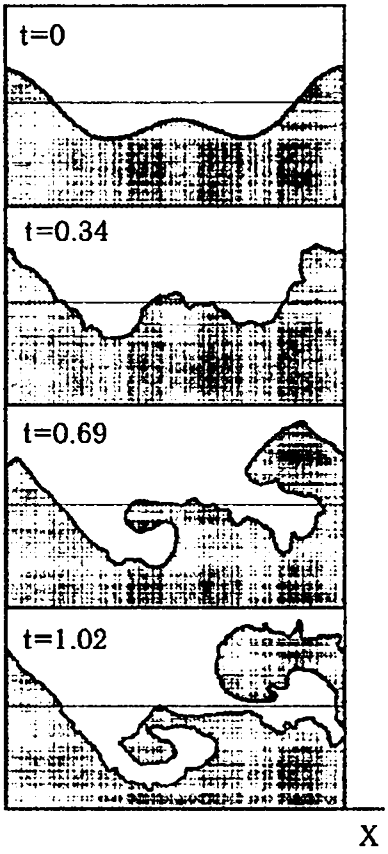

Fig.22.

Interface shape.
Problem №3.

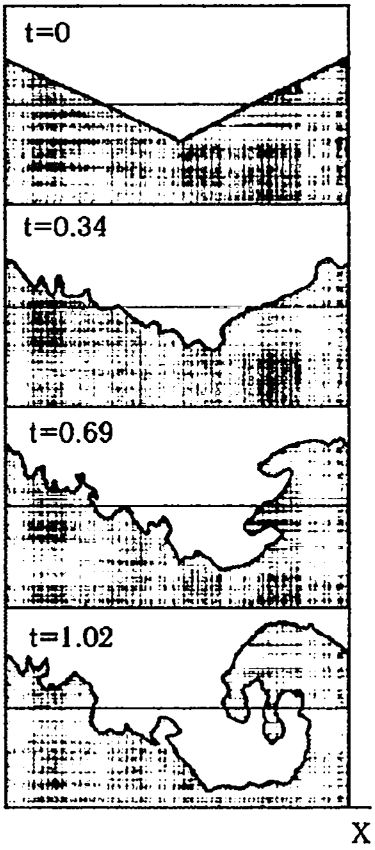

Fig.23.

Interface shape.
Problem №4.

- superposition of two harmonics: $z(t=0,x)=a_1\cos(2\pi x/\lambda_1)+a_k\cos(2\pi x/\lambda_k)$, where $\lambda_k=1/k$ (k=1, 3), and
- saw-tooth shaped.

Table 3 shows some parameters to define initial perturbations.

Table 3. Input parameters and results of the calculations

N	type	A_1	A_2	A_3	A_5	L_0	L
1	-	0.02	-	0.1	-	0.106	0.45
2	-	0.1	-	0.1	-	0.268	0.5
3	-	0.067	0.1	-	-	0.175	0.43
4	saw-tooth	0.082	-	0.03	0.2	0.02	0.43

The following notation is used here:

$A_k=a_k/\lambda_k$ - harmonic amplitude ratio (for saw-tooth type perturbation Fourier coefficients are given),

$L=z_{max}(t,x)-z_{min}(t,x)$ - gas interpenetration thickness

$L_0=z_{max}(t=0,x)-z_{min}(t=0,x)$.

Figure 21 through 23 illustrate the interface shape evolution as obtained in calculations 2 through 4, respectively..

The calculations all observe the gas interpenetration zone stops growing thicker. The final column in Table 3 includes asymptotic values L.

Given the first harmonic has smaller amplitude than the third one (calculation 1), a two-stage flow pattern will be then observed. Initially, there will be the first harmonic rapidly increasing in amplitude, thus making the gas interpenetration zone grow thicker. Over time, the growth rate of L will be decreasing. Then, the increase in L becomes dependent on the amplitude growth of the harmonic of n=3, and thus the zone thickness grows more rapidly. At later times, L growth rate again will decrease. However, when the first harmonic's initial amplitude is larger than that for the harmonic of n=3, no two-stage flow pattern will be observed.

Why the gas interpenetration zone stops growing thicker, can be understood from the following qualitative analogy. By virtue of its periodic nature, the perturbations spectrum is limited and contains for any t only harmonics with the wave number $k \geq 2\pi / L_n$, where L_n is the computational field size in x axis. Shear flow is a rather complex pattern during its nonlinear stage (with a set of spirals forming). If one considers it as averaged flow with continuously distributed velocity, then it should be stable against perturbations having wave number $k > k^* \approx (1-2)/L$ [38]. By times where $L>(1\text{-}2)L_n/2\pi$, this flow should become stable against perturbations having any wave numbers possible.

1.2.3. ON INITIAL PERTURBATION SPECTRA AND CONDITIONS OF GRAVITATIONAL SELF-SIMILAR MIXING REGIME

Usually, gravitational mixing experimental results are analyzed with the assumption that the initial perturbation spectrum is insignificant because it "is not stored in the memory". Acceleration magnitude, g, being constant, one thinks that turbulent mixing zone width, L, depends quadratically on time, i.e. the self-similar function takes place:

$$L=f(A)gt^2, \tag{51}$$

where A is Atwood number. With acceleration changing slightly, variable $X=\left(\int\sqrt{g}\,dt\right)^2$ is introduced instead of gt^2, ex. ref.[23].

Analogues self-similar functions are assumed for values: L_1- penetration depth of a light substance into heavy and L_2- penetration depth of a heavy substance into light ($L_1+L_2=L$).

The experiments, ex. [23] and [39], are analyzed via a mere comparison of self-similar constants f(A) obtained in measurement treatment. These experiments are, mainly, aimed at data acquisition for of different theoretical models of turbulent mixing.

The self-similar statement of a problem must not include the parameters for length dimension, in particular the selected perturbation wavelengths either. In real experiments there are always the parameters for length dimension, for ex. of accelerated layer size. Various physical mechanisms distort perturbation spectrum and inspire the selected harmonics which evolute the fastest. This means that to realize the self-similar regime of mixing in the experiments, a set of requirements should be met:

- mixing zone width must be substantially lesser than the accelerated layer thickness and their transversal dimensions;

physical processes leading to the dominant evolution of the selected harmonics must be minimal;

- by the moment of mixing parameter measurements the initial perturbation spectrum must "be forgotten".

The first requirement depends on the geometrical size of experimental facility and accelerated samples.

The second requirement depends on the real experiment can be violated, for ex., because of the surface tension at liquid-gas or liquid-liquid interface. The surface tension constraints the growing harmonics spectrum in the range of small wavelengths, i.e. the problem contains a supplementary dimensional parameter..

In the experiment this impact can be weakened by the transition to higher acceleration magnitudes when the turbulent mixing is studied. This causes a shift in growing harmonics spectrum boundary to the field of shorter wavelengths, thus reducing the length dimension parameter.

Additional analysis is needed to state the usage of surface-active substances for the same aims, ex. [23]. For example, in ref. [40] it was shown that the surface-active substances available can cause notable attenuation of capillary waves on the liquid surface, i.e. the opposite effect

The most difficult are the questions if the initial perturbation spectrum is really forgotten, what characteristic time for this process is and in how far the extended perturbation spectra are frequent in the uniform spectrum (52) which does not include the length dimension parameter?

$$a_0(k)k=C=\mathrm{Const}, \tag{52}$$

Let us consider the disturbance spectra which originate on the free surface of liquid interface due to heat fluctuations. We shall avail ourselves of Mandelstam analysis results for such fluctuations [44] to explain the peculiarities of light reflection from the different density liquid interface.

Sinusoidal fluctuation amplitude spectrum for square interface surface of DxD dimensions is the following:

$$a_0^2(k)=\frac{4k_BT}{D^2(\sigma k^2+\rho g)}\ , \qquad (53)$$

where k_B is Boltzman constant, T - absolute temperature, σ - surface tension coefficient, g_0 - acceleration of the field of gravity.

At $k>>(\rho g_0/\sigma)^{1/2}$ the spectrum is of a uniform shape

$$a_0(k)k=\sqrt{\frac{k_BT}{D^2\sigma}}=C=\text{Const.} \qquad (54)$$

This means that the thermodynamic fluctuations which are always present in the real experiment, form the uniform spectrum in the short wavelength range.

Now, let us consider the mechanism deforming an arbitrary spectrum of initial perturbations making it more uniform. In the majority of physical experiments the interface region between the substances of different densities starts accelerating with shock or acoustic wave arrival which accompanies Richtmyer-Meshkov instability. The perturbation spectrum formed at the end of this stage is initial for the next stage of gravitational instability evolution at the accelerated interface..

The calculations of RMI non-linear stage have shown that the light liquid penetration depth in the heavy one (in case Atwood number equals a unit) is constrained and depends on the wavelength, $L_l/\lambda\cong0.25$. That means that independent of the initial spectrum, the uniform one is being formed. Primarily, this occurs in the short-length spectrum range because for shorter wavelength, a smaller scale of velocity perturbation and shorter time are required.

The self-similar statement of a problem is not contradicted by mixing constant dependence in eq.(51)not only on Atwood number, but also on dimensionless constant C which characterizes a relative amplitude of initial perturbation.

Let us estimate this dependence with a simple model, taking as an example the case of indefinitely high defference in liquid densities when the instability evolutes with some peculiarities.

The perturbation specified in the form of monochromatic harmonic evolutes in the final asymptotic stage in which independent of the initial perturbation amplitude, the light substance bubbles emerge in the heavy substance at a constant speed, providing that big bubbles emerge to the surface faster. The fluid reaches this stage at the time close to the predicted by small perturbation method.

When the initial perturbation are specified in form of harmonics superposition, long wave perturbations play dominating role in forming the zone of substance interpenetration with time. In case of long-length constrained spectrum due to finite dimensions of accelerated samples, the asymptotic flow pattern is a motion of one bubble.

Based on these peculiar feature, simple mixing models were created, including the models of independent perturbation evolution, for ex. ref.[42]. These models assume that harmonics amplitude grow independently. At the initial stage the amplitude changes according to the linear theory. When the relative amplitude reaches $a_n(t)/\lambda=\alpha$ magnitude, farther it changes at a constant velocity equal to the asymptotic magnitude. The substance interpenetration zone growth velocity equals to harmonics growth velocity, which relative amplitude has reached α magnitude at a given moment. Choosing this magnitude in α=0.2-0.5 interval one can get constant η magnitude in the expression for light substance penetration depth in heavy one

$$L_l=\eta g t^2, \tag{55}$$

close to the experimental data, for ex. in ref.[23].

The more complex models, ex. in ref.[43], assume that the bubbles can unite when approaching each other closer.

Let us consider the mixing model similar to ref.[42] but differing in that the transition from the linear stage to the asymptotic goes continuously in the velocity i.e.

$$\frac{da(k)}{dt}=\begin{cases} a_0(k)\sqrt{gk}\,\mathrm{sh}(\sqrt{gk}\,t) & \text{at } t\le t^* \\ \beta\sqrt{g/k} & \text{at } t\ge t^* \end{cases}, \tag{56}$$

where $a_0(k)$ and $a(k)$ - initial and current perturbation amplitudes with wave number k; $\beta=0.23(2\pi)^{1/2}$;

$$t^*=\frac{1}{\sqrt{gk}}\,\mathrm{Arsh}\left(\frac{\beta}{a_0(k)k}\right). \tag{57}$$

The analysis shows that in case of uniform spectrum $a_0(k)k=C=\mathrm{Const}$, the amplitude growth maximal velocity is realized in the harmonics wave number $k=k^*$ which in the given moment has reached the asymptotic stage of evolution. From eq. (57) it appears that with a specified magnitude t:

$$k^*=\left[\frac{\mathrm{Arsh}(\beta/C)}{\sqrt{gt}}\right]^2$$

Let us consider that this harmonics growth velocity defines the L_l- value growth velocity, i.e.

$$\frac{dL_l}{dt}=\beta\sqrt{g/k^*}.$$

For rather big times when one can neglect initial value $L_l(0)$ compared to its current value L_l, we shall get a self-similar function:

$$h_l=\frac{\beta}{2\,\mathrm{Arsh}\left(\beta/_c\right)}gt^2=\eta t^2 \tag{58}$$

For uniform perturbation velocity spectrum a similar logarithmic function vs. initial perturbation level was obtained in ref. [41].

Difference in experimental self-similar mixing constants obtained in various tests might be related with their dependence on perturbation level, i.e. on constant C.

Let us estimate self-similar constant η for different uniform spectra of initial perturbations with formula (58).

For thermal fluctuations (53), in case of water in the field of gravity $g_0=9.81\,m/s^2$ and for characteristic dimensions D=2 cm, thermal fluctuations spectrum of wavelength less than 1 cm is described by function (54) with $C=10^{-8}$. In this case, $\eta=0.02$.

For the spectrum formed at Richtmyer-Meshkov instability evolution stage, there is an uncertainty in C=0.25-0.5 magnitude which is coupled with identification of final moment in this stage. The corresponding value $\eta=0.18$-0.3 that is a bit higher than the highest value observed in the tests [39].

The estimates obtained give an approximate range of η vs. C value.

At Atwood number $A\cong 1$, the values for η obtained in the experiments differing substantially in the statements, constituted 0.07 in ref. [23] and 0.12 in ref.[39]. The calculation results obtained with numerical model for turbulent mixing [72] and interpolated, give $\eta=0.2$. All values are in 0.02-0.3 range that was derived by the formula (58).

2. TURBULENT MIXING

2.1 USING GAS-DYNAMIC CODES FOR SIMULATION OF TURBULENT MIXING

2.1.1 TURBULENT MIXING MODELING USING EGAK CODES WITHOUT SEMI-EMPIRICAL TURBULENCE MODELS

The direct simulation of various problems involving the mixing of two variable-density media used the EGAK codes [45] without semi-empirical turbulence models. Initial small-scale perturbations of physical quantities were specified in a random manner. Their amplitudes varied. The regions of gas-dynamic flow instabilities demonstrated the growth of quantity fluctuations and the formation of a typical region treated as the turbulent mixing zone. Clearly, the behavior of fluctuations is influenced by the features of a specific computational scheme including artificial viscosity decreasing the fluctuation amplitudes.

TURBULENT MIXING UNDER CONSTANT ACCELERATION

A series of computations was made using the computational domain represented by a 20x20 cm square. The gravity acceleration is directed opposite to z axis. For $0 < z < 10$, the gas with the density $\rho_1 = 1$ was introduced, and the gas which corresponded to $10 < z < 20$. The equation of state of a perfect gas was used for both media. The sound speed was chosen relatively high to consider the media incompressible. The cell sides were 0.2x0.2 cm for the majority of computations. The normal velocity component was zero on the boundary of the computational region. In the vicinity of the interface, randomly distributed density perturbations were set for t=0 with the amplitude being 10% of the density of a heavier material.

The computations were performed for $\delta=\rho_2/\rho_1=3$, 7, 20, 70. with various values of g= 0.1, 1, 10, 100.

Figure 24 presents the dependencies of the total mixing zone width on the deceleration path $S=gt^2/2$, obtained for g =10 with $\delta=3$, 7. The same Figure shows the data for $\delta=20$, 70 with g=1.

The analysis of these dependencies can reveal three typical phases of mixing process:

- initial phase where the solution transits to the self-similar mode;
- self-similar phase where the mixing zone width L linearly depends on the interface travel path S;
- the phase where the relation L(S) is no longer linear (L> 3-4 cm), and the quantity dL / dS decreases due to the rigid walls.

The comparison of computations involving various g values shows that the zone growth rate dL / dS does not depend on g in the linear phase.

The computations where initial perturbations were specified in different ways (random density perturbations were specified in 1, 2, 4 boundary point layers or

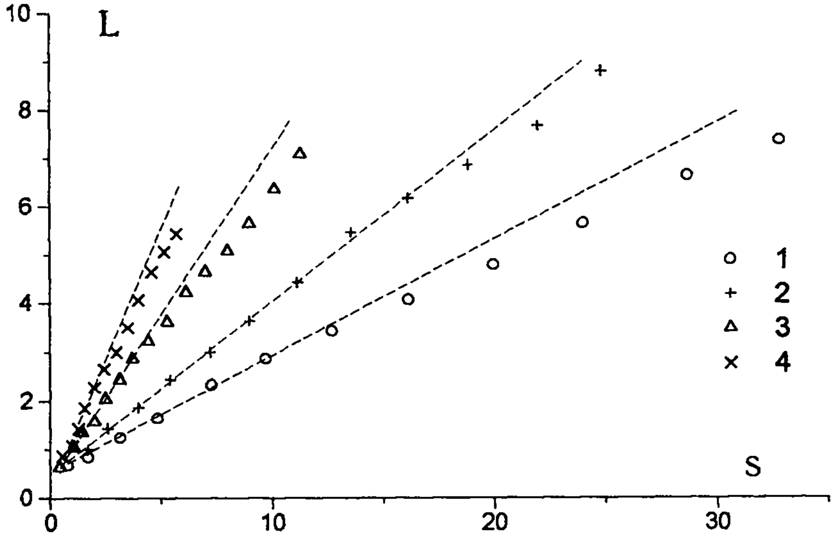

Fig.24. Turbulent mixing zone width vs. deceleration path. Direct gravitational turbulent modeling with 2D EGAK code.
1 - δ=1.66, 2 - δ=3, 3 - δ=20, 4 - δ=70.

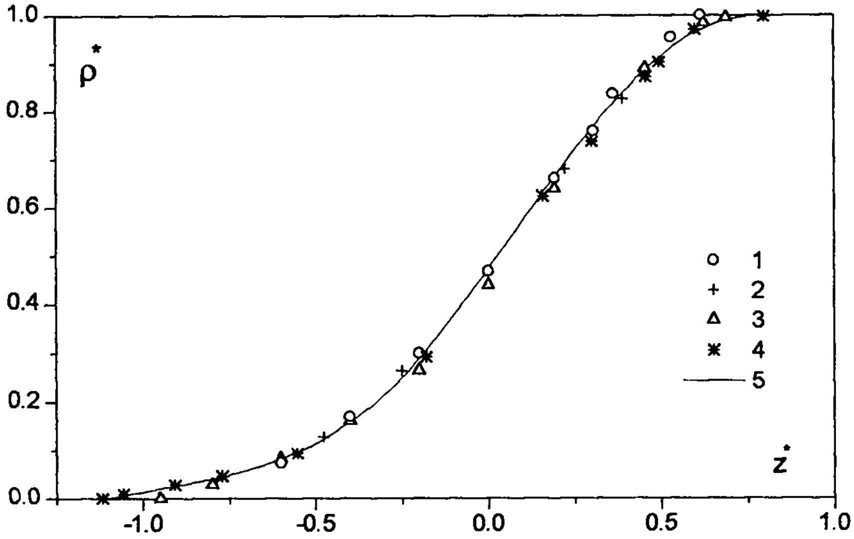

Fig.25. Self similar density profile. Direct turbulent modeling with 2D EGAK code.
1 - δ=3, 2 - δ=7, 3 - δ=20, 4 - δ=70, 5 - VIKHR code.

random velocity perturbations were set in one boundary layer) showed that dL / dS is not actually influenced by how the perturbations are specified in the linear phase.

The data obtained suggest that the computations actually demonstrate the self-similar mode with L< 3-4 cm (except for the initial phase).

It is shown that for $\delta = 3, 7$ the influence of walls on the mixing zone growth rate is manifested even with a relatively small zone width that is 20-30% of the spacing between the walls.

Figure 25 contains dimensionless density profiles in the mixing zone, $\rho^*(z^*)$ computationally obtained for $\delta=\rho_2/\rho_1=3$, 7, 20, 70. (the curves 1, 2, 3, 4, respectively), where $\rho^*=(\rho-\rho_2)/(\rho_2-\rho_1)$, $z^*=z/(z_{0.9}-z_{0.1})$. The values of z are counted from the original position of the interface; $z_{0.9}$, $z_{0.1}$ - correspond to the coordinates where $\rho^*=0.9$ и $\rho^*=0.1$. To generate these profiles, the densities were first averaged over z and then over time reducing them to the mixing zone width. This figure presents a general profile independent on δ obtained with the phenomenology "VIKHR" (curve 5). The dependencies $\rho^*\left(z^*\right)$ are nearly the same for δ=3, 7, 20,70 in the range $0.05<z<0.95$ and approach the curve 5.

Some discrepancies between 2-D EGAK data and VIKHR results are observed only at the mixing zone edges and the discrepancy decreases with δ increase and eventually disappears almost completely with δ=70.

This seems to result from the fact because of limited number of cells 2-D computations do not allow to achieve sufficiently large effective Reynolds number relative to the computational scheme viscosity. In the first approximation this Reynolds number is proportional to the amount of cells in the mixing zone therefore the zone edges resulting from distant single jets are described inaccurately in the computations. The relative smallness of Reynolds number is manifested to a great extent for low δ. For relatively large δ, it is proportional to $\rho' \approx \delta^{0.5}$ where ρ' is the magnitude of density fluctuations in the mixing zone. Another effect of the relative smallness of effective Reynolds number is that the computational material diffusion decreases the density fluctuation in the mixing zone. For example, all computations demonstrated the relative mean square density fluctuations $R^2 = \left\langle \rho'^2 \right\rangle / \rho^2$ 1.5-1.7 times lower than $R^2 = (\delta - 1)^2 c(1 - c)$ obtained for heterogeneous mixing. Here c is the specific concentration of a component.

In the self-similar mode the turbulent mixing zone linearly depends on the deceleration path; $L^*=F(A)S$ where $A=(\delta-1)/(\delta+1)$, L^* is the spacing between the points for which $\rho=\rho_1+0.1(\rho_2-\rho_1)$ and $\rho=\rho_1+0.9(\rho_2-\rho_1)$. Here L^* is used instead of the total width to prevent the effect of the above mentioned uncertainties in the computations of the mixing zone edges.

Figure 26 shows the relation F(A) obtained from 2-D EGAK computations (curve 2). The same figure presents a similar dependence from VIKHR computations (curve 1). The figure indicates that the two curves are close. However, the value F obtained from 2-D computations for all δ of interest is 1.1-1.2 times greater than that from the phenomenology model. Note also that the total mixing zone width from VIKHR computations is 2 times greater than L^*.

The computations gave additional data to verify the description accuracy of VIKHR type methods for the density profile and the dependence of the mixing zone

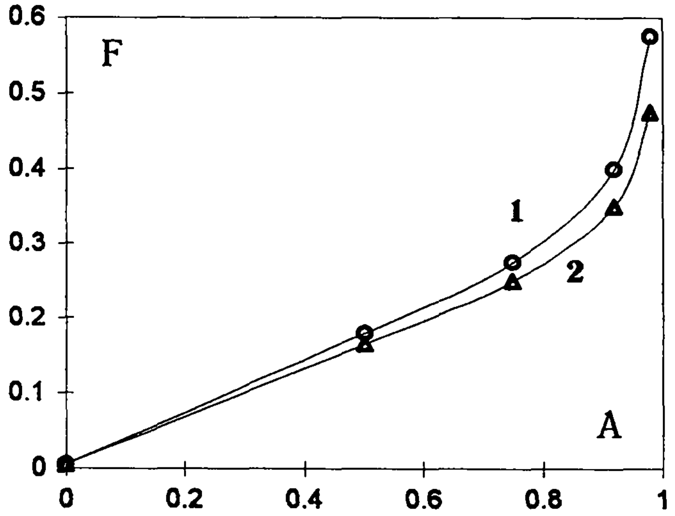

Fig.26. Value of F as function of Atwood number.
1 - VIKHR code; 2 - direct gravitational turbulent modeling with 2D EGAK code.

growth rate on δ since both are determined by great vertices and must differ for 2-D and 3-D cases

THE SHOCK MOTION THROUGH THE MIXING ZONE

Consider the shock motion across a rest-state medium where chaotic density perturbations are set [45]. The wave scattering on these perturbations lead to pulsed motion behind the wave front. At the front, the variation of the mean half square of the pulsed velocity component, u_l', normal to the front is:

$$\Delta e_l = \Delta\left(\frac{1}{2}\left\langle u_l'^2\right\rangle\right) = \frac{1}{2} b^2 R^2 \left(f_l \Delta u\right)^2,$$

$$R^2 = \frac{\left\langle \rho'^2 \right\rangle}{\rho}, \qquad f_l = \frac{1}{R^2} \sum_{n=2}^{\infty} (-1)^n \frac{\left\langle \rho'^n \right\rangle}{\rho^n},$$

where Δu is the mass velocity increment at the shock front b=0.5 within the limit of a strong shock wave. These expressions can be easily obtained with $R^2 << 1$ by using mass, energy and momentum conservation laws.

The value of Δe_l at the wave front is primarily determined by the difference in the accelerations of particles with different densities. These accelerations mainly follow the normal to the front, so we can expect that the values Δe_l will be close in two and three dimensions. However the turbulence decay should differ behind the front in 2-D and 3-D cases.

To model the shock motion across the variable density region, a series of 2-D computations was performed. The computations used a square grid with one side oriented to the wave motion direction. The density perturbations were randomly specified in groups of four cells (2x2 cells). The values R^2, f_l and the shock amplitude were varied. The value of e_l before the shock front was zero and was determined by averaging over several times. The first ten row terms were considered to determine . f_l. Table 4 contains initial data and some computational results.

Table 4. Computational conditions and results

Δu	R^2	f_l	Δe_l	b
2.43	0.0033	1	0.0028	0.54
2.43	0.03	1.06	0.02	0.45
0.23	0.0033	1	0.000021	0.49
0.446	0.03	1.06	0.0008	0.49

The values of b was given by

$$b^2 = \frac{2\Delta e_l}{R^2 f_l^2 \Delta u^2}.$$

The values of b obtained here agree well with the expected value b = 0.5 for a strong shock thus 2-D simulation leads to correct quantitative results in this case.

GAS MODEL EXPERIMENTS

The EGAK codes were used for a series of 2-D computations [45] to model the flow in one of the experiments reported in [46]. The computations were performed in r-z geometry: $0<r<10$cm, $0<z<5$cm. The region $0<r<6$cm is filled with helium having the density 1.663 10^{-4}g/cm^3, and the region $6<r<9.5$cm contained air with the density 1.205 10^{-3}g/cm^3. The initial parameters to normal conditions for $P=1$ at and $T=20$°C. In the region $9.5 \leq r \leq 10$ cm (a gas with the density 9.6 10^{-3}g/cm^3) an instantaneous energy release was specified corresponding to the experiment. Randomly distributed helium density perturbations were set for air-helium interface.

A series of computations was made where the density perturbations and cell size were varied.

Figure 27 contains the constant density lines for several times within a single computation. This figure illustrates the turbulence history.

Figure 28 shows the computational data illustrating how the amplitude of initial density perturbations influences the mixing zone size. The density was perturbed in one layer of helium cells with h=0.125 cm. The peak perturbation amplitude was varied within 0.5% -20% the average helium density. The points 1, 2, 3, 4, 5 correspond to the variations of 0.5%, 2%, 5%, 10%, 20%. The same plot presents the date from the computations where the density was perturbed in two layers of boundary helium cells with the amplitude being 10% of the average density (points 6). Experimental data are given for comparison (points 7).

The figure shows that the mixing zone width is actually independent on the specified perturbation and agrees with the experiment when the perturbation is set in one cell and the amplitudes vary from 0.5 to 10%. The dashed lines correspond to the averaged curves . For large amplitudes (20%) or for greater mixing zone size, the zone growth rate is much higher than on the experiment.

The computations were also performed where the cell sizes were varied. The density perturbation with 10% amplitude was specified in one cell layer these computations indicate that the mixing zone growth rate does not depend on cell sizes for a relatively fine grid.

The total computational mixing zone width growth rate was found to be slightly higher than in the experiments. This is illustrated by Figure 29 that shows the mixing zone width as a function of time on computations (curve 1) and in experiment (curve 2). In addition to the relation $L(t)$ obtained in the experiment [46], Figure 29 contains a similar dependence (curve 3) derived from on improved experiment processing method accounting the "spikes" and "cavities" at the mixing zone edge. The discrepancy between computational and experimental zone growth rates is more pronounced in the deceleration phase of the interface (t<90 mks) and in the inertial phase (t>100mks). The changes in the mixing zone width immediately after the reflected wave arrival (90mks<t<100mks) in computations are close to the experiment which qualitationly corresponds to the data reported in precious sections.

MODELING OF TURBULENT MIXING IN SHEAR FLOWS

Reference [47] considers the following problem (Figure 30). Region 1 ($y>0$) and Region 2 ($y<0$) contain perfect gases with initial densities ρ_1 and ρ_2 and pressure $P_1=P_2$. The gas in Region 1 moves following the interface along x axis with

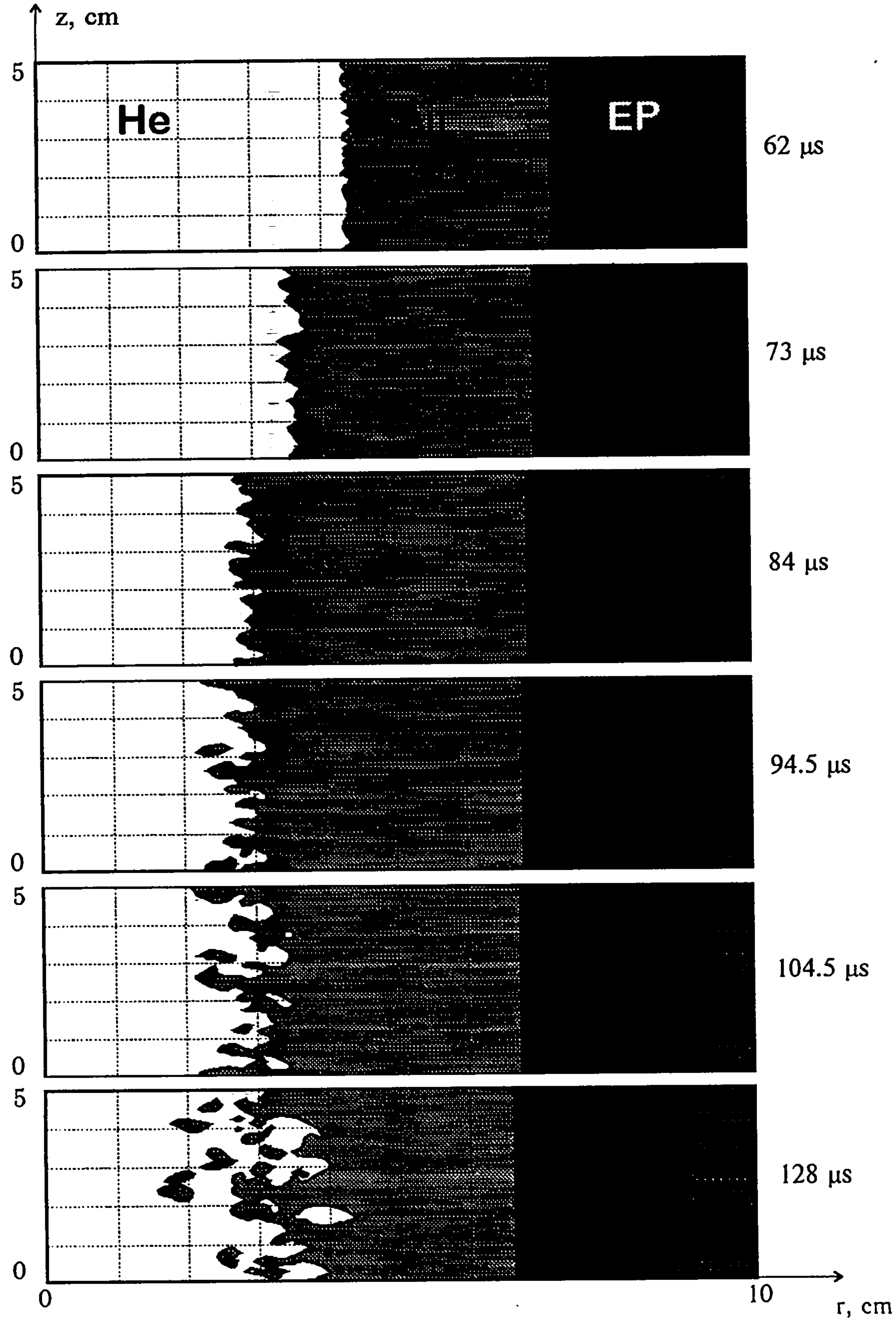

Fig. 27 Direct 2D EGAK code modeling of turbulent mixing. Calculation of cylindrical shock tube experiment.

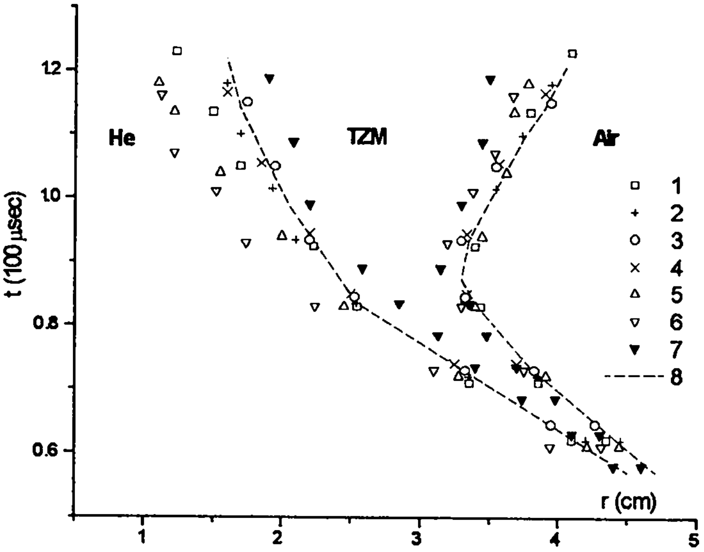

Fig.28. R-t diagram of turbulent mixing zone boundaries. Direct 2D calculation of the experiment [46] with EGAK code.

1 - $\delta\rho$=0.5%; 2 - $\delta\rho$=2%; 3 - $\delta\rho$=5%; 4 - $\delta\rho$=10%; 5 - $\delta\rho$=20%;

6 - $\delta\rho$=10% (doubled thickness of initially perturbed layer);

7 - experiment; 8 - averaged computational curve.

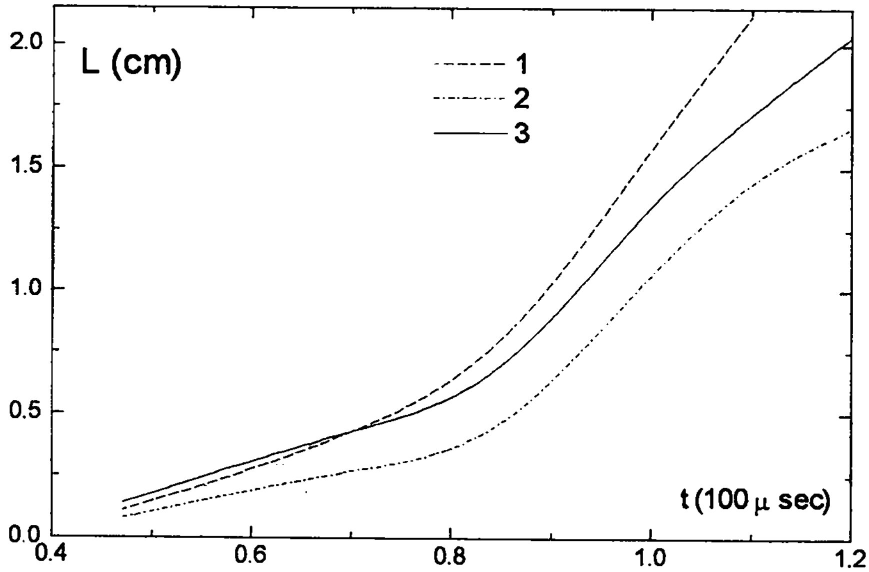

Fig.29. Turbulent mixing zone width dependence on time.

1 - direct modeling, 2 - experiment [46], 3 - experiment [46] (more precize treatment).

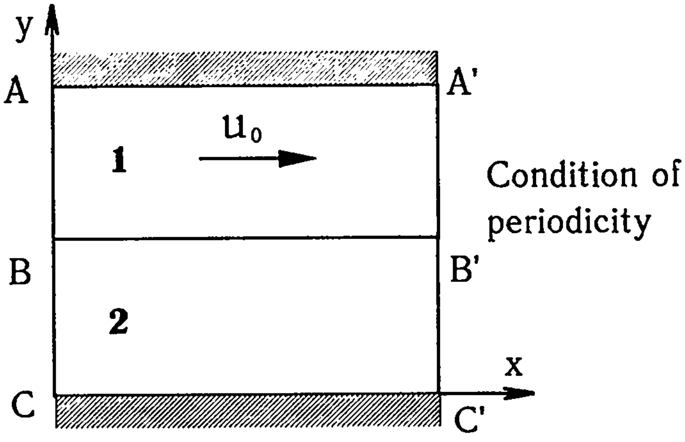

Fig.30. Initial geometry for EGAK calculations of shear flow mixing.

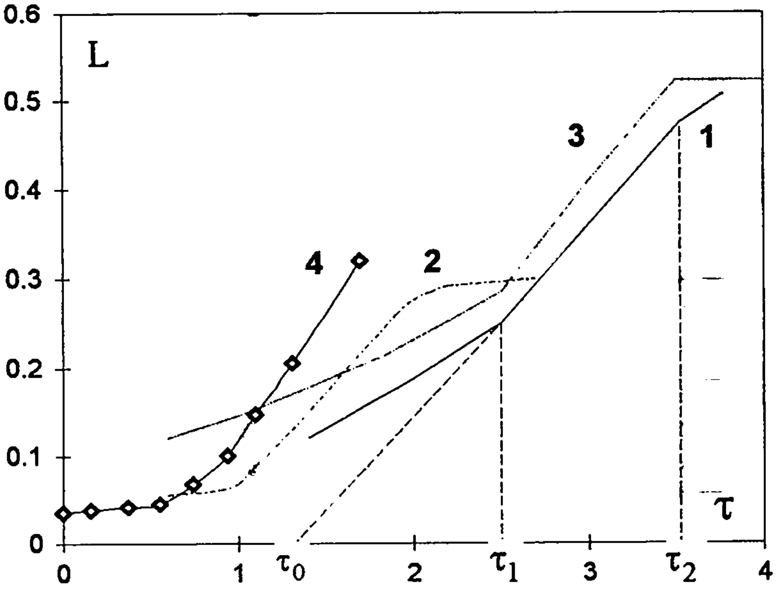

Fig.31. Turbulent mixing zone width vs. time. Direct 2D EGAK code modeling of shear flow mixing. Curve numbers correspond to problem numbers in Table 5.

a velocity $\vec{u}_0 = (u_0, 0)$, and the gas in Region 2 is at rest. The normal velocity component was zero at the boundaries AA′ and CC′ initially, random perturbations of the normal velocity component, w, are set in all the interface. The perturbation amplitude $|w| = \text{Const} = 0.1\,u_0$ and the sign was varied randomly (differing from one computation to another). The application has the following dimensionless parameters:

$$\delta = \frac{\rho_2}{\rho_1}, \quad \delta w = \frac{|w|}{u_0}, \quad \delta h = \frac{h}{\lambda},$$

where h is the cell size.

The solution will be represented as dimensionless functions

$$U(\xi,\eta,\tau)=u(x,y,t)/u_0; \quad R(\xi,\eta,\tau)=\rho(x,y,t)/\rho_1,$$

where $\xi=x/\lambda$; $\eta=y/\lambda$;$\tau=tu_0/\lambda$.

Table 5. Presents initial data for these computations.

Table 5. Initial data.

version	δ	δh	AC/CC'
1	1	1/30	1
2	1	1/60	1
3	10	1/30	2
4	10	1/60	1

The flow evolution typical for all cases of interest is illustrated by Fig.32. The figure shows the constant density lines for version 4.

The next figures contain the computational results averaged over x.

Figure 31 gives the mixing zone width L as a function of time. L was defined as a distance where the averaged velocity x component <U> varied from 0.01 to 0.99. Line in the case of gravitational mixing considered earlier three main phases of mixing history can be also distinguished:

- initial phase where the solution transits to the self-similar mode $\tau<\tau_1$;
- self-similar phase demonstrating the linear dependence of L on τ; $\tau_1<\tau<\tau_2$;
- the phase where $L(\tau)$ is not longer linear and $dL/d\tau$ decreases, $\tau>\tau_2$.

Figure 33, 34 present the profiles of $\langle U(\mu)\rangle$ for the computations 1 and 2. The solid lines correspond to self-similar solutions obtained with the semi-empirical model where $\mu=\eta/S(\tau)$; $S(\tau)=12\alpha^2(\tau-\tau_0)$; $\alpha=0.09$ [47]. The values of τ_0 are given in Figure 32.

Figure 35 and 36 contain the $\langle R(\mu)\rangle$ and $\langle U(\mu)\rangle$ for computation 3. Figure 33-36 relate to the second phase of the self-similar turbulent mode. As is seen from figures, the phase shows a good agreement between the averaged theoretical data and corresponding semi-empirical model predictions. The comparison is made with theory only because the experiments directly related to this problem do not exist. The validity of semi-empirical model was verified [47] by the experiments with stationary shear flows [49-52]. Those data agree well with the self-similar stationary solution.

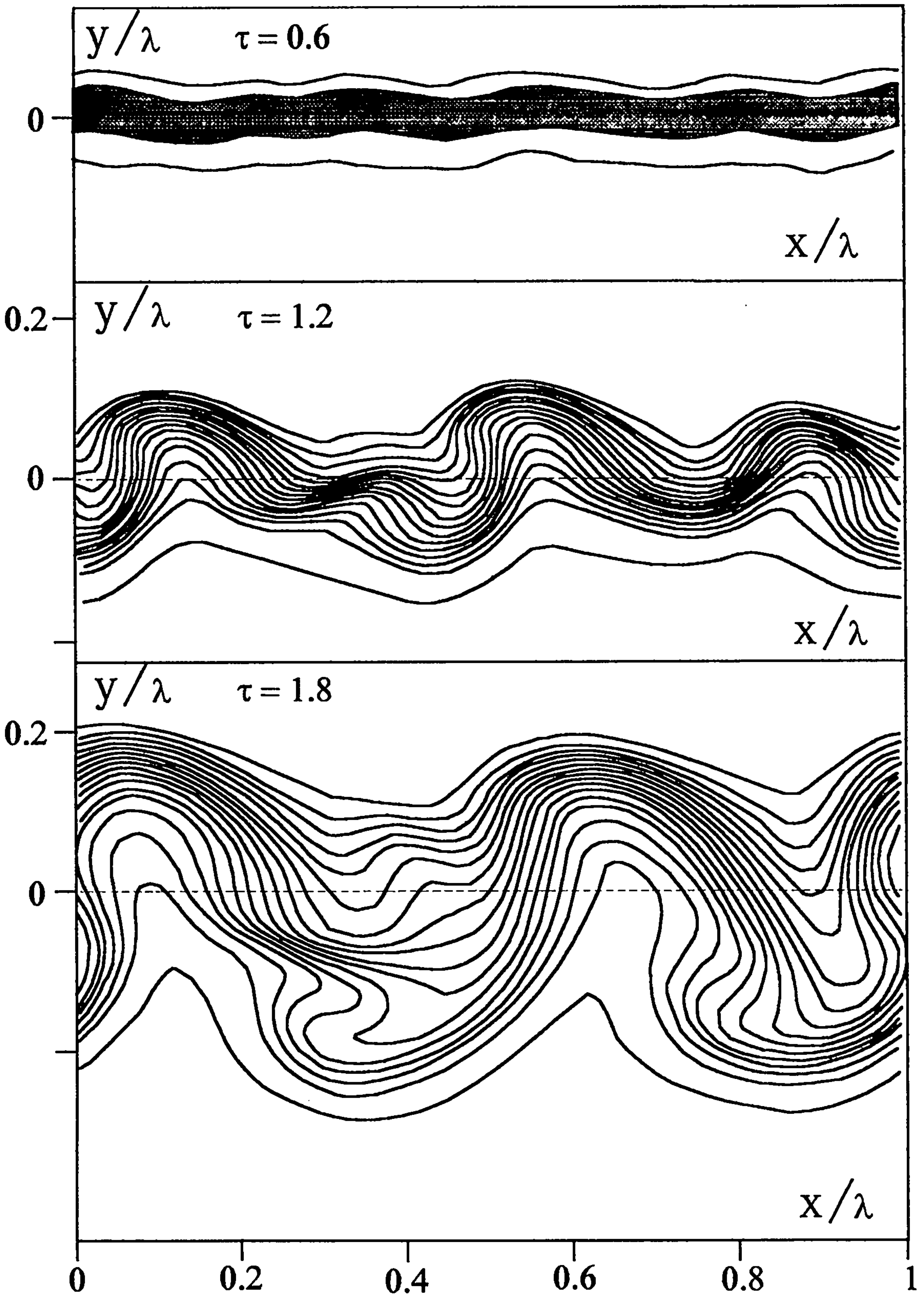

Fig.32. Direct 2D EGAK code modeling of turbulent mixing in shear flows. (problem № 4). Isodenses with $\Delta\rho=0.667$.

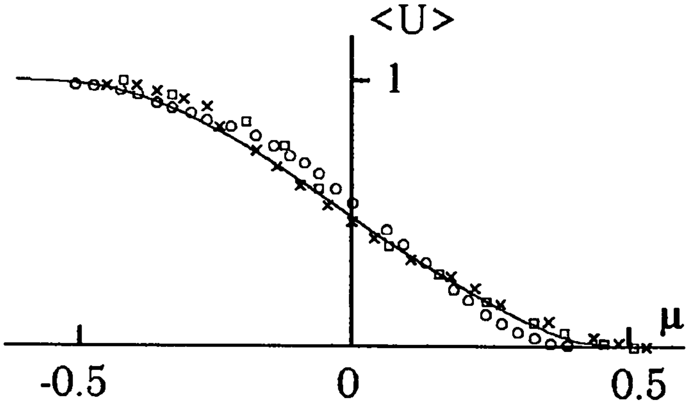

Fig.33. Averaged velocity profile.
Direct 2D modeling of turbulent mixing in shear flows
EGAK code (task №1): □ - t=2.21; X - t=2.52; O - t=3.77;
——— -semiempirical model.

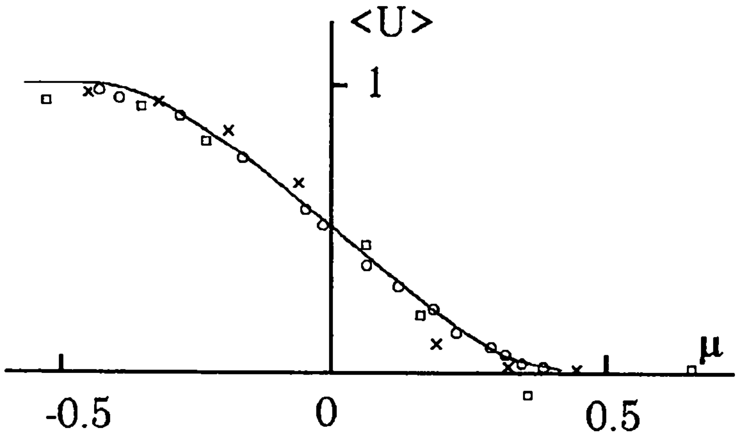

Fig.34. Averaged velocity profile.
Direct 2D modeling of turbulent mixing in shear flows
EGAK code (task №2): □ - t=0.94; X - t=1.25; O - t=1.88;
——— -semiempirical model.

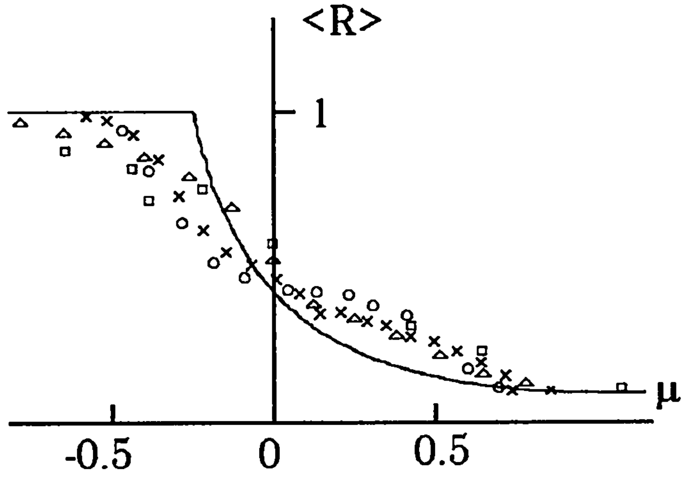

Fig.35. Averaged density profile.
Direct 2D modeling of turbulent mixing in shear flows
EGAK code (task №3): □ - t=2; Δ -t=2.5, X - t=3.5; O - t=4.7;
——— - semiempirical model.

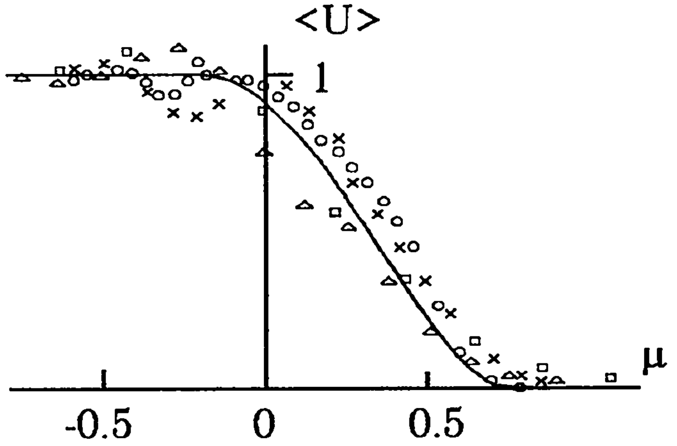

Fig.36. Averaged velocity profile.
Direct 2D modeling of turbulent mixing in shear flows
EGAK code (task №3): □ - t=2; Δ -t=2.5, X - t=3.5; O - t=4.7;
——— - semiempirical model.

A slower growth rate of the mixing zone in the third phase ($\tau > \tau_2$) is explained by the effect of boundary conditions which is important when the zone width becomes comparable with the computational domain size.

The studies of turbulent mixing using direct 2-D simulation show that it can give an acceptable description of turbulent flow parameters for some applications. However this approach has several disadvantages:

- direct simulation cannot adequately describe the small-scale turbulence structure on a limited number of cells;
- 2D simulation cannot in principle describe 3-D effects of the real turbulence.

2.1.2. EGAK MODELING OF TURBULENT MIXING USING SEMI-EMPIRICAL MODELS

There is a broad class of 2-D applications that require to account gravitational and tangent mixing types both separately and in combination. Using direct numerical 2-D hydrodynamics simulation for such applications is possible though it does not always lead to acceptable results. Therefore the most realistic way is to use the codes implementing semi-empirical turbulent mixing models within 2-D hydrodynamic methods.

There exist multiple papers devoted to numerical simulation of gravitational and tangent turbulent mixing (the review of this paper can be found, for example, in [54]). Because of relative simplicity, two-parameter $k-\varepsilon$ models are the most commonly used. Only a few papers consider the gravitational and tangent turbulent mixing in combination.

The EGAK codes use Lagrangian-Eulerian gas-dynamic method described in Section 1.1.3 to implement a two-parameter $e-Q$ model ($k-\varepsilon$ model analog) describing turbulent mixing in a general case of 2-D compressible flows.

TURBULENT MIXING MODEL

The model relies upon the following assumptions:

- the medium represents a mixture of components;
- each component (fluid or gas) is described by a full set of thermodynamic parameters, mass and concentration;
- the mixture is isotropic;
- the component pressures are equated that is $P_i = P$.

The equations for quantities averaged over chaotic fluctuations can be written in the form of conservation laws for a volume V moving with the velocity $\vec{u}^*$.

The equations have the following form:

continuity equations for the i component

$$\frac{dM_i}{dt} + \int_{S_i} \rho_i(\vec{u}_i - \vec{u}^*)d\vec{S} = C_\alpha \int_V \operatorname{div}(\rho D \nabla \alpha_i)dV; \qquad (59)$$

motion equation

$$\frac{d\vec{J}}{dt} + \int_S \rho\vec{u}(\vec{u} - \vec{u}^*)d\vec{S} = \int_S P\,d\vec{S} + \int_V \operatorname{div}\sigma_T dV; \qquad (60)$$

energy equation for the i component

$$\frac{dE_i^{(f)}}{dt} + \int_{S_i} \rho_i E_i(\vec{u}_i - \vec{u}^*)dS = \underbrace{C_E \int_V \operatorname{div}(\rho D \nabla E_i)\, dV}_{\{1\}} +$$

$$+\int_S \left(P + P_T\right)(\vec{u} - \vec{w})d\vec{S} - \int_V Q\, dV; \tag{61}$$

volume conservation equation for the i component

$$\frac{dV_i}{dt} + \int_{S_i} (\vec{u}_i - \vec{u}^*)d\vec{S} = \underbrace{\int_{S_i} \vec{u}_i\, d\vec{S}}_{\{2\}} - \mathrm{DIF}(V_i) \tag{62}$$

The notation corresponds to that from Section 1.1.3.

The second term from the l.h.s. represents the quantity variations due to convective transfer. The terms marked with {1} express the quantity changes due to turbulent diffusion, {2}- due to pressure forces (including turbulent pressure), {3}- due to energy dissipation. The term DIF(V_i) from equation (62) is responsible for relative variation of component volumes under turbulent diffusion.

The following notation is used above:

P_T - turbulent pressure,

σ_T - Reynolds stress tensor,

Q - dissipation rate of turbulent energy e,

$\rho = \left(\sum_{i=1}^{N} \frac{\alpha_i}{\rho_i}\right)^{-1}$ - average density.

The differential equations for turbulent quantities have the form:

turbulent energy equation

$$\frac{de}{dt} = G_1 + G_2 - \frac{1}{\rho}\operatorname{div}\rho e \vec{W} - Q - \frac{2}{3} e \operatorname{div}(\vec{u} - \vec{w}) + C_e \frac{1}{\rho}\operatorname{div}\rho D \nabla e \tag{63}$$

dissipation rate equation

$$\frac{dQ}{dt} = \frac{Q}{e}\left[C_{q_1}(G_1 + G_2) - C_{q_2} Q\right] - \frac{4}{3} Q \operatorname{div}(\vec{u} - \vec{w}) -$$

$$-\operatorname{div} Q\vec{W} + C_q \frac{1}{\rho}\operatorname{div}\rho D \nabla Q \tag{64}$$

where $G_1 = D\left(\frac{\partial u_i}{\partial x_k}\right)^2$, $G_2 = \vec{W}\frac{\nabla P}{\rho}$ - are the terms generating the turbulence

Equations (59)-(64) are closed with the following relations:

for Reynolds stress tensor and turbulent pressure

$$\sigma_T = -\rho D\left(\frac{\partial u_j}{\partial x_k} - \frac{\partial u_k}{\partial x_j}\right) + \frac{2}{3}\rho e\delta_{jk},$$

$$P_T = \frac{2}{3}\rho e, \tag{65}$$

for turbulent diffusion coefficient

$$D = C_D \frac{e^2}{Q}, \tag{66}$$

for turbulent flow $\vec{W}$

$$\vec{W} = D\vec{A}, \tag{67}$$

where $\vec{A} = \dfrac{\nabla P}{\left(\rho\lambda_1 + \dfrac{T}{\rho C_V}\lambda_2^2\right)} - \dfrac{\nabla\rho}{\rho}$, $\lambda_1 = \left.\dfrac{\partial P}{\partial \rho}\right|_T$, $\lambda_2 = \left.\dfrac{\partial P}{\partial T}\right|_S$, $C_V = \left.\dfrac{\partial e}{\partial T}\right|_\rho$.

For the perfect gas

$$\vec{A} = \frac{\nabla P}{\gamma P} - \frac{\nabla \rho}{\rho}, \tag{68}$$

where γ is the adiabatic index.

At the shock front, the turbulent diffusion coefficient is taken to be equal to that before the front and the generating term

$$G_2 = b\vec{W}\frac{\nabla P}{\rho}, \text{ where } b=0.5.$$

The above system contains several constants $C_E, C_e, C_q, C_D, C_{q1}, C_{q2}, C_\alpha$ that can be determined either from theoretical considerations or from comparison of computations with test experiments.

The constants are given in Table 6.

Table 6. Constants values

C_E	C_e	C_q	C_D	C_{q1}	C_{q2}	C_α
2	2	3	0.75	1.55	2	3

Note that the coefficient C_{q2} is chosen from theoretical considerations based on experimental data on the attenuation of uniform isotropic turbulence. The values of remaining constants are taken from test computations given below.

EQUATION APPROXIMATIONS

The finite-difference approximation of equations (59)-(68) is performed in Lagrangian-Eulerian variables on a moving quadrangular grid in several steps using split-step method.

The first step determines the velocity variations due to the deviator terms of stress tensor, the diffusion coefficient D and the quantities $\vec{A}$, $\vec{W}$.

The second step solves gas-dynamic equations in Lagrangian variables including turbulent pressure. To do this, implicit difference scheme is used (Section 1.1.3).

The third step approximates the equations for turbulent energy and dissipation rate without diffusion terms as will as the terms of energy equations for the components related to the turbulent flow and turbulent energy dissipation. The approximation uses the schemes giving a positive solution.

The fourth step approximates the convective terms of equations (59)-(63) For the problems of interest, we assume that a mixture with donor cell parameters flows from one mixed cell to another.

The fifth step approximates the diffusion terms of equations (59)-(63).The difference scheme is described in [15]. After the component diffusion is computed the component volume concentrations are updated to equate the pressures [16].

The entire difference scheme has the first order accuracy over time and space. The number of components both in computational domain and in a mixed cell is unlimited.

SOME COMPUTATIONS

The above method was used for a series of computations of turbulent mixing history under various conditions. Some computations corresponded to the problems from Section 2.1.1. Chaotic initial perturbations required for direct numerical simulation are not necessary for the computations using semi-empirical model. In this case three first problems described below are one-dimensional. Therefore the computations with 2-D method used only three computational cells along the mixing zone to which is the minimum required amount to implement the periodicity requirement along the medium motion. A square grid was used containing 0.1x0.1 cells.

MIXING AT THE INTERFACE OF VARIABLE-DENSITY INCOMPRESSIBLE FLUIDS UNDER CONSTANT ACCELERATION

The problems set-up is similar to that from Section 2.1.1. The computations were made for $\delta=1.66$, 3, 7, 20.

The computational results agree well with VIKHR data [46]. Figure 37 shows the mixing zone width as a function of the quantity L as a function of the deceleration path $S=0.5gt^{2}$. The quantity L was defined as a distance where the volume concentration of one of materials varied from 0.01 to 0.99. The figure shows that these dependencies are linear, as expected. They can be represented as

$$L = F\left(\frac{\delta-1}{\delta+1}\right)S$$

The plot for F function obtained from these computations is given in Fig.38 in comparison with VIKHR data. The same figure contains direct numerical simulation data from Section 2.1.1.

The self-similar nature of the flow is also confirmed by the similarity of density profiles computed at various times. These profiles for $\delta=3$ and $\delta=20$ are given in Figure 40 where the following notation is adopted: $\tilde{\rho}=\frac{\rho-\rho_1}{\rho_2-\rho_1}$ - dimensionless

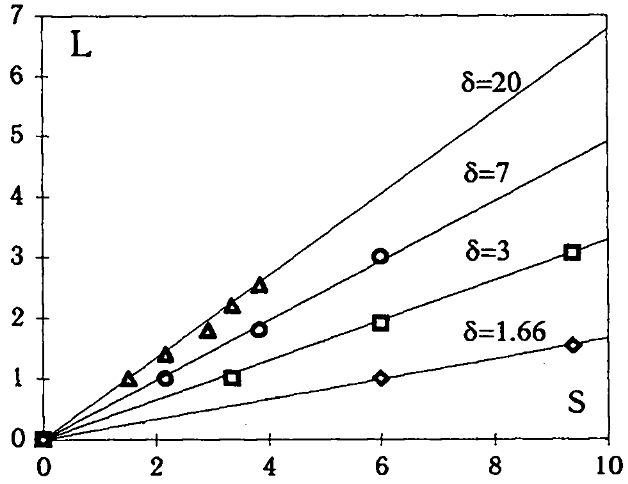

Fig.37. Gravitational turbulent mixing zone width dependence on deceleration path. Calculations with e-Q model.

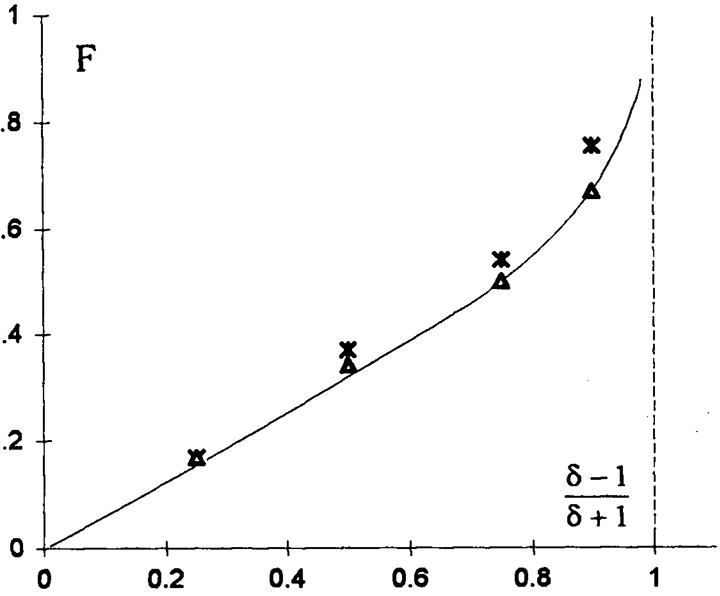

Fig.38. Value F dependence on Atwood number.
—— VIKHR code;
Δ - e-Q model;
ж - direct 2D EGAK modeling.

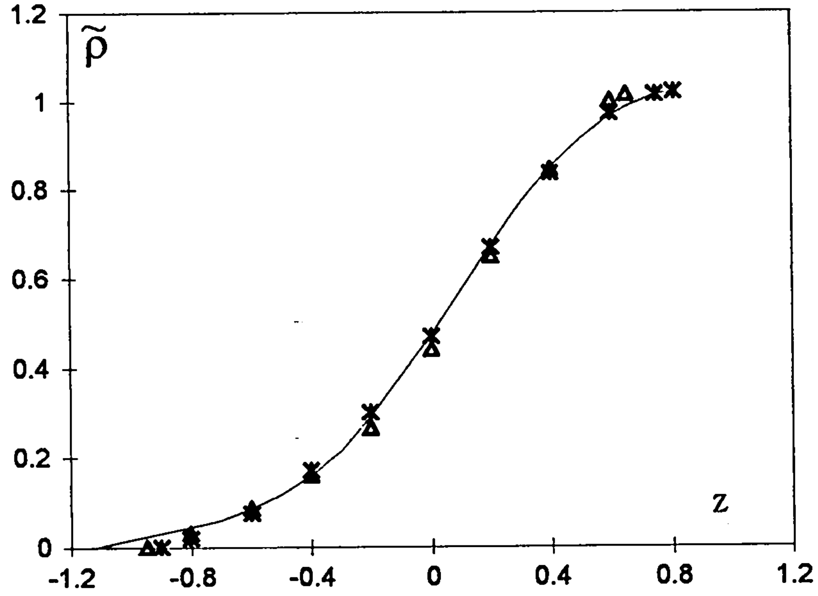

Fig.39. Self similar density profile. Gravitational turbulent mixing calculations.
——— - VIKHR code;
ж - e-Q model (δ=3); Δ - e-Q model (δ=10).

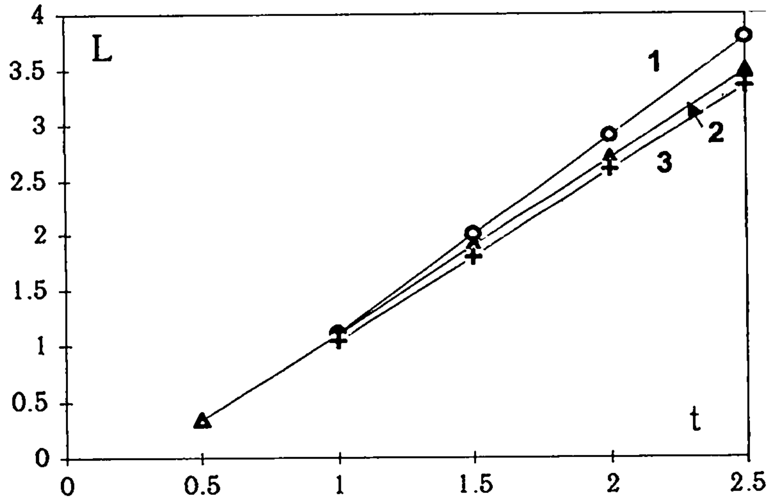

Fig.40. Turbulent mixing zone width vs. time. Calculations of shear flow mixing with e-Q model.
1 - δ=1, 2 - δ=3, 3 - δ=10.

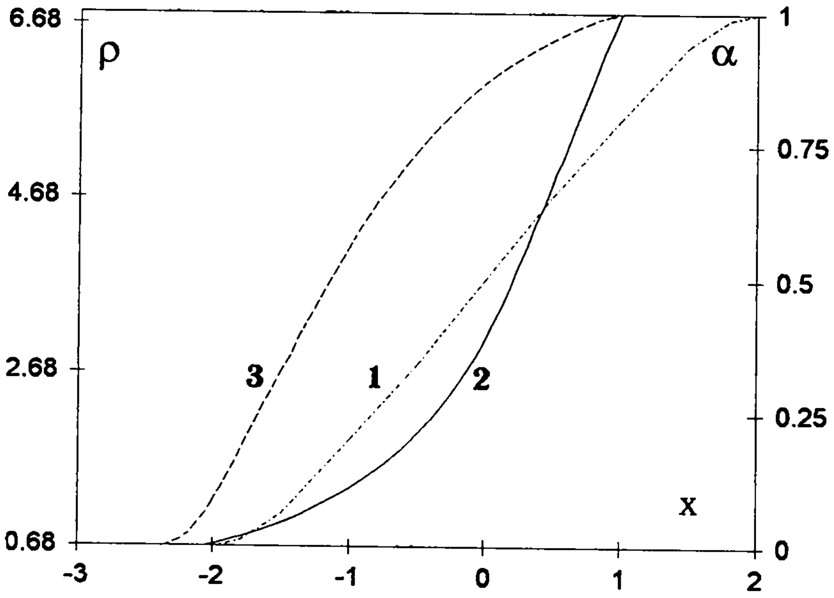

Fig.41. Mass concentration α and density ρ profiles.
Calculations of shear flow mixing with e-Q model.
1 - mass concentration ($\delta=1$);
2 - density ($\delta=10$);
3 - heavy substance mass concentration ($\delta=10$).

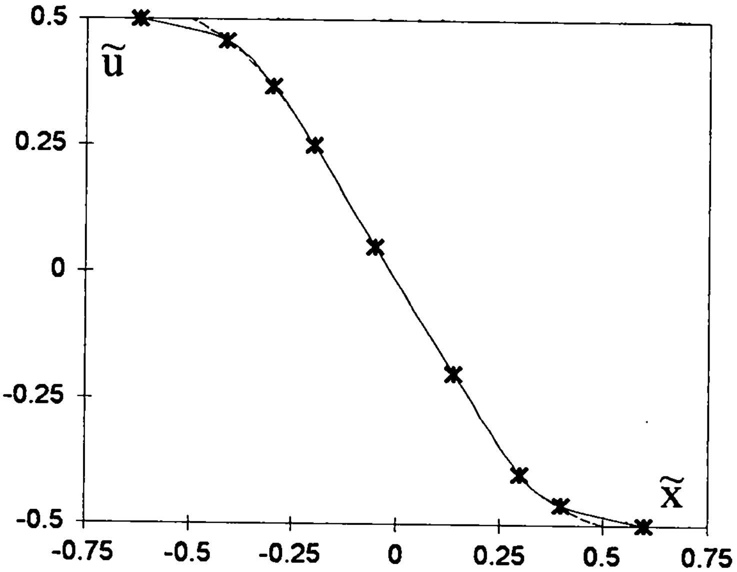

Fig.42. Self similar tangential velocity component profile in shear flow turbulent mixing zone.
················ - semi empirical theory [47];
———— - e-Q model (t=2.5);
ж - e-Q model (t=1.5).

density; $\tilde{z} = \frac{z}{z_{0.9} - z_{0.1}}$ - dimensionless coordinate. The length unit is represented by spacing between $z_{0.1}$ and $z_{0.9}$ points where $\tilde{\rho} = 0.1$ and $\tilde{\rho} = 0.9$, respectively. Note that the density profiles are actually independent on δ for these variables.

TANGENT MIXING

The problem set-up is similar to that from Section 2.1.1.

A tangent velocity discontinuity $u_0=6$ was taken for the plane interface of to incompressible fluids. The normal velocity component was taken to be zero. The computations were made for $\rho_2=\rho_1$ ($\delta=1$), $\rho_2=3\rho_1$ ($\delta=3$) and $\rho_2=10\rho_1$ ($\delta=10$) for $\rho_1=0.68$.

Figure 40 shows the mixing zone width as a function of time as given by the computations. L was defined as a distance where the volume concentration of one of materials varied from 0.01 to 0.99. These dependencies enter the self-similar mode with time. For $\delta=1$ the growth rate of the mixing zone width is 2 in the self-similar phase which corresponds to the value from [47]. The growth rate decreases with increasing δ.

Figure 41 contains the mass concentration profile for one material from the computations with $\delta=1$ at time t=2.5. The same figure shows the density and mass concentration profiles for the heavy material for $\delta=10$, at time t=2.5.

Figure 42 present the self-similar profiles $\tilde{u}(\tilde{x})$, of tangent velocity component at various times together with the self-similar solution from [47].

Analytical and numerical data agree well.

TANGENT-GRAVITATIONAL MIXING

Initially, two incompressible fluids with various densities ($\rho_2=3\rho_1$, $\rho_1=0.68$), are separated by a plane interface (Fig.43). The fluids move with a constant velocity along the boundary containing the velocity jump u_0. The gravity g is directed perpendicular to the interface. This problem combines two problems mentioned above.

It can be shown that for $g > 0$ the mixing zone growth faster than in tangent or gravitational cases. The zone stopes growing for $g < 0$. The expression for the limit zone width L has the form:

$$L = A\frac{u_0^2}{g}. \qquad (69)$$

The proportionally coefficient A was determined computationally. Initial data for five computations are given in Table 7.

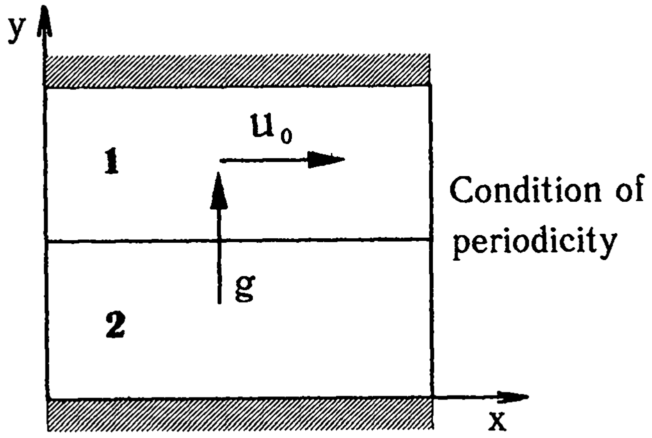

Fig.43. Initial geometry for EGAK calculations of shear flow-gravitational mixing.

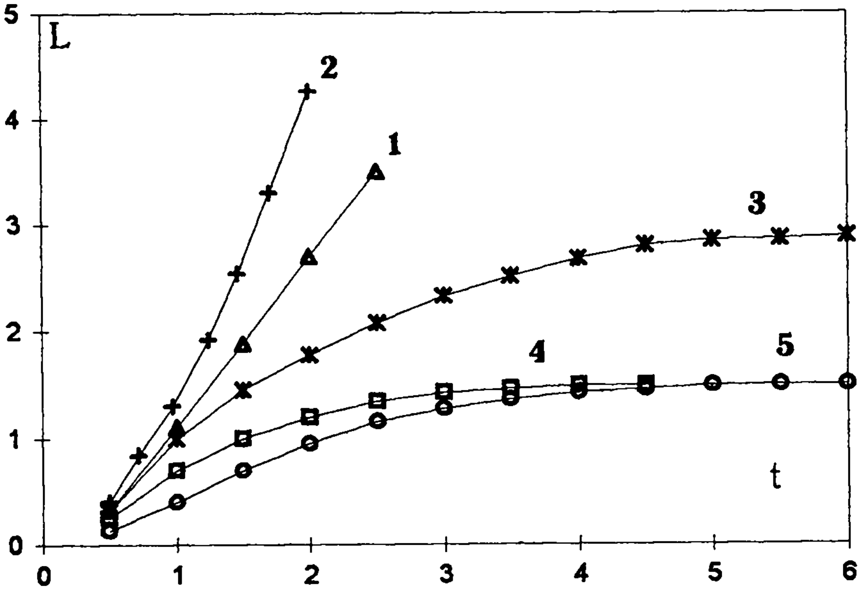

Fig.44. Turbulent mixing zone width dependence on time. Calculations of shear flow - gravitational mixing.
1 - $g=0$, $u_0=6$; 2 - $g=+10$, $u_0=6$; 3 - $g=-10$, $u_0=6$;
4 - $g=-20$, $u_0=6$; 5 - $g=-10$, $u_0=4.24$.

Table 7. Initial data

Computation	g	u_0
1	0	6
2	+10	6
3	-10	6
4	-20	6
5	-10	4.24

The computations completely confirm the above arguments about the mixture of the mixing zone growth (see Figure 44). For all three computations with $g<0$, the coefficient was actually the same ($A = 5/6$). For $g > 0$, the mixing zone width grew much faster than in either of the above cases.

A JET FROM A RESERVOIR

For various applications, it is interesting to consider the jet flowing from a reservoir and the mixing with the environment.

A code using the semi-empirical turbulence model computed a 2-D nonstationary problem describing the injection of a nitrogen jet to air. The initial temperatures of the two gases were 20 °C with the pressures 1 at. The inut diameter was d=1.25cm. The jet velocity $u = 1020$ m/s was taken to be constant in terms of cross-section. The phenomenon was studied experimentally on [53].

Figure 45 shows isolines of nitrogen volume concentration at three times. The jet is highly smeared and come apex is close to the experimental value ($tg\alpha \approx 0.09$) on the portion of the steady-state flow. The early time jet path $L/d \cong 14$, computationally defined as the distance where the nitrogen concentration is $\beta > 0.95$ at the symmetry axis, is also close to the experiment.

Figure 46 shows the nitrogen volume concentration profile in the cross-section perpendicular to the symmetry axis x/d=21.6 at the time t=2.8ms when the flow is close steady-state here. The experimental data from [53] are also presented.

We can note that computational data agree well with experiment in the steady-state portion.

The semi-empirical $e-Q$ model implemented within EGAK codes allows to compute a wide spectrum of turbulent flows.

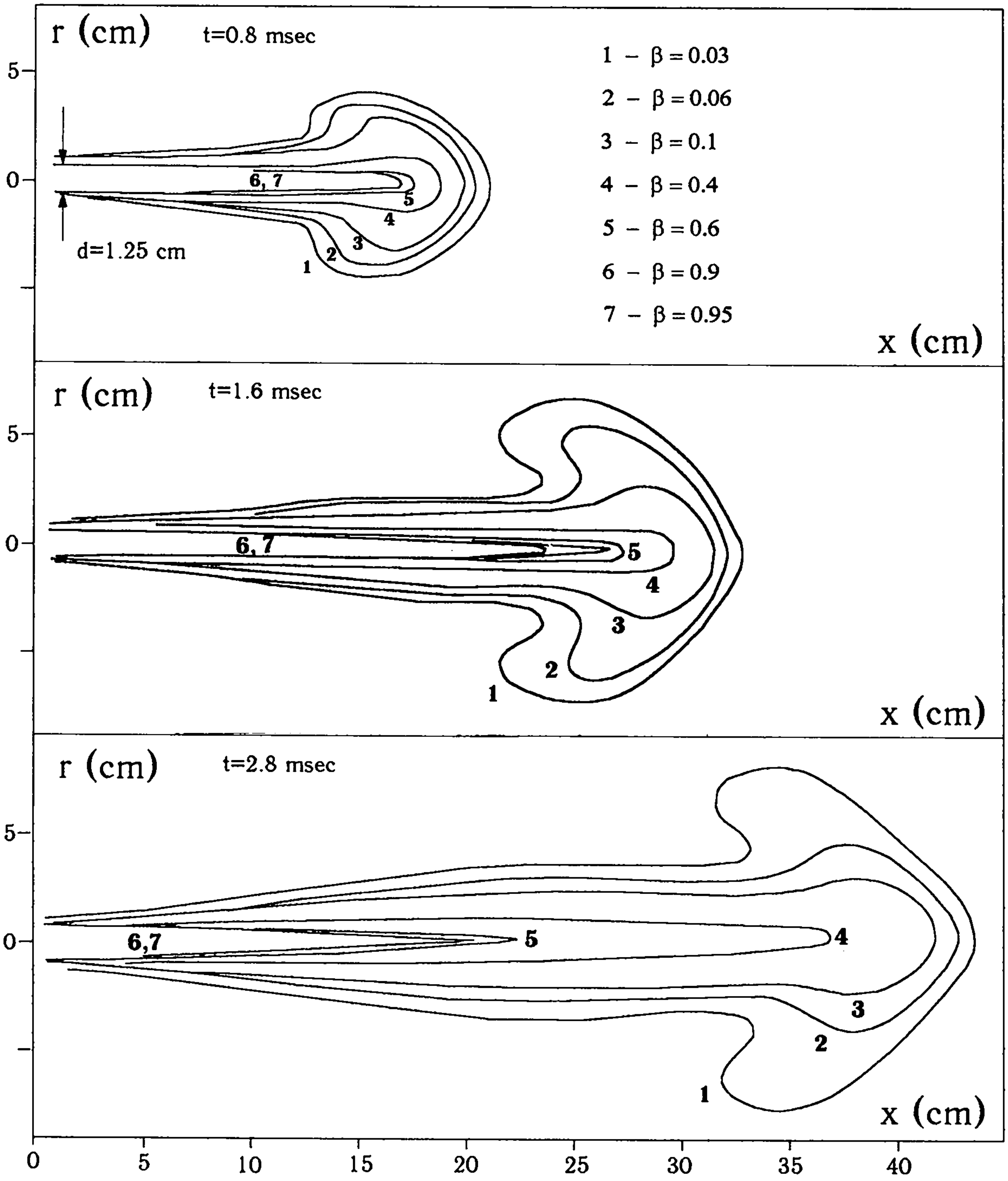

Fig.45. Nitrogen jet in air calculated with e-Q model. β - Nitrogen volume concentration. Curves correspond to constant β values.

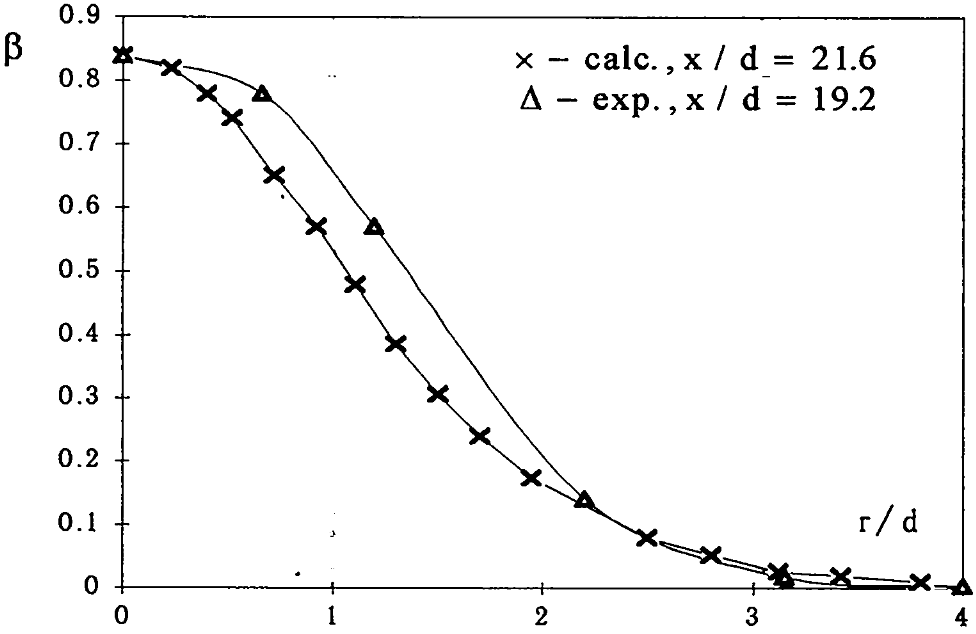

Fig.46. Nitrogen volume concentration profile.

2.2.SEMIEMPIRICAL MULTIFLOW MODEL.

2.2.1. FORMULATION OF EQUATIONS.

We will formulate a semiempirical set of equations describing turbulent flow, based on simultaneous gasdynamics equations for a viscous medium representing a mixture of different substances:

$$\begin{aligned}
&\frac{\partial \rho}{\partial t}+\frac{\partial \rho u_j}{\partial x_j}=0 \ , \\
&\frac{\partial \rho u_i}{\partial t}+\frac{\partial \rho u_i u_j}{\partial x_j}=-\frac{\partial P}{\partial x_i}+\frac{\partial \Sigma_{ij}}{\partial x_j}, \\
&\frac{\partial \rho E}{\partial t}+\frac{\partial \rho E u_j}{\partial x_j}=-P\frac{\partial u_j}{\partial x_j}+\Sigma_{ij}\frac{\partial u_i}{\partial x_j}-\frac{\partial}{\partial x_j}q_j^{(E)}, \\
&\frac{\partial \rho \alpha_k}{\partial t}+\frac{\partial \rho \alpha_k u_j}{\partial x_j}=\frac{\partial}{\partial x_j}q_j^{(\alpha_k)}.
\end{aligned} \tag{70}$$

here, ρ is the density, u_i- i-th velocity component, and P- pressure; E- specific internal pressure, α_k- mass concentration of k-th mixture constituent $(0 \le \alpha_k \le 1)$, $\Sigma_{ij}=\rho\nu_0\left(\frac{\partial u_i}{\partial x_j}+\frac{\partial u_j}{\partial x_i}-\frac{2}{3}\delta_{ij}\frac{\partial u_l}{\partial x_l}\right)$ - viscous tensor (ν_0-viscosity factor), $q_j^{(E)}, q_j^{(\alpha_k)}$ - molecular energy and mass fluxes of mixed constituents.

Recurring induces will hereafter imply summation, unless otherwise specified.

Then, what is generally to be done is express all the quantities in the expanded form $Y=\langle Y\rangle+Y'$, where $\langle Y\rangle$ is the average value and Y' - fluctuation surplus.

By substituting these expansions into (70) and averaging, we have the following set of equations for averaged quantities:

$$\begin{aligned}
&\frac{d\langle\rho\rangle}{dt}=-\langle\rho\rangle\frac{\partial V_j}{\partial x_j}, \\
&\frac{dV_i}{dt}=-\frac{1}{\langle\rho\rangle}\frac{\partial\langle P\rangle}{\partial x_i}+\frac{1}{\langle\rho\rangle}\frac{\partial 2\rho\Phi_{ij}}{\partial x_j}, \\
&\frac{d\mathcal{E}}{dt}=-\frac{\langle P\rangle}{\langle\rho\rangle}\frac{\partial\left(V_j-W_j\right)}{\partial x_j}-\frac{1}{\langle\rho\rangle}\frac{\partial}{\partial x_j}\langle\rho\rangle\left(W_j^{(0)}-W_j\mathcal{E}\right)-\frac{\partial}{\partial x_j}q_j^{(E)}+Q^{(E)}, \\
&\frac{dc_k}{dt}=-\frac{1}{\langle\rho\rangle}\frac{\partial}{\partial x_j}\langle\rho\rangle\left(W_j^{(k)}-W_jc_k\right), \quad k=1\cdots n.
\end{aligned} \tag{71}$$

These equations use the following notation:

$$\frac{d}{dt}\equiv\frac{\partial}{\partial t}+V_j\frac{\partial}{\partial x_j};$$

$V_i=\frac{1}{\langle\rho\rangle}\langle\rho u_i\rangle=\langle u_i\rangle+\frac{1}{\langle\rho\rangle}\langle\rho' u_i'\rangle$ -Favre average velocity;

$\mathcal{E}=\frac{1}{\langle\rho\rangle}\langle\rho E\rangle=\langle E\rangle+\frac{1}{\langle\rho\rangle}\langle\rho' E'\rangle$ - Favre average energy:

$c_k = \frac{1}{\langle\rho\rangle}\langle\rho\alpha_k\rangle = \langle\alpha_k\rangle + \frac{1}{\langle\rho\rangle}\langle\rho'\alpha'_k\rangle$ - Favre average concentration;

$W^{(k)} = \frac{1}{\rho}\left\langle(\rho\alpha_k)' u'_1\right\rangle$; here k=1...n;

$W_i^{(0)} = \frac{1}{\langle\rho\rangle}\left\langle(\rho E)' u'_i\right\rangle$, here k=0;

$\Phi_{ij} = \left(\varepsilon_{ij} - \frac{W_i W_j}{2}\right)$ - total turbulent energy;

$W_i = \sum\limits_k W_i^{(k)} = \frac{1}{\langle\rho\rangle}\langle\rho' u'_i\rangle$, (k=1...n, where n is the number of mixed constituents);

$$\varepsilon_{ij} = \frac{1}{2}\left(\langle u'_i u'_j\rangle + \frac{1}{\langle\rho\rangle}\langle\rho' u'_i u'_j\rangle\right);$$

$Q^{(E)} = \frac{1}{\langle\rho\rangle}\left\langle\Sigma_{ij}{}' \frac{\partial u'_i}{\partial x_j}\right\rangle$ -viscous dissipation of turbulent energy;

$q_j^{(E)}$-heat flux due to radiant or electronic heat conduction.

The equations (71) should be added by the mixture equation of state $\langle P\rangle = P(\langle\rho\rangle, \mathcal{E})$.

These equations were formulated assuming Reynolds number for turbulence high and Mach number small. This made it possible to neglect some terms in the equations., such as $\frac{1}{\langle\rho\rangle}\frac{\partial\langle\Sigma_{ij}\rangle}{\partial x_j}$ in the equation for V_i, $\frac{1}{\langle\rho\rangle}\langle\Sigma_{ij}\rangle\frac{\partial\langle u_i\rangle}{\partial x_j}$ in the equation for $\mathcal{E}$, and also discount the heat flux due to molecular heat conduction and molecular diffusion as well.

This written set of equation is not closed, for the quantities ε_{ij}, $W_i^{(k)}$, $W_i^{(E)}$, $Q^{(E)}$.have not been defined. They also require pertinent equations to be formulated. To formulate the equations, we will consider by now that the medium is incompressible and, generally, has variable density. We will include compressibility correction later.

The equation for ε_{ik} is obtained in a usual fashion (see [60]) and expressed as follows:

$$\frac{d\varepsilon_{ik}}{dt} = -\frac{1}{\langle\rho\rangle}\frac{\partial}{\partial x_j}\left\{\frac{1}{2}\langle\rho\rangle\langle u'_i u'_k u'_j\rangle + \frac{1}{2}\langle\rho' u'_i u'_k u'_j\rangle - \langle\rho\rangle W_j \varepsilon_{ik}\right\} - \tag{72}$$

$$-\frac{1}{2\langle\rho\rangle}\left\{\frac{\partial\langle P' u'_i\rangle}{\partial x_k} + \frac{\partial\langle P' u'_k\rangle}{\partial x_i}\right\} - \left\{\Phi_{ij}\frac{\partial(V_k - W_k)}{\partial x_j} + \Phi_{kj}\frac{\partial(V_i - W_i)}{\partial x_j}\right\} -$$

$$-\frac{1}{2}\left\{W_i\frac{d(V_k - W_k)}{dt} + W_k\frac{d(V_i - W_i)}{dt}\right\} - L_{ik}^{(\varepsilon)} - Q_{ik}^{(\varepsilon)}.$$

The notation included here is

$$L_{ik}^{(\varepsilon)} = -\frac{1}{2\langle\rho\rangle}\left\{\left\langle P'\frac{\partial u_i'}{\partial x_k}\right\rangle + \left\langle P'\frac{\partial u_k'}{\partial x_i}\right\rangle\right\}; \quad Q_{ik}^{(\varepsilon)} = \frac{1}{2\langle\rho\rangle}\left\{\Sigma_{ij}'\frac{\partial u_k'}{\partial x_j} + \Sigma_{kj}'\frac{\partial u_i'}{\partial x_j}\right\};.$$

The equation for correlation $\left\langle(\rho\alpha_k)' u_i'\right\rangle = \langle\rho\rangle W_i^{(k)}$ is

$$\frac{d\langle\rho\rangle W_i^{(k)}}{dt} = -\frac{\partial}{\partial x_j}\left\{\left\langle m_k' u_i' u_j'\right\rangle - W_j\left\langle m_k' u_i'\right\rangle\right\} - \left\langle m_k' u_i'\right\rangle\frac{\partial V_j}{\partial x_j} - \left\langle m_k' u_j'\right\rangle\frac{\partial(V_i - W_i)}{\partial x_j} -$$

$$-\left\langle u_i' u_j'\right\rangle\frac{\partial\langle\rho\rangle c_k}{\partial x_j} - \frac{1}{\langle\rho\rangle}\left\langle\rho' m_k' F_i\right\rangle - \langle\rho\rangle Q_i^{(W)}, \tag{73}$$

where $m_k' = (\rho\alpha_k)'$,

$$Q_i^{(W)} = \frac{1}{\langle\rho\rangle^2}\left\langle\Sigma_{ij}'\frac{\partial m_k'}{\partial x_j}\right\rangle + \frac{1}{\langle\rho\rangle^2}\left\langle m_k'\frac{\partial P'}{\partial x_j}\right\rangle + \frac{1}{\langle\rho\rangle}\left\langle u_i'\frac{\partial\left(q_j^{\alpha_k}\right)'}{\partial x_j}\right\rangle,$$

$$F_i = \frac{\partial\left(\langle u_i\rangle + u_i'\right)}{\partial t} + \left(\langle u_j\rangle + u_j'\right)\frac{\partial\left(\langle u_i\rangle + u_i'\right)}{\partial x_j}.$$

Further, there will be needed an equation for correlation $\langle\rho' m_k'\rangle = \langle\rho\rangle^2 B^{(k)}$. It is expressed as

$$\frac{d\langle\rho\rangle^2 B^{(k)}}{dt} = -\frac{\partial}{\partial x_j}\left\{\left\langle\rho' m_k' u_j'\right\rangle - W_j\left\langle\rho' m_k'\right\rangle\right\} - 2\left\langle\rho' m_k'\right\rangle\frac{\partial V_j}{\partial x_j} + \left\langle\rho' m_k'\right\rangle\frac{\partial W_j}{\partial x_j} -$$

$$-\left\langle m_k' u_j'\right\rangle\frac{\partial\langle\rho\rangle}{\partial x_j} - \left\langle\rho' u_j'\right\rangle\frac{\partial\langle\rho c_k\rangle}{\partial x_j} - \langle\rho\rangle^2 Q^{(B_k)}. \tag{74}$$

where $Q^{(B_k)} = \frac{1}{\langle\rho\rangle}\left\langle m_k'\frac{\partial u_j'}{\partial x_j}\right\rangle + \frac{c_k}{\langle\rho\rangle}\left\langle\rho'\frac{\partial u_j'}{\partial x_j}\right\rangle + \frac{1}{\langle\rho\rangle^2}\left\langle\rho'\frac{\partial\left(q_j^{\alpha_k}\right)'}{\partial x_j}\right\rangle.$

The equations for correlations $\langle H' u_i'\rangle = \langle\rho\rangle W_i^{(0)}, \langle\rho' H'\rangle = \langle\rho\rangle^2 B^{(0)}$, where $H' = (\rho E)'$, have similar forms, though with $\mathcal{E}, H', q_j^{(E)}$ included instead of $c_k, m_k', q_j^{(\alpha_k)}$, respectively.

There are some third-order correlations included in the equations for second-order correlations. These are:

$$D_{ikl} = \frac{1}{2}\left\langle u_i' u_k' u_l'\right\rangle, D_{ik}^{(k)} = \frac{1}{2\langle\rho\rangle}\left\langle m_k' u_i' u_k'\right\rangle, D_i^{(k)} = \frac{1}{\langle\rho\rangle}\left\langle\rho' m_k' u_i'\right\rangle.$$

The following equations are to be obtained for these correlations

$$\frac{dD_{ikn}}{dt}=-\frac{\partial}{\partial x_j}\left\{\frac{1}{2}u'_iu'_k\,u'_nu'_j-W_jD_{ikn}\right\}-D_{ikn}\frac{\partial W_j}{\partial x_j}-$$
$$+\sum_{ikn}\left\{D_{ikn}-\frac{1}{2}W_j\langle u'_iu'_k\rangle\right\}\frac{\partial(V_n-W_n)}{\partial x_j}+$$
$$+\frac{1}{2}\sum_{ikn}\langle u'_iu'_k\rangle\left\{\frac{dW_n}{dt}+\frac{2}{\langle\rho\rangle}\frac{\partial\langle\rho\rangle\Phi_{nj}}{\partial x_j}\right\}-\frac{1}{2}\sum_{ikl}\langle\rho'u'_iu'_kF_n\rangle-Q^{(D)}_{ikn}, \tag{75}$$

$$Q^{(D)}_{ikn}=\frac{1}{\langle\rho\rangle}\sum_{ikn}\left\langle\Sigma_{ij}\frac{\partial u'_ku'_n}{\partial x_j}\right\rangle-\frac{1}{\langle\rho\rangle}\sum_{ikn}\left\langle P'\frac{\partial u'_iu'_k}{\partial x_n}\right\rangle.$$

The symbol $\sum\limits_{ikn}$ in (75) signifies summation over all permutations of indices.

$$\frac{dD^{(k)}_{ik}}{dt}=-\frac{1}{\langle\rho\rangle}\frac{\partial}{\partial x_j}\left\{\frac{1}{2}\langle m'_ku'_iu'_ku'_j\rangle-W_jD^{(k)}_{ik}\right\}+\frac{1}{2\langle\rho\rangle}\langle u'_iu'_k\rangle\frac{\partial\langle\rho\rangle W^{(k)}_j}{\partial x}-$$
$$-\sum_{ik}\left(D^{(k)}_{ik}-\frac{1}{2}W^{(k)}_jW_j\right)\frac{\partial(V_k-W_k)}{\partial x_j}-D_{ikj}\frac{1}{\langle\rho\rangle}\frac{\partial\rho c_k}{\partial x_j}+ \tag{76}$$
$$+\sum_{ik}\frac{1}{2}W^{(k)}_i\left\{\frac{dW_k}{dt}+\frac{2}{\langle\rho\rangle}\frac{\partial\langle\rho\rangle\Phi_{kj}}{\partial x_j}\right\}-\frac{1}{2\langle\rho\rangle^2}\sum_{ik}\left\{\langle\rho'm'_ku'_iF_k\rangle+\left\langle m'_k\,u'_i\frac{\partial P'}{\partial x_k}\right\rangle\right\}-Q^{(D_k)}_{ik},$$

$$Q^{(D_k)}_{ik}=\sum_{ik}\left\langle\Sigma'_{ij}\frac{\partial m'_k\,u'_k}{\partial x_j}\right\rangle.$$

The symbol $\sum\limits_{ik}{}'$ in (76) signifies summation over the permutations of i and k indices

$$\frac{dD^{(k)}_i}{dt}=-\frac{1}{\langle\rho\rangle^2}\frac{\partial}{\partial x_j}\left\{\langle\rho'm'_k\,u'_iu'_j\rangle-\langle\rho\rangle^2W_jD^{(k)}_i\right\}+D^{(k)}_i\frac{\partial W_j}{\partial x_j}-$$
$$-\left(D^{(k)}_j-W_j\langle\rho'm'_k\rangle\right)\frac{\partial(V_i-W_i)}{\partial x_j}+\frac{1}{\langle\rho\rangle}W^{(k)}_i\frac{\partial\langle\rho\rangle W_j}{\partial x_j}+\frac{1}{\langle\rho\rangle}W_i\frac{\partial\langle\rho\rangle W^{(k)}_j}{\partial x_j}- \tag{77}$$
$$-2D_{ij}\frac{1}{\langle\rho\rangle}\frac{\partial\langle\rho\rangle c_k}{\partial x_j}-2D^{(k)}_{ij}\frac{1}{\rho}\frac{\partial\langle\rho\rangle}{\partial x_j}-\langle\rho'm'_k\rangle\left\{\frac{dW_i}{dt}+\frac{2}{\langle\rho\rangle}\frac{\partial\langle\rho\rangle\Phi_{ij}}{\partial x_j}\right\}-$$
$$-\frac{1}{\langle\rho\rangle^2}\langle\rho'\rho'm'_kF_i\rangle-Q^{(D_k)}_i,$$

$$Q^{(D_k)}_i=\frac{1}{\langle\rho\rangle^3}\left\langle\Sigma'_{ij}\frac{\partial\rho'm'_k}{\partial x_j}\right\rangle+2\frac{1}{\langle\rho\rangle^3}\left\langle\rho'm'_k\frac{\partial P'}{\partial x_j}\right\rangle. \tag{77}$$

As is clear from the equations for $W_i^{(k)}$ (73), one of the generating terms is proportional to $2e_{ik} = \langle u_i' u_k' \rangle$, rather than $2\varepsilon_{ik} = \langle u_i' u_k' \rangle + \frac{1}{\langle \rho \rangle} \langle \rho' u_i' u_k' \rangle$. The equation for $2e_{ik} = \langle u_i' u_k' \rangle$ can be derived from eqs. (72) and (75) to have the form

$$\begin{aligned}\frac{\partial e_{ik}}{\partial t} = & -\frac{\partial}{\partial x_j}\left\{\frac{1}{2}D_{ikj} - W_j e_{ik}\right\} - e_{ik}\frac{\partial W_j}{\partial x_j} - \frac{1}{2\langle \rho \rangle}\left\{\frac{\partial}{\partial x_k}\langle P' u_i' \rangle + \frac{\partial}{\partial x_i}\langle P' u_k' \rangle\right\} \\ & - e_{ij}\frac{\partial}{\partial x_j}\left(V_k - W_k\right) - e_{kj}\frac{\partial}{\partial x_j}\left(V_i - W_i\right) - \frac{1}{2}\left\{W_i \frac{1}{\langle \rho \rangle}\frac{\partial \langle P \rangle}{\partial x_k} + \right. \\ & \left. + W_k \frac{1}{\langle r \rangle}\frac{\partial \langle P \rangle}{\partial x_i}\right\} + \frac{1}{2\langle r \rangle^2}\left\{\langle r' r' u_i' F_k \rangle + \langle r' r' u_k' F_i \rangle\right\} - L_{ik} - Q_{ik},\end{aligned} \tag{78}$$

$$L_{ik} = -\frac{1}{2\langle \rho \rangle}\left\{\left\langle P' \frac{\partial u_i'}{\partial x_k}\right\rangle + \left\langle P' \frac{\partial u_k'}{\partial x_i}\right\rangle\right\} - \frac{1}{2\langle \rho \rangle^2}\left\{\left\langle \rho' u_i' \frac{\partial P'}{\partial x_k}\right\rangle + \left\langle \rho' u_k' \frac{\partial P'}{\partial x_i}\right\rangle\right\},$$

$$Q_{ik} = \frac{1}{2\langle \rho \rangle}\left\{\left\langle \Sigma_{ij}' \frac{\partial u_k'}{\partial x_j}\right\rangle + \left\langle \Sigma_{kj}' \frac{\partial u_i'}{\partial x_j}\right\rangle\right\} - \frac{1}{2\langle \rho \rangle^2}\left\{\left\langle \Sigma_{ij}' \frac{\partial u_k' \rho'}{\partial x_j}\right\rangle + \left\langle \Sigma_{kj}' \frac{\partial u_i' \rho'}{\partial x_j}\right\rangle\right\}.$$

The above equations are useful to describe both gravitational and tangential mixing, i.e. resulting from Rayleigh-Taylor and Kelvin-Helmholtz instabilities, respectively. However, the equations have some terms with their forms not defined. To have the set of equations closed, we will restrict the problem to consider one-dimensional, on average, flow case. We take the frame of reference such that one of the axes will coincide with the flow direction and identify this axis with the index "1" or axis "x". For this flow, e_{ik} and ε_{ik} tensors will be diagonal, i.e. $e_{ik} = e_i \delta_{ik}$, where δ_{ik} is the unit tensor, while of all $W_i^{(k)}$ flow constituents the only nonzero is that indexed "1". Therefore, to save time and space, we will omit this index together with the sign < > with average pressure and density values.

2.2.2. EQUATIONS CLOSURE

There are some terms in the resulting equations, having their forms still undefined. These are terms including F_i quantity, and we call them inertial; exchange terms to describe the energy exchange between the various fluctuating motion components through pressure fluctuations; dissipative terms, and transport terms, represented by third-order correlations. While it is impossible to define them exactly, modeling, dimensional and other considerations have to be used for their definition.

REPRESENTATION OF INERTIAL TERMS

Correlations including the quantity

$$F_i = \frac{\partial\left(\langle u_i \rangle + u_i'\right)}{\partial t} + \left(\langle u_j \rangle + u_j'\right)\frac{\partial\left(\langle u_i \rangle + u_i'\right)}{\partial x_j}$$

are to describe the effects of inertia forces on turbulent flows, i.e. the consideration that the medium acceleration, e.g. due to pressure gradient, makes its heavier constituents ($\rho' > 0$) accelerate to lower, and lighter constituents ($\rho' < 0$) - to higher velocities, than the average medium velocity.

Consider the correlation $\langle \rho' m'_k F_i \rangle$ included in the equation for the quantity $\rho W_i^{(k)}$ (73). From the equation of motion we have

$$F_i = -\frac{\rho'}{\rho} F_i - \frac{1}{\rho}\frac{\partial P}{\partial x_i} - \frac{1}{\rho}\frac{\partial P'}{\partial x_i} - \frac{1}{\rho}\frac{\partial}{\partial x_j}\left(\Sigma_{ij} + \Sigma'_{ij}\right) .$$

By sequentially substituting this expression into the correlation $\langle \rho' m'_k F_i \rangle$, we obtain

$$\frac{1}{\rho^2}\langle \rho' m'_k F_i \rangle = -\left\{ \frac{1}{\rho^2}\langle \rho' m'_k \rangle - \langle \rho'\rho' m'_k \rangle + \langle \rho'\rho'\rho' m'_k \rangle - \cdots \right\} \frac{1}{\rho}\frac{\partial P}{\partial x_i} + S_i =$$

$$= \sum_{n=1}^{n=\infty} (-1)^1 \frac{\langle \rho'^n \, m'_k \rangle}{\rho^1} \cdot \frac{1}{\rho}\frac{\partial P}{\partial x} + S_i \,. \qquad (79)$$

S_i is a term used to designate the combination of terms including $P'$and Σ'_{ij}. Most likely, these terms should be referred to as dissipative.

To achieve closure for (79), we assume the turbulent mixing zone as a region where two substances of ρ_1 and ρ_2 ($\rho_1 < \rho_2$). are heterogeneously mixed.

$$\frac{V_1}{V} = \frac{c_1}{\delta - (\delta - 1)c_1}; \quad \frac{V_2}{V} = \frac{\delta(1 - c_1)}{\delta - (\delta - 1)c_1} ,$$

where: $\delta = \frac{\rho_2}{\rho_1}$, and c_2 is the concentration of substance 2..

The average medium density is $\rho = \rho_2[\delta - (\delta - 1)c_2]^{-1}$.

Let us denote $y_1 = \frac{\rho_1}{\rho}$ and $y_2 = \frac{\rho_2}{\rho}$. Then the fractional volumes of substances and the concentration of the heavier one c_2 can be expressed in terms of y_1 and y_2 as follows:

$$\frac{V_1}{V} = \frac{1 - y_2}{y_1 - y_2}; \quad \frac{V_2}{V} = \frac{y_1 - 1}{y_1 - y_2}; \quad c_1 = \frac{y_1(1 - y_2)}{y_1 - y_2} . \qquad (80)$$

For correlations $B^{(1)} = \frac{1}{\rho^2}\langle \rho' m'_1 \rangle$and $B^{(2)} = \frac{1}{\rho^2}\langle \rho' m'_2 \rangle$ allowing for (80) we have

$$B^{(1)} = (y_1 - 1)(y_1 - c_1)\frac{V_1}{V} - (y_2 - 1)c_1\frac{V_2}{V} = (y_1 - 1)(1 - y_2)\frac{y_1}{y_1 - y_2};$$

$$(81)$$

$$B^{(2)} = -(y_1 - 1)c_2\frac{V_1}{V} + (y_2 - 1)(y_2 - c_2)\frac{V_2}{V} = -(y_1 - 1)(1 - y_2)\frac{y_2}{y_1 - y_2} .$$

Density fluctuations have relative mean-square value

$$R^2 = \frac{\langle \rho' \rho' \rangle}{\rho^2} = B^{(1)} + B^{(2)} = (y_2 - 1)(1 - y_1) \ .$$

It can be expressed in terms of c_2 concentraton and δ

$$R^2 = \frac{(\delta - 1)^2}{\delta} c_2 (1 - c_2) \ .$$

Assuming small density ratio δ, we obtain

$$\left(\frac{\langle \rho' m_1' \rangle}{\rho^2} - \frac{\langle \rho'^2 m_1 \rangle}{\rho^3} + \cdots \right) = \left\{ (y_1 - 1)(y_1 - c_1) - \left((y_1 - 1)^2 (y_1 - c_1) \right) + \cdots \right\} \frac{V_1}{V} +$$

$$+ \left\{ (1 - y_2) c_1 - (1 - y_2)^2 c_1 + \cdots \right\} \frac{V_2}{V} = \frac{(y_1 - 1)}{y_1} (y_1 - c_1) \frac{V_1}{V} + \frac{(1 - y_2)}{y_2} c_1 \frac{V_2}{V} =$$

$$= \frac{(y_1 - 1)(1 - y_2)}{(y_1 - y_2)} \frac{1}{y_2} \ .$$

Similarly,

$$\left(\frac{\langle \rho' m_1' \rangle}{\rho^2} - \frac{\langle \rho'^2 m_1 \rangle}{\rho^3} + \cdots \right) = \frac{(y_1 - 1)(1 - y_2)}{(y_1 - y_2)} \frac{1}{y_1} \ .$$

Given these relationships (without S_i terms), we have the following expression

$$\langle \rho' m_1' F_1 \rangle = \frac{B^{(1)}}{y_1 y_2} \frac{1}{\rho} \frac{\partial P}{\partial x}; \qquad \langle \rho' m_2' F_1 \rangle = \frac{B^{(2)}}{y_1 y_2} \frac{1}{\rho} \frac{\partial P}{\partial x}. \qquad (82)$$

As it can be clearly seen, the function $f_1 = \frac{1}{y_1 y_2}$ behaves within the mixing zone like this: for $c_1 = 0.5$, i.e. where R^2 has the highest value, $f_1 = (1 + R^2)^{-1}$; for $c_2 \to 0$ $f_1 \to \delta^{-1}$; $c_2 \to 1$ $f_1 \to \delta$.

Now, consider the correlation $\frac{1}{\rho^2} \langle F_1 \rho' \rho' u_1' \rangle$ included in the equation for e_1 (78). We will define the form of this, further assuming the correlation factor for density and velocity fluctuations in the mixing zone to be $\eta = 1$ ($\eta^2 = \frac{W^2}{2R^2 e_1}$). Substance 1 particles move along the axis 1 at the velocity $u_{(1)}$, and substance 2 particles move in the opposite directions at the velocity $u_{(2)}$. Then the following can be written

$$2e_1 = \langle u_1' u_1' \rangle = u_{(1)}^2 \frac{V_1}{V} + u_{(2)}^2 \frac{V_2}{V};$$

$$W = \frac{\langle \rho' u_1' \rangle}{\rho} = (y_1 - 1) u_{(1)} \frac{V_1}{V} + (y_2 - 1) u_{(2)} \frac{V_2}{V}; \qquad W^2 = 2R^2 e_1 \ .$$

Resolving these equations yields

$$u_{(2)} = \frac{W}{R^2}(y_2 - 1); \quad u_{(1)} = -\frac{W}{R^2}(1 - y_1);.$$

With these expressions, the requirement $\langle u_1' \rangle = 0$ can be satisfied..

For correlation $\frac{\langle F_1 \rho' \rho' u_1' \rangle}{\rho^2}$, we express the equation involving the same assumptions as previous

$$\frac{\langle F_1 r' r' u_1' \rangle}{r^2} = -\frac{1}{r}\frac{\partial P}{\partial x}\left\{ u_{(1)}\left[(y_1 - 1)^2 - (y_1 - 1)^3 + \cdots\right]\frac{V_1}{V} + \right.$$

$$\left. + u_{(2)}\left[(y_2 - 1)^2 - (y_2 - 1)^3 + \cdots\right]\frac{V_2}{V} \right\} =$$

$$= \frac{1}{\rho}\frac{\partial P}{\partial x}\frac{W}{R^2}\left\{ \frac{(y_1 - 1)^3}{y_1}\frac{V_1}{V} + \frac{(y_2 - 1)^3}{y_2}\frac{V_2}{V} \right\} = -W\frac{y_1 y_2 - 1}{y_1 y_2}\frac{1}{\rho}\frac{\partial P}{\partial x} =$$

$$= -W(1 - f_1)\frac{1}{\rho}\frac{\partial P}{\partial x} .$$

Given ρ‘ and u_1’ fluctuations are small, then the correlation is $\frac{\langle F_1 \rho' \rho' u_1' \rangle}{\rho^2} = -D_1 \frac{1}{\rho}\frac{\partial P}{\partial x}$. Therefore, it would seem reasonable to express it in terms of $D_1 = \frac{\langle \rho' \rho' u_1' \rangle}{\rho^2}$. What we have in the assumptions under consideration is

$$D_1 = u_{(1)}(y_1 - 1)^2 \frac{V_1}{V} + u_{(1)}(y_2 - 1)^2 \frac{V_2}{V} = W(y_1 + y_2 - 2) .$$

While, on the other hand, ,

$$R^2 = (y_1 - 1)(1 - y_2) = (y_1 + y_2 - 2) + 1 - y_1 y_2,$$

the following can be written for D_1:

$$D_1 = W\left\{y_1 y_2 - 1 + R^2\right\}.$$

Thus, we obtain for $f_1 = \frac{1}{y_1 y_2}$ the equation

$$f_1 = \left[1 + \frac{D_1 - WR^2}{W}\right]^{-1} . \qquad (83)$$

Allowing for (83) we have

$$\frac{\langle F_1 \rho' \rho' u_1' \rangle}{\rho^2} = -\frac{D_1 - WR^2}{W} f_1 W \frac{1}{\rho}\frac{\partial P}{\partial x} = -(1 - f_1) W \frac{1}{\rho}\frac{\partial P}{\partial x} .$$

In this way, we formulate the following equation for the sum of two generating terms proportional to $g = -\frac{1}{\rho}\frac{\partial P}{\partial x}$, in equation (78)

$$Wg+\frac{\langle F_1\rho'\rho'u_1\rangle}{\rho^2}=Wg-(1-f_1)Wg=f_1Wg\ .$$

DISSIPATIVE AND EXCHANGE TERMS

Consider first of all the form of exchange interaction tensor L_{ik} in the equation for e_{ik}. For turbulent Mach number $M_t \ll 1$ this tensor will account for the energy exchange between the various components of fluctuation motion through pressure fluctuations. The equation we use for this tensor is:

$$L_{ik}=\frac{3}{2}\frac{1}{10}\alpha k f_1\left\{W_i g_k+W_k g_i-\frac{2}{3}\delta_{ik}W_j g_j\right\}+\gamma\frac{Q}{e}\left(e_{ik}-\frac{1}{3}\delta_{ik}e_{jj}\right). \qquad (84)$$

The second term in this equation has been introduced by Rotta [55] and is frequently used by various semi-empirical models. The form for the first term was suggested in [56]. It has been added with the function f_1 so, that it will have the same form as the similar term in the equation for e_{ik}. The need for this modification can be shown by considering the equation of turbulent anisotropy $\sigma=e_1/e_2$.

Also, the factor $k=3\sqrt{3}\sqrt{\frac{e_1e_2e_3}{e^3}}$ $(e=e_1+e_2+e_3)$ has been added to make the exchange interaction between the fluctuation motion components tend to zero with one of the components degenerating. The factor's having this form is due to the following considerations. Turbulent energy dissipation rate can be formulated as $Q\sim\omega e$, where ω is some frequency. Isotropic turbulence case has ω the same as large-scale fluctuations frequency $\omega_t\sim\frac{\sqrt{e}}{l_t}$, where l_t is the turbulence scale. However, this is not case for anisotropic turbulence. There are suggestions in ([57], [58], [59]), that 2D turbulence with $Re_t\to\infty$ has turbulent energy dissipation tending to zero, i.e. $\omega\to 0$, though ω_t is finite. Any two turbulent energy components, such as e_1 and e_2, have dissipation rate proportional to the stretching velocity of vortex tubes directed normally to plane 1-2, i.e. proportional to $\sqrt{e_3}$. Therefore, it has been suggested that $\omega\approx k\omega_t$. The same factor k has been used above in the equation to formulate the exchange term.

Referring back to eq. (84), let us assume as in [56], that γ is dependent on the characterization of averaged and fluctuative motion. Ref. [56] suggests the following formulation $\gamma\sim\gamma_1-\gamma_3\frac{e_{ik}V_{ik}}{Q}=\gamma_1-\varphi_3$.

For the given gravitational mixing case, it would be reasonable to assume that γ is also dependent on the density gradient. In terms of dimensional considerations, we take γ to depend on the parameter $\varphi_2=-\gamma_2\frac{W}{R^2}\frac{1}{\rho}\frac{\partial\rho}{\partial x}\frac{e}{Q}$. While φ_2 and φ_3 may be negative and γ must be positive, we should use the following equation:

$$\gamma=1+\frac{\varphi_2}{2}+\frac{\varphi_3}{2}+\sqrt{\left(\frac{\gamma_1-1}{2}\right)^2+\frac{\varphi_2^2}{4}}+\sqrt{\left(\frac{\gamma_1-1}{2}\right)^2+\frac{\varphi_3^2}{4}}$$

It is this equation the calculations have used.

The above-formulated equations all include dissipative terms depending on either viscous tensor fluctuations or velocity divergence fluctuations resulting from molecular diffusion in multicomponent mixture. All the correlations, but c_{ik}, have been given the following form $Q^{(Y)} = k_Y \omega Y$, where $Q^{(Y)}$ is the dissipative term for the correlation Y and $\omega = \frac{Q}{e}$, $Q = Q_{jj}$

Consider now equations for $Q_{ik}^{(E)}$ and Q_{ik}. Turbulent energy dissipation generally occurs in the small-scale spectral region which is isotropic, therefore it would be natural to expect that dissipative tensors are isotropic as well. In other words, assume that $Q_{ik} = \frac{1}{3} Q \delta_{ik}$, where $Q = Q_{jj}$. This assumption is supported by the consideration that the contribution of gravity responsible for anisotropy in the large-scale spectral region should reduce with moving into the small-scale spectral region. Moreover, as shown by direct experimental measurements of turbulent energy dissipation rates for other flows (such as turbulence distortion, shear flow turbulence, etc.), despite the anisotropy existing for large vortices, the dissipation rate is near isotropic [61].

The value of Q is

$$Q = \frac{1}{\rho}\left\langle \Sigma'_{ij} \frac{\partial u_i}{\partial x_j} \right\rangle - \frac{1}{\rho^2}\left\langle \Sigma'_{ij} \frac{\partial \rho' u'_j}{\partial x_j} \right\rangle, \qquad \text{where}$$

$$\Sigma_{ij} = \rho \nu_0 \left\{ \left(\frac{\partial u'_i}{\partial x_j} + \frac{\partial u_j}{\partial x_i} \right) - \frac{2}{3} \delta_{ij} \frac{\partial u_l}{\partial x_l} \right\} = \rho \nu_0 \sigma_{ij}.$$

Here ν_0 is the kinematic viscosity factor.

By substituting the equation for Σ'_{ij} into that for Q, we have

$$Q = \nu_0 \left\{ \left\langle \sigma'_{ij} \frac{\partial u'_i}{\partial x_j} \right\rangle + \left\langle \sigma'_{ij} \right\rangle \frac{1}{\rho} \left\langle \rho' \frac{\partial u'_i}{\partial x_j} \right\rangle + \frac{1}{\rho} \left\langle \rho' \sigma'_{ij} \frac{\partial u'_i}{\partial x_j} \right\rangle - \right.$$

$$- \frac{1}{\rho} \left\langle \sigma'_{ij} \frac{\partial \rho' u'_i}{\partial x_j} \right\rangle - \left\langle \sigma'_{ij} \right\rangle \frac{1}{\rho^2} \left\langle \rho' \frac{\partial \rho' u'_i}{\partial x_j} \right\rangle - \frac{1}{\rho^2} \left\langle \rho' \sigma'_{ij} \frac{\partial \rho' u'_i}{\partial x_j} \right\rangle -$$

$$\left. - \left\langle \sigma_{ij} \right\rangle \left\langle \frac{\partial \rho' u'_i}{\partial x_j} \right\rangle \right\}.$$

There is viscous turbulent energy dissipation occurring in the vortices having typical length scale $l_Q \approx l_t \, Re_t^{-3/4}$ and typical velocity scale $u_Q \approx \sqrt{e} \, Re_t^{-1/4}$, where l_t, $\sqrt{e}$ are the typical scale and velocity of large-scale vortices and $Re_t = \frac{l_t \sqrt{e}}{\nu_0}$ - turbulence Reynolds number. Assuming density fluctuations in the small vorticity region to have also characteristic scale $\rho'_Q \approx \sqrt{\rho' \rho'} \, Re_t^{-1/4}$, we obtain that for

$Re_t \to \infty$ the major contribution to Q is the correlation $\nu_0\left\langle \sigma'_{ij}\frac{\partial u'_i}{\partial x_j}\right\rangle$. The others contribute in proportion to $Re_t^{-\alpha}$, where $\alpha \geq 1/4$. This, particularly, means that $Q_{jj}^{(E)} = Q$.

As long as low Mach number turbulence is under consideration, the major contribution to the value $\frac{\partial u'_l}{\partial x_l}$ is due to molecular diffusion in the small-scale spectral region. On the assumption that density fluctuations in this spectral region have characteristic degeneration time τ_ρ of the same order of magnitude as that of velocity fluctuations $\tau_u \approx \frac{l_Q}{u_Q}$, we will obtain the following estimate for fluctuating velocity divergence:

$$\left|\frac{\partial u'_l}{\partial x_l}\right| \approx \left|\frac{1}{\rho}\frac{\partial \rho'_q}{\partial t}\right| \approx \frac{1}{\rho}\frac{\rho'_q}{\tau_\rho} \approx \frac{\sqrt{e}}{l_t} Re_t^{\frac{1}{4}},$$

while: $\frac{\partial u'_i}{\partial x_j} \approx \frac{\sqrt{e}}{l_t} Re_t^{\frac{1}{2}}$. That is, for $Re_t \to \infty$ the second term can be ignored in the equation for σ_{ij}.

Thus, we have

$$Q = \nu_0\left\langle\left(\frac{\partial u'_i}{\partial x_j} + \frac{\partial u'_j}{\partial x_i}\right)\frac{\partial u'_i}{\partial x_j}\right\rangle,$$

or, allowing for the small-scale turbulence isotropy,

$$Q = \left\langle\frac{\partial u'_i}{\partial x_j}\frac{\partial u'_i}{\partial x_j}\right\rangle.$$

The equation for Q is derived the same way as for other correlations and expressed as

$$\frac{dQ}{dt} = -\frac{\partial}{\partial x_j}\left\{\nu_0\left\langle u'_j\frac{\partial u'_i}{\partial x_k}\frac{\partial u'_i}{\partial x_k}\right\rangle - W_j Q\right\} - Q\frac{\partial W_j}{\partial x_j} - 2D_{ll}^{ij}\frac{\partial(V_i - W_i)}{\partial x_j} -$$
$$-2D_{lj}^{ii}\frac{\partial(V_j - W_j)}{\partial x_l} - 2D_{llj,}^{iij} - \frac{2\nu_0}{\rho}\left\langle F_i\frac{\partial u'_i}{\partial x_l}\frac{\partial \rho'}{\partial x_l}\right\rangle - \frac{2\nu_0}{\rho}\left\langle \rho'\frac{\partial u'_i}{\partial x_l}\frac{\partial F_i}{\partial x_l}\right\rangle - \Pi. \tag{85}$$

The following notation is used here:

$$D_{ll}^{ij} = \nu_0\left\langle\frac{\partial u'_i}{\partial x_l}\frac{\partial u'_j}{\partial x_l}\right\rangle; \qquad D_{lj}^{ii} = \nu_0\left\langle\frac{\partial u'_i}{\partial x_l}\frac{\partial u'_i}{\partial x_j}\right\rangle;$$

$$D_{llj}^{iij} = 2\nu_0\left\langle\frac{\partial u'_i}{\partial x_l}\frac{\partial u'_i}{\partial x_j}\frac{\partial u'_j}{\partial x_l}\right\rangle - \nu_0\left\langle\frac{\partial u'_i}{\partial x_l}\frac{\partial u'_i}{\partial x_l}\frac{\partial u'_j}{\partial x_j}\right\rangle.$$

The symbol Π is used to indicate the group of correlations including viscous tensor fluctuations Σ'_{ij}. The terms including coordinate derivatives of density fluctuations such as $\nu_0\left\langle \frac{\partial u'_i}{\partial x_l}\frac{\partial^2 P'}{\partial x_i \partial x_l}\right\rangle$ have been omitted in eq. (85). Also, the terms of the order of $Re_t^{-\alpha}$ with $\alpha>0$ have been discounted.

With the use of the equation of motion

$$F_i = -\frac{\rho'}{\rho}F_i - \frac{1}{\rho}\frac{\partial P}{\partial x_i} - \frac{1}{\rho}\frac{\partial P'}{\partial x_i} - \frac{1}{\rho}\frac{\partial}{\partial x_j}\left(\Sigma_{ij} + \Sigma'_{ij}\right) ,$$

the term of eq. (85) including $\frac{\partial F_i}{\partial x_l}$, can be rewritten as:

$$\frac{\nu_0}{\rho^2}\left\langle \rho'\frac{\partial u'_i}{\partial x_l}\frac{\partial F_i}{\partial x_l}\right\rangle = -\frac{\nu_0}{\rho^2}\left\langle \rho' F_i \frac{\partial u'_i}{\partial x_l}\frac{\partial \rho'}{\partial x_l}\right\rangle + \frac{\nu_0}{\rho^2}\left\langle \frac{\partial \rho'}{\partial x_i}\frac{\partial u'_i}{\partial x_l}\frac{\partial P'}{\partial x_l}\right\rangle -$$

$$-\frac{2\nu_0}{\rho^2}\left\langle \rho'\frac{\partial \rho'}{\partial x_i}\frac{\partial u'_i}{\partial x_l}\frac{\partial P'}{\partial x_l}\right\rangle + \frac{\nu_0}{\rho^2}\left\langle \rho'\frac{\partial^2 u'_i}{\partial x_i \partial x_l}\frac{\partial P'}{\partial x_l}\right\rangle .$$

Like previously, this equation has only retained the terms of the order of Re_t^0. The terms involving Σ'_{ij}, have been included in Π group.

Thus, we obtain the following equation for Q:

$$\frac{dQ}{\partial t} = \underbrace{-\frac{\partial}{\partial x_j}\left\{\nu_0\left\langle u'_j \frac{\partial u'_i}{\partial x_l}\frac{\partial u'_i}{\partial x_l}\right\rangle - W_j Q\right\}}_{1} \underbrace{-\,Q\frac{\partial W_j}{\partial x_j}}_{2} - \tag{86}$$

$$\underbrace{-\left\{2D_{ll}^{ij}\frac{\partial(V_i - W_i)}{\partial x_j} - 2D_{lj}^{ii}\frac{\partial(V_j - W_j)}{\partial x_l}\right\}}_{3} - \underbrace{2D_{llj}^{iij}}_{4} -$$

$$\underbrace{-\frac{2\nu_0}{\rho}\left\{\left\langle F_i \frac{\partial u'_i}{\partial x_l}\frac{\partial \rho'}{\partial x_l}\right\rangle - \frac{1}{\rho^2}\left\langle \rho' F_i \frac{\partial u'_i}{\partial x_l}\frac{\partial \rho'}{\partial x_l}\right\rangle\right\}}_{5} -$$

$$\underbrace{-\frac{2\nu_0}{\rho^2}\left\{\left\langle \frac{\partial P'}{\partial x_l}\frac{\partial \rho'}{\partial x_i}\frac{\partial u'_i}{\partial x_l}\right\rangle - \frac{2}{\rho^2}\left\langle \rho'\frac{\partial P'}{\partial x_l}\frac{\partial \rho'}{\partial x_i}\frac{\partial u'_i}{\partial x_l}\right\rangle + \frac{1}{\rho^2}\left\langle \rho'\frac{\partial P'}{\partial x_l}\frac{\partial^2 u'_i}{\partial x_l \partial x_i}\right\rangle\right\}}_{6} - \Pi .$$

While it has been assumed above that the dissipation may be considered isotropic for $Re_t \to \infty$, the energy dissipation rate tensor can be expressed as: $Q_{ik} = \frac{1}{3}Q\delta_{ik}$, where $Q = Q_{jj}$. By virtue of this, the term $2D_{ll}^{ij}\frac{\partial(V_i - W_i)}{\partial x_j}$ in (86), given the relation $D_{ll}^{ij} = Q_{ij}$, can be expressed as $\frac{1}{3}Q\delta_{ij}\frac{\partial(V_i - W_i)}{\partial x_j}$. By making use of the relationships for fluctuation velocity derivatives with respect to coordinates existing in isotropic turbulence (see, e.q., [61]), the term $2D^{ii}_{lj}\frac{\partial\left(V_j - W_j\right)}{\partial x_l}$ can also be expressed in the similar form. The sum of these two terms is:

$$(3) = \frac{4}{3}Q\delta_{ij}\frac{\partial\left(V_i - W_i\right)}{\partial x_j} .$$

Referring to the next terms in (86), it is difficult to make any definite statements. Therefore, one has to involve additional considerations to represent them.

Thus, for $\left\langle\rho'^2\right\rangle \to 0$ the 5th term in (86) is part of the dissipative term in the equation for W_i, multiplied by $g_i = -\frac{1}{\rho}\frac{\partial P}{\partial x_i}$. Therefore, we take the following expression

$$(5) = \frac{1}{3}\frac{e}{e_l}\frac{Q}{e}f_l W g_i .$$

$$D^{iij}_{llj} - \Pi = -\beta_1\gamma\frac{Q}{e}\left(e_{ik} - \frac{1}{3}e\delta_{ik}\right)\frac{\partial\left(V_i - W_i\right)}{\partial x_k} - 2\frac{Q^2}{ke} ,$$

where β_l is the constant.

The 6th term in (86) involves pressure, density and velocity fluctuations. We have two quantities available that involve these fluctuations: exchange interaction tensor L_{ik} and W_i.To set up a dimensional expression (6) out of these, a vector is also needed having inverse length dimension. Such vector in the problem is $\frac{1}{\rho}\frac{\partial\rho}{\partial x_i}$. Given this, the following is specified for the 6th term in (86):

$$(6) = \frac{1}{2}\beta L_{ij}W_j A_i \ \varphi\left(R^2\right); \quad A_i = -\frac{1}{\rho}\frac{\partial\rho}{\partial x_i},$$

where β_2 is the constant, $\varphi\left(R^2\right)$ - function of $R^2 = \frac{\langle\rho'\rho'\rangle}{\rho^2}$. From calculations, this function has been selected as $\varphi\left(R^2\right) = \frac{1+R^2}{R^2}$.

There are two more terms, D^{iij}_{llj} and Π, still undefined in (86). Ref.[62] has the following equation assumed to express the difference of three terms

$$D^{iij}_{llj} - \Pi = \beta_l\frac{Q}{e}\left\langle u'_i u'_j\right\rangle\frac{\partial\langle u_i\rangle}{\partial x_j} - 2\frac{Q^2}{e} .$$

We will adopt the similar expression though having the following two modifications. Firstly, instead of the tensor $\left\langle u'_i u'_j\right\rangle$ in the first term we will partly use the exchange interaction tensor $L^{(1)}_{ik} = \gamma\frac{Q}{e}\left(e_{ik} - \frac{1}{3}\delta_{ik}\right)$. The reason is that with isotropic turbulence undergoing all-round and uniform compression (where the tensor $\frac{\partial\langle u_i\rangle}{\partial x_j} \approx a\delta_{ij}$, where a=const), the following requirement should be satisfied: $l_t^2 e = \text{const}$, where l_t is the turbulence scale. Since $l_t \approx e^{3/2}/Q$, there should be

$\frac{e^2}{Q} \approx \text{const}$. Clearly, this requirement is already satisfied in the equation for Q by the group of terms including D^{ij}_{ll}, D^{ii}_{ij} (3rd term in (86)). The contribution of the term $D^{iij}_{llj} - \Pi$ has been assumed in the form

$$D^{iij}_{llj} - \Pi = -\beta_1 \gamma \frac{Q}{e}\left(e_{ik} - \frac{1}{3} e\delta_{ik}\right)\frac{\partial\left(V_i - W_i\right)}{\partial x_k} - 2\frac{Q^2}{k\,e},$$

where β_1 is the constant.

The last term has the factor 2 accounting for the energy dissipation of uniform isotropic turbulence as t^{-1}. Moreover, this term includes the factor k defined previously to allow for the dissipation rate tending to zero for the limiting 2D turbulence case.

By summarizing the above statements we obtain the following equation for Q

$$\begin{aligned}\frac{dQ}{dt} = &-\frac{\partial}{\partial x_j}\left\{\nu_0\left\langle u'_j\left(\frac{\partial u'_i}{\partial x_l}\right)^2\right\rangle - W_j Q\right\} - Q\frac{\partial W_j}{\partial x_j} - \\ &-\left\{\frac{4}{3}Q\delta_{ij} + \beta_1\gamma\frac{Q}{e}\left(e_{ij} - \frac{1}{3}e\delta_{ij}\right)\right\}\frac{\partial\left(V_i - W_i\right)}{\partial x_j} + \frac{Q}{3e_1} f_1 W g + \\ &+\beta_2\left\{\frac{3}{20}\alpha k f_1\left(W_i g_k + W_k g_i - \frac{2}{3}\delta_{ik} W_j g_j\right) + \gamma\frac{Q}{e}\left(e_{ik} - \frac{1}{3}e\delta_{ik}\right)\right\} W_i A_k \varphi\left(R^2\right) - \\ &-2\frac{Q^2}{k\,e}\,.\end{aligned} \tag{87}$$

TRANSPORT TERMS

Transport terms in second-order correlation equations are represented by third-order correlation divergences. For the third-order correlations, a representation as sum of the two terms is used. The one is proportional to the second-order correlation gradient, the other being the product of the second-order correlations. The equations for third-order correlations (75) through (77), include fourth-order correlations. To represent these, we make use of Millionshikov hypothesis (normal distribution hypothesis) by which the fourth-order correlations are to be expressed in terms of second-order correlations in the following way: $\langle a'b'c'd'\rangle = \sum_{abcd}{}' \langle a'b'\rangle\langle c'd'\rangle$, where the symbol $\sum_{abcd}{}'$ implies summation over all the permutations of a, b, c, d. Using this hypothesis as applied to the case where fluctuations are small, and ignoring the time derivatives and some other terms in eqs (75) through (77), we obtain.

$$\frac{1}{2}\left\langle u_1'^3\right\rangle \approx -\frac{6}{k_\gamma}\frac{e_1 e}{Q}\frac{\partial e_1}{\partial x}; \quad \frac{1}{2}\left\langle u'_1 u_2'^2\right\rangle \approx -\frac{2}{k_\gamma}\frac{e_1 e}{Q}\frac{\partial e_2}{\partial x};$$

$$\frac{1}{\rho}\left\langle m'_k u_1'^2\right\rangle \approx -\frac{4}{k_\gamma}\frac{e_1 e}{Q}\frac{\partial W^{(k)}}{\partial x}; \quad \frac{1}{\rho^2}\left\langle \rho' m'_k u'_1\right\rangle \approx -\frac{2}{k_\gamma}\frac{e_1 e}{Q}\frac{\partial B^{(k)}}{\partial x}.$$

It is assumed here, that dissipative terms in the equations for third-order correlations have the same form as for second-order correlations, and that the factors they include are equal to k_γ. For k_γ, the expression taken is

$$k_\gamma = \frac{3}{2} + \frac{e}{6e_1} + \frac{\gamma}{2}.$$

For finite density fluctuations, these equations have been added with the terms that are products of the second-order correlations.

The third-order correlations were written as

$$\frac{1}{2}\left\langle u_1'^3 \right\rangle \approx 2We_1 - D_t^{(e_1)} \frac{\partial e_1}{\partial x}; \quad \frac{1}{2}\left\langle u_1' u_2'^2 \right\rangle \approx 2We_2 - D_t^{(e_2)} \frac{\partial e_2}{\partial x};$$

$$\frac{1}{r}\left\langle m_k' u_1'^2 \right\rangle \approx 2WW^{(k)} - D_t^{(W)} \frac{\partial W^{(k)}}{\partial x}; \quad \frac{1}{r^2}\left\langle r' m_k' u_1' \right\rangle \approx 2WB^{(k)} - D_t^{(B)} \frac{\partial B^{(k)}}{\partial x};$$

$$\nu_0 \left\langle u_j' \left(\frac{\partial u_i'}{\partial x_1} \right)^2 \right\rangle = 2WQ - D_t^{(Q)} \frac{\partial Q}{\partial x},$$

where $D_t^{(e_1)} = 3D_t$; $D_t^{(e_2)} = D_t^{(e_3)} = D_t$; $D_t^{(W)} = 2D_t$; $D_t^{(B)} = D_t$; $D_t^{(Q)} = \frac{5}{3} D_t$;

$D_t = 2\alpha_1 \frac{e_1 e}{k_\gamma Q}$, α_1-const.

This is a somewhat arbitrary choice. However, some grounds to justify this choice can be given when we refer to the equation for correlation $D_1 = \frac{1}{\rho^2}\langle \rho' \rho' u_1' \rangle$ mentioned above in the section "Representation of inertial terms". At the point where R^2 is maximum and $\partial R^2 / \partial x = 0$, the value $D_1 = 2WR^2$. Similarly, the correlations are $D_1^{(k)} = \frac{1}{\rho^2}\langle \rho' m_k' u_1' \rangle = 2WB^{(k)}$.

The representation of third-order correlations as given above, has been obtained in a quasistationary approximation, i.e. neglecting time derivatives of the third-order correlations. Most likely, the deviation from this approximation should be larger at the edge of the mixing zone. This is accounted using a cutoff factor $\frac{1}{1+b}$, where

$$b = \frac{1}{4} \frac{k^{(B)}}{k_\gamma} (\xi + |\xi|), \quad \xi = \frac{2WAe}{k_B Q R^2} - 1, \quad A = -\frac{1}{\rho} \frac{\partial \rho}{\partial x}.$$

With the restriction factor included, the value D_t is expressed as

$$D_t = 2\alpha_1 \frac{e_1 e}{k_\gamma Q} \frac{1}{1+b}.$$

Thus, this factor makes D_t value become decrease by as many times as R^2 is smaller than its quasistationary representation.

FINAL SET OF EQUATIONS

Thus, by summarizing the date from the previous Sections and transforming the equations (73), (74), (78) and (87), we come to the following set of equations

$$\frac{d\rho}{dt} = -\rho \operatorname{div} V;$$

$$\frac{dV}{dt} = -\frac{1}{\rho}\frac{\partial P}{\partial x} - \frac{1}{\rho}\frac{\partial}{\partial x} 2\rho\Phi_{11};$$

$$\frac{d\mathcal{E}}{dt} = -\frac{P}{\rho}\operatorname{div}(V - W) - \frac{1}{\rho}\operatorname{div}\left(W^{(0)} - \mathcal{E}\, W\right) - \frac{1}{\rho}\operatorname{div}\rho q^{(f)} + Q; \tag{88}$$

$$\frac{dc_k}{dt} = -\frac{1}{\rho}\operatorname{div}\left(W^{(k)} - c_k W\right);$$

$$\frac{de_1}{dt} = \operatorname{div}\left(D_t^{(e_1)}\frac{\partial e_1}{\partial x} - We_1\right) - e_1 \operatorname{div} W - 2e_1 V_{11} + \left(1 - \frac{2}{10}\alpha k\right) f_1 W g - \gamma\,\omega\left(e_1 - \frac{1}{3}e\right) - \frac{Q}{3};$$

$$\frac{de_2}{dt} = \operatorname{div}\left(D_t^{(e_2)}\frac{\partial e_2}{\partial x} - We_2\right) - e_2 \operatorname{div} W - 2e_2 V_{22} + \frac{1}{10}\alpha k f_1 W g - \gamma\,\omega\left(e_2 - \frac{1}{3}e\right) - \frac{Q}{3};$$

$$\frac{de_3}{dt} = \operatorname{div}\left(D_t^{(e_3)}\frac{\partial e_3}{\partial x} - We_3\right) - e_3 \operatorname{div} W - 2e_3 V_{33} + \frac{1}{10}\alpha k f_1 W g - \gamma\,\omega\left(e_3 - \frac{1}{3}e\right) - \frac{Q}{3};$$

$$\frac{dW^{(k)}}{dt} = \frac{1}{\rho}\operatorname{div}\rho\left(D_t^{(W)}\frac{\partial W^{(k)}}{\partial x} - WW^{(k)}\right) - W^{(k)}V_{11} + 2e_1 A + f_1 B^{(k)} g - k_W\,\omega\, W^{(k)};$$

$$\frac{dB^{(k)}}{dt} = \frac{1}{\rho^2}\operatorname{div}\rho^2\left(D_t^{(B)}\frac{\partial B^{(k)}}{\partial x} - WB^{(k)}\right) + B^{(k)}\operatorname{div} W + W^{(k)}A + WA_k - k_B\,\omega B^{(k)};$$

$$\frac{dQ}{dt} = \operatorname{div}\left\{D_t^{(Q)}\frac{\partial Q}{\partial x} - W_j Q\right\} - Q\frac{\partial W}{\partial x} -$$

$$-Q\left\{\frac{4}{3} + \beta_1\gamma\left(\frac{e_1}{e} - \frac{1}{3}\right)\right\}V_{11} - Q\left\{\frac{4}{3} + \beta_1\gamma\left(\frac{e_2}{e} - \frac{1}{3}\right)\right\}V_{22} - Q\left\{\frac{4}{3} + \beta_1\gamma\left(\frac{e_3}{e} - \frac{1}{3}\right)\right\}V_{33} +$$

$$+\frac{Q}{3e_1} f_1 W g + \beta_2\left\{\frac{1}{5}\alpha\, k\, f_1 W g + \left(e_1 - \frac{1}{3}e\right)\right\} WA\,\frac{1 + R^2}{R^2} - \frac{Q^2}{ke};$$

$$k = 0 \cdots n\ .$$

The following notation is used here:

$$g = -\frac{1}{\rho}\frac{\partial P}{\partial r}, \quad A = -\frac{1}{\rho}\frac{\partial \rho}{\partial r}, \quad A_k = -\frac{1}{\rho}\frac{\partial \rho c_k}{\partial r} \ (k = 1 \ldots n), \quad A_o = -\frac{1}{\rho}\frac{\partial \rho\mathcal{E}}{\partial r}$$

V_{11}, V_{22}, V_{33} -are deformation tensor components.

For plane geometry: $V_{11} = \dfrac{\partial(V - W)}{\partial r}$, $V_{22} = V_{33} = 0$.

For cylindrical geometry: $V_{11} = \dfrac{\partial (V - W)}{\partial r}$, $V_{22} = \dfrac{V - W}{r}$, $V_{33} = 0$.

For spherical geometry: $V_{11} = \dfrac{\partial (V - W)}{\partial r}$, $V_{22} = V_{33} = \dfrac{V - W}{r}$.

$q^{(f)}$ - heat flux due to heat conduction

It is assumed here, that $\Phi_{11} = \dfrac{e_1}{e}\Phi$, where $\Phi = \Phi_{jj}$. For total kinetic turbulent energy Φ, we use equations for e_{ik}, W to have

$$\frac{d\Phi}{dt} = \frac{1}{\rho}\operatorname{div}\rho\left(D_t^{(\Phi)}\frac{\partial\Phi}{\partial x} - W\Phi\right) - 2\Phi_{ij}V_{ij} - W\frac{dV}{dt} - Q \ .$$

The transport term is expressed here similarly to the other equations, there being $D_t^{(\Phi)} = \frac{5}{3}D_t$.

Note, that the above set of equations is conservative and can be used as a basis to formulate the following total energy conservation law:

$$\frac{\partial}{\partial t}\rho\left(\mathcal{E} + \frac{1}{2}V_i^2 + \Phi\right) =$$

$$= -\frac{\partial}{\partial x_j}\rho\left\{V_j\left(\mathcal{E} + \frac{1}{2}V_i^2 + \Phi\right) + \frac{P}{\rho}\left(V_j - W_j\right) + q_j^{(f)} + W_j^{(0)} - W_j\mathcal{E} + 2\Phi_{ij}\left(V_i - W_i\right) - \right.$$

$$\left. -D_t^{(\Phi)}\frac{\partial\Phi}{\partial x_j}\right\}$$

This set of equations should be added by the equation of state of substance with the pressure and energy therein dependent on the mixture heterogeneity as well as on its density, temperature and concentrations. The calculations used as a first approximation the linear interpolation between the equation of state for the various mixture components, of the form:

$$P = \sum_k c_k P_k(\rho, T), \quad \mathcal{E} = \sum_k c_k E_k(\rho, T),$$

where $P_k(\rho_k, T_k)$, $E_k(\rho_k, T_k)$ - is the equation of state of the k-th constituent of the mixture. The constituents' densities and temperatures ρ_k and T_k were assumed equal to the mixture ρ and T, respectively.

COMPRESSIBILITY AND HEAT CONDUCTION EFFECTS

The equations as described in the previous section refer to incompressible medium case. This section includes corrections to the equations, allowing for medium compressibility and heat conduction. In this discussion, we will consider small gradients for all the values.

Consider density and temperature variations of an elementary mass as it is transported by vortex from point x_1 to point x_2, with the distance between them being, on average, of the order of turbulence scale l_t. Denote with ρ_1, T_1 and ρ_2, T_2 the average density and temperature values at points x_1 and x_2, respectively, and with ρ_{12}, T_{12}- density and temperature for the elementary mass at point x_2, after its being transported by vortex from point x_1. We will estimate squared values of density $\langle\rho'\rho'\rangle$ and temperature fluctuations $\langle T'T'\rangle$ from the following relationships:

$$\langle\rho'\rho'\rangle \approx (\rho_{12}-\rho_2)^2, \quad \langle T'T'\rangle \approx (T_{12}-T_2)^2$$

Instantaneous value of $\rho' = \rho_{12} - \rho_2$ at x_2 point is approximately

$$\rho' = \rho_1 + \delta\rho - \rho_2 \approx -l_t\nabla\rho + \left.\frac{\partial\rho}{\partial P}\right|_S \delta P + \left.\frac{\partial\rho}{\partial S}\right|_P \delta S,$$

where $\delta P, \delta S$ are the pressure and entropy variations in the elementary mass during the transport. The value of δP for low turbulent Mach number is obviously $\delta P \approx l_t\nabla P$. Therefore:

$$\rho' \approx l_t\left(\left.\frac{\partial\rho}{\partial P}\right|_S \nabla P - \nabla\rho\right) + \left.\frac{\partial\rho}{\partial S}\right|_P \delta S = l_t\left(\left.\frac{\partial\rho}{\partial P}\right|_S \nabla P - \nabla\rho\right) + \frac{T}{c_p}\left.\frac{\partial\rho}{\partial T}\right|_P \delta S,$$

where c_p is the heat capacity at constant pressure.

When there is no radiant or electronic heat conduction, $\delta S = 0$. Molecular heat conduction can be ignored, since the turbulence case of interest is that at high Reynolds numbers. With heat conduction specified for $\frac{dS}{dt}$ we have approximately

$$\rho T\frac{dS}{dt} = \operatorname{div}\chi\nabla T \approx -\frac{\chi}{l_t^2}(T - T_0),$$

where $T-T_0$ is the current difference between temperatures of the elementary mass transported and the environment, χ- heat conductivity. To define $T - T_0$, we use the relationship

$$\frac{dE}{dt} = T\frac{dS}{dt} + \frac{P}{\rho^2}\frac{d\rho}{dt}.$$

Since

$$\frac{dE}{dt} = \left.\frac{\partial E}{\partial T}\right|_P \frac{dT}{dt} + \left.\frac{\partial E}{\partial P}\right|_T \frac{dP}{dt}; \quad \frac{d\rho}{dt} = \left.\frac{\partial\rho}{\partial T}\right|_P \frac{dT}{dt} + \left.\frac{\partial\rho}{\partial P}\right|_T \frac{dP}{dt};$$

$$\left.\frac{\partial E}{\partial T}\right|_P = c_p + \frac{P}{\rho^2}\left.\frac{\partial\rho}{\partial T}\right|_P; \quad \left.\frac{\partial E}{\partial P}\right|_T = \frac{T}{\rho^2}\left.\frac{\partial\rho}{\partial T}\right|_P + \frac{P}{\rho^2}\left.\frac{\partial\rho}{\partial P}\right|_T,$$

then we obtain

$$c_p\frac{dT}{dt} = T\frac{dS}{dt} - \frac{T}{\rho^2}\left.\frac{\partial\rho}{\partial T}\right|_P \frac{dP}{dt};$$

or, using the approximation for $\frac{dS}{dt}$, we have

$$c_p\frac{dT}{dt} \approx -b_1\frac{\chi}{\rho l_t^2}(T - T_0) - \frac{T}{\rho^2}\left.\frac{\partial\rho}{\partial T}\right|_P \frac{dP}{dt},$$

where b_1 is the constant of the order of unity.

While elementary mass is transported at a velocity, on average, of the order of $\sqrt{2e_1}$, it may be approximated that

$$\frac{dP}{dt} \approx \sqrt{2e_1}\nabla P; \quad \frac{dT_0}{dt} \approx \sqrt{2e_1}\nabla T.$$

By denoting $\tau = T - T_0$, we obtain

$$c_p \frac{d\tau}{dt} \approx -b_1 \frac{\chi}{\rho l_t^2}\tau - \sqrt{2e_1}\left(c_p \nabla T + \frac{T}{\rho^2}\frac{\partial\rho}{\partial T}\bigg|_P \nabla P\right).$$

By solving this equation, we have

$$\tau = T - T_0 \approx -\frac{\rho l_t^2}{b_1\chi}\sqrt{2e_1}\left(c_p\nabla T + \frac{T}{\rho^2}\frac{\partial\rho}{\partial T}\bigg|_P \nabla P\right)\left\{1-\exp\left(-\frac{b_1\chi}{\rho c_p l_t^2}t\right)\right\}.$$

For entropy variation during the transport, we use the following equation

$$\delta S \approx -b_1\frac{\chi}{\rho l_t^2}\int_0^t (T-T_0)\,dt \approx$$

$$\approx \sqrt{2e_1}\left(c_p\frac{\nabla T}{T} + \frac{1}{\rho}\frac{\partial\rho}{\partial T}\bigg|_P \frac{\nabla\rho}{\rho}\right)\left\{t - \frac{\rho c_p l_t^2}{b_1\chi}\left[1-\exp\left(-\frac{b_1\chi}{\rho c_p l_t^2}t\right)\right]\right\}.$$

Elementary masses are transported, on average, in the time of the order of the period of turbulent fluctuations $\tau_t \approx \frac{l_t}{\sqrt{2e_1}}$. Therefore, for temperature fluctuation value at x_2 point we have $T' \approx T_{12} - T_2 \approx \tau(t = \tau_t)$, and for complete change of entropy $\delta S = \delta S(t = \tau_t)$ we have

$$T' \approx -l_t\left(\nabla T + \frac{T}{c_p}\frac{1}{\rho}\frac{\partial\rho}{\partial T}\bigg|_P \frac{\nabla P}{\rho}\right)y(\varphi); \qquad (89)$$

$$\delta S \approx l_t\left(c_p\frac{\nabla T}{T} + \frac{1}{\rho}\frac{\partial\rho}{\partial T}\bigg|_P \frac{\nabla P}{\rho}\right)\left[1-y(\varphi)\right],$$

where $y(\varphi) = \frac{1}{\varphi}\left(1-e^{-\varphi}\right)$, $\varphi = b_1\frac{\chi}{\rho c_p l_t\sqrt{2e_1}}$.

Employing this relationship, we write the following to express the density fluctuation value at x_2 point $\rho' \approx \rho_{12} - \rho_2 = \rho l_t A$, with the notation involved

$$A = A_S + \left(A_T - A_S\right)\left[1-y(\varphi)\right];$$

$$A_S = \frac{1}{\rho}\frac{\partial\rho}{\partial P}\bigg|_S - \frac{\nabla P}{\rho},\quad A_T = \frac{1}{\rho}\frac{\partial\rho}{\partial P}\bigg|_T \nabla P + \frac{1}{\rho}\frac{\partial\rho}{\partial T}\bigg|_P \nabla T - \frac{\nabla\rho}{\rho}. \qquad (90)$$

We use expressions (89) and (90) to define more exactly the rhs generating terms of eqs. (88). From (88), with only convective terms included for $W = \sum_k W^{(k)} = \frac{1}{\rho}\langle\rho' u_1'\rangle$ and $R^2 = \sum_k B^{(k)} = \frac{1}{\rho^2}\langle\rho'\rho'\rangle$, we have

$$W \approx -\frac{e_1}{\omega}\frac{1}{\rho}\frac{\partial\rho}{\partial x},\quad R^2 \approx -\frac{W}{\omega}\frac{1}{\rho}\frac{\partial\rho}{\partial x} \approx \frac{e_1}{\omega}\frac{1}{\rho^2}\left(\frac{1}{\rho}\frac{\partial\rho}{\partial x}\right)^2,$$

where $\omega = \frac{Q}{e}$.

These expressions have density gradient terms omitted as being of purely inertial nature and thus insignificant for this discussion.

As long as $l_t \approx \frac{\sqrt{2e_1}}{\omega}$, they may be rewritten as follows

$$W \approx -l_t\sqrt{e_1}\,\frac{1}{\rho}\frac{\partial\rho}{\partial x}, \quad R^2 \approx l_t^2\left(\frac{1}{\rho}\frac{\partial\rho}{\partial x}\right)^2.$$

On the other hand, we obtain from (90)

$$W = \frac{1}{\rho}\left\langle\rho' u_1'\right\rangle \approx \frac{\sqrt{\rho'^2}}{\rho}\sqrt{e_1} \approx l_t\sqrt{e_1}\,A, \quad R^2 = \frac{\langle\rho'\rho'\rangle}{\rho^2} \approx l_t^2 A^2.$$

It can be seen from comparing these expressions, that to make allowance for compressibility and heat conduction, the generating terms in equations for W, R^2 must use A value as found from (90) instead of $-\frac{1}{\rho}\frac{\partial\rho}{\partial x}$.

From eqs. (88), we obtain for $W^{(k)} = \frac{1}{\rho}\left\langle\left(\rho\alpha_k\right)' u_1'\right\rangle$ on the same assumptions

$$W^{(k)} \approx -\frac{e_1}{\omega}\frac{1}{\rho}\frac{\partial\rho c_k}{\partial x} = -\frac{e_1}{\omega}\left(c_k\frac{1}{\rho}\frac{\partial\rho}{\partial x} + \frac{\partial c_k}{\partial x}\right).$$

On the other hand,

$$W^{(k)} \approx \frac{\sqrt{e_1}}{\rho}\left[\left(\rho c_k\right)_{12} - \left(\rho c_k\right)_2\right] = \frac{\sqrt{e_1}}{\rho}\left[\left(\rho c_k\right)_1 + \left(c_k\right)_1\delta\rho - \left(\left(\rho c_k\right)_2\right)\right]$$

This expression has no δc_k value, since molecular diffusion is neglected. Since

$$\delta\rho = \rho_{12} - \rho_1 = \left(\rho_{12} - \rho_2\right) + \left(\rho_2 - \rho_1\right) = \rho' + \left(\rho_2 - \rho_1\right),$$

then

$$W^{(k)} \approx \frac{\sqrt{e_1}}{\rho}\left\{\left(c_k\right)_1\rho' - \rho\left\{\left(c_k\right)_2 - \left(c_k\right)\right\}_1\right\}.$$

Considering that $\rho' \approx l_t A$, $\left(c_k\right)_2 - \left(c_k\right)_1 \approx l_t\frac{\partial c_k}{\partial x}$, $l_t \approx \frac{\sqrt{e_1}}{\omega}$, we obtain

$$W^{(k)} \approx \frac{e_1}{\omega}\left(c_k A - \frac{\partial c_k}{\partial x}\right).$$

As we compare the expressions for $W^{(k)}$, we conclude that the equation (88) for $W^{(k)}$ ($k = 1....n$) should use the following instead of $-\frac{1}{\rho}\frac{\partial\rho c_k}{\partial x}$

$$A_k = c_k A - \frac{\partial c_k}{\partial x}. \tag{91}$$

Similarly, the terms to be used in the equation for $B^{(k)}$ instead of

$$-W^{(k)}\frac{1}{\rho}\frac{\partial\rho}{\partial x} - W\frac{1}{\rho}\frac{\partial\rho c_k}{\partial x}$$

are $W^{(k)}A + W A_k$, where A, A_k are defined by eqs. (90), (91).

Now let us move on to an equation for energy flux $W^{(0)} = \frac{1}{\rho}\left\langle (\rho E)' u_1' \right\rangle$. We have from (88) that $W^{(0)} \approx -\frac{e_1}{\omega}\frac{1}{\rho}\frac{\partial \rho \mathcal{E}}{\partial x}$. On the other hand,

$$W^{(0)} \approx \frac{\sqrt{e_1}}{\rho}\left[(\rho E)_{12} - (\rho E)_2\right] = \frac{\sqrt{e_1}}{\rho}\left[(\rho E)_1 + \delta(\rho \mathring{A}) - (\rho E)_2\right] \approx$$

$$\approx \frac{\sqrt{e_1}}{\rho}\left[-l_t \frac{\partial \rho \mathcal{E}}{\partial x} + E\delta\rho + \rho\delta E\right]$$

Considering that

$$\delta E = \left.\frac{\partial E}{\partial \rho}\right|_T \delta\rho + \left.\frac{\partial E}{\partial T}\right|_\rho \delta T$$

$$\delta\rho = \rho_{12} - \rho_1 = (\rho_{12} - \rho_2) + (\rho_2 - \rho_1) \approx l_t \frac{\partial \rho}{\partial x} + \rho',$$

$$\delta T = T_{12} - T_1 = (T_{12} - T_2) + (T_2 - T_1) \approx l_t \frac{\partial T}{\partial x} + T',$$

and using (89), (90), and also the relationship $l_t \approx \frac{\sqrt{e_1}}{\omega}$, we obtain that $W^{(0)} \approx \frac{e_1}{\omega} A_0$, where

$$A_0 = \mathcal{E} A - \frac{\partial \mathcal{E}}{\partial x} + \left.\frac{\partial E}{\partial \rho}\right|_T \left\{ \left.\frac{\partial \rho}{\partial P}\right|_S \nabla P + (A_T - A_S)[1 - y(\varphi)] \right\} -$$
$$-\left.\frac{\partial E}{\partial T}\right|_\rho \left\{ \frac{T}{\rho c_p} \left.\frac{\partial \rho}{\partial T}\right|_P \frac{\nabla P}{\rho} y(\varphi) - [1 - y(\varphi)]\nabla T \right\}. \qquad (92)$$

Thus, it becomes clear that the equation for $W^{(0)}$ must incorporate A_0 value defined by eq. (92) instead of $-\frac{1}{\rho}\frac{\partial \rho \mathcal{E}}{\partial x}$.

The equation for $B^{(0)}$ must use instead of the group

$$-W^{(0)}\frac{1}{\rho}\frac{\partial \rho}{\partial x} - W\frac{1}{\rho}\frac{\partial \rho \mathcal{E}}{\partial x}$$

the following terms $W^{(0)}A + WA_0$.

It is necessary to consider medium compressibility and solve the complete set of equations (88) together with the corrections allowed herein, when the requirement $\frac{\nabla P}{P} << \frac{\nabla \rho}{\rho}$ is not satisfied. However, given this requirement is satisfied, one need not solve all equations for $W^{(k)}$, $B^{(k)}$ in (88), but just confine oneself to solving two equations for total turbulent mass flow $W = \sum_k W^{(k)}$ and relative mean-square density fluctuations $R^2 = \sum_k B^{(k)}$. In this case, the mass flows of individual components and the energy fluxes can be expressed in terms of gradients: $W^{(k)} = -D_w \nabla c_k$, $W^{(0)} = -D_w \nabla \mathcal{E}$ with diffusion coefficient $D_w = W/A$. Following this, one can easily see that the equation for concentrations in (88) and the terms accounting for turbulent transport of energy both become diffusive kind. The available numerical techniques can provide calculations for both complete and reduced sets of equations.

When the requirement $\frac{\nabla P}{P} << \frac{\nabla \rho}{\rho}$ is not satisfied, then there may be situations where gradient representation keeps while diffusion coefficient D_w for total mass flow would turn out to be infinite. However, effective diffusion coefficients for the mass flows of individual components would be finite and distinct.

Note one more effect that results from medium compressibility. Let there be a uniform steady turbulence in a single-constituted medium. To account for the energy variation of this medium due to turbulent transport, we use

$$\frac{d\mathcal{E}}{dt} = -\frac{1}{\rho}\operatorname{div} q_h, \quad q_h = W^{(0)} - \mathcal{E} W .$$

Since $W^{(0)} \approx \frac{e_1}{\omega} A_0$, $W \approx \frac{e_1}{\omega} A$, then we obtain for q_h using (90), (92)

$$q_h \approx -\frac{e_1}{\omega} c_v \left(\frac{\partial T}{\partial x} + \frac{T}{c_p} \frac{1}{\rho} \frac{\partial \rho}{\partial T}\Big|_p \frac{1}{\rho} \frac{\partial P}{\partial x} \right),$$

where c_v, c_p - are the heat capacity at constant volume and pressure, respectively.

This expression implies that there may be cases where turbulent heat flow is directed down and not up the temperature gradient. That is, where heat could be transferred from lower-temperature locations to those with higher temperatures, while the associated effective turbulent heat conductivity would be below zero. It can be seen from the equation for q_h that the heat flow will be so abnormally directed, given

$$c_p \frac{\partial T}{\partial x} + \frac{T}{\rho} \frac{\partial \rho}{\partial T}\Big|_p \frac{1}{\rho} \frac{\partial P}{\partial x} < 0 .$$

For ideal gas, this condition is expressed as: $\frac{1}{T}\frac{\partial T}{\partial x} < \frac{\gamma - 1}{\gamma} \frac{1}{P} \frac{\partial P}{\partial x}$ (here γ is the gas adiabatic index). In other words, the turbulent heat flow will have abnormal direction when there is temperature gradient smaller than with adiabatic temperature distribution. This flow would make the temperature distribution approach adiabatic form.

SHOCK FRONT VARIATIONS OF TURBULENT QUANTITIES

The set of eqs. (88) is useful to describe 1D flows without shock waves involved. However, if there are shock waves involved in the problem then these equations should be added by the conditions to connect second-order correlation values on both sides of the shock front. For this purpose, based on simplifying assumptions we consider a problem for a shock wave passing through a uniform (in terms of mean-square fluctuations being invariable in space) turbulized medium. We assume relative mean-square density fluctuations R^2 to be a small value. The shock will be considered strong, implying that mass velocity increment at the wave front is much larger than fluctuation velocities before and after the wave front. For convenient writing, we will use on this point the symbol u to denote the velocity component normal to the wave front, v- that parallel to it and indices 1 and 2 will indicate the conditions before and after the front, respectively.

Based on the conservation laws of energy, mass and momentum, we obtain the following relationships to the first order of smallness in ρ', u'

$$\begin{aligned}
&\rho_1 u_1' + \rho_1' u_1 - \rho_1 D' = \rho_2 u_2' + \rho_2' u_2 - \rho_2 D',\\
&P_1' + \rho_1' u_1^2 + 2\rho_1 u_1 u_1' - 2\rho_1 u_1 D' = P_2' + \rho_2' u_2^2 + 2\rho_2 u_2 u_2' - 2\rho_2 u_2 D', \qquad (93)\\
&W_1' + u_1 u_1' - u_1 D' = W_2' + u_2 u_2' - u_2 D',
\end{aligned}$$

where W is the enthalpy, D'- shock front velocity fluctuations. The velocity components parallel to the front are the same: $v_1 = v_2$, $v_1' = v_2'$.

Thus, there are three equations associated with the four unknown quantities: ρ_2', u_2', P_2', D'. Assume in addition that the medium may be regarded as ideal gas having adiabatic index γ. This allows the consideration that in strong shock case (in its usual meaning now) ρ_1 and $\rho 2$ will be related as: $\rho_2' = h\rho_1'$, where h is the shock front compression. By formulating enthalpy fluctuations in terms of density and pressure fluctuations

$$W' = \frac{\gamma}{\gamma-1}\frac{1}{\rho}P' + \frac{W}{\rho}\rho'$$

and ignoring P_1', due to small turbulent Mach number, we obtain from the equation (93)

$$u_2' = u_1' - \frac{1}{2}\frac{\rho_1'}{\rho_1}\Delta V, \quad P_2' = 0, \quad \frac{\rho_2'}{\rho_2} = \frac{\rho_1'}{\rho_1}, \quad v_2' = v_1',$$

where ΔV is the shock front increment to mean mass velocity. Allowance for the finiteness of density fluctuation values results in the requirement that the cofactor ΔV should be replaced by $f_1\Delta V$.

These expressions have been formulated for strong shock case. The effects of weak shock wave should be equivalent to a medium being simply driven by pressure gradient. To make weak shock effects have the same results as follow from (88), u_2', u_1' must be related as

$$u_2' = h\,u_1' - \frac{\rho_1'}{\rho_1} f_1\,\Delta V,$$

where h is the shock wave compression $(h - 1 << 1)$.

Taking into account this expression, the following interpolation relationship has been adopted

$$u_2' = a\,u_1' - b\frac{\rho_1'}{\rho_1} f_1\,\Delta V,$$

where $a = \frac{h+\psi^2}{1+\psi^2}$, $b = \frac{1+\psi^2}{2+\psi^2}$.

The quantity ψ is taken in the form $\psi = \sqrt{R^2}\,\frac{P_1}{P_2 - P_1}$, where P_1, P_2 are pressures before and after the front.

Thus , to characterize turbulence before and after the shock front we obtain

$$e_1^{(2)} = a^2 e_1^{(1)} - a\, b W_{(1)}\, f_1^{(1)} \Delta V + \frac{1}{2} b^2 R_{(1)}^2 \left(f_1^{(1)} \Delta V \right)^2;$$

$$e_2^{(2)} = e_2^{(1)}, \quad e_3^{(2)} = e_3^{(1)};$$

$$W_{(2)} = a W_{(1)} - b R_{(1)}^2\, f_1^{(1)} \Delta V; \quad R_{(2)}^2 = R_{(1)}^2;$$

$$W_{(2)}^{(k)} = a W_{\cdot(1)}^{(k)} - b B_{(1)}^{(k)}\, f_1^{(1)} \Delta V; \quad B_{(2)}^{(k)} = R_{(1)}^{(k)}.$$

It would be difficult to use these conditions in any particular numerical calculation due to the shock front spreading over many computational cells. Therefore, the set of equations (88) is solved for the wave front with some variations included. Particularly, A_k, V_{11}, f_1, g are replaced by $A_k^{(1)}$, $V_{11}(2b - 1)$, $f_1^{(1)}$, gb, where $A_k^{(1)}$, $f_1^{(1)}$ are the respective values before the front. These variations provide consistency with the above-formulated conditions for strong shock front and at the same time make the effects of a series of weak shock waves equivalent to simple deceleration.

2.2.3. SELECTION OF SEMIEMPIRICAL CONSTANTS

There are semiempirical constant included in equations (88). These are k_W, k_B constants in the dissipative terms of the equations for $W^{(k)}$, $B^{(k)}$; $\alpha, \gamma_1, \gamma_2, \gamma_3$ - constants in the exchange interaction tensor, and β_1, β_2 in the equation for Q. Additionally, there has been a constant in the dissipative term of the equation for Q, taken equal to 2, to allow the energy of uniform and isotropic turbulence to decrease as t^{-1}. Further, there is α_1 constant in the gradient representation of the third-order correlations.

The value of k_B can be found based on the experimental data on fluctuation decay of scalar quantities (density, temperature) within uniform and isotropic turbulence. Reportedly, scalar fluctuations would decay under these conditions as $t^{-\alpha}$, where α value is ranging within 1.3 and 1.5, while turbulent energy decay rate is rather well approximated as t^{-1}. An attempt was made in [60] to formulate in theory the law $t^{-1.5}$ for scalar fluctuation decay rate. This law was used to select the value of $k_B = 1.5$. Note, that this value is only suitable where Schmidt number for medium is not too much different from unity, i. e. where molecular diffusion and viscosity coefficients are of the same order of magnitude. However, in general, k_B value should depend on Schmidt number. For example, in a limiting case for mixing of molecularly insoluble liquids, $k_B = 0$.

We find a limitation on k_W value by considering an equation for squared correlation coefficient for density and velocity fluctuations $\eta^2 = \frac{W^2}{2R^2 e_1}$. This equation is to be derived from the equations for $W, R^2 e_1$, thus being expressed as

$$\frac{d\eta^2}{dt} = -2 \frac{W}{R^2} \frac{1}{\rho} \frac{\partial \rho}{\partial x} \left(1 - \eta^2\right) + f_1 \frac{W}{e_1} \frac{1}{\rho} \frac{\partial P}{\partial x} \left(1 - \eta^2\right) -$$

$$-\left\{ 2k_W - k_B - \frac{e}{3e_1} - \frac{2}{10} \alpha k f_1 \frac{W}{e_1} \frac{e}{Q} \frac{1}{\rho} \frac{\partial P}{\partial x} - \gamma \left(1 - \frac{e}{3e_1} \right) \right\} \frac{Q}{e} \eta^2.$$

Omitted here are transport terms as insignificant for this particular consideration.

By definition, the value of η^2 cannot be more than unity. This requires that the sum of terms enclosed in braces in the equation for η^2 be positive. Thus, the following inequality should be satisfied:

$$k_W > \frac{1}{2}\left\{k_B + \frac{e}{3e_1} + \frac{2}{10}\alpha k f_1 \frac{W}{e_1}\frac{e}{Q}\frac{1}{\rho}\frac{\partial P}{\partial x} + \gamma\left(1 - \frac{e}{3e_1}\right)\right\}.$$

Given this inequality, we take the following value for k_W:

$$k_W = \frac{e}{6e_1} + \frac{1}{10}\alpha k f_1 \frac{W}{e_1}\frac{e}{Q}\frac{1}{\rho}\frac{\partial P}{\partial x} + \frac{\gamma}{2} + \frac{k_B}{2}.$$

The value of α can be estimated by considering a turbulent anisotropy equation $\sigma = e_1 / e_2$. This equation can be easily derived from equations for e_1, e_2, thus having the following form for uniform turbulence case:

$$\frac{1}{\sigma}\frac{d\sigma}{dt} = -\left[1 - \frac{1}{10}\alpha(2+\sigma)k(\sigma)\right]\frac{Wg}{e_1} - (\gamma - 1)\omega(\sigma - 1).$$

The first term must have expression in brackets always positive, since turbulence generation should result in anisotropy. Specifically, for $\sigma \to \infty$ this expression would tend to $(1 - \frac{1}{10}\alpha 3\sqrt{3})$. Thus there follows the inequality $\frac{1}{10}\alpha < \frac{1}{3\sqrt{3}}$. Refs. [63], [56] obtained $\frac{1}{10}\alpha = 0.1$, i.e. $\alpha = 1$.

Furthermore, with decay consideration of uniform and nonisotropic turbulence, there would be but the last term left in the equation for σ , with $\gamma = \gamma_1$. The characteristic time of turbulent energy decrease is $\tau_e \sim \omega^{-1}$. Thus, is follows that, firstly, $\gamma_1 > 1$, and secondly, assuming $\tau_\sigma \approx \tau_e$, that $\gamma_1 \approx 2$. This value of γ_1 was verified using the experimental data [64].

The experiments [64] addressed stationary turbulent air flow inside a varying-section tube. The tube had a turbulizer grid positioned at its input end. The cylindrical channel behind this had fixed section S_1. Next, over a short length (i.e. turbulence deformation length) it became narrower to transform to another cylindrical channel of fixed section $S_2 < S_1$. While the flow had low velocity, the air could be considered as incompressible medium.

When this problem was numerically simulated based on the equations (88), the initial turbulence condition was specified (longitudinal fluctuations energy e_1, transverse fluctuations energy e_2, and energy dissipation rate Q) with respect to where the narrow channel portion begins. The situation considered by the calculations was $\frac{S_1}{S_2} = 4$. The value of γ_1 was varied.

Actually, $\gamma_1 = 2$ was found provide the best agreement with the experiment. These calculations together with the experimental data are illustrated by Fig. 47. For illustrative purpose, the figure also present the calculated data for $\gamma_1 = 1.5$ and $\gamma_1 = 2.5$.

The value of β_1 constant can be related to γ_1, by using the data from the theoretical studies of small high-rate deformation of a uniform isotropic turbulence [61], [64], [65]. Thus the following relationships [64] were obtained for rapid axisymmetric compression.

$$\tilde{e}_1 = \frac{1}{c^2} e_1, \tilde{e}_2 = ce_2 = \tilde{e}_3 = ce_3, \quad \tilde{\varsigma}^2 = c^2\varsigma^2, \tilde{\eta} = \frac{1}{c}\eta^2 = \tilde{\xi}^2 = \frac{1}{c}\xi^2,$$

where e_1 is the fluctuation energy longitudinally, $e_2 = e_3$- fluctuation energy in two mutually perpendicular transverse directions, while ς, η, ξ are the associated vorticity components: $c = \frac{S_1}{S_2}$. The "tilde" signifies the respective quantity following the turbulence deformation.

For isotropic turbulence case, the dissipation is equal to the mean-square vorticity multiplied by viscosity. While assuming the deformation small, we include the value $\varepsilon = c - 1 = \int V_{11}dt$. Here, $V_{11} = \frac{\partial V}{\partial x}$, V-is the flow velocity at the turbulence deformation length. Due to the incompressible medium and axisymmetric considerations, we have $V_{22} = V_{33} = -\frac{1}{2}V_{11}$. Thus, for the total turbulent energy $e = e_1 + e_2 + e_3$ and dissipation rate $Q = \nu_0\left(\varsigma^2 + \eta^2 + \xi^2\right)$, given small ε, we obtain

$$\tilde{e} = \frac{e}{3}\left(\frac{1}{c^2} + 2c\right) = \frac{e}{3}\left\{\frac{1}{(1+\varepsilon)^2} + 2(1+\varepsilon)\right\} \approx \left(1+\varepsilon^2\right)e,$$

$$\tilde{Q} = \frac{Q}{3}\left(c^2 + \frac{2}{c}\right) = \frac{Q}{3}\left\{(1+\varepsilon)^2 + \frac{2}{1+\varepsilon}\right\} \approx \left(1+\varepsilon^2\right)Q. \qquad (94)$$

On the other hand, equation (88) gives for e, Q, $\vartheta = \frac{e_1}{e_2}$:

$$\frac{1}{e}\frac{de}{dt} = -2\frac{\vartheta}{1+\vartheta}V_{11} - \frac{2}{2+\vartheta}V_{22} = -2\frac{\vartheta - 1}{2+\vartheta}V_{11};$$

$$\frac{1}{Q}\frac{dQ}{dt} = -\frac{4}{3}\left(V_{11} + 2V_{22}\right) - \beta_1\gamma_1\left\{\left(\frac{\vartheta}{2+\vartheta} - \frac{1}{3}\right)V_{11} + 2\left(\frac{1}{2+\vartheta} - \frac{1}{3}\right)V_{22}\right\} =$$

$$= -\frac{2}{3}\beta_1\gamma_1\frac{\vartheta - 1}{2+\vartheta}V_{11};$$

$$\frac{1}{\vartheta}\frac{d\vartheta}{dt} = -2\left(V_{11} - V_{22}\right) = -3V_{11}.$$

This has taken into account that $V_{11} + 2V_{22} = 0$ in the case of interest. Moreover, small distortion consideration may allow the expression for γ to have the term γ_3 omitted and specify $\gamma = \gamma_1$. The other terms in the equations for e, Q, ϑ are insignificant, since deformation has been predetermined as high-rate. Resolving these equations on the assumption that V_{11}=const, gives

$$\ln\frac{\tilde{\vartheta}}{\vartheta} = -3\int V_{11}dt = -3V_{11}t = -3\varepsilon;$$

$$\ln\frac{\tilde{e}}{e} = V_{11}^2 t^2 = \varepsilon^2;$$

$$\ln\frac{\tilde{Q}}{Q}=\frac{1}{2}\beta_1\gamma_1V_{11}^2\,t^2=\frac{1}{2}\beta_1\gamma_1\varepsilon^2.$$

Involving the turbulence deformation smallness, we eventually obtain

$$\tilde{e}=\left(1+\varepsilon^2\right)e,\quad \tilde{Q}=\left(1+\frac{1}{2}\beta_1\gamma_1\varepsilon^2\right)Q.$$

It follows from comparing this with (94), that $\frac{1}{2}\beta_1\gamma_1=1$. Since $\gamma_1=2$, we find that $\beta_1=1$.

The constant γ_3 value was also selected from comparing the calculations and the experimental data [64]. This comparison will be described further in Section 2.2.5. The best agreement observed was for $\gamma_3=1$.

The constants β_2,γ_2 were found from comparing the calculations with the experimental turbulent mixing data obtained by E. Meshkov and associates for cylindrical and plane geometries. The best agreement with experiments achieved was found for $\beta_2=1$, $\gamma_2=1$. The constant α_1 in the gradient transport term representation was selected based on comparing the calculated and experimental average density profiles within the mixing zone. The value taken for this was also $\alpha_1=1$.

2.2.4. NUMERICAL REPRESENTATION. (THE CODE "VIKHR")

The equations (88) are to be solved using split physical phenomena technique.

As a first step, gasdynamic equations are to be solved in terms of turbulent pressure:

$$\frac{d\rho}{dt}=-\rho\,\mathrm{div}U,$$

$$\frac{dU}{dt}=-\frac{1}{\rho}\nabla\left(P+P_t\right),$$

$$\frac{d\mathcal{E}}{dt}=-\frac{P}{\rho}\,\mathrm{div}U,$$

$$P=P(\rho,\mathcal{E},c_i),\ P_t=2\rho\Phi_{11}.$$

Then the equations for turbulent. quantities are integrated without diffusive terms involved:

$$\frac{de_1}{dt}=Y_1e_1-\gamma\left(e_1-\frac{1}{3}e\right)\omega-\omega_1e_1,$$

$$Y_1=-2\,\mathrm{div}W-W\frac{\nabla e_1}{e_1}-2V_{11}+\left(H-2N\right)\frac{1}{e_1},$$

$$\frac{de_2}{dt}=Y_2e_2-\gamma\left(e_2-\frac{1}{3}e\right)\omega-\omega_2e_2,$$

$$Y_2=-2\,\mathrm{div}W-W\frac{\nabla e_2}{e_2}-2V_{22}+\frac{N}{e_2},$$

$$\frac{de_3}{dt}=Y_3e_3-\gamma\left(e_3-\frac{1}{3}e\right)\omega-\omega_3e_3,$$

$$Y_3 = -2\,\mathrm{div}W - W\frac{\nabla e_3}{e_3} - 2V_{33} + \frac{N}{e_3},$$

$$\frac{dW^{(k)}}{dt} = Y_4\,W^{(k)} - W\,\mathrm{div}W^{(k)} + 2e_1 A_i + f_1 B^{(k)} G - k_1 \omega W^{(k)},$$

$$Y_4 = -\mathrm{div}W - W\frac{\nabla\rho}{\rho} - V_{11},$$

$$\frac{dB^{(k)}}{dt} = Y_5\,B^{(k)} + W A_k + A\,W^{(k)} - k_2\,\omega B^{(k)}, \quad k = 0,\ldots,n,$$

$$Y_5 = -2W\frac{\nabla\rho}{\rho} - W\frac{\nabla B^{(k)}}{B^{(k)}},$$

$$\frac{dQ}{dt} = Y_6\,Q - 2\frac{\omega}{k}Q,$$

$$Y_6 = -2\,\mathrm{div}W - W\frac{\nabla Q}{Q} - \left[\frac{4}{3} + \frac{\beta_1\gamma}{e}\left(e_1 - \frac{1}{3}e\right)\right]V_{11} -$$

$$-\left[\frac{4}{3} + \frac{\beta_1\gamma}{e}\left(e_2 - \frac{1}{3}e\right)\right]V_{22} - \left[\frac{4}{3} + \frac{\beta_1\gamma}{e}\left(e_3 - \frac{1}{3}e\right)\right]V_{33} +$$

$$+\frac{H}{3e_1} + \beta_2\left[2N + \gamma\omega\left(e_1 - \frac{1}{3}e\right)\right]\frac{W\,A}{Q}\,\frac{1+B}{B},$$

$$\frac{d\Phi}{dt} = Y_7\,\Phi - \omega\,\Phi,$$

$$Y_7 = -\mathrm{div}W - W\,\frac{\nabla\Phi}{\Phi} - W\,\frac{\nabla\rho}{\rho} -$$

$$-\frac{2}{\Phi}\left(\Phi_{11}V_{11} + \Phi_{22}V_{22} + \Phi_{33}V_{33}\right) - \frac{W}{\Phi}\frac{dU}{dt},$$

$$P = P\left(\rho, \mathcal{E}, c_i\right). \qquad (96)$$

Here the following notation is used:

$$H = f_1 G W, \quad N = \frac{\alpha k H}{10},$$

$$\omega = \frac{Q}{e}, \quad \omega_1 = \frac{Q}{3e_1}, \quad \omega_2 = \frac{Q}{3e_2}, \quad \omega_3 = \frac{Q}{3e_3}.$$

The same step also includes recalculation of the gasdynamic energy

$$\frac{d\mathcal{E}}{dt} = \frac{P}{\rho}\,\mathrm{div}W + \omega\,\Phi$$

and calculation of diffusion coefficients for turbulent quantities

Next, the heat equation is to be solved

$$\frac{d\mathcal{E}}{dt} = \frac{1}{\rho}\,\mathrm{div}q + F. \qquad (97)$$

Further, the equations for $\mathcal{E}$ and c_i concentrations should be solved: :

$$\frac{d\mathcal{E}}{dt} = -\frac{1}{\rho}\,\mathrm{div}\left[\rho\left(W_0 - \mathcal{E}\,W\right)\right],$$

$$\frac{dc_i}{dt} = -\frac{1}{\rho}\,\mathrm{div}\left[\rho\left(W_i - c_i\,W\right)\right], \quad i = 1 \ldots n. \tag{98}$$

As a final step, diffusion equations for $e_1, e_2, e_3, \Phi, Q, W_i, B_i$ $(i = 0,\ldots,n)$ are to be solved.

A set of split differencial equations is to be solved using finite-difference method. There is a difference grid set into the computational field. Coordinates and velocities are defined at the grid nodes, and the other quantities-at the computational cell centers.

Solving gasdynamic equations involves either explicit or implicit difference schemes.

The calculational formulae for explicit difference scheme are commonly known. The advantages of the difference scheme include the second order of accuracy in space and time, and little spreading of the shock wave (SW) front. However, the disadvantages of the explicit scheme with the computational viscosity used may become apparent for highly non-uniform grids. Therefore, the solution of gasdynamics equations uses, together with explicit difference scheme, the implicit difference scheme as described in [66].

The implicit scheme features the second order of accuracy in space and the first that in time. It makes the shock wave front spread 2 or 3 cells more than the explicit scheme.

The equations for turbulent quantities are integrated based on the combined explicit-implicit scheme. The calculation of heat equation is made using the weighted implicit difference scheme. The implicit difference scheme is also used to integrate the diffusion equations for turbulent quantities. Equations (98) are integrated using explicit difference scheme involving upstream differences.

There is the following sequence for solving gasdynamic equations based on the implicit scheme.

A sweep method is used to find mass velocity, calculate new coordinates, density and predetermined pressure vs. viscosity, internal energy and computational viscosity.

It is very important in solving the equations for turbulent quantities (96), that the solution for e_1, e_2, e_3, Q, Φ. should be positive. To explain the basic approach to the difference scheme consistent with this requirement, we use an equation representing the contributions of individual r.h.s terms of the equations (96)

$$\frac{dx}{dt} = Y_i x, \quad x(t_0) = x_0 \geq 0. \tag{99}$$

This equation has an accurate solution as $x = x_0\,e^{Y_i t}$. It may be either decreasing or increasing, depending on the sign for Y_i. The following difference scheme will be used to make the numerical solution of equation (99) positive for any τ:

$$\frac{x^{n+1}_{k+1/2} - x^{n}_{k+1/2}}{\tau} = x^{n}_{k+1/2}\,\frac{Y_i + |Y_i|}{2} + x^{n+1}_{k+1/2}\,\frac{Y_i - |Y_i|}{2}.$$

One can easily notice, that for $Y_i > 0$ it is explicit scheme that the equation is integrated by, and for $Y_i < 0$ - it is implicit scheme. By resolving this equation in terms of the sought function, we obtain

$$x^{n+1} = \frac{x^n\left[1+\frac{\tau}{2}\left(Y_i+|Y_i|\right)\right]}{1-\frac{\tau}{2}\left(Y_i-|Y_i|\right)}.$$

Subscript $(k+1/2)$ is omitted here.

This difference scheme is used to approximate the equations (96)'

The equations for e_1, e_2, e_3 are to be solved in three steps, with generating, exchange and dissipative terms considered successively. Then, the equations for $W^{(k)}$, $B^{(k)}$, Q. are sequentially solved using the explicit-implicit scheme.

2.2.5. CALCULATED RESULTS. COMPARISON AGAINST THE EXPERIMENT

All turbulent mixing calculations, excluding these fore shock-tube experiments, had two boundary cells at the interface, with very small but non-zero values of $B^{(k)}$ or R^2. This was required for the set of equations to have non-zero solution. The initial values of $B^{(k)}$ were such that whatever large variation of these would not affect the thickness of the turbulent mixing zone (TMZ), if it included more than ~10 computational cells. The calculations for shock-tube experiments had the initial values of $B^{(k)}$selected such, that the thickness of initial TMZ experimentally resulting from the gas-separating film disruption could be simulated.

RAPID AXISYMMETRIC TURBULENCE DEFORMATION

Section 2.2.3 describes the selection of γ_1 constant relying on the relevant data of ref. [64] obtained in stationary turbulent flow experiments using varying-section tubes. The experiments are also summarized there.

VIKHR code was used to conduct the detailed numerical simulation of the experiments [64] for large-to-small of sections ratios $S_1/S_2 = 4, 9, 16$.

An initial turbulence condition (e_1, e_2, Q), was specified in the calculations, which exists past the turbulizer grid; this was established from the experimental data. The axis of x_1 is aligned with that of the tube. The values and time histories of the deformation tensor components V_{11}, V_{22} were found from the experimentally measured mean flow velocity V as a function of x_1.coordinate. The equation of state of ideal gas was used for the air.

The analysis has seen made for the calculations involving different β_1 γ_3 constants, to show that $\beta_1=1$ and $\gamma_3=1$ are the values that can provide rather good account of the turbulence evolution over the whole flow length for three cases of interest. Fig. 48, 49 and 50 show the calculated and experimental values of $\sqrt{2e_1}/V_0$, $\sqrt{2e_2}/V_0$ and V/V_0 versus x_1/M for $S_1/S_2 = 4, 9, 16$. Here e_1 and e_2 are fluctuation energies along and transverse to the flow axis, respectively, V_0- flow velocity past the turbulizer grid, V- flow velocity at an arbitrary section of the channel, M - turbulizer mesh size. These calculations used the values $\beta_1 = 1$, $\gamma_3 = 1$.

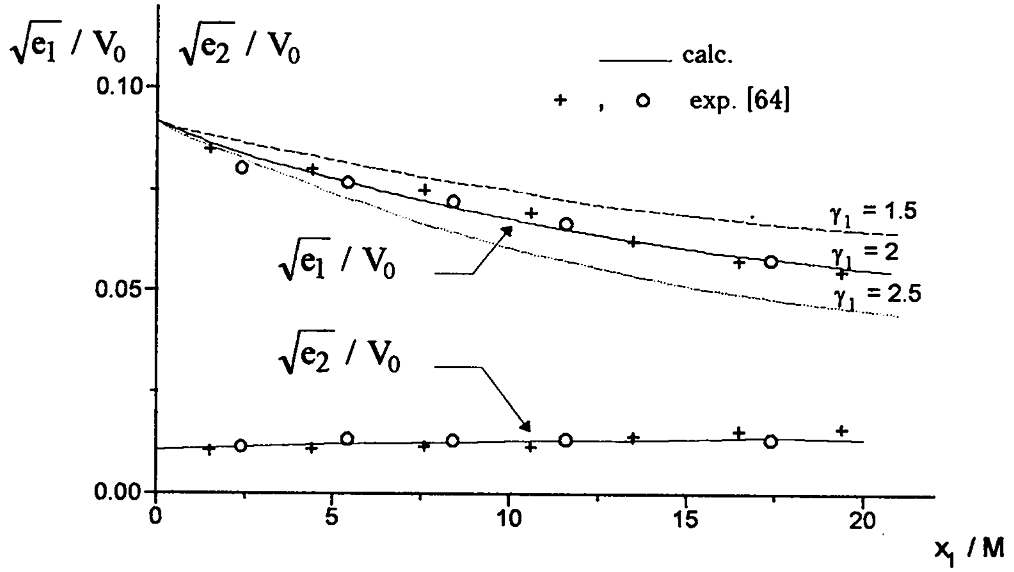

Fig.47. Values of $\sqrt{e_1} / V_0$, $\sqrt{e_2} / V_0$ as function of x_1/M for different γ_1 values.
M - turbulizer grid size, V_0 - flow velocity past the grid.

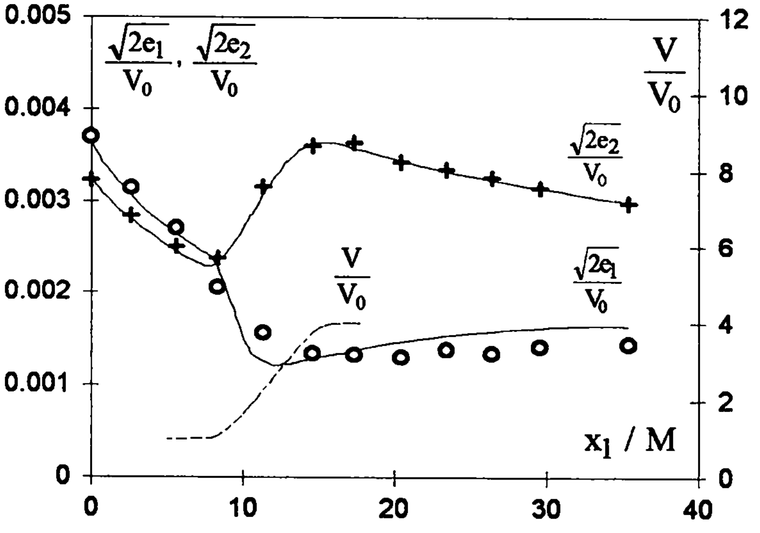

Fig.48. Values of $\sqrt{e_1} / V_0$, $\sqrt{e_2} / V_0$, V/V_0 as function of x_1/M for $S_1/S_2=4$.
M - turbulizer grid size, V_0 - flow velocity past the grid.
o, + - experiment; .... , ——— - calculation.

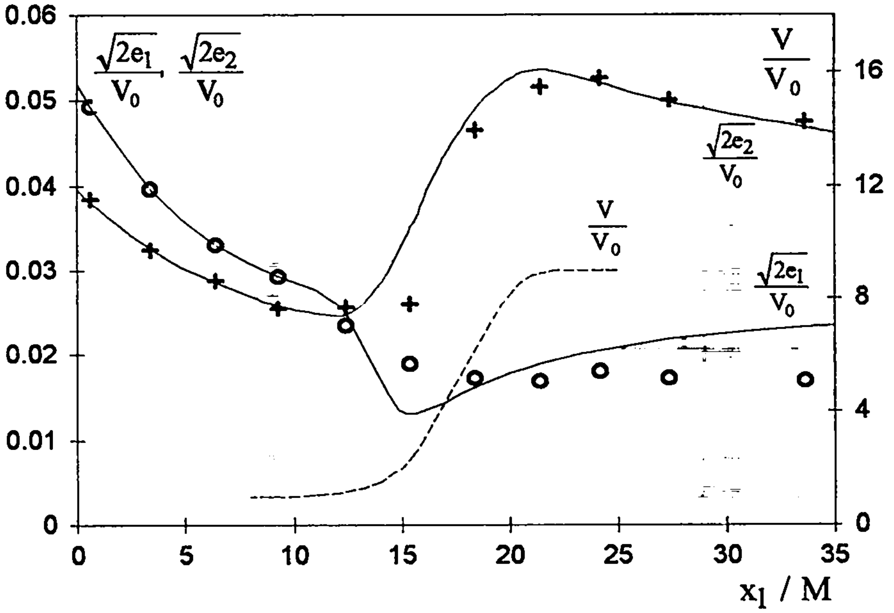

Fig.49. Values of $\sqrt{e_1}$ / V_0, $\sqrt{e_2}$ / V_0, V/V_0 as function of x_1/M for $S_1/S_2=9$.
M - turbulizer grid size, V_0 - flow velocity past the grid.
o, + - experiment; .... , ——— - calculation.

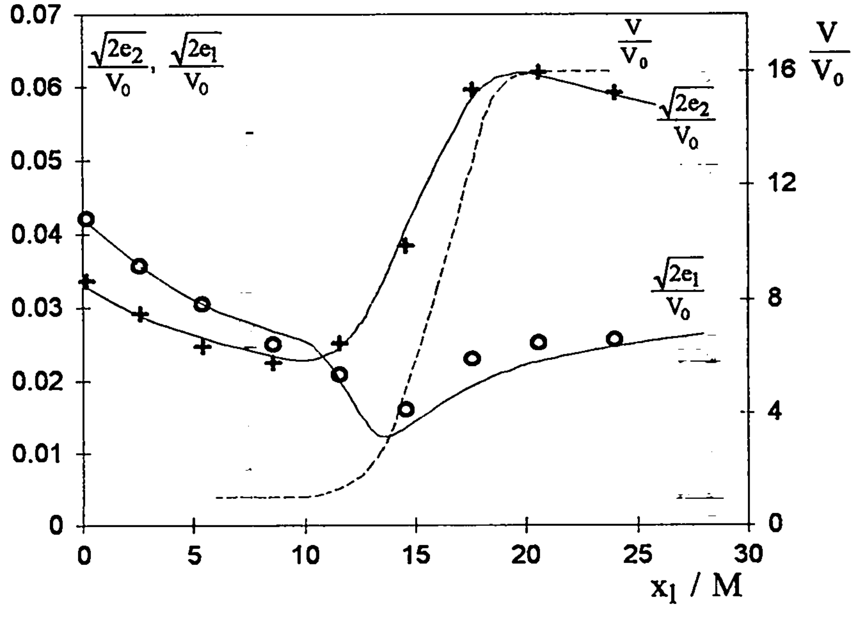

Fig.50. Values of $\sqrt{e_1}$ / V_0, $\sqrt{e_2}$ / V_0, V/V_0 as function of x_1/M for $S_1/S_2=16$.
o, + - эксперимент; .... , ——— - расчет.
M - turbulizer grid size, V_0 - flow velocity past the grid.

The figure demonstrate a good agreement between the calculated and experimental curves..

SELF-SIMILAR PROBLEM

Consider a self-similar problem for turbulent mixing at the interface between two invariable-density liquids existing within the gravity field where g = Const. The liquids have density ratio $\delta=\rho_2/\rho_1>1$. The substance incompressibility was provided in the .calculations, by specifying high sound velocity.

This problem has the following relationship to describe the turbulent mixing zone (TMZ) thickness L

$$L = F\left(\frac{\delta-1}{\delta+1}\right)S, \text{ where } S = gt^2/2.$$

The function $F\left(\frac{\delta-1}{\delta+1}\right)$ is illustrated in Fig. 51. For $\delta<10$ F function is approximated as $F \approx 0.65\frac{\delta-1}{\delta+1}$. The same figure gives the data of [67] obtained in electromagnetic shock-tube experiments for different density ratios of liquids.

Fig 52 illustrates the density profile within TMZ as obtained by calculations. The profile is represented through dimensionless variables

$$\tilde{\rho} = \frac{\rho-\rho_1}{\rho_2-\rho_1}, \quad \tilde{x} = \frac{x}{x_{0.9}-x_{0.1}},$$

where $x_{0.9}, x_{0.1}$ are the coordinates for $\tilde{\rho}=0.9$ и $\tilde{\rho}=0.1$, respectively. In terms of dimensionless variables, the calculated density profile has been found independent of the density ratio δ. The profile asymmetry is $L_2/L_1 \approx 1.24$, where L_2, L_1 are the depths TMZ penetrates into the lighter substance and the heavier one, $(L_1+L_2=L)$. Ref.[68] reports the measurement data on the TMZ density profile for $\delta=3$ case, also illustrated by Fig. 52.

It should be noted,.that there is one substantial inconsistency in the available experimental data on TMZ growth rate. The point is that TMZ growth rates observed in self-similar gas flows (e.g.[67]) are 2 or 2.5 times those in liquids (e.g.[68], [69]). It is not understood by now what the cause of this situation is. Maybe it arises from a different dissipation mechanism of the turbulent energy when insoluble liquids are mixing (as in a vast majority of the equations). Should this be the case, the turbulent energy would go reversibly into a free energy of the interface between the unmixable liquids, and thus the initial interface might recover as the acceleration sign changed. For gases, the turbulent energy would go irreversibly into heat, so that the initial interface recovery would be impossible due to molecular diffusion phenomena.

Most apparently, actual value of the surface tension coefficient is not important if it is reasonably small, the same as for gases, where actual viscosity value is insignificant for energy dissipation rate when the turbulent Reynolds number is rather high. There is an additional problem with intersoluble liquids experiments, arising from the effects of diffused transitional layer produced at the interface on TMZ growth rate. The difference in TMZ growth rates between gases and insoluble

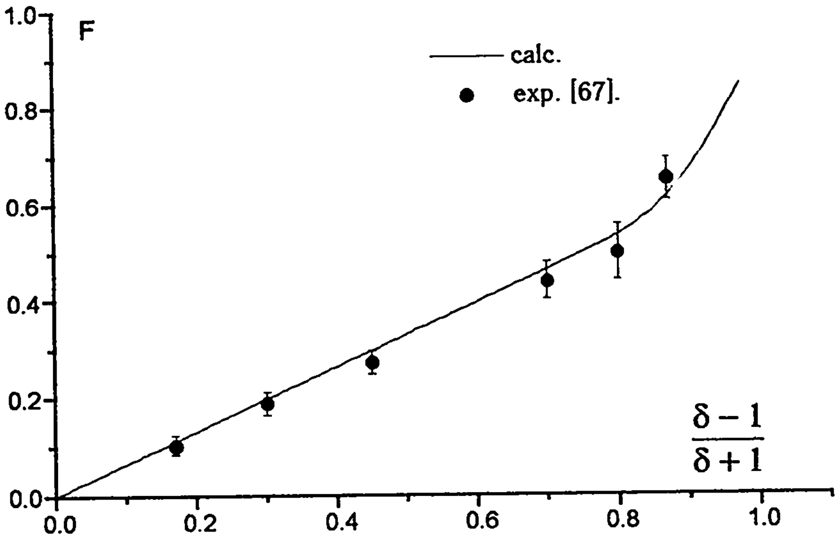

Fig.51. The function $F\left(\frac{\delta-1}{\delta+1}\right)$.

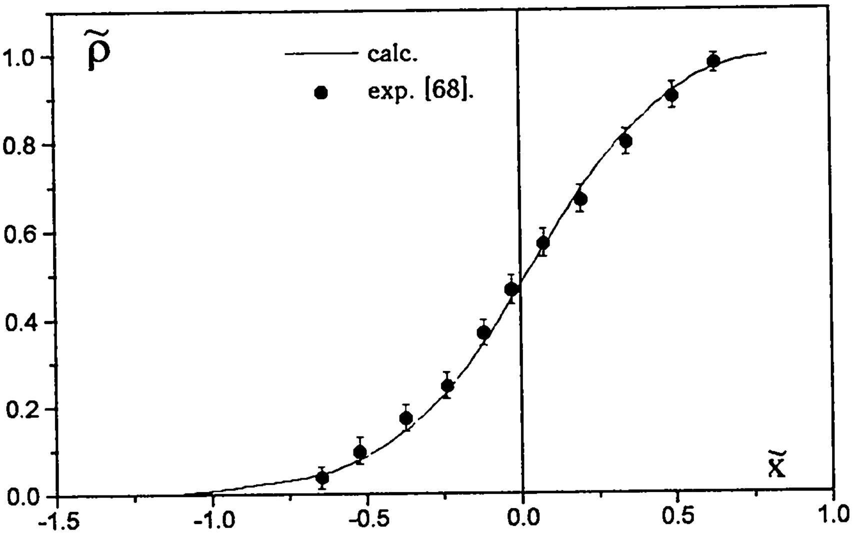

Fig.52. Density profile in self-similar problem.

liquids is a subject that needs further investigation. The numerical techniques of VIKHR code package were tested against the experimental data for gases

TMZ DEVELOPMENT BY INERTIA

TMZ development by inertia was investigated numerically using VIKHR codes, with the conditions like those stated for the self-similar problem. The acceleration was constant until some time, from which and on it was assumed equal to zero.

As shown by the calculations, the acceleration cutoff is followed by the TMZ growth rate changing over to asymptotic conditions as $L \sim t^n$, where n is slightly dependent on the density ratio of the two media and ranges within ~ 0.2 and ~ 0.26 with δ varying from 1.66 to 70.

TRANSITIONAL LAYER EFFECTS ON THE TMZ GROWTH RATE

It would be of interest to look at how the transitional density layer would affect the TMZ growth rate and the time the mixing conditions become self-similar. For this purpose, a series of calculations have been carried out with the problem stated as for self-similar case. The only difference was that there would be a zone of Δ thickness specified for initial time between the two substances, with its density smoothly changing from ρ_1 to ρ_2.

Density fluctuation values within this zone were specified as $R^2 = k\frac{(\delta-1)^2}{\delta}c(1-c)$, where $\delta = \frac{\rho_1}{\rho_2}$, and c is the mass concentration of either substance, $0<G<1$.

The value of $G=1$ accounts for the heterogeneous structure of the transitional zone. That is, there exists a random perturbation of distinctive amplitude Δ at the liquid-liquid interface. Smaller G represents the interface perturbation spreading as far as the diffused transitional layer, where $G=0$.

Numerical simulations were carried out for various δ values.

Fig. 53 shows TMZ thickness values L as functions of $S = \frac{1}{2}gt^2$, as obtained by the calculations for $\delta = 3$ with G values varied.

As shown by the figure, for high G values the TMZ growth rate at earlier times is substantially higher than in self-similar case,. As G value decreases, there become increasingly more apparent the effects of the transitional layer as stabilizer. When $G=0$, no turbulent mixing exists.

The calculations suggest the fundamental possibility to use the transitional layer to reduce turbulent mixing effects on gasdynamic flow behavior, such as in application to ICF target problems.

CALCULATIONS ON SHOCK-TUBE EXPERIMENTS

Plane geometry experiments were conducted using a shock tube with air and helium. The experimental geometry is described in detail in the second part of this report. The gases were separated with a thin film. The shock wave generated in the air passed through the air-helium interface to break down the film, thereby resulting in a "priming" turbulent mixing zone. Following its reflection from the rigid wall, the

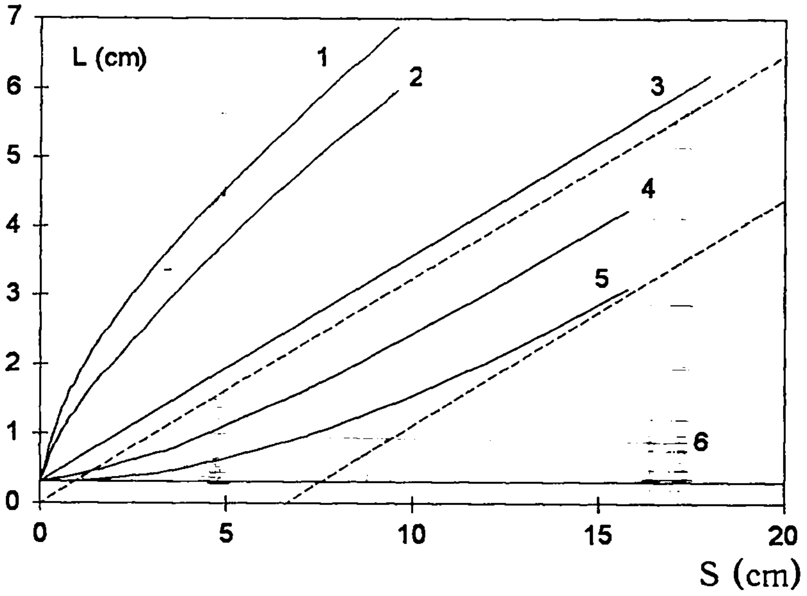

Fig.53. TMZ thickness L as a function of S=$gt^2/2$, involving transitional layer incorporating varying density fluctuations.
1 - G=1; 2 - G=0.6; 3 - G=0.075; 4 - G=0.0075; 5 - G=0.00075; 6 - G=0.

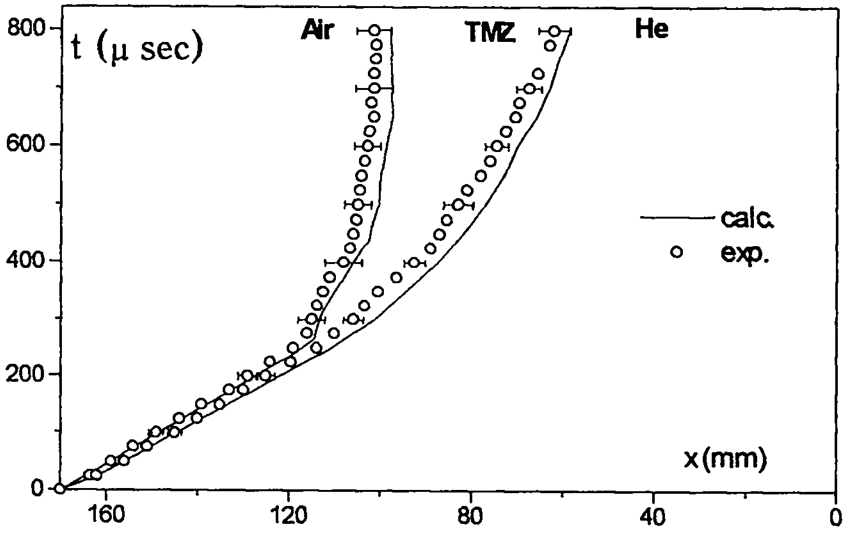

Fig.54. Time history of TMZ boundary locations in plane air-helium experiment.

shock wave went back to the interface, thus violently enhancing the turbulent mixing.

Numerically, the geometry included two regions: the left region was air, and the right-helium. A stationary shock wave of Mach number M=1.3 was generated at the left air boundary. Helium boundary on the right was a rigid wall. The distance between the rigid wall and the interface was x=16.9 cm. The equations of state of ideal gas were used with the respective adiabatic indices.

Finite values of $B^{(k)}$ were specified at the air-helium interface. These were selected such that the "priming" TMZ as observed in experiments following the film disruption would be simulated.

Fig.54 shows the experimental and calculated locations of TMZ boundaries.

Fig.55 gives the mean density profile of air in TMZ, visualized using "laser knife" technique, as compared with the calculated profile. The figure shows the density ratio ρ / ρ_0, where ρ is average air density within TMZ, ρ_0- air density outside TMZ.

In terms of this experiment, one comment should be made. When calculation is done without account of turbulent mixing, the air-helium interface would be decelerated by a sequence of shock waves. With TMZ existing, it is only the first one reflected from the rigid wall that would a shock wave. Thus, the subsequent waves would be no longer shock waves. They are produced by reflections from a spreading interface, and the time they are passing through helium is not enough for their characteristics to intersect and produce the shock wave. Therefore, the interface deceleration following the first shock wave proceeds smoothly.

The TMZ growth rate following the first reflected shock wave reaching the interface, depends on the amount of density fluctuations resulting from film disruption. For some time following the film disruption, the air and helium mixture is virtually heterogeneous. As the vorticity spectrum forms, the density fluctuations are gradually decreasing. Therefore, the TMZ growth rate following the first shock wave arrival should be expected different depending on x-the distance between the interface and the rigid wall. The larger the x distance, the lower the TMZ growth rate.

It seems attractive to conduct a series of experiments with distance variations between the interface and rigid wall. The data from these could be used to refine k_B coefficients in equations for $B^{(k)}$.

The calculated time histories of TMZ thickness L(t) for different x distances are given in Fig. 56. These calculations used the same initial values of $B^{(k)}$. The experimental data of [46], [70] are also given in this figure.

As is clear from the figure, for x=123.8 cm the calculated TMZ growth rate following the first reflected shock wave exceed the experimental. This is likely to due to the turbulence that has subsided so much by this time in the experiment, that molecular dissipation phenomena have become effective. As a matter of fact, the calculated turbulent diffusion coefficient by this time is ~ $8 cm^2/s$, while molecular diffusion coefficient is ~$1 cm^2/s$. Molecular diffusion is what additionally reduced the density fluctuations with respect to the calculation assuming high turbulent Reynolds number. Accordingly, the experimental TMZ growth rate was found lower than in the calculation. For short distances to the rigid wall or substantially stronger shock wave, this effect is not observed.

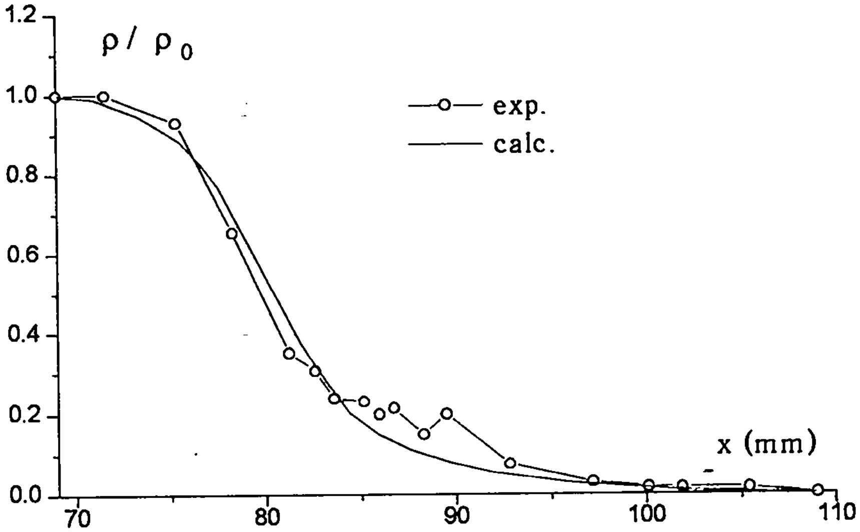

Fig.55. Relative air density profile in TMZ for plane air-helium experiment.

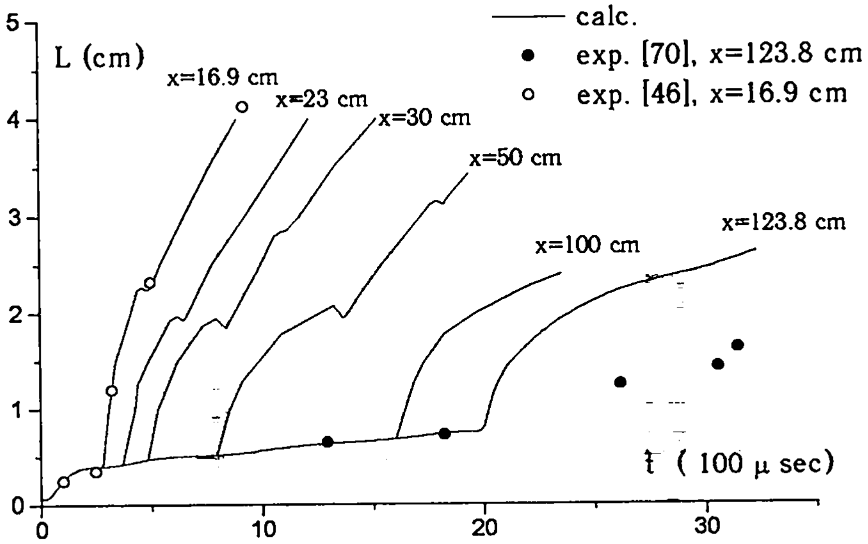

Fig.56. TMZ thickness L versus time for different distances to the rigid wall.

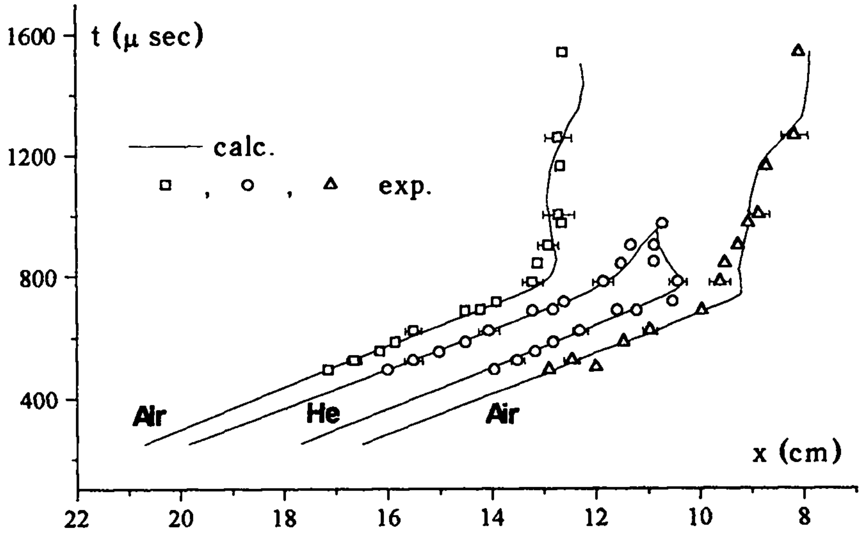

Fig.57. Time history of TMZ boundary locations in plane air-helium-air experiment.

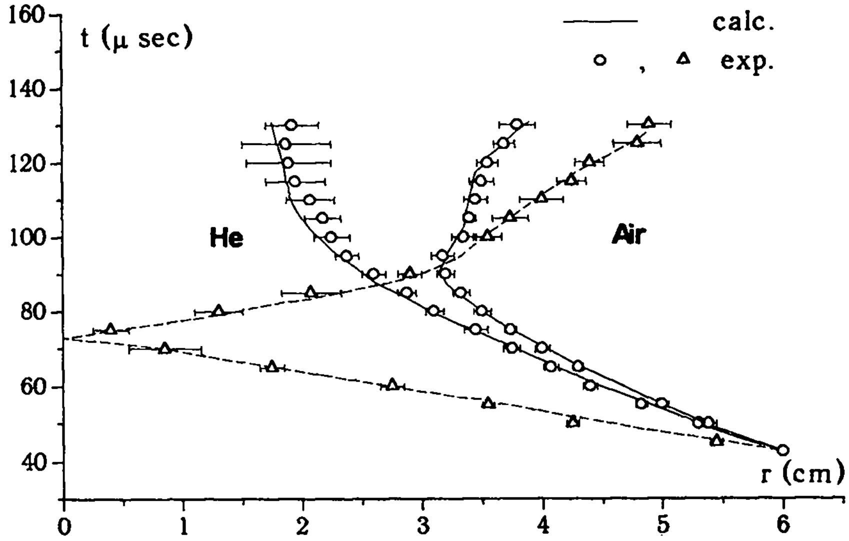

Fig.58. Time history of TMZ boundary locations in cylindrical air-helium experiment.

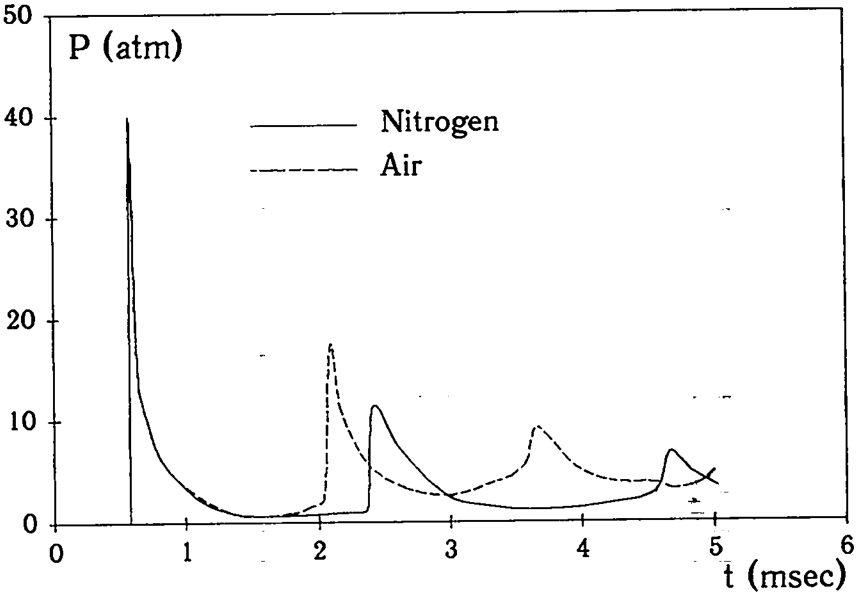

Fig.59. Calculated chamber wall pressure versus time (air and nitrogen).

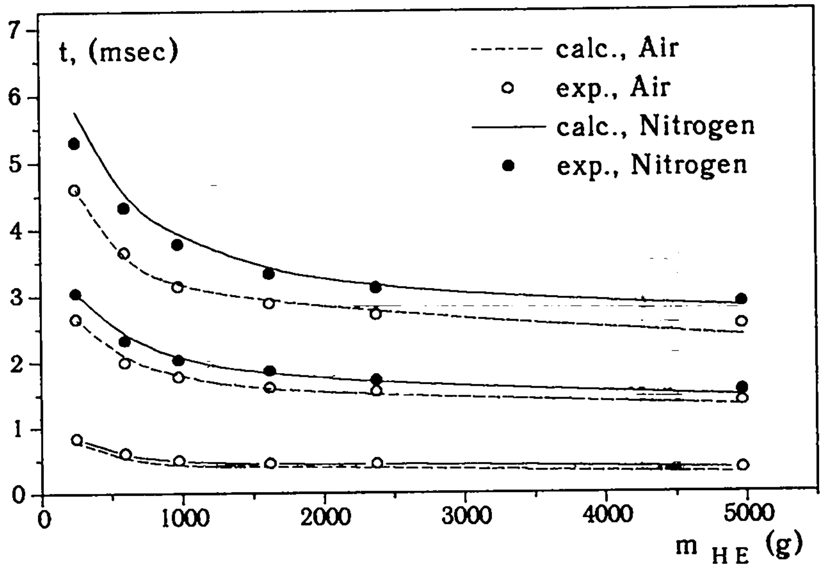

Fig.60. Times of the first three shock wave coming to the wall versus HE mass (air and nitrogen).

In addition to mixing experiments considering one interface, there were experiments conducted where mixing was made to develop at two interface. Two air layers with helium layer in between were enclosed into a shock tube. The right air layer had a rigid wall boundary. A shock wave of Mach number M=1.3 was generated in the left air layer.

The calculation scheme for this experiment is like that described above.

Fig. 57 shows the calculated vs. experimental time histories of TMZ boundaries. The calculation and experiment are shown to be in a good agreement.

CALCULATIONS FOR CYLINDRICAL-GEOMETRY EXPERIMENTS

VIKHR code used cylindrical geometry to calculate the TMZ development at the air-helium interface, accelerated by convergent shock waves. The calculation scheme was equivalent to the experiment described in Section 2.5 in the second part of this report. Electric wire explosion was simulated by specifying instantaneous energy release in a thin air layer near its outer boundary.

Fig. 58 shows the calculated and experimental time histories of air-helium DMZ boundary locations.

CALCULATIONS OF HE EXPLOSIONS IN SPHERICAL CHAMBER

Ref.[71] describe experiments to investigate the response of the walls of spherical chamber 2 m in diameter to chemical HE explosion confined therein. An HE charge which is one of mixed HE type having negative oxygen balance, was placed at the center. The post-explosion chamber wall pressure was measured as a function of time.

The experiments were conducted in two versions. The first with the tank filled with nitrogen, the other-with air.

Following the HE explosion, the explosion gases start mixing with the chamber - filling gas. If the chamber contains air, then the turbulent mixing of E.G. and oxygen going as far as molecular level results in E.G. burn-up and the total energy release increased by a factor of 2.5. This effect makes the chamber wall pressure vs. time different from the case where the chamber contains nitrogen.

These experiments were calculated by VIKHR code added by equations describing the dynamics of mixed constituents mixing up to molecular level. Chemical reaction rates were assumed infinite.

Fig. 59 shows calculated time histories of the chamber wall pressure for nitrogen and air experiments, i.e. with and without account of HE burnup. HE mass was 570g.

Fig. 60 gives the experimental and calculated times at the wall for the first three shock waves as a function of HE mass in nitrogen and air experiments.

2.2.6. COMPARING AGAINST OTHER MODELS

For turbulent flow calculations, k-ε models are the most commonly accepted approach. But they have a limitation, which is one and the same set of semiempirical constants insufficient to describe different turbulent flow types, such as gravitational mixing and turbulence decay. This arises from k-ε model disregarding turbulence anisotropy and nongradient nature of turbulent flows. The k-ε model equations can be derived from equations (88) upon substantial simplifications. It will be clear then, that the coefficients in the generating and dissipative terms are functions of anisotropy and some other factors, rather than constants. Therefore, they will depend on the flow type and previous history, As shown by the calculations, the model described above is substantially more flexible.

CONCLUSION

As follows from the results described in this report, numerical simulation of turbulent flows can be quite successfully done employing both gasdynamic 2D codes and semiempirical techniques. Naturally, both approaches have their own limitations.

Two dimensional gasdynamic codes can not basically simulate all the details of a real 3D flow. Moreover the limited number of computational points do not allow one to describe flows where turbulent Reynolds number is rather high..

Semiempirical models are insufficiently strict physically. There always exist uncertainties in the forms of individual terms and constant values.

Therefore, continuing development and applications of turbulent flow calculations will be impossible without experimental support.

Today, there are numerous experimental data on tangential mixing in stationary flows. However, gravitational mixing data are comparatively few. Mostly, these experiments only measured the mixing zone thickness. Since the zone has spreading boundaries, its measured thickness may be dependent on the measurement technique and even experimentalist's will (e.g., to include or not a single long outlier in TMZ). Therefore, experimental information is required on the density profile and component concentrations within TMZ.

The results of what may seen identical experiments may depended on the technology involved. This may be observed, for example, in shock-tube experiments with gases separated by a film, and this is where the results may be very much dominated by the film quality. Thus, within the same technology series of experiments should be conducted with any one of parameters varied.

Further improvement of semiempirical models requires also experimental information on TMZ structure in detail (velocity, density, etc. fluctuations).

REFERENCES (PART 1)

1. R.Richtmyer, K.Morton. Difference methods for boundary value problems (in Russian). Mir, M. 1972.

2. G.A.Grishina. Vector form of equations for small perturbations in gas dynamics including heat conduction or magnetic properties of the medium, VANT, ser.: Mat. I Prog. (in Russian), №.3, p.10, 1986.

3. G.A.Grishina, V.Ya.Bukharova, O.M.Zotova. A code for small perturbations in gas dynamics, VANT, ser.: Mat. I Prog. (in Russian), №.3, pp.22-30, 1986

4. G.A.Grishina, V.Ya.Bukharova, O.M.Zotova, T.G.Ivchenko. Linearization of multidimensional gas-dynamic equations with heat conduction on Lagrangian variables. VANT, ser.: Mat. I Prog. (in Russian), №.2 (4) pp.6-11, 1979

5. S.M.Bakhrakh, G.A.Grishina, N.P.Kovalev, E.E.Meshkov, A.I.Tolshmyakov, Yu.V.Yanilkin. Some aspects of experimental and numerical studies of Rayleigh-Taylor instability. VANT, ser.: Chisl. met. mekh. sploshn. sredy (in Russian), v.10, №.1, pp.17-30. 1979.

6. G.A.Grishina, P.M.Seidel, O.M.Zotova. Solution of 2-D gas-dynamic problems in linear approximation, PMM (in Russian), v.30, №5, pp.975-976, 1966.

7. P.M.Seidel. A shock wave produced by a slightly curved piston, PMM (in Russian), v.24, №2, pp.219-227, 1960,

8. I.G.Zhidov, V.G.Rogachev. Evolution of axisymmetric perturbations under gas cavity compression by a perfect fluid, Zhurn. Vych. Mat. i Mat. Fiz., (in Russian) №3, pp.794-797, 1981..

9. G.A.Konstantinov, Yu.A.Yakimenko. Numerical method for nonstationary problems of perfect fluid hydrodynamics with free surfaces, Izv. AN SSSR, MZhG (in Russian) , №4, p.162, 1969.

10. O.V.Voinov, V.V.Voinov. Numerical method for nonstationary movement of incompressible fluid with free surfaces, DAN SSSR (in Russian), v.221, №3, p.23, 1975.

11. Yu.V.Yanilkin, A.A.Shanin et all. EGAK codes for computing 2-D flows in multicomponent media, VANT, Ser. Mat. Modelir. Fiz. Proc. (in Russian), №4, 1993.

12. S.M.Bakhrakh, Yu.P.Glagoleva, M.S.Samigulin, V.D.Frolov, N.N.Yanenko, Yu.V.Yanilkin. Gas-dynamic flow computations based in the method of concentrations, DAN SSSR (in Russian), v.257, №3, pp.566-569, 1981.

13. S.Bakhrakh, M Samigulin, B.Sevastianov, Y.Yanilkin. The EGAK method for Calculating Gas Flows of Heterogencous Media in Eulerian Coordinates. Numerical Methods in Fluid Dynamics, Mir, M., 1984.

14. A.A.Shanin, Yu.V.Yanilkin. EGAK codes. Gas-dynamic difference schemes in Eulerian variables. VANT, ser.: Mat. Mod. Fiz. Proc. (in Russian), №1, pp.24-30, 1993.

15. N.S.Darova, O.A.Dibirov, G.V.Zharova, A.A.Shanin, Yu.V.Yanilkin. EGAK codes. Lagrangian-Eulerian method for 2-D gas-dynamic flows in multicomponent media. VANT, ser.: Mat. Mod. Fiz. Proc. (in Russian), №4, 1993.

16. G.V.Zharova, Yu.V.Yanilkin. EGAK codes. An algorithm for equating the material pressures in mixed cells. VANT, ser.: Mat. Mod. Fiz. Proc. (in Russian), №3, pp.77-81,1993.

17. D.H.Sharp. An Overview of Rayleign-Taylor Instability. Physica 12D pp.3-18, 1984.

18. F.H.Harlow, J.E.Welch. Numerical study of large-amplitude free-surface motion. Phys. Fluid 9, №5, p.842, 1966.

19. C.P.Verdon, R.L.McCrory. Nonlinear effect of multi-frequency hydrodynamic instabilities on ablatively accelerated thin shells. Phys.Fluids 25, №9, pp.1653-1673, 1982.

20. Yu.A.Davydov, M.S.Panteleev. Evolution of 3-D perturbations under Rayleigh- Taylor instability, PMTF, (in Russian), №1, pp.117-121, 1981.

21. E.G.Gamalii. Boundary stability of a cavitating bubble in incompressible fluid. Brief notes in Physics (in Russian),. №5, p.23, 1976.

22. V.A.Andronov, S.M.Bakhrakh, E.E.Meshkov, V.N.Mokhov, V.V.Nikiforov, A.V.Pevnitskii, A.I.Tolshmiakov. ZhETF (in Russian), v.71, №8, p.806, 1976.

23. K.I.Read. Experimental investigation of turbulent mixing by Rayleigh-Taylor instability. Physica 12D, pp.45-58, 1984.

24. N.N.Anuchina, Yu.A.Kucherenko, V.E.Neuvazhaev, V.N.Ogibina, L.I.Shibarshov, V.G.Yakovlev. Izv. AN SSSR, MZhG (in Russian), №6, pp.157-160, 1978.

25.. D.J.Lewis. The instability of liquid surfaces when accelerated in a direction perpendicular to their planes.II. Proc.Roy.Soc., v.A202, 1068, pp.81-96, 1950.

26. E.E.Meshkov. Izv. AN SSSR, MZhG (in Russian), №5, pp.151-157, 1969

27. H.W.Emmons, G.T.Chang, B.C.Watson.. Taylor instability of finite surface waves. J. of Fluid Mech., v7, pp.177-193, 1960.

28. A.Zufiria. Phys. of Fluids 31(3), p. 440, 1988.

29. Glimm, X.L.Li, Phys. of Fluids 31(8), p. 2077, 1988.

30. O.I.Volchenko, I.G.Zhidov E.E.Meshkov, V.G.Rogatchev. Localized perturbations growing at the unstable boundary of accelerated liquid layer. Letters to ZhTF (in Russian), v.15, pp.47-51, 1989.

31. G.K.Batchelor. An Introduction to Fluid Dynamics. Cambridge, 1970.

32. O.I.Volchenko, I.G.Zhidov, B.V.Klopov, E.E.Meshkov, V.V.Popov, V.G.Rogatchev, A.I.Tolshmyakov. Simulation technique for nonstationary incompressible fluid flows. AC. 1026154, Bulletin of OIPOTZ (in Russian), №24, 1983

33. V.Rogatchov, I.Zhidov, B.Klopov, E. Meshkov, A.Tolshmyakov. Non-stationary flows in proximity of angular points of gas accelerated liquid. The

Proceedings of the 3rd Int. Workshop on the Phys. of Comp. Turb. Mix... Abbey of Royaumont, France, (1991).

34. S.M.Bakhrakh, I.G.Zhidov, V.G.Rogachev, Yu.V.Yanilkin. Numerical stability studies of tangent velocity discontinuity in compressible gases, Izv. AN SSSR, MZhG (in Russian), №2, pp.146-149, 1983.

35. S.M.Bakhrakh, I.G.Zhidov, V.G.Rogachev, Yu.V.Yanilkin. "Numerical simulation of tangent velocity discontinuity in compressible gases", In "Problems of the viscous fluid dynamics". Proc. of the 10-th All-Union Workshop (in Russian), Novosibirsk, pp.12-16, 1985.

36. L.D.Lanlau. On stability of tangent discontinuities in compressible gases, DAN SSSR (in Russian), v.64, №4, p.151, 1944.

37. S.Chandrasekhar. Hydrodynamic and hydromagnetic stability. London, Oxford.Clarendon Press., 1968.

38. Ya.B.Zeldovich, P.I.Kolykhaev. Instability of stretched tangent discontinuity. DAN SSSR (in Russian), v.266, №2, pp.302-304, 1982.

39. I.G.Zhidov, E.E.Meshkov, N.V.Nevmerzhitskii. "Experimental studies of mixing dynamics on unstable interfaces of accelerated fluid layers." In: "Experimental studies of gravitational instability and turbulent mixing of stratified flows in acceleration field in terms of ICF problems". (in Russian), Preprint №56 , FIAN AN SSSR, M., pp.52-63,1990.

40. V.G.Levich. Physical and chemical hydrodynamics. (in Russian), Fizmatgiz. M., 1959.

41. N.A.Inogamov, A.V.Cheklov, A.Y.Dem'yanov, S.I.Anisimov, O.M.Belotserkovski. Analitical and numerical studies of Rayleigh-Taylor Instability. Proceedings of 3rd Int.Workshop on The Phys. of Comp. Turb.Mix.. Abbey of Royaumont, France, (1991).

42. M.J. de C.Henshaw, G.J.Pert, D.L.Youngs.Non-linear Rayleih-Taylor instability in spherical laser accelerated targets. Plasma Phys.and Cont.Fusion, v.29, №3, pp.405-418, 1987.

43. C.L.Gardner, J.Glimm, OMcBryan, R.Menikoff, D.H.Sharp, G.Zhang. The dynamics of buble growth for Rayleigh-Taylor unstable interfaces. Phys.Fluids 31(3), pp.447-465, 1988.

44. L.I.Mandelstam. "On roughness of free fluid surface "(in Russian). Proceedings v.1, edited by Ac. of Sci. of SSSR. pp.246-260, 1946.
(Ann. d. Phys. 41, 609-624, 1913).

45. V.A.Andronov, S.M.Bakhrakh, V.V.Nikiforov, Yu.V.Yanilkin.. Numerical simulation of some turbulent flows in a 2D turbulence approximation. Izv. AN SSSR, MZhG (in Russian), v.6, 1981, pp.20-26.

46. V.A.Andronov, E.E.Meshkov, V.V.Nikiforov.et all. Experimental investigation and numerical simulation of turbulent mixing in one- dimentional flows. DAN SSSR (in Russian), 1982, v.264, №1, pp. 76-82.

47. S.M.Bakhrakh, V.A.Zhmailo, V.P.Statsenko, Yu.V.Yanilkin.. Numerical simulation of turbulent mixing in shear flows.. ChMMSS (in Russian),1983, v.14, №2, 1983, pp.11-27.

48. S.M.Bakhrakh, G.A.Grishina, N.P.Kovalev, E.E.Meskov, A.I.Tolshmyakov, Yu.V.Yanilkin. Some aspects of experimental and numerical investigations of Taylor instability. ChMMSS (in Russian), 1979, v.10, №1, pp. 17-30.

49. Turbulent mixing of gas jets (in Russian). Ed. by G.Abramovish. Nauka, M, 1974

50. G.L.Brown, A.Roshko. On Density effects and large structure in turbulent mixing layers. J.of Fluids Mech., 1974, v.64, part.4.

51. S.M.Dat, O.G. Wilmot, H.S. Pergament. Calculation method for mixing zone evolution in the near jet field (in Russian). RTK, v.17, №9, 1979.

52. W.Rodi. A Review of experimental data of uniform density free turbulent boundary layers. Studies in Convection, v.1, Acad.Press.London, 1975.

53. E.Gutmark, K.C.Shadow, K.J.Wilson. Effect of sonvective Mach number on mixing of coaxial circular and rectangular jets. Phys. Fluids A3(1), 1991, pp. 29-36.

54. "Turbulent flow calculation methods." Translation from English under edition of V. Kolman." (in Russian). M., MIR, 1984.

55. J.Rotta. "Statistische Theory nihthomohener Turbulenz". Z. Phyz., 1951, Bd. 129, № 6; Bd. 131, № 1.

56. B.J.Daly, F.H.Harlow. "Transport Equations in Turbulence". The Phys. of Fluids, 1970, v 13, № 11.

57. G.K.Batchelor. Theory of Homogeneous Turbulence (in Russian). IL, M, 1955.

58. G.K.Batchelor. "Computation of the Energy Spectrum in Homoheneous Turbulence" The Phys. of Fluids, 1969, v. 12, part 2, № 12.

59. L.G.Genkin, S.I.Kolev, T.E.Krasnoshchekova. Investigation of elementary turbulence models using amplitude equation. Teplofiz.V.Tem. (in Russian), v.14, № 6, 1976,

60. I.O.Hinze. "Turbulence ".(in Russian). Fizmatgiz, M, 1963.

61. A.A.Townsand. "The stucture of laterally sheared turbulent flow."(in Russian) IL, M, 1959

62. J.M.Lumley, B.K.Khajeh-Nouri. "Computational Modelling of Turbulent Transport" 'Turbulent Diffusion in Environmental Pollution", (Pr. of Symp. held at Charlottesville, Virginia, 1973), Acad. Press, N.Y., 1974.

63. "Turbulence"(in Russian). Ed. by P.Bredshow. Mashinstr. M, 1980.

64. M.S.Uberoi. "Effect of Wind-Tunnel Contraction on Free-Stream Turbulence". 1956, Jorn. of Aeronautical Scieces, v. 23, № 8.

65. V.M.Ievlev. "Turbulent flow of high-tempreture media" (in Russian). Nauka, M, 1975.

66. G.V.Dolgoleva “Numerical techniques for two-temperature radiant gas flow. (SND)”. VANT, ser.: Mat. I Prog. (in Russian), 1983, 2(13), pp. 29-33.

67. A.M. Vasilenko, V.I.Olhovskaya, O.V.Buryakov, V.G.Yakovlev. Experimental investigation for turbulent mixing of gases at the plane interface under the influence of decelerating shock wave. Report on 3-rd Int. Workshop on The Physics of Compressible Turbulent Mixing, Abbey of Royaumont, France, (1991).

68. Yu.Kucherenko, L.Shibarshov, V.hitaikin et all. Experimental study of the gravitational turbulent mixing self-similar mode. Report on 3-rd Intern. Workshop on The Physics of Compressible Turbulent Mixing, Abbey of Royaumont, France, (1991).

69. V.S.Smeeton, D.L.Youngs. “ Experimental Investigation of Turbulent Mixing by Rayleigh-Taylor Instability”. 1988, Pt. 3, AWE report NO-35/87.

70. L.Houas, I.Chemouni, A.Touat and R.Brun. Experimental investigation of Richtmyer-Meshkov induced turbulent mixing over long distances. Report on 3-rd Intern. Workshop on The Physics of Compressible Turbulent Mixing, Abbey of Royaumont, France, (1991).

71. V.A.Andronov, S.M.Bakhrakh, V.A.Mazanov, V.V.Nikiforov. et all. Turbulent burnup effects of chemical HE explosion gases on confined gasdynamic events. DAN SSSR (in Russian), v.314, №6. 1990.

72. V.V.Nikiforov.Turbulent mixing on the contact boundary of media differering in density. VANT, ser.:Teor.i prik. fiz. (in Russian), №1, pp.3-8, 1985.

II. EXPERIMENTAL STUDIES OF HYDRODYNAMIC INSTABILITIES AND TURBULENT MIXING

CONTENTS

1. EXPERIMENTAL TECHNIQUES FOR HYDRODYNAMIC INSTABILITIES AND TURBULENT MIXING STUDIES

1.1. INTRODUCTION

As early as first efforts to achieve extremely high energy densities made one realize the need for experimental studies of hydrodynamic instabilities. While there were limited opportunities then to run these studies only relying on high energy density test facilities, simulation techniques have been commonly accepted and developed to study instabilities and turbulent mixing.

The earliest turbulent mixing experiments were performed at VNIIEF in mid-1940 by its scientists Alekseev, Zelentsova and Proscurin on the initiative of Academician Sakharov. These experiments observed turbulent mixing evolving in the gravitational field at the interface between two liquids separated by a plate to be removed just when the experiment started. The technique like this was later used in [1-3].

Following the publications of Taylor and Lewies [4-5] on the instability of an interface between two liquids driven under acceleration from lighter to heavier liquid, these investigations would increase in number. Particularly, very frequent were the experiments with vessels containing different density liquids, driven vertically downwards under much higher than gravity accelerations [6-16]

In 1960, Richtmyer [17] showed in theory that the gas-gas interface shock-driven from the lighter gas side is unstable.

VNIIEF developed a technique in mid-1960s to experimentally investigate this instability type, which employed a shock tube and a thin organic film for gas separation [18]. This technique was used in [19-25, 29-44, 49-58].

Mid-1970s saw VNIIEF develop another technique to separate gases in a vertical shock tube with a plane fast-removable partition plate. Later, this technique was developed in [31, 32, 38-42, 54, 55].

Next, a technique was developed in mid-1970s to investigate initial perturbations and turbulent mixing at the cylindrical interface of two gases separated by a thin film driven by cylindrical converging shock-wave [20, 54].

In late 1970s, VNIIEF developed a technique to study unsteady hydrodynamic behaviors using jellies [60-63]. This approach would substantially increase the experimental capabilities for R-T instability studies. Specifically, it would also make it possible to investigate R-T instabilities in cylindrical geometry [63].

Jelly experiments are what also led to create an experimental technique for instabilities and turbulent mixing studies, involving acceleration of flat liquid layers driven by compressed gas [64, 65].

1.2. THIN-FILM GAS-GAS SEPARATION

Very thin films to separate different gases were used by shock-tube experiments to investigate one-dimensional interactions between shock-wave and interfaces [66], and also shock reflection and refraction behaviors at the interface between two gases having different densities, in relation to the incidence angle [67].

The film technology used by the experiments is like that described in [68]. About 5 milliliters of 5-10% collodion solution in isoamylacetate is poured out on a clean water surface of a wide bowl (~ 0.2 m^2). The dissolvent evaporates to produce a film to be then taken out from the water with a wire frame positioned in water in the plane perpendicular to the film surface. In this way, the film folds and, when dried up, makes up a double coalescent layer, thus minimizing the occurrence of through pores.

Some experiments used films having a different formulation. This involved ~10% solution of chemically resistant lacquer slightly added by collodion (<1%). The film fabricated by this technology is less elastic and tears down into smaller pieces when driven by a shock wave. These films were used by turbulent mixing experiments.

As indicated by the interference colors, the films produced by these technologies had thickness ranging between 0.2 and 1μm. Any individual film had thickness gradient within ±50% about the average. It was shown by selectively weighing the films that their mass density was $(2.5\text{-}6)\cdot 10^{-5}$ g/cm^2., i.e. equivalent to air layer 0.2 - 0.5 mm thick.

Typically, films used by the experiments were about 0.4 μm thick and (3-4) $\cdot 10^{-5}$ g/cm^2 specific mass.

The experiments involving flat interface between differently dense gases had the film applied on to the flat ends of a unit of the shock-tube test section immediately from the frame (the unit end faces were oiled or smeared with glue containing no film dissolvent).

The experiments with the interface perturbed (e.g. sinusoidally), had the film applied on to the shaped end face of the unit in the following fashion. The film was taken from the frame and laid on to a metal backing having flat surface. It was then wrapped on a thin cylinder with the following wrapping this out on the shaped surface.

The shock-tube test section included units separated to form closed spaces filled with different gases. The gas was fed slowly through pipes from expendable rubber balloons. This gradually forced the air out of the unit through a hole on the opposite. Gases having higher than air densities were pumped through the space from the bottom upwards, and lighter gases- from the top downwards (Fig. 1.*a*).

Selective analysis for gas purity in the test sections used measurements on the air condenser inside the gas outlet.

As it was found, quite satisfactory a purity level for gases is achievable when the volume of working gas blowing through the experimental section is 5-10 times its volume. In so doing, the space to be filled must be made leak-tight, since even very small holes may result in significant gas leakage.

There were also experiments where the gas going out from the test model was analyzed for purity with standard interferometer type SHI-10 used in mining industry for mine gas analyses.

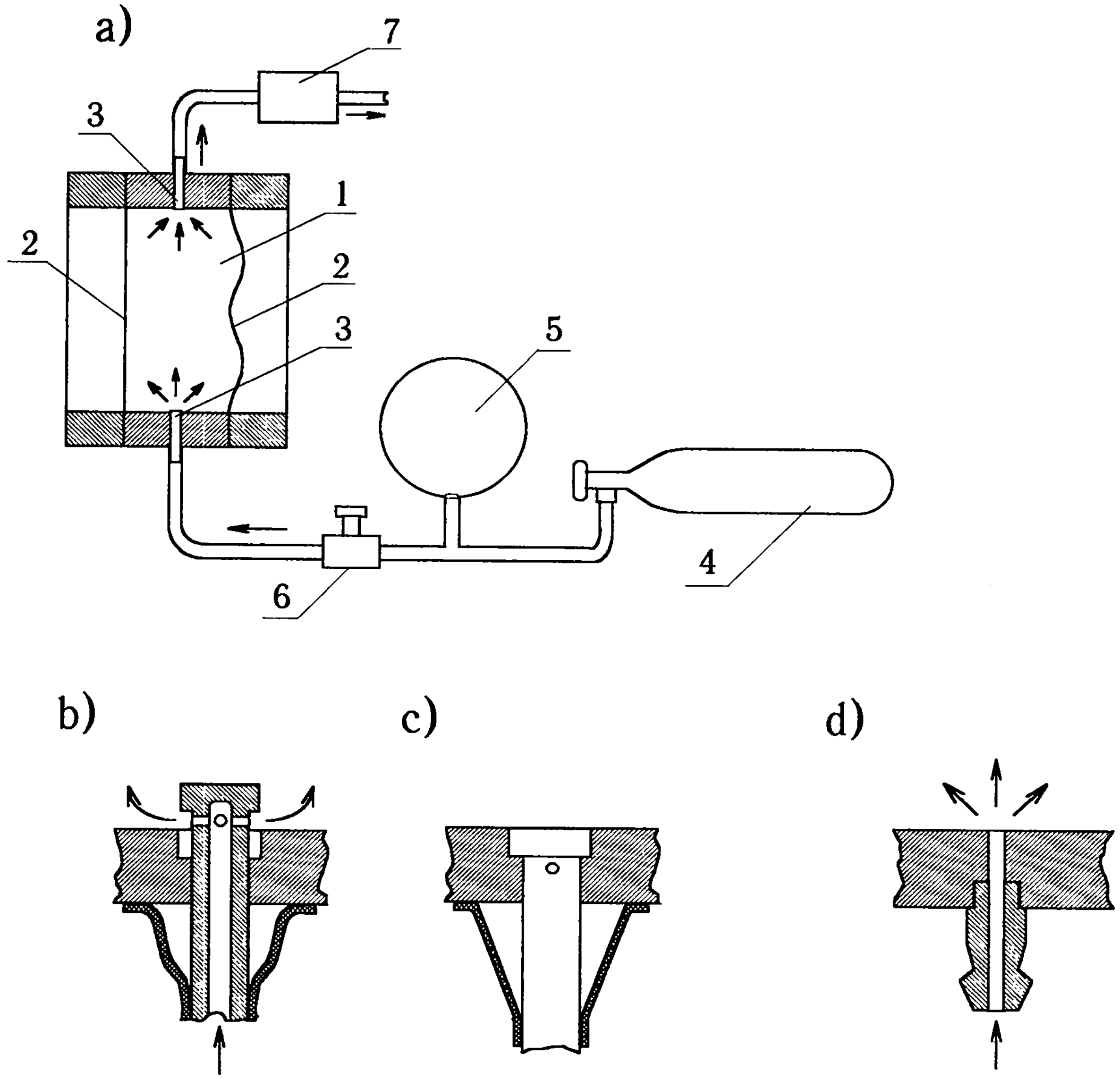

Fig.1. Schematic for experimental model gas filling.
a) Thin film model filling with working gas (heavier than air).
1 - shock tube measuring set; 2 - thin film; 3 - gas inlet tubes;
4 - working compressed gas balloon; 5 - rubber ball; 6 - regulator;
7 - gas purity control device.
b), c) Gated gas inlet tube with a flexible rubber jacket in opened and closed positions, respectively.
d) Opened gas inlet tube.

Gas inlet devices were designed such that when the unit has been filled with the working gas its wall holes were all blocked to eliminate any influence of these on the in-tube channel flows during the experiment (Fig. 1,b). The gas inlet device was provided with flexible rubber jacket to avoid the gas leakage from the unit through the gap in between the gas inlet and the hole walls.

There were also non-blocking gas inlets used in some cases (see Fig.1c).

Worth noting are also the other ways to create interfaces in gases, particularly using

-fire front in combustible mixture gases as interface in question [69, 70],

-partition plate [1, 31, 32, 38-42],

-gas jet blown across the channel normal to its axis [47, 48].

1.3. SHOCK TUBES

1.3.1. HORIZONTAL SHOCK TUBE

Investigations of shock-induced instabilities and their associated turbulent mixing were carried out mostly using a horizontal shock tube which is schematically shown in Fig. 2. This is similar to that described by Schardin [71]. The chamber (1) and the shock-tube channel (section (3)) were made of an ordinary steel tube of 208 mm inner diameter. The chamber and the channel were separated with a diaphragm as double or triple layered triacetate film 0.2 mm thick. The chamber was filled with pressurized air, while the channel (3) was communicating with the surrounding air. The diaphragm breakdown would cause a plane stationary shock wave to generate.

The shock tube channel includes two subchannels: cylindrical (3) and rectangular-shaped (4) of 120×40 mm^2 sectional dimension. The subchannel (4) is inserted inside the cylindrical to 0.7 m length. It has its front end edges sharpened.

This makes the shock wave generated in the cylindrical subchannel separate spatially into two portions: the one to travel through the square subchannel, the other to enter the blocked section and thus not affect the flow pattern in the square subchannel.

There was a test section (5) having transparent side walls positioned at the end of the subchannel (4). This test section was made of individual units separated by thin films. The unit confined different gas fillings.

Flow patterns of the test section channel were observed with shadow device type IAB-451 optically coupled with high speep camera (SFR) using the technique described in [72].

1.3.2. VERTICAL SHOCK TUBE

Some experiments to investigate turbulent mixing at shock-driven interface used a vertically positioned shock tube with gases therein separated by a thin partition plate. The plate was to be rapidly pulled out before the shock reached the interface. The tube design like this was used in [31, 32, 38-42].

Schematically, the vertical shock tube is shown in Fig. 3. The square tube of 35x35 mm^2 included three major sections: chamber (1), channel (3) and test sections (4). The chamber was separated from the channel by a diaphragm (2) which was single triacetate film 0.2 mm thick, and filled with pressurized air. The channel was open to the surrounding atmosphere.

There was a sliding diaphragm (5) representing a steel foil plate 0.1 mm thick placed at the junction between the test section and the channel. This was used to separate the helium-filled upper test section unit from the other channel portion. During the experiment, the plate was pulled out as quickly as 10 m/s with a piston (6) driven by atmospheric pressure into the evacuated cylinder (7).

The test section had its upper unit plugged with a stopper at the end. There were two gas inlets through the plug and the side wall of the unit used to fill the unit with helium.

The flow pattern in the vertical shock tube was observed in the same way as for the horizontal tube case.

Timing techniques used in operating the shock tube and SFR high-speed camera (see Section 1.7) made it possible to control the delay times of shock arrival at the interface of interest against the diaphragm plate removal, t_{del}.

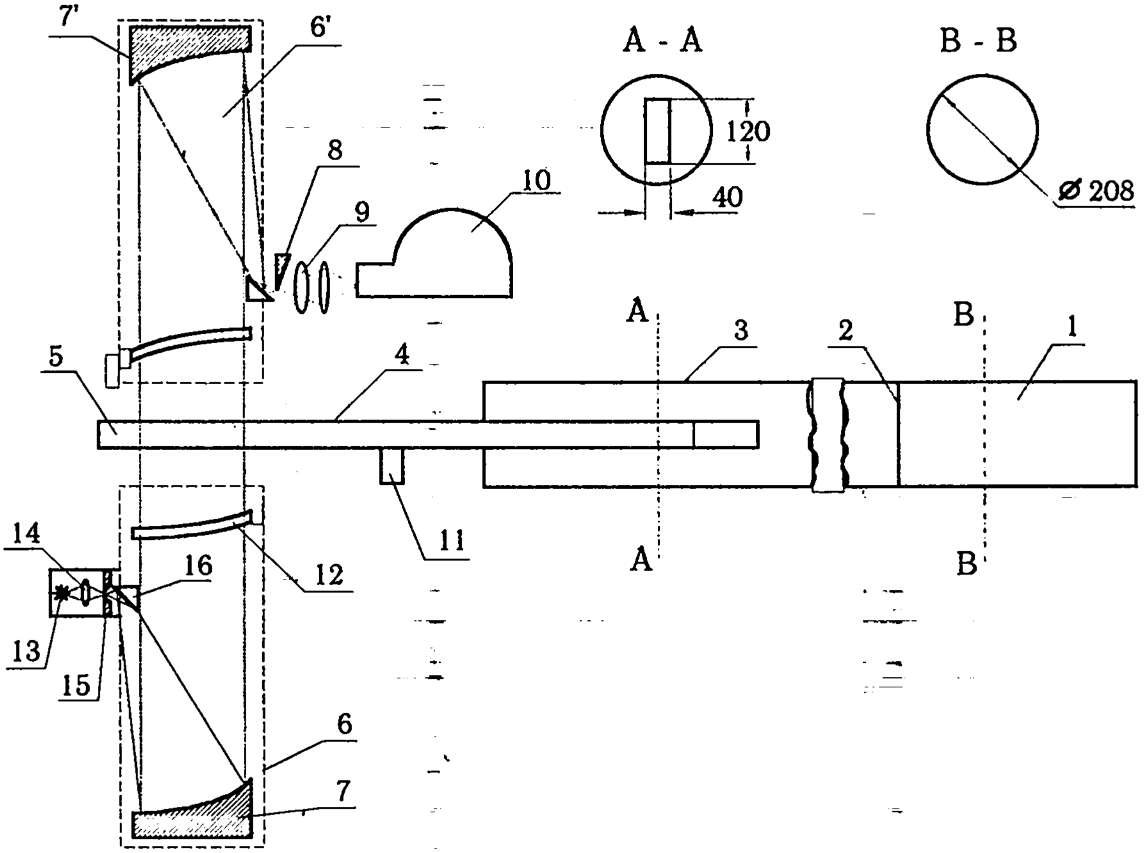

Fig.2. Schematic for shock tube & shadow device IAB-451 coupled with high speed camera (top view).
1 - compressed gas chamber; 2 - diaphragm;
3 - channel cylindrical section; 4 - channel rectangular section;
5 - measuring section; 6, 6' - collimator and telescope; 7,7' - parabolic mirrors; 8 - Foucout knife; 9 - two objective telescope; 10 - SFR (high speed camera); 11 - piezo gauge; 12 - lens; 13 - light source;
14 - condenser; 15 - slit diaphragm; 16 - prism.
Dimensions are in mm.

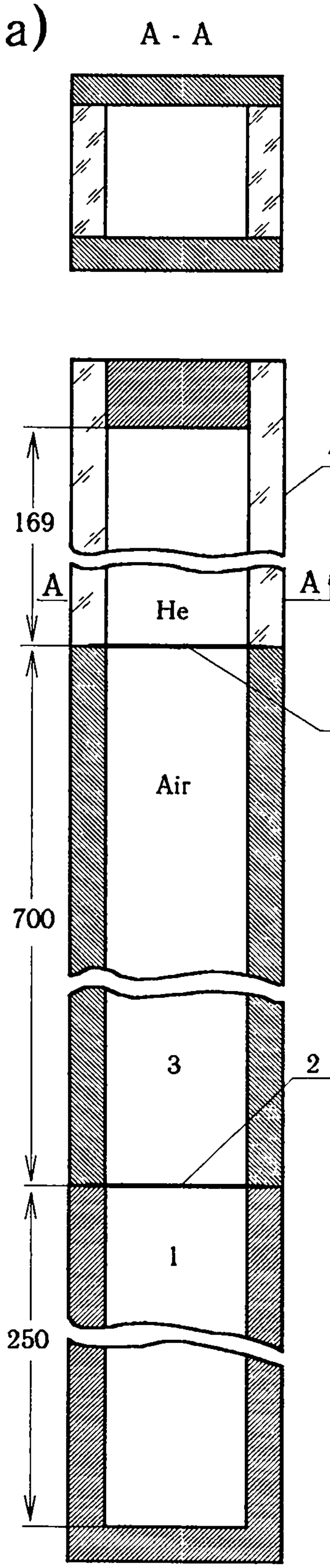

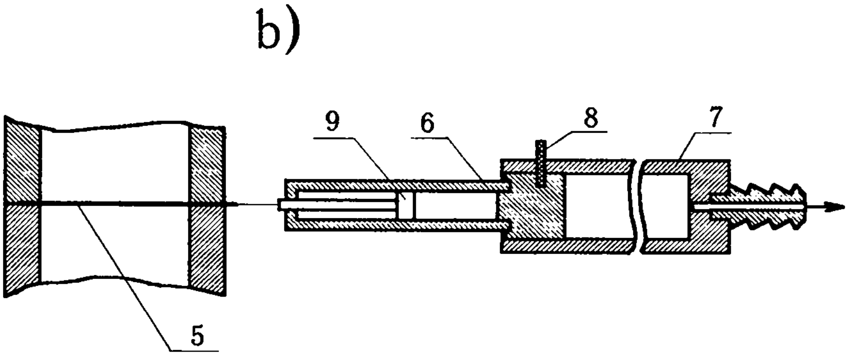

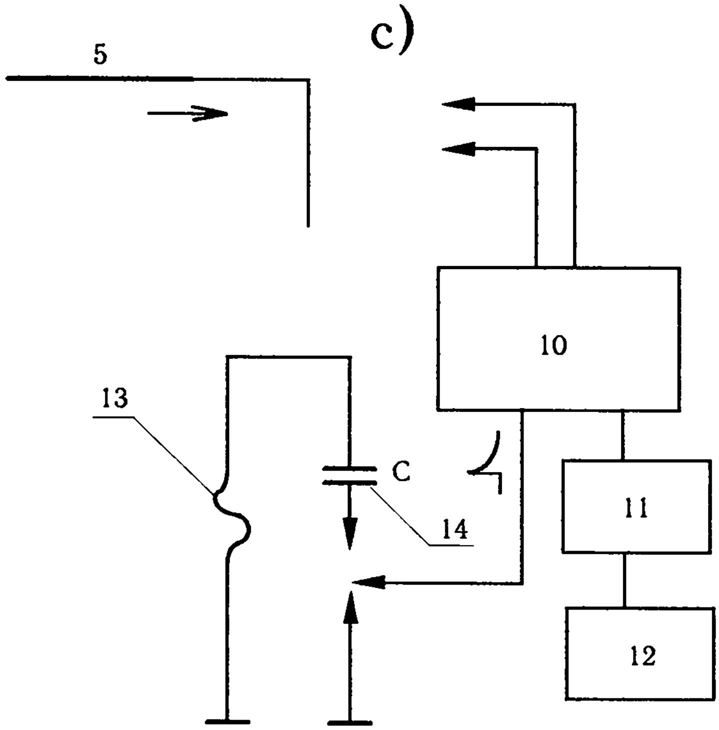

Fig.3a. Schematic of vertical shock tube. 1 - chamber; 2 - diaphragm; 3 - channel; 4 - measuring section.

Fig.3b. Puller. 5 - sliding diaphragm; 6 - big pusher; 7 - cylinder; 8 - pin; 9 - small pusher.

Fig.3c. Control electronic for experiment. 10 - high speed camera control panel; 11 - periodic pulse generator; 12 - pulsed light source; 13 - exploding wire (on diaphragm); 14 - capacitor bank.

The experiments were run for two t_{del}. values:

a) t_{del}=0.5-1s, b) t_{del}=2-13ms.

There occurs helium and air interdiffusion during this time. Their interpenetrating depths ($L=\sqrt{Dt_{del}}$) are estimated as L=0.6-0.8 cm, and L=0.04-0.1 cm for t_{del}=0.5-1s and t_{del}=2-13ms, respectively. Here, D=0.62 cm^2/s [96] is the gas molecular diffusion coefficient.

1.4. ELECTROEXPLOSIVE CYLINDRICAL SHOCK TUBE WITH INITIAL SHOCK MACH NUMBER M=3

There are two most common ways to generate a cylindrical convergent shock wave. The one used a cylindrical shock tube having a droplike axisymmetric body placed at the end of the channel [73], [74]. Shock wave generation occurs there in between the transparent wall and the plane end face of the drop like body. The other case used electric explosion of a thin metal film applied to the inside surface of a glass cylinder [75] to produce convergent shock wave.

VNIIEF experiments used a modification of the technique [75]. The experimental setup is schematically shown in Fig. 4. Convergent semicylindrical shock wave was generated by electrically exploding 90 nichrome wires 0.1 mm in diameter (1) arranged as generatrices of the organic glass semicylinder (2). The wires were soldered to copper busbars (3) mounted on the end faces of the semicylinder (2). The busbars were connected to a capacitor bank via high-voltage controllable switch. The capacitor bank having 6μF capacitance was charged to 32kV voltage. Energy stored by the capacitor bank was about 3 kJ. The high-voltage switch used was operated by pressurized air at 7-8 atm. pressure. It was triggered by a high-voltage pulse from the control board that operated the SFR camera. The switching circuit had inductance within $1.5 \cdot 10^{-7}$ H.

The wires exploding produce divergent shock waves that interact to result in the generation of a single convergent shock wave. This wave was divided spatially into three constituents. One of these got into the test section channel (20 mm wide) formed by the walls (4). The others entered the sections formed by the walls (4), steel semicylinders (5) and light shields (6) and they did not affect the flow pattern in the test section channel. The walls (4) were sharpened to avoid large perturbations. The complete test section included two mated units with their junction being at the radius 55 mm or 60 mm.

The abrupt change in pressure at the convergent shock front was about 12 atm at the radius about 50 mm. The front shape distortion was within ~0.5 mm, and the wave center displacement about the system geometric center was about 2 mm for the front radius R=50 mm.

The film (8) was applied to the cylindrical surface of the section (7), thus isolating it from the outer section. Prior to the experiment, the central section was filled with different gases at atmospheric pressures. The procedure used for filling the central unit with gases is like that described in Section 1.2.

Gases used by the experiments include helium (ρ=0.163kg/m^3, γ=1.63), hydrogen (ρ=0.0837kg/m^3, γ=1.401) and freon-12 (ρ=5.13kg/m^3, γ=1.139). Gas densities are given hereinafter at atmospheric pressure and temperature 20^{o}C.

Instability and turbulent mixing growths were observed using shadow device optically coupled with SFR camera in framing mode.

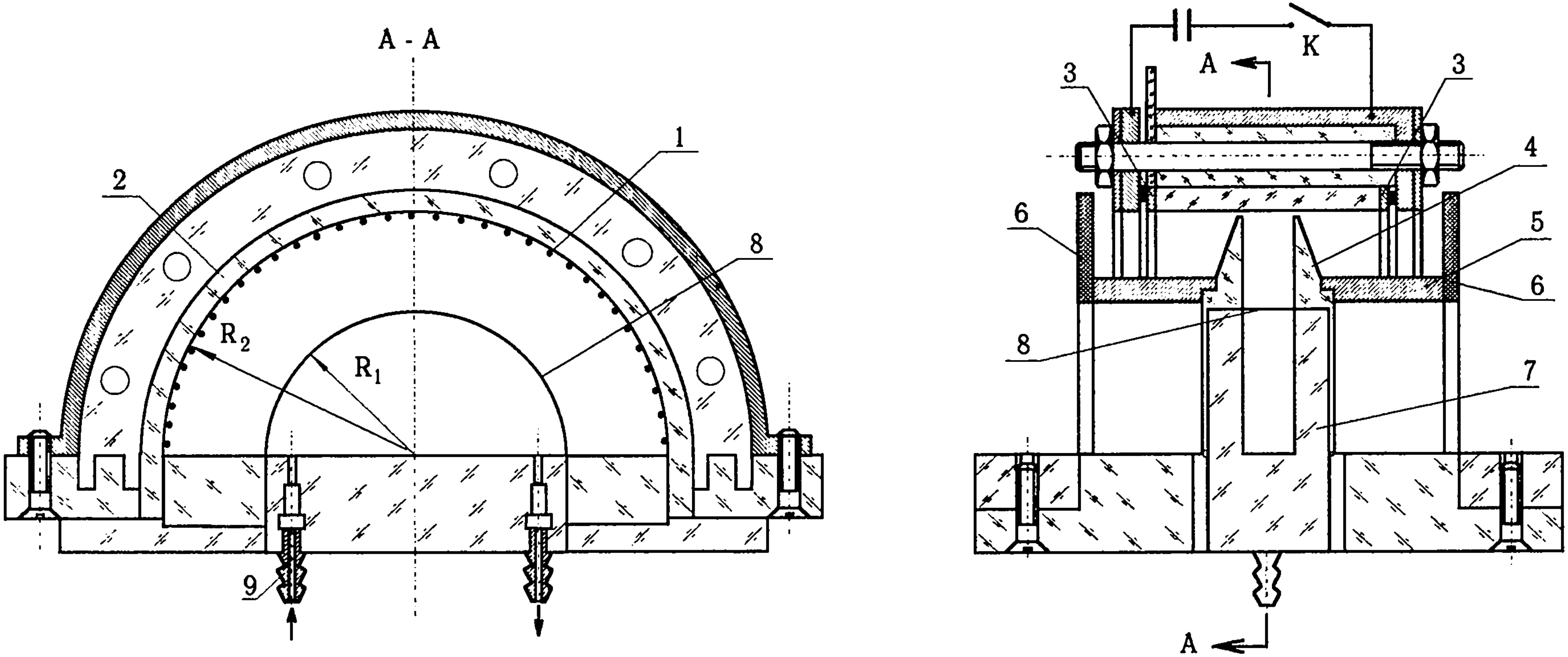

Fig.4. Experimental device scheme for cylindrical converging shock wave generation.

1. - exploding wires; 2 - organic glass semi cylinder of 100mm radius; 3 - copper buses; 4 - limiting walls; 5 - semi cylindrical screens; 6 - shields; 7 - measuring section; 8 - thin film; 9 - connection for gas input into the measuring section.

1.5. JELLY TECHNIQUE

Additional opportunities to investigate Rayleigh-Taylor instabilities at liquid-gas interface are offered by simulation of unsteady hydrodynamic flows using jellies [60-63]. This is the technique based on the use of test samples made of jelly [76] that are subjected to pulsed pressure. Due to its relatively high strength, jelly is suitable for making quite intricately shaped test samples. Moreover, when loaded by several atmospheres' pressure it behaves like incompressible liquid. Given jelly transparency, photography techniques can be used for observations.

Basically, the experiments used jelly made of water-solved gelatin at the concentration C=4.4% (typical concentration in cooking).

Fabrication of jelly test samples includes the following steps. Initially, a solution is made. For this purpose, a weighed portion of dry gelatin is put into water to swell there. Then the water heated up to about 50^0C or 60^0C temperature. Thereby, the solution is produced which is then filtered and poured into specifically shaped forms. Further, the solution is held for two hours in these forms at T=+6°C to cool down. When the jelly has set, it is removed from the former.

In this way, test samples can be fabricated as plane layers, rings, wedges and other shapes. The surface roughness is checked by thickness variation of the vaseline layer applied to the surface, being less than 0.2 mm. To reduce the jelly sticking to the surfaces of experimental setup or former, the latter are smeared with vaseline before jelly or solution are put there.

Cylindrical test samples can be also cut out of a flat jelly plate with a knife revolving about the ring center. This results in slightly more rough cut surface (~0.4 mm).

What should be taken into account in fabricating test models is that jelly may undergo deformations due to its own weight, and thus result in deflections to form at the interfaces of interest. To avoid this, the layer (ring) thickness must be made less than its length (diameter). Typically, jelly models are fabricated right in the experimental setup which is a dismountable structure. This provides better precision in the model fabrication and also reduces the risk of its damage.

Reference [63] describes measurement data for σ_{com} , i.e. critical stress value for jelly sample being under unilateral static compression. These measurements were performed at room temperature using cylindrical samples 20 mm in diameter and 20 mm high made of jellies differing in gelatin concentrations. The dependence $\sigma_{com}(C)$ has been shown to be near-linear: for C=4.4% σ_{com}~0.1kg/cm^2, and for C=35.2% σ_{com}~2.8kg/cm^2), see Figure 5. These results are approximately consistent with the data of reference [77].

Pulsed loading of models can be performed using gas pressurized to much higher than σ_{com} level. In practice, it has proved more preferable to use for this purpose the explosion of gas explosive mixture (GEM), specifically, acetylene-oxygen mixture (C_2H_2+2.5O_2). A firing chamber was field with this explosive mixture by its prolonged pumping through gas inlets (the pumped mixture volume should be about 5-10 times that of the firing chamber).

GEM detonation can be rather easily achieved by electric spark initiation.

Stoichiometrically formulated GEM at T_0=20°C, and P_0=760 mm Hg is characterized as follows:

- density ρ_0=1.38 10^{-3}g/cm^3;

- detonation velocity D=2450m/s;
- detonation front pressure P_J=41atm.;
- critical diameter - 2 mm.

Generally, pressure leveling time of GEM explosion gases is much shorter than the typical time taken to drive the jelly shell. Therefore, the interpretation of experimental results may ignore this pressure leveling time of explosion gases, and assume the shell being driven by equilibrium pressure P_0=13 atm. By estimates based on gasdynamic experiments, explosion gases can be approximately described by the equation of state of ideal gas having adiabatic index γ=1.23.

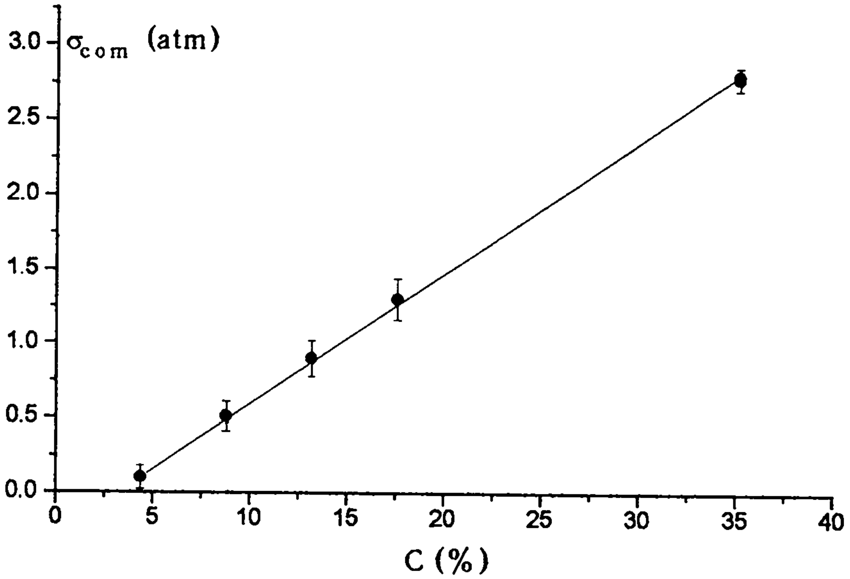

Fig.5. Jelly strength σ_{com} (atm) dependence on gelatin weight concentration C%.

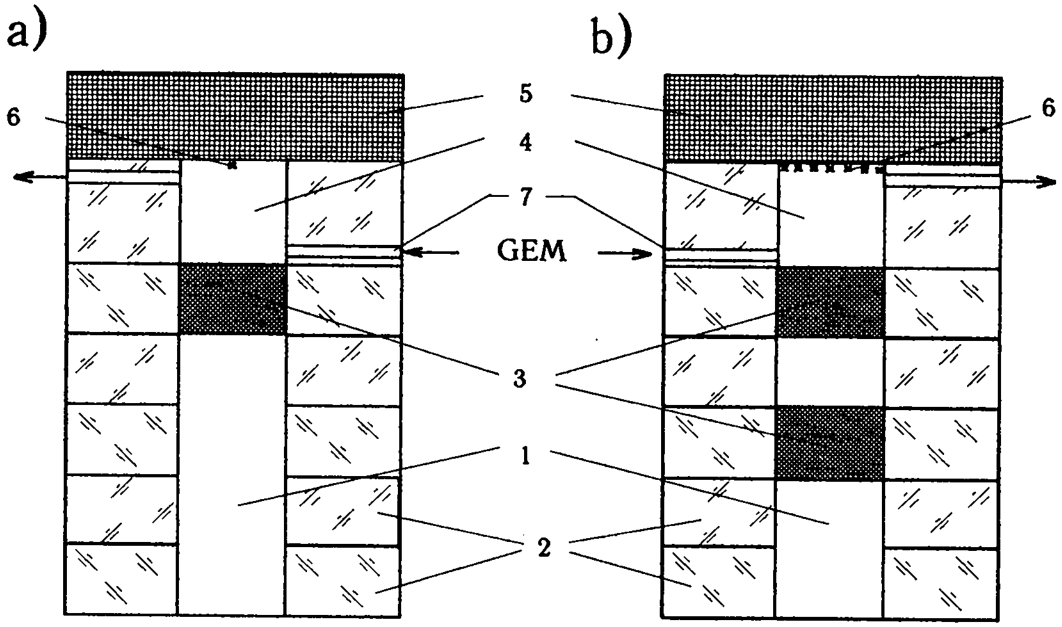

Fig.6. Plane jelly layer acceleration unit.

a) Jelly layer acceleration by gas explosive mixture (GEM) pressure. 1 - channel; 2 - organic glass plates with holes 40x40mm^2 which are the cannel casing; 3 - jelly layer; 4 - chamber filled with GEM; 5 - textolite cover; 6 - spark gaps; 7 - gas inlet tubes.

b) Acceleration of two jelly layer separated with air inter layer.

1.6 GAS-DRIVEN LIQUID LAYER TECHNIQUE

Investigations of R-T instability and its associated turbulent mixing have been very commonly using experiments with vessels containing liquids of different densities, driven vertically downwards at much higher than gravity acceleration [5-16]. The drivers used include rubber tension bars [5,6], pressurized gas [7-13] and rockets [14-16].

Currently, Lawrence Livermore National Laboratory (USA) are working on the vessel driving technique based on ponderomotive forces [79]. Any of these techniques involves a vessel with its mass comparable to or exceeding that of the liquid. This is what considerably reduces the acceleration value to be achieved.

The VNIIEF-developed technique has liquid layer 20-80 mm thick driven through the square-shaped channel (40x40 mm^2 or 80x80 mm^2), basically without any container. With this technique, the accelerations can be achieved as high as possible (up to 10^5 m/s^2). Liquid layers are driven by either GEM explosion gas pressure or pressurized gas.

This technique has been developed as extension of the jelly technique. Experiments to investigate local perturbations [61] and turbulent mixing zone growing at the gas-liquid interface [35] have used plane jelly layers. These experiments involved both single and double layers [35] with the setup as shown by Fig. 6. In these experiments, one (Fig. 6.a) or two plane jelly layers (Fig. 6.b) were placed inside the channel body 40x40 mm^2 square-shaped (1), with its one end tightly closed with a cover (5). The chamber confinement (4) was filled with GEM (C_2H_2+2.5O_2) through gas inlets (7) by pumping the mixture through the chamber. The GEM detonation was initiated by electric sparks at one or many (up to 64) points. The flows resulting from driving the layers were observed using SFR camera in framing mode both laterally and axially.

The experimental setup used for tests to investigate R-T instability with the liquid layer driven by GEM explosion products is shown in Fig. 7a. The channel body (1) is made of organic glass and tightly closed on one end with a cover (7). The liquid layer (2) is fixed inside the channel with a stiff plate (3) and a sealant (4). The other free end of the channel is open to the atmosphere. The chamber (5) is filled with gas explosive mixture fed through gas inlets (10) by pumping. The mixture was detonated by electric-spark breakdown at one point (8) with the detonation transmitted through distributor (9) to 64 points (for 40x40 mm^2 channel) or 256 points (for 80x80 mm^2 channel) uniformly arranged across the channel.

Detonation wave reflects from the liquid layer surface as unsteady shock waves. The reflections from the chamber walls and liquid surface result in a sequence of waves damping with time. GEM explosive products' pressure drives the layer vertically downwards. Chamber (5) height variations make it possible to investigate both the wave effects on the turbulent mixing dynamics and the mixing evolution for waveless and quasi stationary driving of the layer by explosion gases. In this case, initial perturbations at the liquid layer boundary are due to detonation wave dynamic variations.

Investigation of R-T instability with plane liquid layers being driven by pressurized gases used an experimental setup designed similar to that described above (Fig. 7b). Here, the liquid layer (2) divides the acceleration channel of the setup into two sections: working chamber (13) and supporting chamber (12) connected through a passage (14) (2 mm in diameter). The chamber (12) is tightly

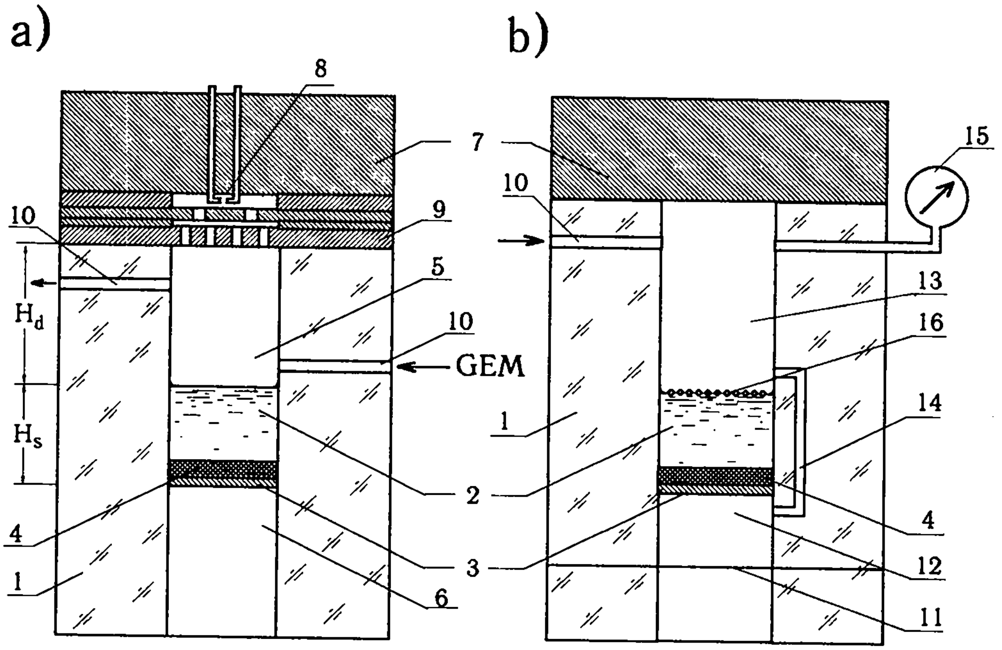

Fig.7. Plane liquid layer acceleration unit.

a) Liquid layer acceleration by gas explosive mixture (GEM) pressure.
1 - channel casing; 2 - liquid layer; 3 - moving plate (plywood 3mm thickness); 4 - thin jelly layer; 5 - chamber filled with GEM; 6 - channel; 7 - cover; 8 - spark gap; 9 - splitter; 10 - gas inlet tube.

b) Liquid layer acceleration by compressed gas.
11 - diaphragm; 12, 13 - channel parts filled with compressed gas; 14 - coupling channel; 15 - manometer; 16 - polypropylene fragments on water surface.

isolated from the environment with diaphragm (11). After the liquid layer has been placed into the channel and all the components tightly connected, pressurized air is fed into the chamber (13) through the gas inlet (10). The gas also gets through the passage (14) into the supporting chamber (12), and there occurs leveling of pressures above and under the layer. The setup is to be filled with pressurized gas rather slowly. Pressure is checked using manometer (15).

Upon filling the chamber (13) to the required pressure, the diaphragm (11) is made to disrupt by exploding a nichrome wire glued thereto. The pressurized gas will rapidly release from the space (12) to the environment. This results in pressure differential, which makes the liquid layer go accelerating vertically down. With P_0=45 atm., the acceleration may go as high as $g \sim 10^5$ m/s^2.

There may be priming initial perturbations specified by spreading crumbles varied in grain size, i.e. initial perturbations amplitude, on the free surface of liquid layer.

1.7. OBSERVATION TECHNIQUES

1.7.1 FILMING AND PHOTOGRAPHY

For the purpose of imaging the flow patterns, most experiment used high-speed framing camera SFR [72] with optical mechanical image switching and synchronism between the recorded and recording events. This camera is schematically shown in Fig.8. The object image is produced by the objective (2) and collective (4) near rotating one-sided mirror (5) motor-driven (6) through a reduction gears (7). With lenses (8) fitted into a specific mount, this image is transmitted to the film (9). The figure shows a two-step diaphragm (1) having its image produced by the objective (2) and collective (4) at the lenses (8) positioned in two lines. As the mirror (5) rotates, the diaphragm image moves from lens to lens, thus undergoing optical mechanical switching. The device is equipped with an electromagnetic shutter (3) allowing the beam interruption to avoid another image on the previous one, and also clock pulse generation system with electromagnetic detector.

The same camera with slight modifications can be used as photo recorder. In the experiments described below, SFR camera operated mostly in framing mode with the frame of 10 mm diameter and resolution 16 lines/mm, and measurement accuracy for mirror rotation velocity was 0.1%.

1.7.2. SYNCHRONISM IN SHOCK TUBE AND SFR OPERATIONS

There were some problems with synchronism in the shock tube and SFR camera operations due to inadequate stability in the camera operation, on the one hand, and sluggish diaphragm destruction on the other.

Reliable synchronism requires that useful recording time should be much longer than the time spread value for diaphragm destruction, Δt. As shown by measurements, this requirement is rather well satisfied, since Δt=20-50 μs, while flow imaging time for the experiments described was about 500-1000 μs.

The diaphragm was broken by electrically exploding a nichrome wire 0.03 mm in diameter and about 10 mm long that was glued on to the diaphragm at the center. An electric capacitor 2 μF charged to 10 kV was discharged through this wire. The discharge was initiated from the SFR control board.

The experience in operating this device has shown it is sufficiently reliable.

1.7.3. SHADOW DEVICE IAB-451

Shadow device IAB-451 [80] was used to visualize flows in the observation unit of the shock tube measuring section. This device is designed based on Teppler's method (Fig.2). It includes two components: a collimator (6) and a telescope (6'). The collimator is a mirror-lens objective with focal length 1978 mm and relative aperture 1:8. It incorporates a mirror (7) and a lens (12) to correct for the optical system aberrations. The image of the light source (13) is produced by the condenser (14) in the plane of a slit diaphragm (15) adjusted in width. The prism (16) serves as deflector mirror.

The telescope (6') is designed similarly to the collimator (particularly, it has the same focal length and relative aperture). There is a knife (8) placed at the focus of the mirror (7'), to cut off the deflected light rays that have passed through the

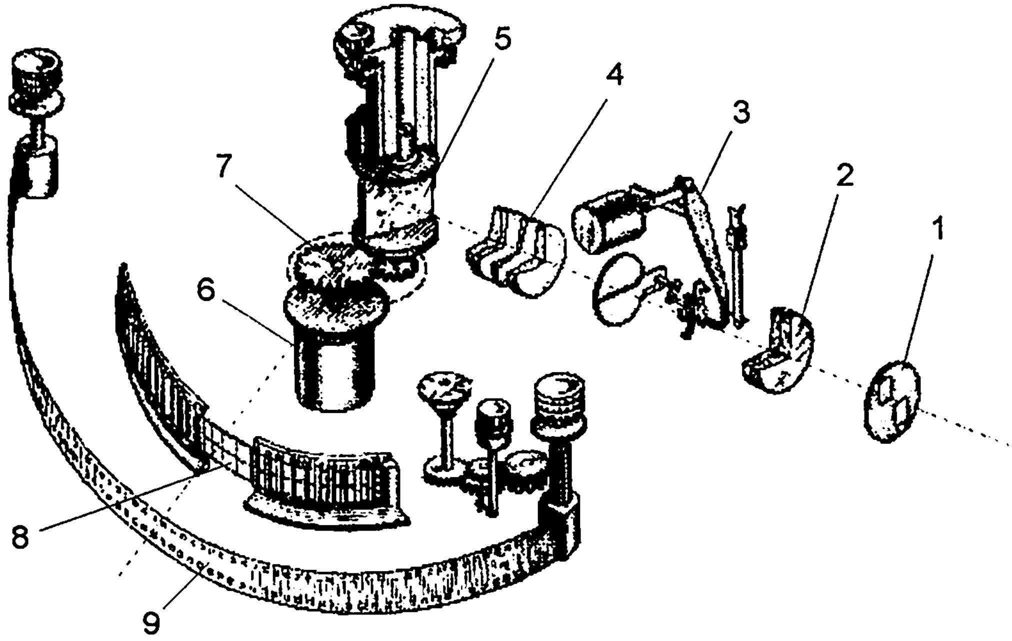

Fig.8. High speed camera (SFR) scheme.
1 - stepped diaphragm; 2 - objective; 3 - electromagnetic shutter; 4 - collective; 5 - rotating mirror; 6 - electric motor; 7 - reduction gears; 8 - lenses; 9 - film.

regions with density gradient perturbations in the flow of interest (Foucaut knife) [78]. The shadow device has the field of view of 230 mm diameter.

Flow photo recording in the measuring section was performed with two techniques:

a) using a standard photo accessory to the device, with frame diameter 25 mm. The light source used was a short spark discharge (0.1μs). This technique provided one shot at specified time with high spatial resolution for each one experiment;

b) using high-speed SFR camera.

The light source used was a flash-lamp IFK-120 with luminescence time 1.2ms. SFR-camera was coupled with IAB-451 shadow device using the technique [72]. For framing photography, SFR-camera was coupled with IAB-451 through a telescopic system including two objectives (9) (Fig.2). The SFR frame image can be controlled in scale by varying the focal length of the second telescopic objective.

For streak imaging of flows (i.e. x-t diagrams), the slit was fixed directly in the viewing, or observation, portion of the shock tube measuring section. The optical adapter (9) used was an objective having 50, 110 or 210 mm focal length. The image size became larger with the increase of the adapter focal length.

Sometimes, experiments were performed such as those involving liquid layer technology, where the viewing section of IAB-451 device was used as objective having large focal length (Fig.9a). For light source, an acetylene flash-lamp was used [81].

1.7.4. LIGHT SOURCES

SPARK-DISCHARGE SOURCE

This source represents a discharge circuit including 4 low-inductance capacitors type KOB-500 (2000 pF total capacitance) charged to U_w=12-15 kV, and a spark gap, these being interconnected by two metal plates. The main gap breakdown and spark generation are initiated by a sparkover in the rear gap. High-voltage triggering pulse is generated by pulsed transformer. To stabilize the spark position, a slight laminar jet of argon is injected through a hole in the upper electrode. The light source like this is described in [78].

The light flash time for this source is about 0.1μs. The spark light source was only used in combination with shadow device IAB-451 for instantaneous photography.

FLASH LIGHT SOURCE

This is a source developed around standard flashlamp type IFK-120 with luminescence time ~1-2 milliseconds or more, which is dependent on discharge circuit inductance. It was used both in combination with IAB-451 device and in other configurations to produce framing and streak photographs involving SFR camera.

ACETYLENE FLASH LAMP

This light source uses explosive gases from confined explosion of acetylene-oxygen mixture as luminescent body [81].

The flash lamp used by the experiments (Fig.9b) included a cylindrical steel can (6) of 100 mm inner diameter and 40 mm height, with organic glass window (7).

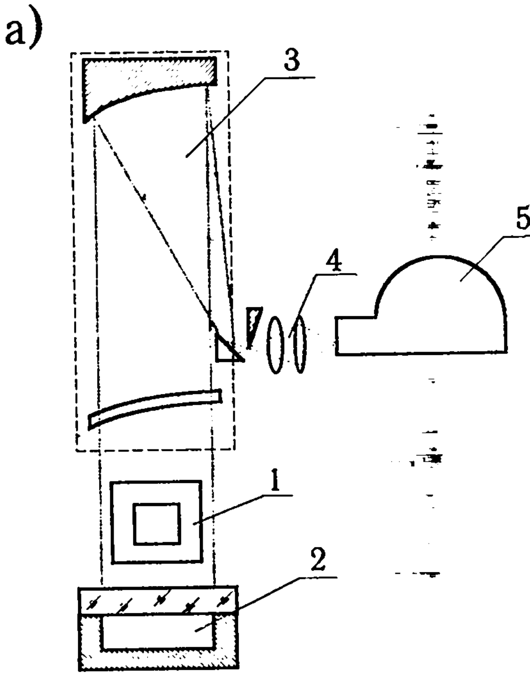

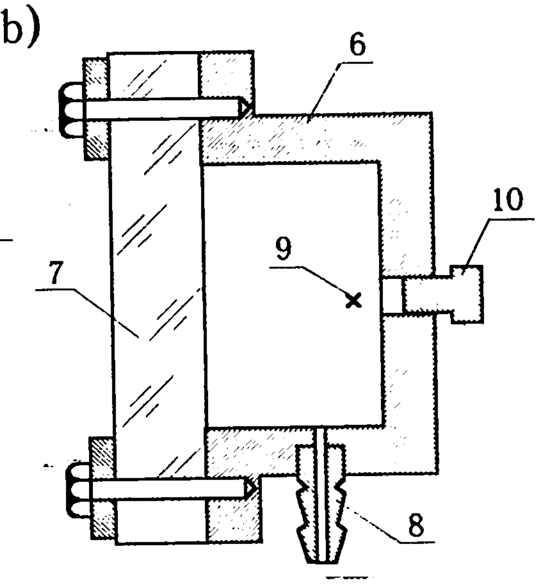

Fig.9a. Recording schematic of flows in liquid layer experiments (top view).
1 - experimental device; 2 - acetylene flash lamp; 3 - telescope;
4 - two objective telescope; 5 - high speed camera (SFR).

Fig.9b. Acetylene flash lamp.
6 - steel casing filled with acetylene-oxygen mixture; 7 - organic glass window; 8 - gas inlet tube; 9 - spark gap; 10 - plug.

The lamp inside space was evacuated and filled with gas explosive mixture at atmospheric pressure. Detonation was initiated by the spark-gap (9) breakdown.

The luminescence time depends on the source size. For flash lamp of 100 mm diameter and 40 mm height (inner flash lamp dimensions), the light pulse half-width is ~3ms.

The luminescence time can be made shorter by abruptly decreasing the explosive gases pressure, this being achievable with a smooth plug (10) to be forced out by the explosive gases. The time delay for this pressure release can be controlled by varying the plug insertion depth.

1.7.5. LASER KNIFE TECHNIQUE

When a thin flat light beam (or light knife) passes through a turbulized gas flow containing finely distributed impurities (dust, smoke, etc.), the light scattered by the impurity particles can be used to observe the flow pattern in the beam plane. This technique was used to investigate the turbulent mixing zone structure at shock-driven air-helium interface [23]. Light-knife experiments were conducted in the arrangement like that for experiments described in [19-20] (see Fig.22).

Referring to [23], the air was admixed with cigarette smoke prior to the experiment. Following the interface being driven by shock waves with air-helium turbulent mixing zone forming, a short-pulse thin and flat laser beam was transmitted therethrough. In the helium region, there was no light scattering observed. However, as the beam was passing through the turbulent mixing zone and air, the light would scatter. The scattering intensity was proportional to smoke particles' concentration in the beam plane. The smoke particles are so small that they move at the air velocity, thereby resulting in the light scattering pattern which unambiguously accounts for the air distribution in the turbulent mixing zone.

Fig.10 illustrates the recording geometry for the experiment. A beam from pulsed ruby Q-switched laser (wavelength λ=6943Å, pulse width 40 ns, energy 25 mJ) was transformed into a flat sheet of light less than 2mm thick using a system including cylindrical mirrors and lenses and a diaphragm. Smoke particles' distribution in the mixing zone was recorded by an open-shuttered photo camera. To reduce the effects of the background light incident on the objective, the shock-tube channel and photo camera were provided with a light shield. With a semi-transmitting mirror (2), the light pulse was partly split out to form an electric signal needed to measure the laser shot time.

Each experiment including densitometric wedge photography simultaneously with the process, or work, exposure. For this purpose, another part of the light pulse was split out by a semi-transmitting mirror to be then transmitted to the system including a semi-transmitting and totally reflecting mirrors with their planes positioned at an angle to each other (wedge) [82]. There was a scatter filter of milk glass placed in the beam path to eliminate granularity in the wedge field image. The wedge field imaging was performed with an open-shuttered photo camera. The wedge and the work exposure photographs (taken with the same film pack) were both developed at a time. With these measurements, quantitative information can be obtained on intensity distribution of the scattered light, and accordingly, relative air density distribution in turbulent mixing zone.

Consider in more detail the techniques for experimental data analysis. Given particles have much less mass than gas, then their influence on the gas flow may be

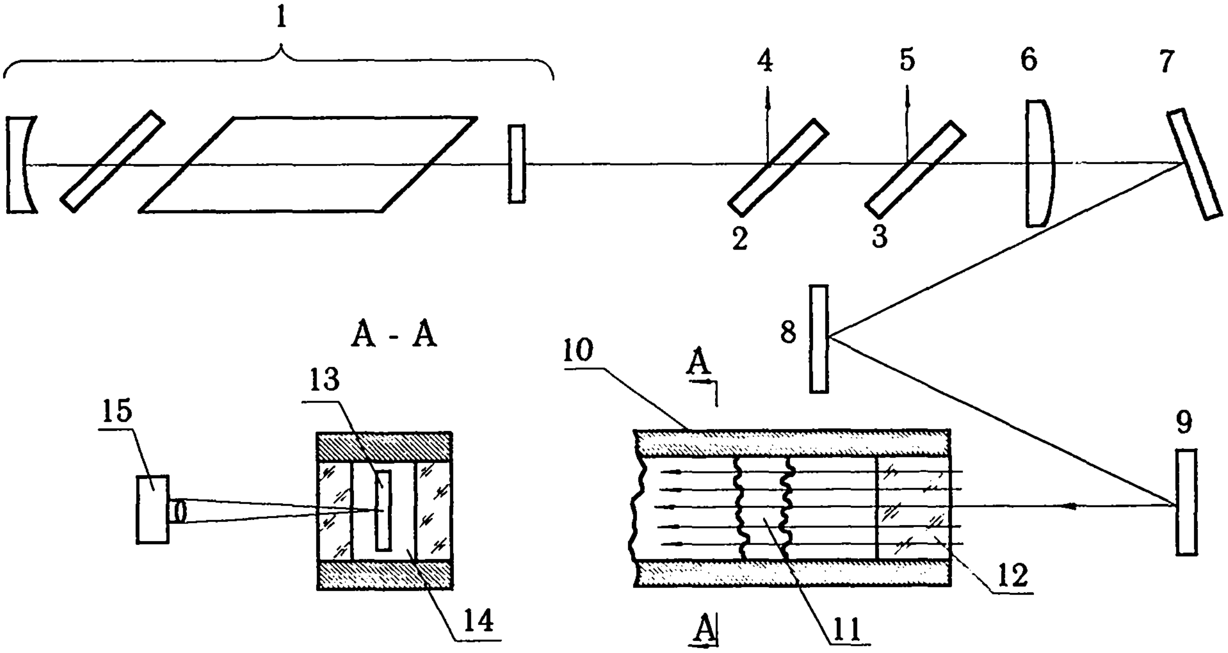

Fig.10. Schematic representation of laser beam transformation and control. 1 - pulsed laser; 2, 3 - semi transparent mirrors; 4 - beam to photo cathode; 5 - part of laser beam for measurements; 6 - 9 - optical system of cylindrical lenses and mirrors for light knife formation; 10 - shock tube section for measurements; 11 - turbulent mixing zone; 12 - transparent plug; 13 - light beam cross section; 14 - shock tube channel; 15 - photo camera.

neglected. When there is no gravitational field existing, the equation of particle motion is

$$\ddot{\vec{r}} = \frac{Sc_w\rho_g}{2m}|\vec{u} - \vec{v}|(\vec{u} - \vec{v}),$$

where m, S, $\vec{v}$ are the particle mass, cross-sectional area and velocity, respectively; $\vec{r}$ - radius-vector of the particle; $\vec{u}$ - gas velocity at particle location; c_w - drag coefficient, and ρ_g- gas density.

The quantity $\lambda = \frac{2m}{Sc_w\rho_g} = \frac{4}{3}\frac{d}{c_w}\frac{\rho_s}{\rho_g}$, having dimensions of length, represents the distance where a spherical particle of d-diameter and ρ_s- substance density is to be driven by gas up to the gas flow velocity [83]. This quantity limits the spatial fluctuation scale of the parameters of the turbulent flow, δ, that the particle will follow. For $\lambda \ll \delta$, the particle will be readily entrapped by the gas to move without any lag.

Let us look at the spatial fluctuation scale $\delta^*=\lambda$ that may be resolved , using smoke particles. Typically, cigarette smoke particles have size $d \approx 0.1$-$1\mu m$ and density, $\rho_s \approx 2.3 g/cm^3$ [84]. We take the gas density in turbulent zone, with allowance for its shock compression ($\sigma \approx 1.5$), as $\rho_{Air}=1.8\ 10^{-3}$ g/cm^3 and $\rho_{He}=0.25\ 10^{-3}$ g/cm^3. To find c_w, we estimate Reynolds number Re=dv/v, where v -is the kinematic gas viscosity. With velocity fluctuation in the turbulent zone v=10 m/s and 100m/s taken as typical of the experiments, we have Re=1.2 and 12 (for air) and Re=0.17 and 1.7 (for helium), respectively. By evaluating c_w according to [85] and substituting the evaluated quantities into the formula for λ , we can evaluate δ^* (Table 1)

Table 1. Values of δ^* parameter.

-	air		helium	
Re	12	1.2	1.7	0.17
c_w	4	25	20	170
δ^*, mm	0.4	0.07	0.6	0.07

As is clear from the table, spatial resolution scale of the technique considered that depends on the particles' inertia is rather small.

Consider how the laser knife light scatters in a slightly smoked region. Let x-axis be directed along the light beam, y-axis lie in the light knife plane, and z-axis coincide with the camera optical axis. The intensity of signal I(x,y), recorded by the photo camera, depends on the intensity of incident light $I_0(y)$, smoke particles per unit volume N(x,y), light knife thickness h and coefficient k defining the scattering efficiency.

Assuming N(x,y)~ρ(x,y), where ρ(x,y) - is the air density in the mixing zone, we obtain an elementary expression for I(x,y)

$$I(x,y) \cong k\ h\ \alpha\ I_0(y)\ n(x,y) = k_1\ \rho_0(x,y)$$

where k, k_1 are dimensional constants.

As shown by this expression, the ratio of the intensity of the measured signal referring to any arbitrary point in the mixing zone, $I(x,y)$, to that referring to the smoked region outside this zone, I^*, is independent of the above-mentioned constant, thus allowing to measure the relative air density profile in the mixing zone

$$\frac{I(x,y)}{I^*} = \frac{\rho(x,y)}{\rho^*},$$

where ρ^* - is the air density outside the mixing zone.

Smoke particle concentrations and measurement conditions were selected in the experiments such, that light absorption and secondary scattering in smoked gas could be neglected.

1.7.6 TECHNIQUES FOR EXPERIMENTAL DATA PROCESSING

For most experiments, photographs (negative images) were subjected to measurements using measuring microscope IMC-100x50.A to the 'accuracy 0.001 mm. The measurement data were processed by computers.

Fig.11 shown measurement geometry for interface perturbations amplitudes and shock waves in the experiments to investigate shock-induced instabilities.

For turbulent mixing zone growth experiments, streak photographs were used to measure the distance from a stiff wall to the TMZ (turbulent mixing zone) boundary at 10 to 30 points, and following this the data were averaged.

The same kind of measurements were done for turbulent mixing zone thickness in the experiments involving cylindrical electro-explosive shock tube.

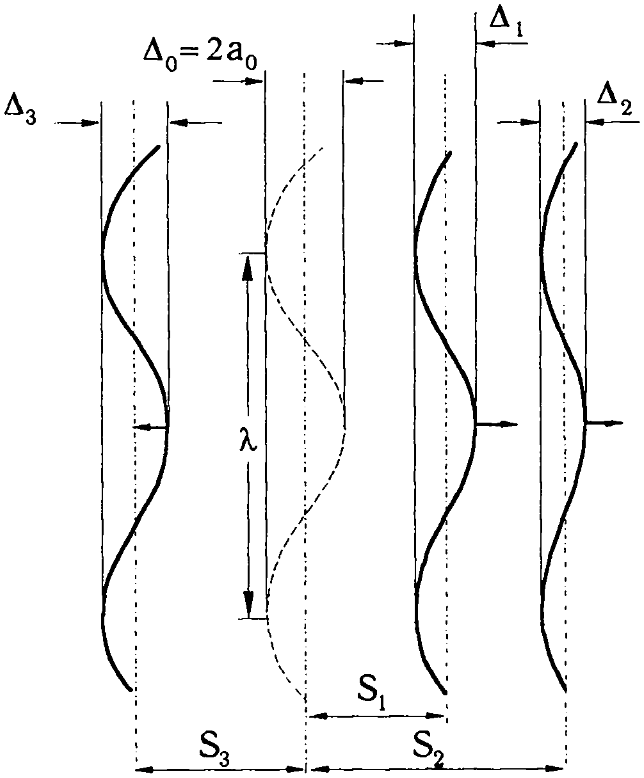

Fig.11. Definition of amplitude values.

Δ_1 - interface perturbation amplitude; Δ_2 - passed shock wave front perturbation amplitude; Δ_3 - reflected shock wave front perturbation amplitude; S_1, S_2, S_3 - paths of interface, passed and reflected wave fronts, respectively.

2. SUMMARY OF THE EXPERIMENTAL RESEARCH

2.1. INTRODUCTION

In mid-1960s, experimental investigations of shock-induced hydrodynamic instabilities [18-24,59] were started by VNIIEF as part of gasdynamic fusion research program [86].

For the purpose of these, the experimental technique was developed to study instabilities using a shock tube with gases separated by thin organic films.

It was used to investigate initial interface [18]; shock and rarefaction wave fronts perturbations growth [25,26], local cumulating and other effects [27,28].

The development of thin-film gas model as experimental technique on the one hand, and semi-empirical turbulent mixing models on the other, have promoted the turbulent mixing studies of shock-driven interface [19,20]. Later, the same techniques were used by other works [19-25,29-44,49-58].

In mid-1970s, VNIIEF developed the technique to investigate initial perturbations growth and turbulent mixing at gas-gas interface driven by convergent cylindrical shock wave.

In the late 1970s, VNIIEF created the technique for testing nonstationary hydrodynamic flows based on jelly models [60], that added to the experimental capabilities of Rayleigh-Taylor instability research. It was used to investigate localized perturbations growing at the boundary of pressurized gas-driven plane layer [61] and the surface of fractured jelly layer [62], and also for testing instability evolution at the boundary of converging cylindrical shell [63].

This variety of experimental techniques available has provided a substantial advance in understanding of hydrodynamic instabilities and turbulent mixing physics and allowed testing of numerical models.

2.2. INVESTIGATIONS OF PERTURBATIONS GROWTH AT GAS-GAS INTERFACE ACCELERATED BY PLANE SHOCK

2.2.1. EXPERIMENTAL GEOMETRY

Experiments to investigate perturbations growing at gas-gas interface accelerated by plane shock wave, used a horizontal shock tube and the technique as described in Sections 1.2 and 1.3.

The shock tube channel had a rectangular end section, 40x120 mm, (test section, Fig.12) divided into subsections using a thin film. These subsections were filled with different gases. In most cases, the initial interface perturbation was specified as $y=a_0\cos kx$ (or as conjugated circular arcs) [18,21,22,24,26]. Some experiments addressed the perturbations growth for more intricate initial geometry specified [94]. Flow visualization following the shock wave passage was performed by shadow technique (or shlieren-technique).

2.2.2. QUALITATIVE PATTERN OF INTERFACE PERTURBATIONS GROWTH

Fig. 13 shows graphically reproduced photographs illustrating perturbations growth at the interface between two gases: air and freon-12. Each was taken for an individual experiment.

When a shock wave is crossing the interface in lighter-to-heavier gas direction (air-freon-12) (Fig.13a), the perturbations amplitude would initially decrease slightly, but then increase monotonously. Over time, heavier gas protuberances projected forwards would transform into narrow jets, this resulting in the same perturbations pattern as for R-T instability case. The gas-gas interface smears due to random small-scale perturbations developing.

When a shock wave passes through the interface in heavier-to-lighter gas direction (from freon-12 to air) (Fig.13b), the perturbations amplitude would initially change the sign, and then increase significantly. Here, the specific details of the interface geometry changes were observed the same as in the previous case.

There are vortices forming and developing at the slopes of the interface (Fig.14a). These would occur the earlier, the larger is the amplitude of initial perturbation and the higher is the gas density ratio. Vortices form due to Kelvin-Helmholtz instability at the heavy gas jets penetrating into the lighter gas. For stepped-shape initial perturbations (Figs. 14.b- 14.c), the vortex would form almost immediately following the shock wave passage through the interface.

2.2.3. INVESTIGATION RESULTS

INITIAL CONDITION EFFECTS ON THE PERTURBATIONS GROWTH BEHAVIOR INTERPRETATION OF RESULTS

Figs. 15 through 17 illustrate the data from experiments performed by Drs. Meshkov and Klopov in 1970, using air and freon-12. The experimental data are presented in terms of variables $a(t)/a_0 \sim f(S/\lambda)$, where $a(t)$ is the current perturbations amplitude (see Fig. 11), S- distance covered by the interface. These experiments involved variations of wavelength λ, initial perturbations amplitude a_0 and perturbation shape (sinusoidal or as conjugated circular arcs). The following shock wave characteristics in the air were actually used: Mach number $M=1.42$, pressure amplitude $\Delta P=1.2$ atm, air compression ratio $h=1.73$.

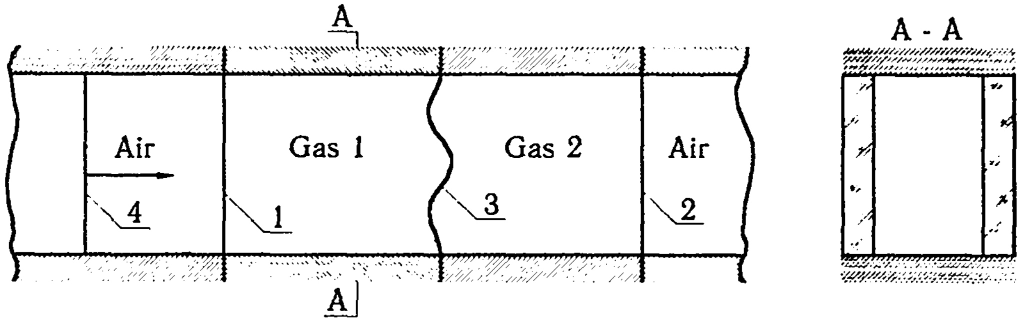

Fig.12. Shock tube test section for experiments to investigate instability of gas-gas interface accelerated by shock wave.
1,2,3-thin films to isolate test subsections; 3-interface of interest; 4-plane stationery shock wave.

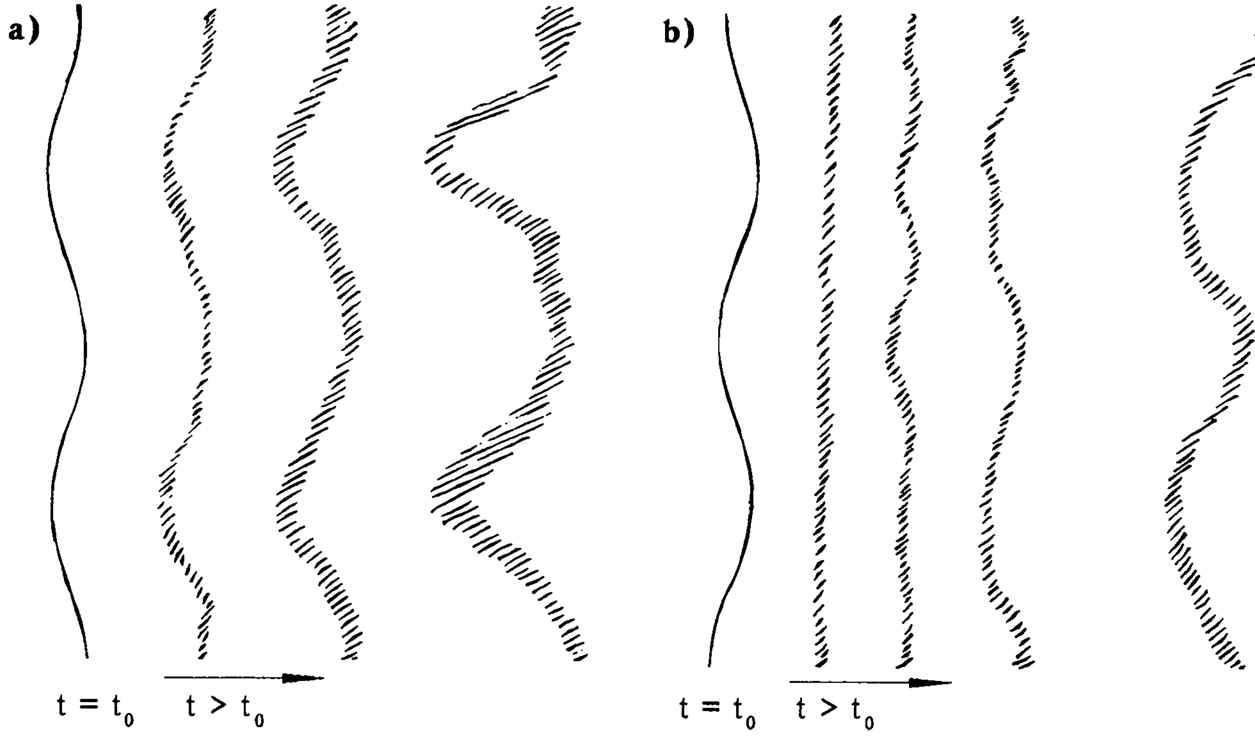

Fig.13. Time history of the perturbations amplitude and geometry of shock-accelerated interface.
Graphically reproduce photos of gas-gas interface perturbations: a) air - freon-12, b) freon-12 - air.
t_0 - time of shock wave passage through the interface. Mach number of the shock wave in the air M=1.42.
Perturbation wave length λ=60 mm.

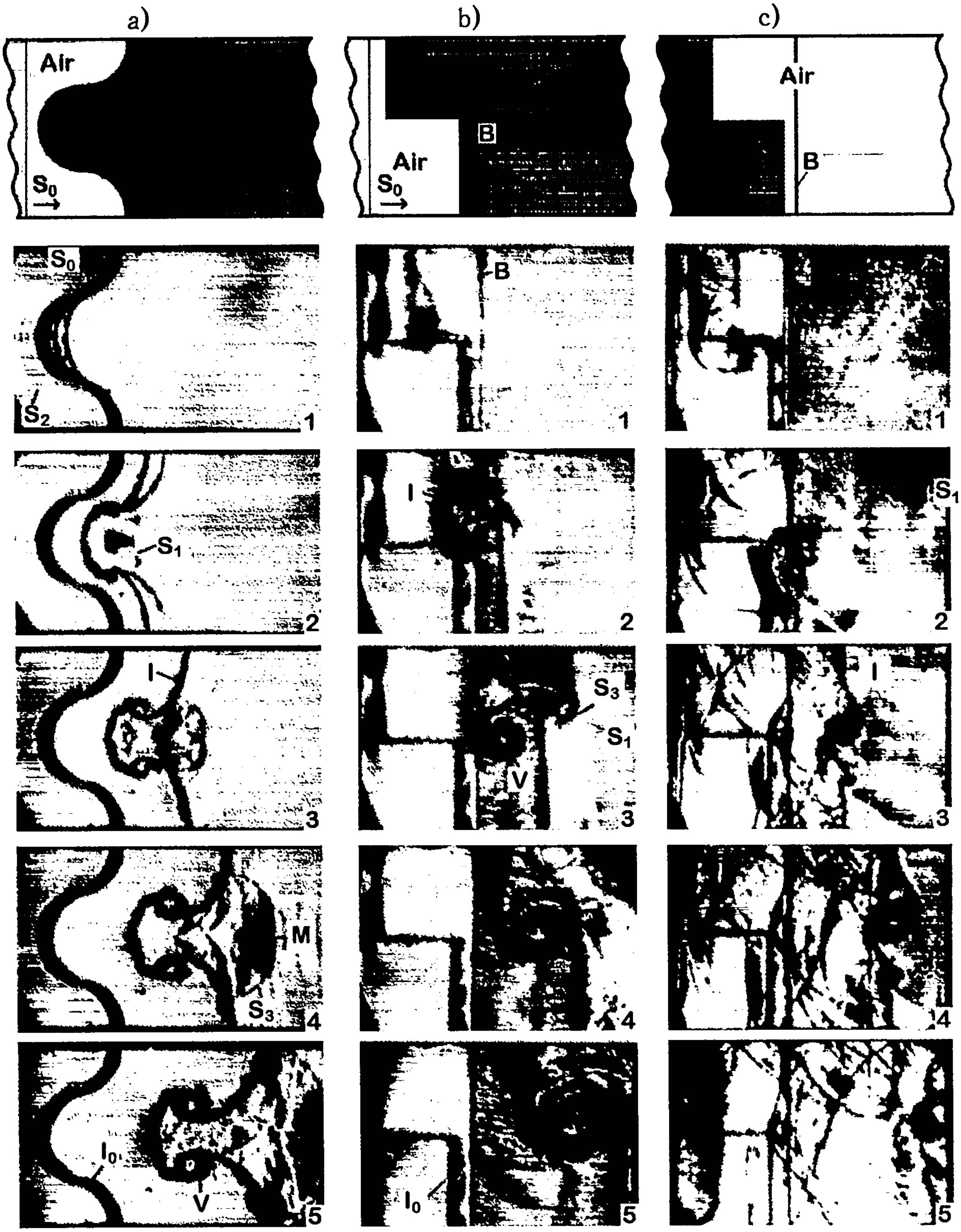

Fig. 14 Shock wave accelerated Air-Freon-12 interface perturbation development.
a) conjugate circles shape initial perturbation. b), c) stepped initial perturbation.
B - boundary between two parts of channel; I_0, I - initial and current interface locations; S_0, S_1, S_2, S_3 - incident, passed, reflected & transverse shock wave fronts; M - Mach wave; V - vortex zone.

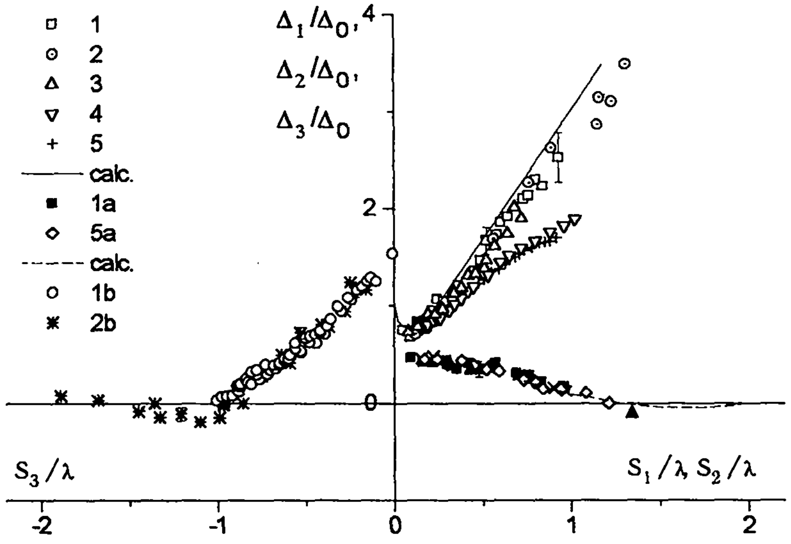

Fig.15. Amplitude of air - freon-12 interface perturbations; amplitude perturbations of passing and reflected shock waves as a functions of its passage distances during interface acceleration by the shock wave ($M=1.42$).

Points - experiments, curves - calculations by MV technique [87].

Interface perturbations:

1 - $\lambda=120$mm, $\Delta_0=0.1\lambda$; 2 - $\lambda=60$mm, $\Delta_0=0.1\lambda$; 3 - $\lambda=120$mm, $\Delta_0=0.2\lambda$; 4 - $\lambda=120$mm, $\Delta_0=0.3\lambda$; 5 - $\lambda=120$mm, $\Delta_0=0.4\lambda$.

Passing shock wave front perturbations:

1a - $\lambda=120$mm, $\Delta_0=0.1\lambda$; 5a - $\lambda=120$ mm, $\Delta_0=0.4\lambda$..

Reflected shock wave front perturbations:

1b - $\lambda=120$mm, $\Delta_0=0.1\lambda$; 2b - $\lambda=60$mm, $\Delta_0 = 0.1\lambda$.

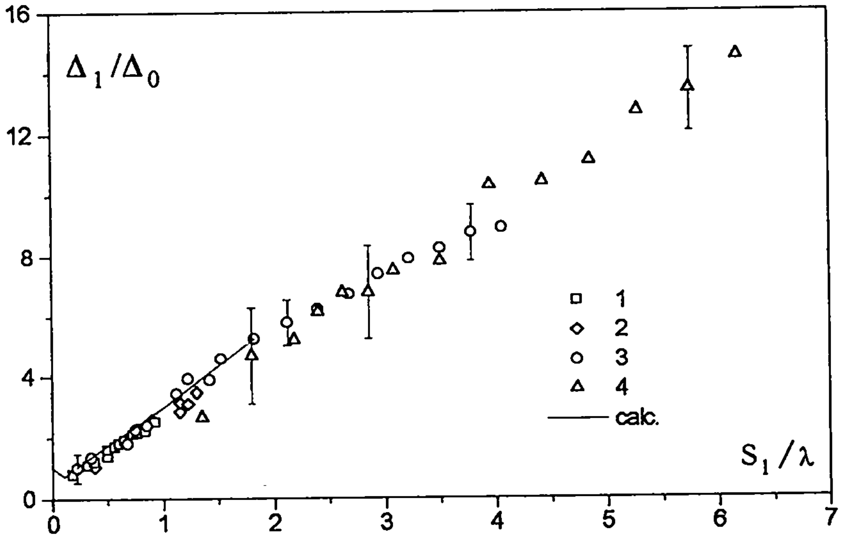

Fig.16. Perturbation amplitude of air-freon-12 interface as a function of the distance it has passed upon acceleration by shock wave of M=1.42.
Points-experiments, curve - MV calculation [87].
1 - λ=120mm; 2 - λ=60mm; 3 - λ=30mm; 4 - λ=20mm.
In every case $\Delta_0=0.1\lambda$.

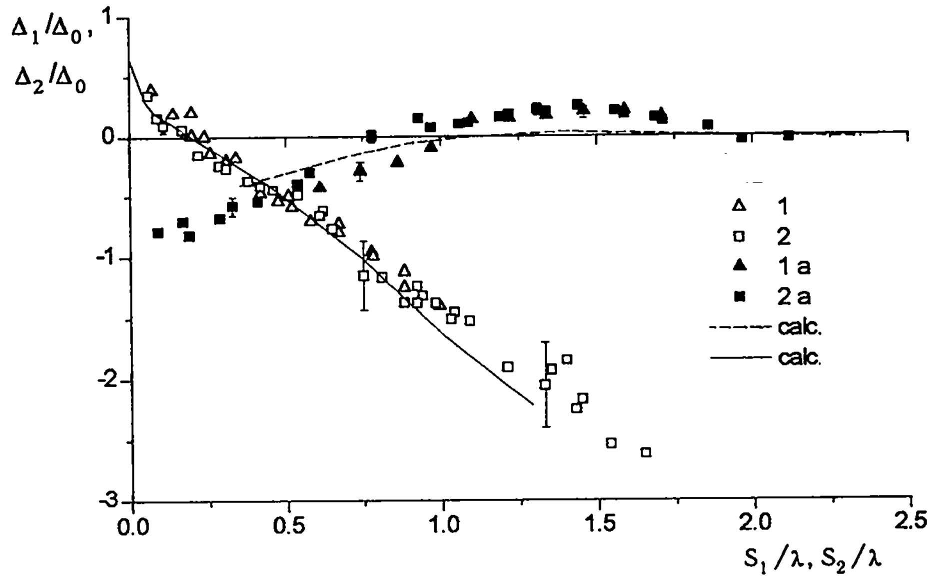

Fig.17. Perturbation amplitude of freon-12- air interface and perturbation amplitude of the passing shock wave front versus their passage distances (M=1.42).
Points - experiment, curves - MV calculation [87]. Interface: 1 - λ=60mm, $\Delta_0=0.1\lambda$; 2 - λ=120mm, $\Delta_0=0.1\lambda$.Passing shock wave: :1a - λ=60mm $\Delta_0=0.1\lambda$; 2a - λ=120 mm, $\Delta_0=0.1\lambda$.

As follows from the figures, for wavelength variations within λ=30-120mm and for $a_0/\lambda<0.1$, perturbations growth behaviors are similar. These experiments agree reasonably well with MV calculations [87].

Both for the shock wave passage from lighter to heavier substance (L-H) and the opposite case (H-L), the following three distinct stages are observed for the perturbations amplitude growth:

- stage 1: upon the shock wave passage, the perturbations amplitude of the interface decreases virtually in a jump due to gas compression behind the shock front ($0 \leq S \leq 0.05\lambda$);
- stage 2: ($0.05\lambda \leq S \leq 0.25\lambda$) perturbation amplitude grows at increasingly higher rate;
- stage 3: ($S \geq 0.25\lambda$) perturbation growth rate achieves saturation; perturbation amplitude (within the accuracy of the experiment) increases at a fixed rate.

Fig. 18 shows graphic copies of experimental photographs to illustrate reflected and refracted wave configurations and interface shape upon the shock wave passage. For L-H case, the reflected and refracted waves are both shock wave having their perturbation phase the same as the initial perturbation phase of the interface (Fig.18b). However, given shock wave crossing the interface in heavier-to-lighter substance direction (H-L), the reflected wave is rarefaction wave with the perturbation matching in phase with the initial interface perturbation. The refracted wave in this case would change the phase (Fig.18c).

Behind the perturbed shock waves, there are points where their fronts locally converge, thus resulting in higher pressure zones (+), and also where they locally diverge, resulting in lower-pressure zone (-).

The opposite situation is observed for rarefaction wave, behind the locally converging front portions there occur low pressure zones and behind the diverging portions - high pressure zones.

Due to pressure gradient, substances are made to flow over in the direction normal to the interface, from high-pressure to low-pressure zone, and interface perturbations would grow. Simultaneously, the substance also flows over along the interface, this resulting in diverging compression waves to generate. These waves have their perturbations amplitude rapidly decreasing with time.

The interface perturbations growth rate for L-H case can be approximately described by the formula [17]:

$$da/dt \cong a_0' \cdot A \cdot k \cdot u, \qquad (1)$$

where u is the interface velocity increment upon plane shock wave passage, a_0' - amplitude of initial interface perturbations allowing for material compression by shock wave; A- Atwood number, $k=2\pi/\lambda$.

Equation (1) can be used to estimate perturbations amplitude for H-L case as well. Here, the value of a_0' is found as arithmetic average of amplitudes before and after the shock wave passage through the interface [89].

The experiments with $a_0/\lambda>0.1$ as illustrated by Fig.15 observe perturbation growth rate decreasing with a_0/λ parameter increasing. This sets a limitation on the applicability of equation (1) that proves valid only for relatively small amplitude of initial interface perturbation.

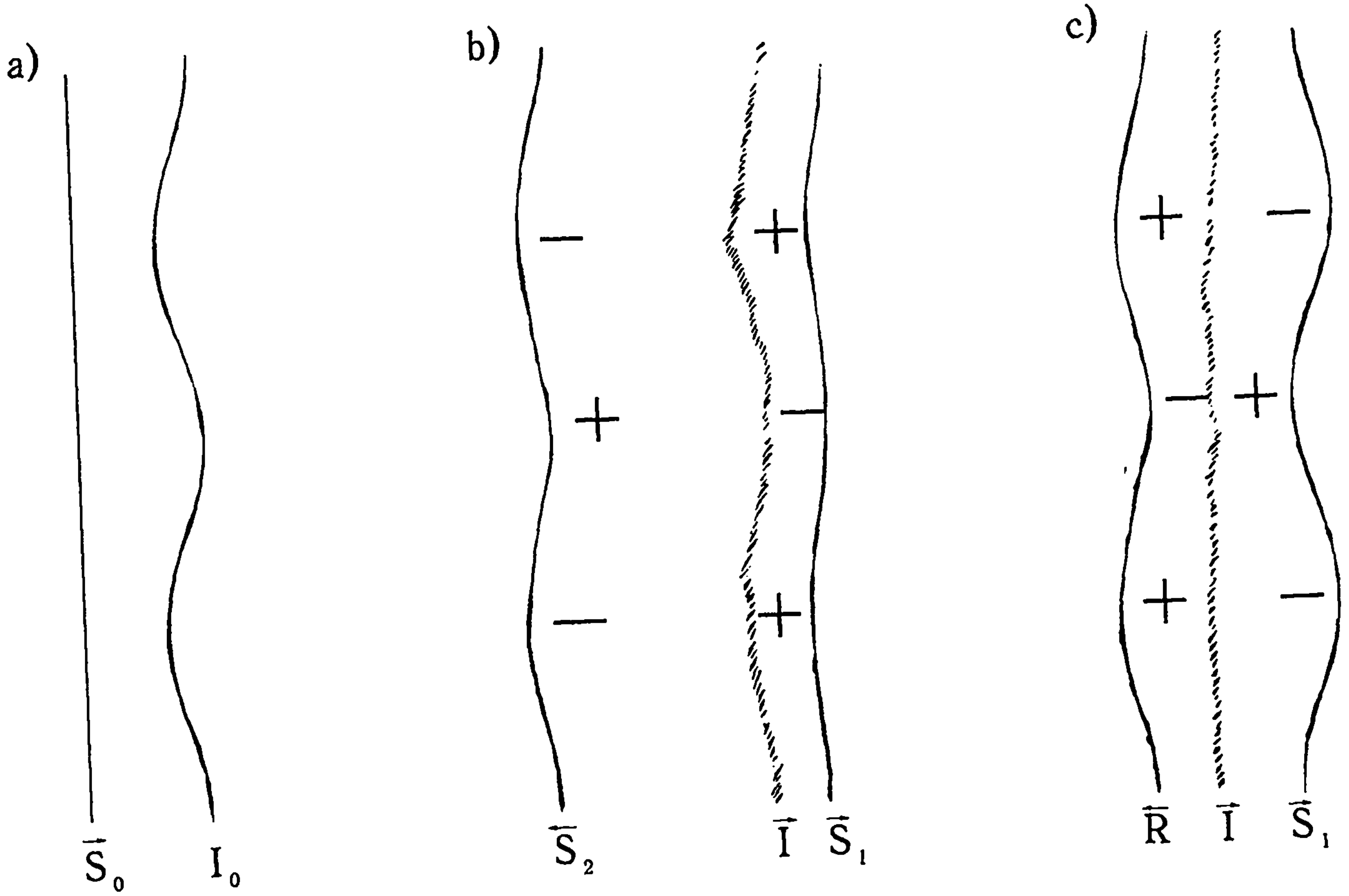

Fig.18. Higher-pressure (+) and lower-pressure (-) zone distributions behind the wave fronts.

a) Initial geometry; I_0 - interface in question, S_0 - incident shock wave.

b) Graphically reproduced photos of the initial flow phase in air-freon-12 test. S_1, S_2 passing and reflected shock waves, respectively.

c) Graphically reproduced photos of the initial flow phase in freon-12-air test. R - rarefaction wave. Arrows indicate wave and interface directions

As follows from experiments [34] conducted involving argon and xenon for shock wave Mach $M=3.5$, equation (1) accounts for the total perturbation amplitude (i.e. distance from the bubble top to the jet tip) until $a(t)<(0.3\text{-}0.4)\lambda$ (linear stage). At nonlinear stage, where $a(t)>(0.7\text{-}1)\lambda$, the lighter gas no longer penetrates into the heavier one, while the heavier gas penetration into the lighter gas becomes slower. Moreover, there is a specific mushroom-shaped structure forming at the jet tip.

It should be noted, that the problem of interest is two-dimensional. In general the flow is three-dimensional, and not only the interface, but also incident shock wave may be subjected to perturbations. Plane shock wave is stable against front perturbations. These perturbations have amplitudes decreasing as power law [90]. Behind the front, there generate diverging transverse compression waves with their interface governing the perturbations growth pattern of the interface. These waves will irreversibly transform over time into weak shock waves, thus causing inflections at the main shock front [25]. When this perturbed wave accelerates the interface, this results with time in the jet propagating in the wave direction.

Similarly to instability for the interface being accelerated by shock wave, there should exist that for the interface accelerated by expansion wave. For the purpose of simplicity, consider a centered rarefaction wave case. Denote with $L_R(t)$ the distance between its leading and rear fronts. When $L_R(t)>>a_0$, there occur perturbations growth conditions similar to those for R-T instability developing at constant acceleration [57]. For $L_R(t)<<a_0$, there should exist the conditions equivalent to the case for shock wave acceleration of the interface, characterized by the perturbations amplitude linearly dependent on time (1). The difference is that for L-H case (where rarefaction wave crosses the interface from lighter to heavier gas) there should be the situation similar to shock wave H-L case and vice versa.

Let us briefly consider the effects of gas-separating film. The following condition is essential as smallness criterion for such effects.

$$L\cdot\rho_{gas} >> \Delta_f\cdot\rho_f, \tag{2}$$

where L is the characteristic flow scale, $\rho_{gas}\sim10^{-3}g/cm^3$ - gas density, Δ_f ~0.3 microns, ρ_f ~$1g/cm^3$ - film material thickness and density. This film has mass thickness equivalent to the air layer 0.3 mm thick. The characteristic flow scale in this case is perturbation wavelength λ varying within 30-120 mm, and the condition (2) is satisfied with large margin. This is additionally supported by the similarity of $a(t)$ functions with variations in λ and a_0 (Figs. 15,16).

2.2.4. NONLINEAR EFFECTS OF SHOCK AND RAREFACTION WAVE PERTURBATIONS GROWTH

Shock wave perturbations development involves the occurrence of additional gasdynamic flow discontinuities behind the shock front [24,25] as well as the wave front distortions. Fig.19 shows shadow graphs to illustrate the shock wave reflection in air from rigid wave-shaped wall. These experiments considered amplitude variation of the wall shape perturbations at fixed wavelength.

As it is shown, reflected wave is deviating from sinusoidal form in time. Particularly, this shows itself in the occurrence of inflection points of front B. Simultaneously, there are discontinuities at transverse wave fronts W in the flow behind the reflected wave front.

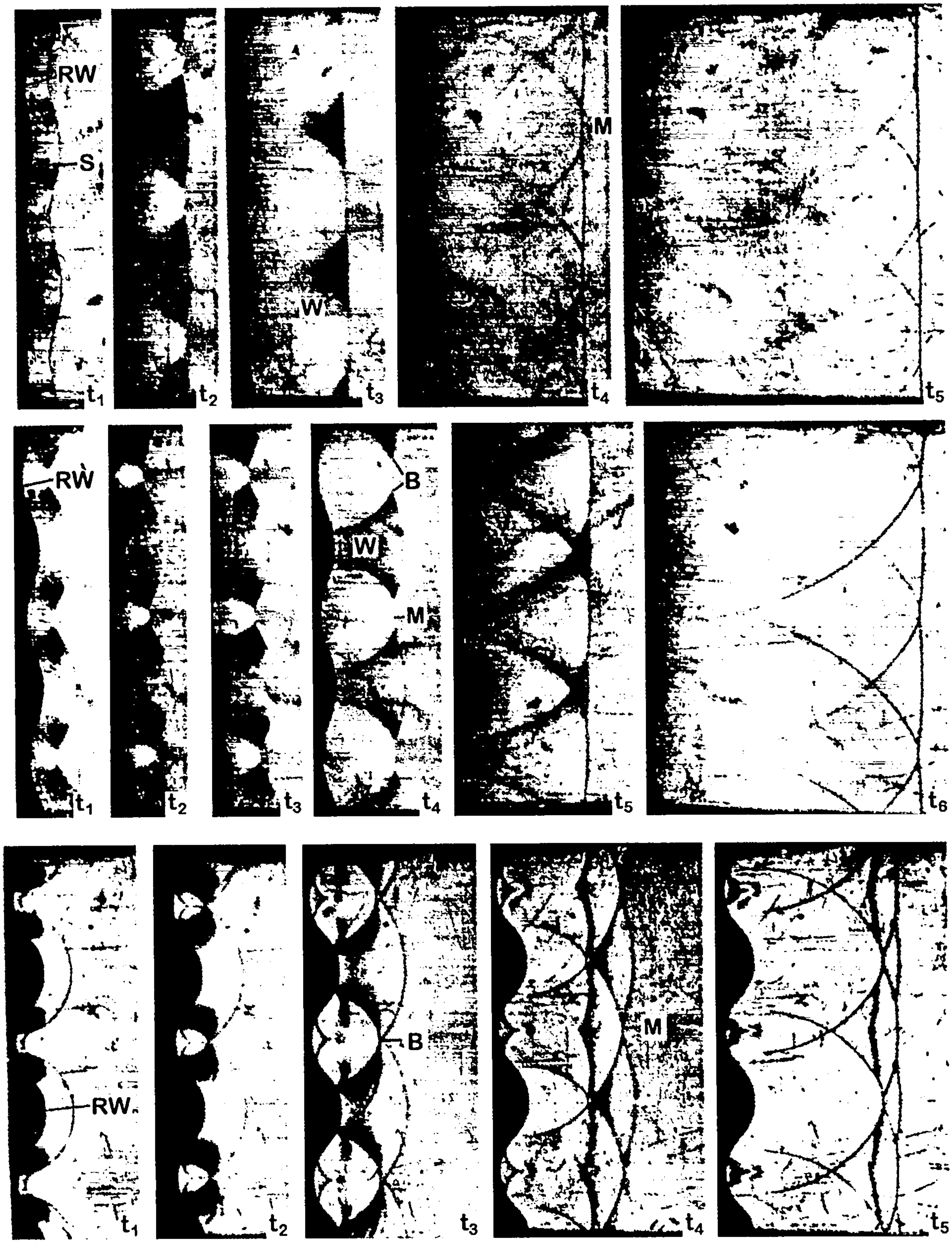

Fig. 19 Shock wave front perturbation development after its reflection at the wavy shape rigid wall. a) $a_0k=0.2$ ($a_0=0{,}025\lambda$); b) $a_0k=0.4$ ($a_0=0.05\lambda$); c) $a_0k=0.8$ ($a_0=0.1\lambda$). RW - rigid wall, S - reflected shock wave; B - shock wave front break point, W - transverse wave front, $M=1.3$ - Mach number. Initial shock wave moves from right to left. Time increases from t_1 to t_6.

Initially, gases have densities continuously distributed in space, this being apparent from the smeared transverse waves as observed in the photographs.

Over time, density discontinuities would form, the fronts becoming more clearly defined with their image in the photographs getting more sharp. As the initial perturbation amplitude decreases, the development of flow discontinuities and deviations from sinusoidal form becomes slower. Qualitatively, what is eventually observed is generally the same flow pattern as Mach waves M intersecting and interacting.

Fig.20 shows the photographs of the rarefaction wave front perturbations occurring with stationary shock wave passing through the interface between carbon dioxide gas (ρ_0=1.85 10^{-3} g/cm^3; γ=1.30) and air.

Every point of the rarefaction wave leading front moves at local sound velocity in the direction normal to the surface. Since the flow is uniform behind the incident shock front, then the points of the rarefaction wave will move at the same velocity. Therefore, the evolution of the wave front form should proceed over time as formulated by the Huygens' principle accepted in optics: each subsequent front position represents an envelope of spherical waves originating from the points of the front for a previous instant of time. This perturbations growth pattern has been supported by experiment.

There is a distinctive feature with the front evolution, which is a special point that would come to exit where the front form is inflected. These special points do not occur due to initial perturbation amplitude being too large. It can be shown in terms of geometry, that these points should occur sooner or later for however small, though finite perturbations.

Until special point appears, the perturbation amplitude has not changed with time. When these special points appear, there are secondary expansion waves R_1 generated in the gas flow behind the leading wave front, as extensions of the initial front sections (see Fig.20a). Here the whole wave front disintegrates into intersecting arcs. Importantly, the front R_1 develops at different times at every point, and thus the density derivative discontinuity propagates along the front at a finite velocity (this is clearly apparent from Fig. 20a)

. With the initial perturbation amplitude of rarefaction wave increasing, both the front inflection and the secondary wave generations occur significantly earlier (see Fig. 20.b) There are compression waves generated in the flow behind the leading wave front.

For the two cases considered, beginning from the time t_o when the front inflection point comes to exist, the perturbation amplitude of the leading wave front Δ decreases, and this asymptotically tends to zero. For considerably long times, the divergent wave sections approach cylindrical symmetric forms, so that the initial form effects can be neglected. It can be easily shown, that based on this assumption, $\Delta \sim$ Const/t $\sim$ Const/S, where t is the time, and S - the distance covered by the wave. However, as a linear approximation, the perturbation amplitude of the expansion wave front should remain constant for an infinitely long time. This suggests, that it will be insufficient to satisfy the condition $a_0k<<1$ to solve small perturbations growth problem in a linear approximation, and that smallness criterion must be satisfied for the time span where this approximation would be valid [24]

$$t<<t_0=1/c_0\ a_0\ k^2.$$

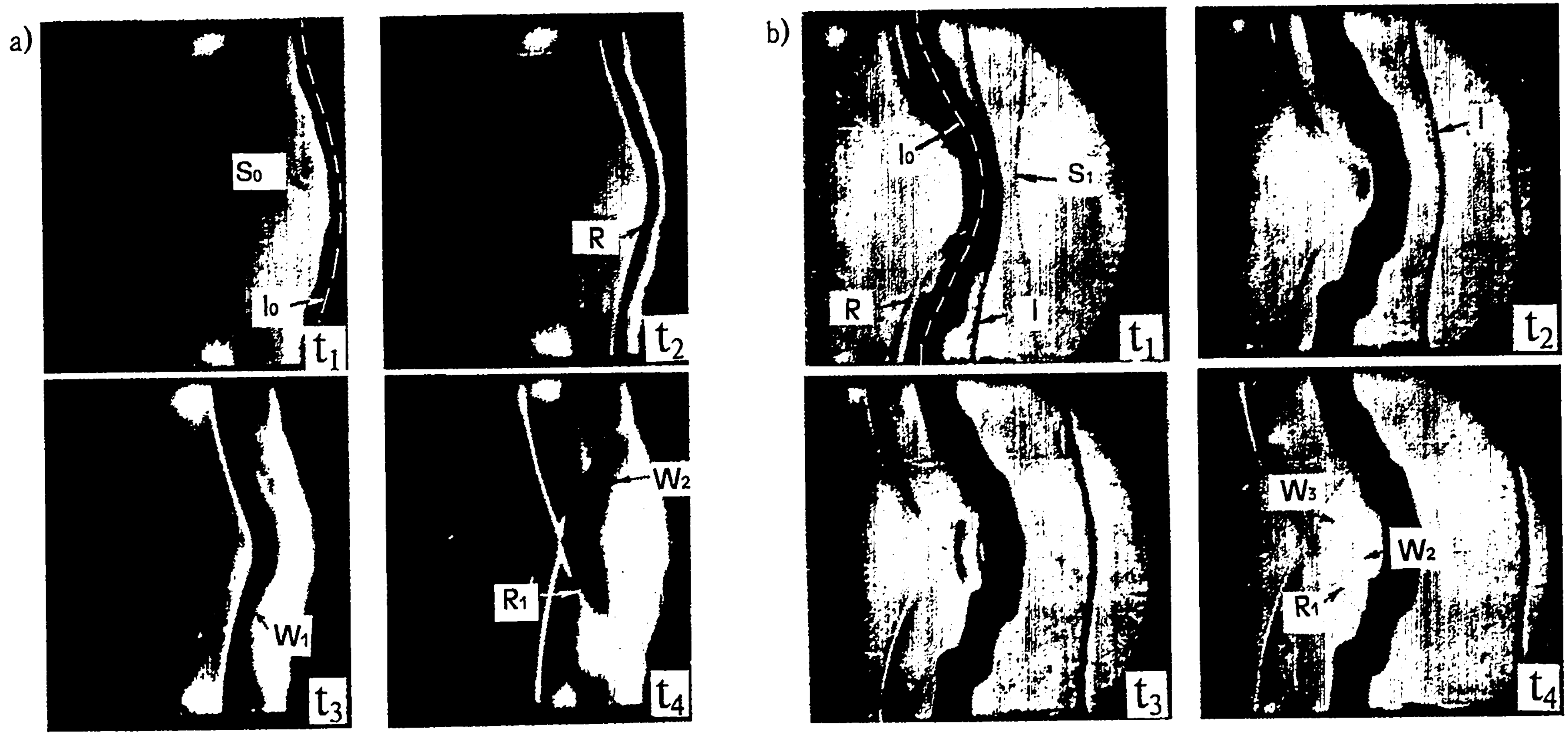

Fig. 20 Rarefication wave front perturbation development. Rarefication wave arises after shock wave pass through CO$_2$-Air interface (from left to right): a) a_0=6 mm, λ=120 mm; b) a_0=12 mm, λ=120 mm.
Interval between frames - 128 μs.
I_0 - initial interface location; I - CO$_2$-Air interface location at t>t_0; I_1 - Air-CO$_2$ interface; S_0 - incident shock wave; S_1 - passed shock wave front; R - reflected rarefication wave front; R_1 - secondary rarefication wave fronts; W_1, W_2, W_3 - secondary compression waves.

Here, c_0 is the characteristic sound velocity.

2.2.5. LOCAL CUMULATING EFFECTS

Substance motion in the neighborhood of perturbed interface, caused by the shock wave passing therethrough, may result in considerable local concentrations of energy. The following experiments have illustrated the scale of these concentrations.

For the first case [27], the experiment was performed using a shock tube with rectangular test section channel. The channel was plugged at the end with a stopper having a concave cylindrical shaped inside surface. Shadow photographs were taken to image the plane stationary shock wave reflecting from this concave wall, and streak photographs (x-t diagrams) made for the flow in horizontal symmetry plane of the channel.

In the neighborhood of the symmetry plane of the channel, the reflected wave takes cylindrical form. The reflected wave central section is converging symmetrically, this terminating in the collision of transverse compression waves moving from the periphery towards the symmetry plane. These waves result from tangential flows caused by the shock wave reflection from inclined wall areas. Upon the collision of transverse waves in the central region, there is an abrupt increase in the reflected wave front velocity.

With the experimental x-t diagrams of flow in the symmetrical plane, one can determine the velocity of shock wave diverging from high-pressure region. The knowledge of flow parameters behind the incident shock wave and the equation of state of the medium (ideal gas of $\gamma=1.4$ in this particular case) makes it possible to calculate the parameters of state behind the front of reflected wave diverging from the high-pressure region.

Fig.21 shows the ratio of maximum temperature T_{max} achieved in the high-pressure region, to the temperature T_1 behind the front of the incident shock wave, as a function of $\eta=H/R$, where R is curvature radius of the concavity, and H - concavity depth. Curve 1 in the figure represents the case in question. The value of T_{max} was found to be comparatively low. It is only by a factor of 1.5 higher than the temperature observed for the shock wave reflection from a flat wall.

This effect is much more pronounced for the shock wave reflecting from a spherical concave wall [28]. As is clear from Fig. 21 (curve 2), the temperature achieved in the case is more than an order of magnitude higher than that behind the front of the shock wave reflected from a flat wall. Such stronger an effect arises from the transverse cylindrical wave cumulating along the symmetry axis.

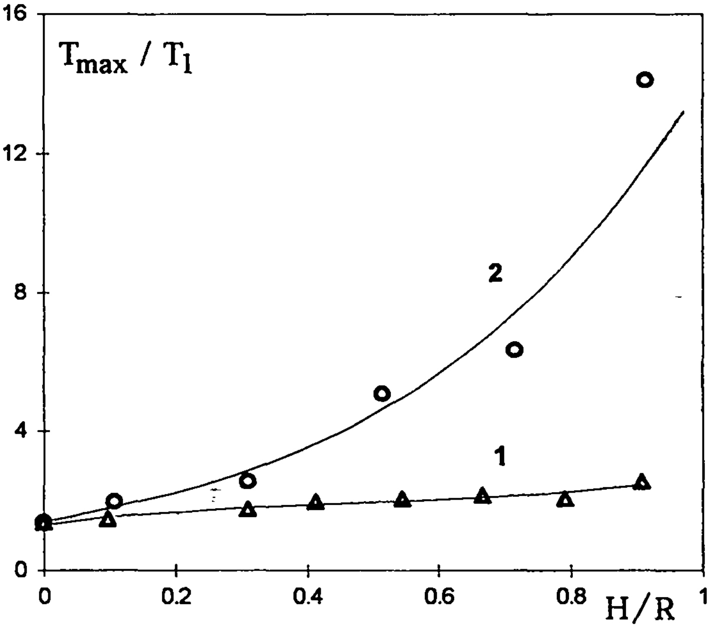

Fig.21. Ratio of maximum temperature T_{max} behind the reflected shock front to temperature T_l behind the incident wave front versus wall concavity. $\eta = H/R$ (R - curvature radius, H - cavity depth). 1 - reflection from cylindrical wall, 2 - reflection from spherical wall. Incident wave Mach number $M=1.27$.

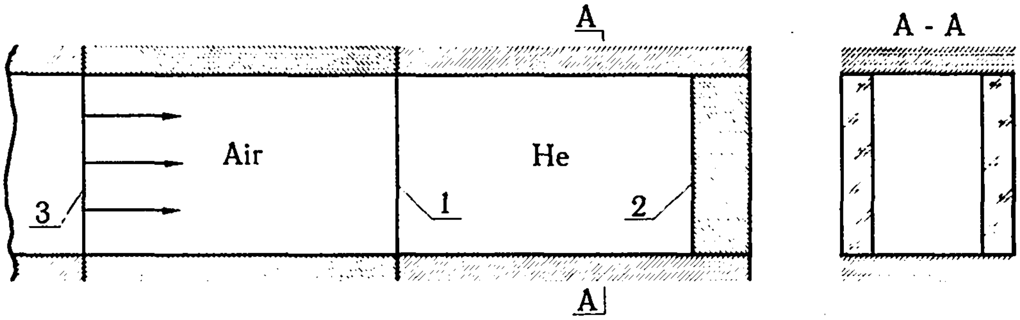

Fig.22. Experimental geometry to test turbulent mixing at shock-driven air-helium interface ($M=1.3$).
1-thin gas-separating film; 2- flat-faced plug; 3- shock wave.

2.3. STUDY OF TURBULENT MIXING GROWTH AT SHOCK-DRIVEN GAS-GAS INTERFACE

2.3.1. EXPERIMENTAL GEOMETRY

The experiments mostly employed horizontal shock tubes (Fig.2) based on the technique described in sections 1.2-1.3. Fig.22 illustrates the experimental setup. The measuring section channel was plugged with a flat-faced stopper at the end. The channel had a separation by thin flat film. The closed space towards the end of the channel was filled with helium. Its other portion was filled with air at atmospheric pressure. A plane steady shock wave was passing through the interface in the direction H-L(air-helium) to drive it. Once the shock reflected from the flat plug face serving as rigid wall, it passed then through the interface backwards to reflect from this and again from the wall and so on. In this way, a sequence of shock waves was made to pass through the interface (in L-H, or helium-air, direction), with their amplitudes successively decreasing. Step-by-step, these waves were damping the interface until it stopped moving at all.

The flow pattern was visualized using shadow [19,20] and laser knife [23] techniques.

There were some experiments using a vertical shock tube with the tests designed similarly to horizontal shock-tube experiments. In every case, the helium-filled space had 169 mm length.

2.3.2. QUALITATIVE PATTERN OF TURBULENT MIXING ZONE DEVELOPMENT. DEVELOPED TMZ STRUCTURE

Fig.23 shows photo frames to illustrate turbulent mixing. zone (TMZ) development at air-helium interface in horizontal shock tube experiments.

Immediately following its initial motion, the interface would smear as a result of small perturbations growing with their typical scale below the resolution limit of photography equipment. Originally, these perturbations arise from the film thickness variations (within ±50% of its average thickness) and very tiny shrinks of the film surface.

As observed, turbulent mixing zone would generate and develop, its image showing a cellular pattern typical of turbulent flow photographs. TMZ has irregular boundaries. These irregularities would increase in average size with time.

Fig. 24 shows the mixing zone photograph taken by scattered light. There is a well defined boundary between the air and the mixing zone. The air would enter the mixing zone as jets with their characteristic size increasing with time. Jet boundaries are smeared by K-H instability.

Once initial shock wave has passed, the gas-separating film disrupts into tiny pieces further rolling up in curls. This results in lower drag and, thus, less efficient deceleration of film pieces by the subsequent shock wave . Over time, the film curled pieces would go from the mixing zone to the lighter gas region (Fig.24).

Fig. 25 gives the experimental data from vertical shock-tube tests. Fig.25a illustrates the mixing pattern at the shock passing through a density discontinuity. In this case, the delay time from the plate removal to the shock arrival at the interface is short (t_{del}~2-13 ms). This is the time not enough for molecular diffusion to change substantially the density profile, therefore the gas-gas inter diffusion region may be considered as discontinuity. Following the shock wave passage the

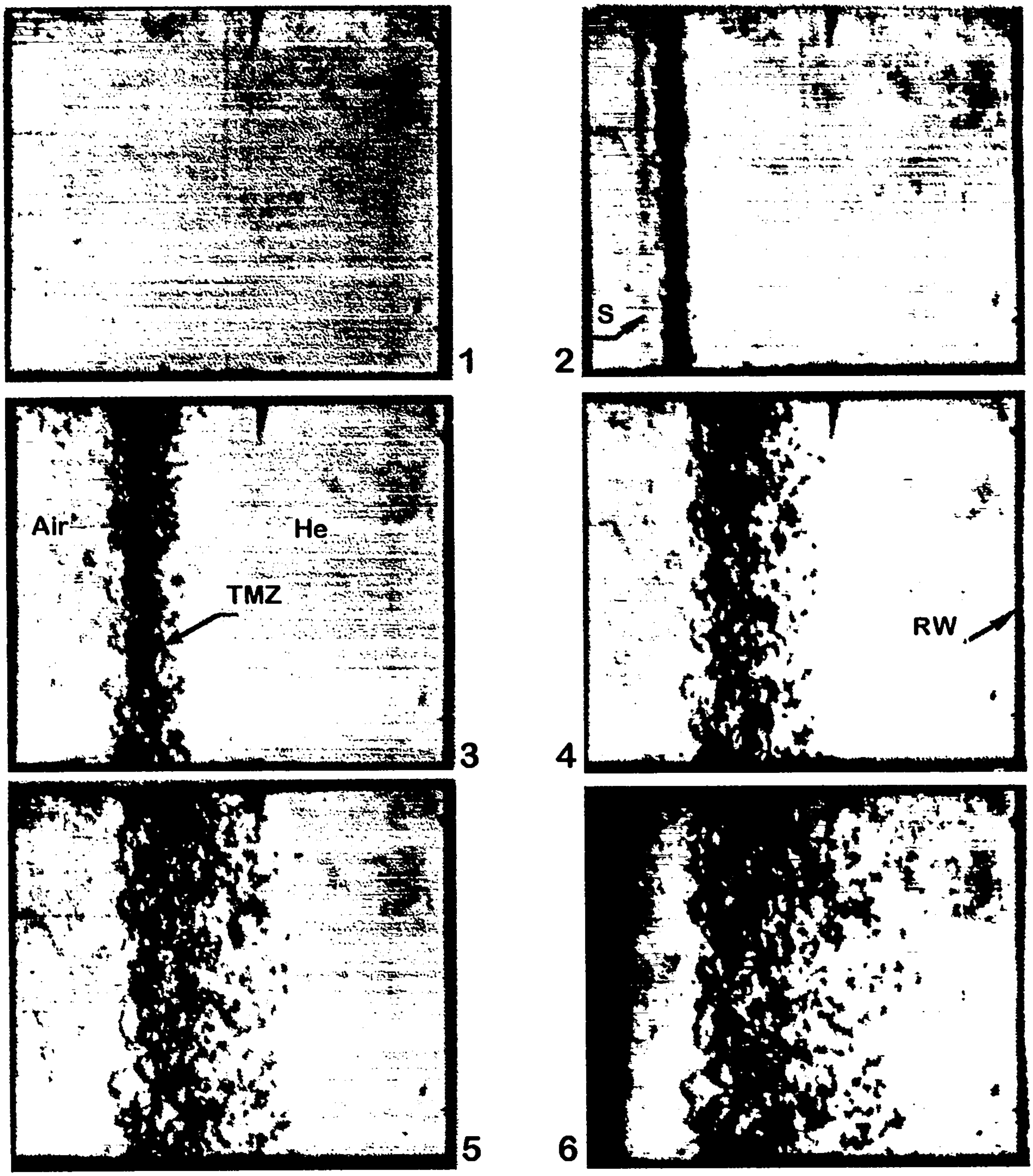

Fig. 23. Shadow graphs of turbulent mixing zone at Air-He interface, accelerated by the shock wave ($M=1.3$).

Time interval between frames $\Delta t = 160$ μs.

RW- rigid wall;

S - rigid wall reflected shock wave;

TMZ - turbulent mixing zone.

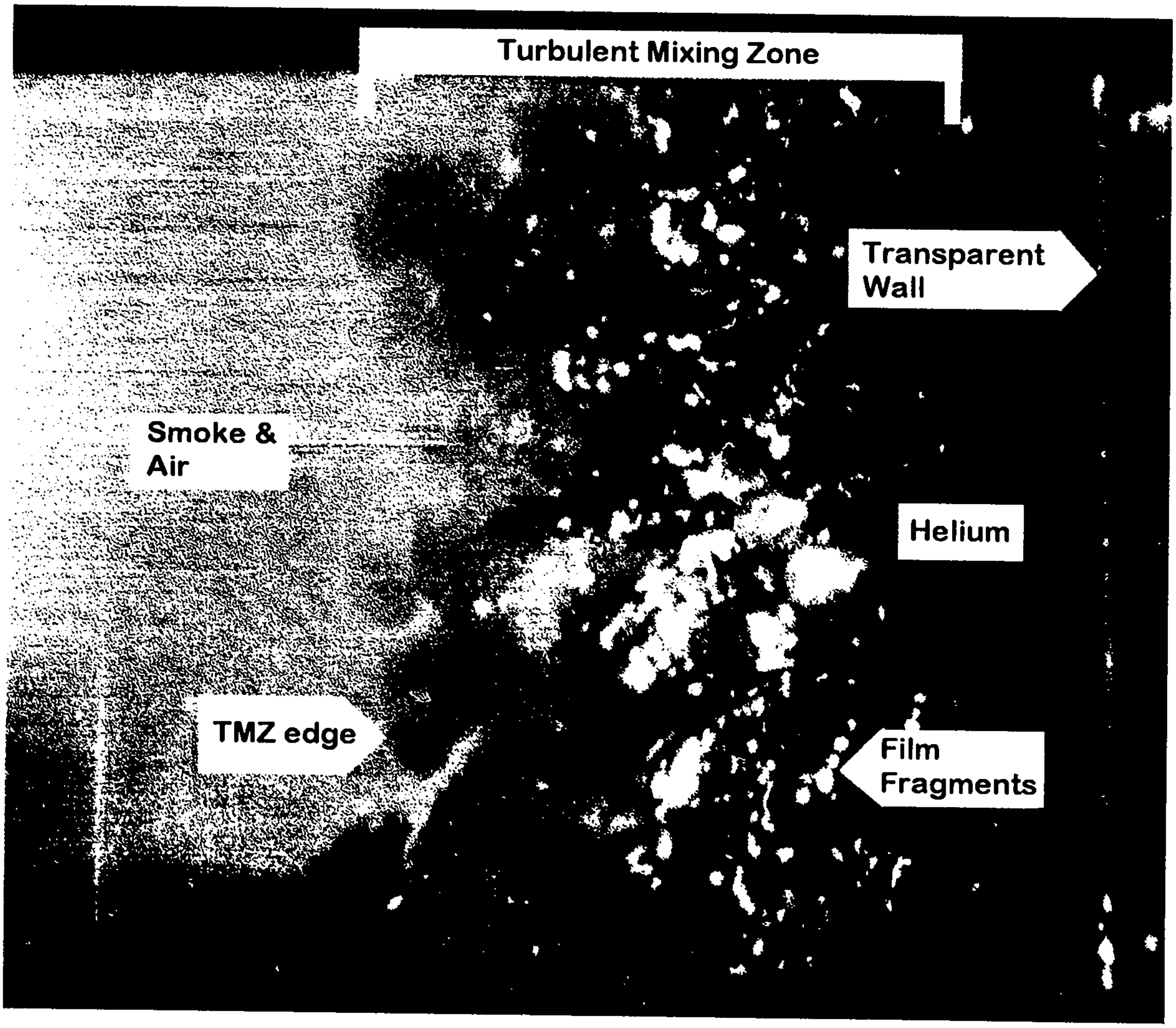

Fig. 24 Photo of the mixing zone at smoked Air-He interface in scattered light. Laser beam crosses chamber from left to right.

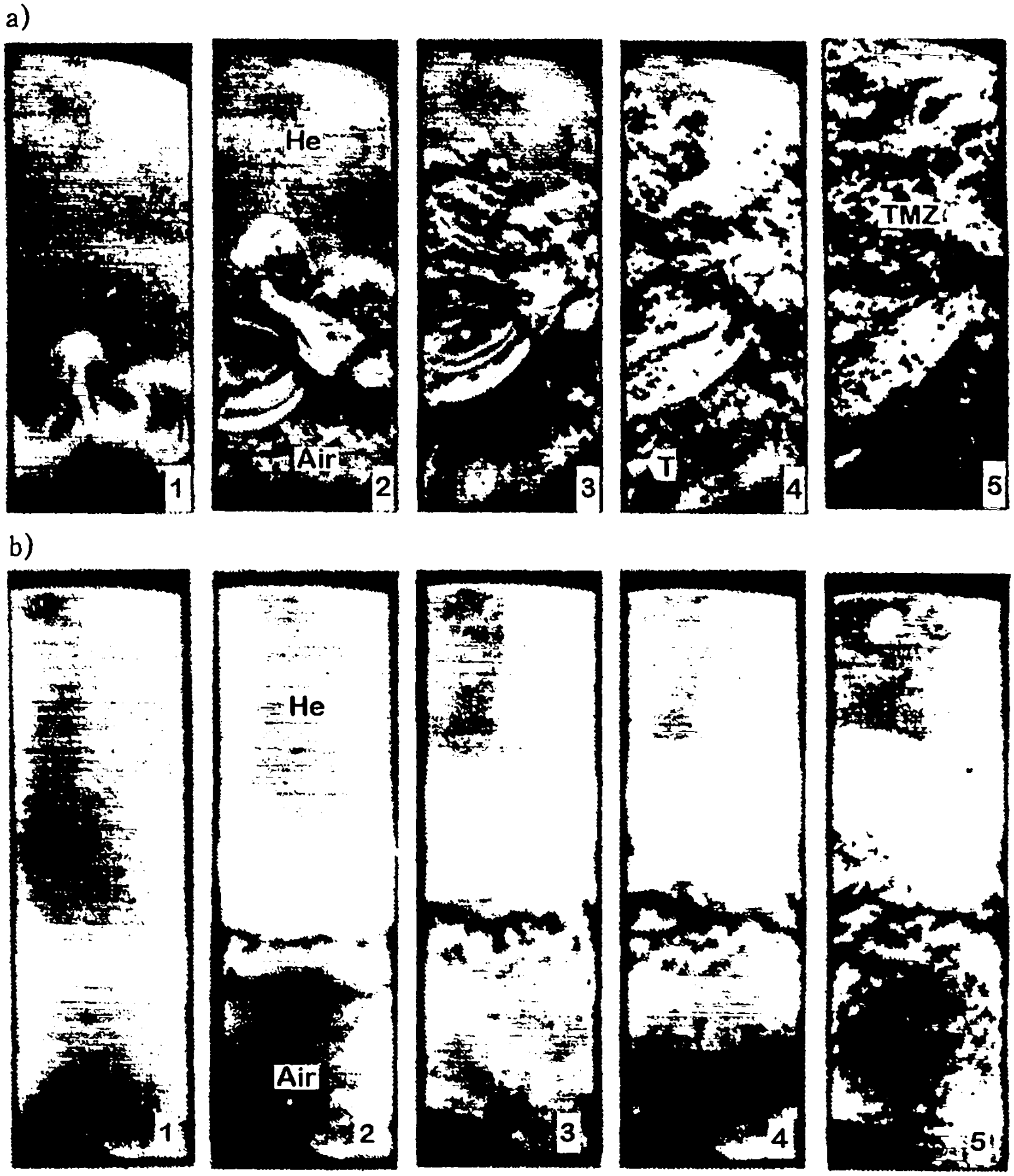

Fig. 25 Turbulent zone development in vertical shock tube experiments:
a) time delay $t_{del}\sim 2\div 13$ мс;
b) time delay $t_{del}\sim 1$ с.
TMZ - turbulent mixing zone; T - "train".

interface becomes very much perturbed, so that the perturbation amplitude exceeds the gas-gas inter diffusion zone. Later this perturbations growth would result in the turbulent mixing zone development.

For long delays in shock front arrival t_{del}~1s (Fig.25b), the molecular diffusion has enough time to form a thick layer with the density smoothly changing from helium to air density. This layer having distributed density causes the perturbations to grow slower, and delays the TMZ formation. The stabilizing effects of this transitional density layer on R-T instability development have been pointed out in [95].

2.3.3. EXPERIMENTAL RESULTS

Fig. 26 compares the averaged results for 9 horizontal shock-tube experiments with shadow techniques used to observe mixing, and those of similar set of experiments involving laser knife technique, with calculations using VIKHR code.

The mixing zone thickness at a fixed time is shown to vary from test to test, due to initial perturbations caused by film disruption, being different in amplitudes. However, the thickness growth rate, particularly at later times, shows virtually the same for all tests. Numerical calculations are consistent with the experimental data.

Photometry of the negative image from one of laser-knife experiments has provided data to evaluate relative air distribution in the mixing zone. (Fig.27).

Fig.28 gives TMZ thickness vs. time, L~f(t), obtained by both horizontal and vertical shock-tube experiments for various visualization techniques. Laser-knife measurements show somewhat smaller L(t) values than the shadow technique.

Vertical shock tube experiments performed for short delay time t_{del}~2-13 ms, have observed the mixing zone thickness to be slightly in excess of that in the experiments using film techniques, though there is virtually no difference in TMZ growth rate.

2.3.4. TMZ DEVELOPMENT DUE TO SHOCK-WAVE PASSAGE

When a shock-wave is passing through the turbulent mixing zone, its thickness growth is observed to be more rapid. Let us consider some qualitatively possible mechanisms that may result in this effect. The perturbations amplitude at the interface between heavier gas and TMZ is not small, being of the order of the mixing zone thickness. As shock wave passes, there develops Kelvin-Helmholtz instability that should cause mushroom-shaped structures such as vortex zones at the jet tips, to form and develop more vigorously.

Moreover, another mechanism may be also of important contribution. There occur density fluctuations in the mixing zone, i.e. inclusions of lighter or heavier gases adding to the mean density level of the environment. Reportedly [91], shock wave passing through the gas added by lighter inclusions makes the latter accelerate to higher velocities than that of the environment. Also, heavier inclusions, as average, should lag behind the environment. Thus, shock wave passing through the turbulent mixing zone should result in the tendency for heavier gas inclusions to move towards the lighter gas and vice versa. These inclusions being shock-accelerated, this results in vortex rings additionally forming [92].

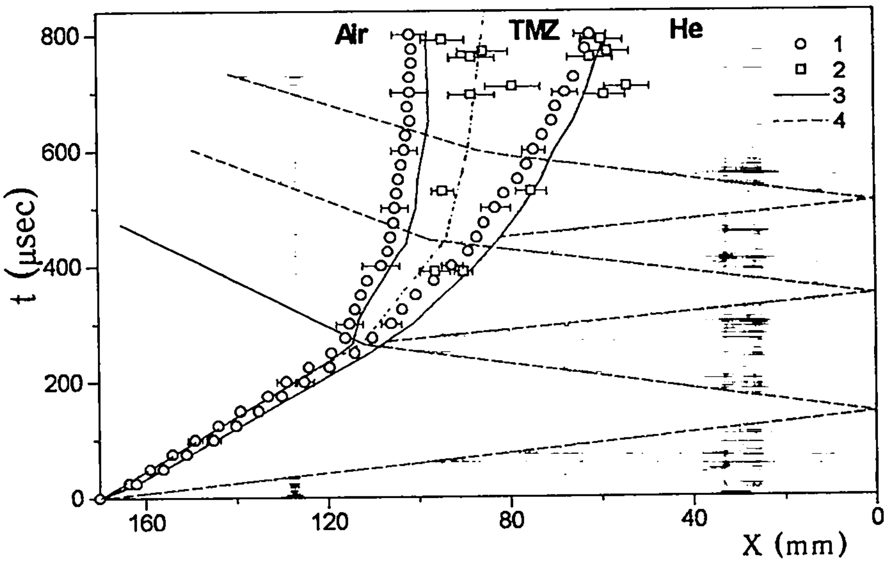

Fig.26. Flow x-t diagram in experiments using geometry as shown in fig. 22. Points- experimental results: 1- shadow technique; 2- laser knife. Solid curves- VIKHR calculations. Dashed and dot-dash lines - interface and shock-waves trajectories, respectively, calculated without turbulent mixing involved.

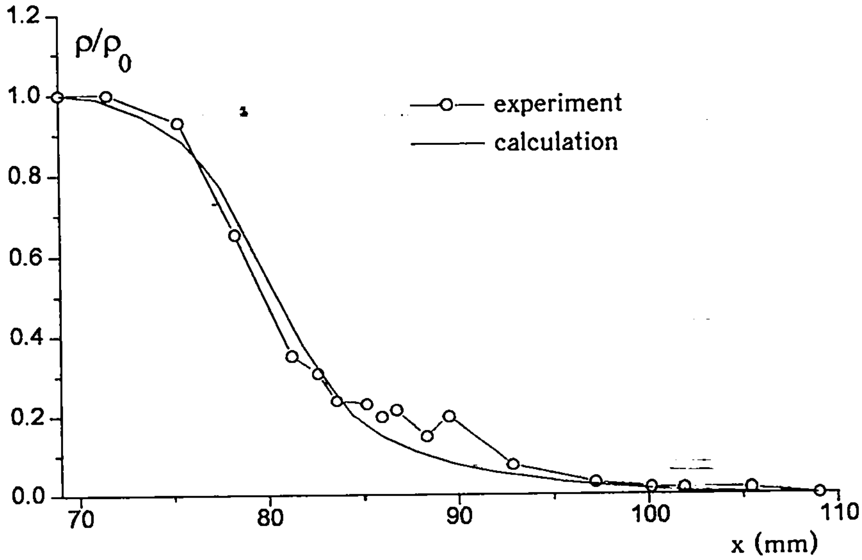

Fig.27. Averaged relative air density distribution in the mixing zone. The distance x is taken from the initial position of air-helium interface. 1- VIKHR calculations; 2 - experiment.

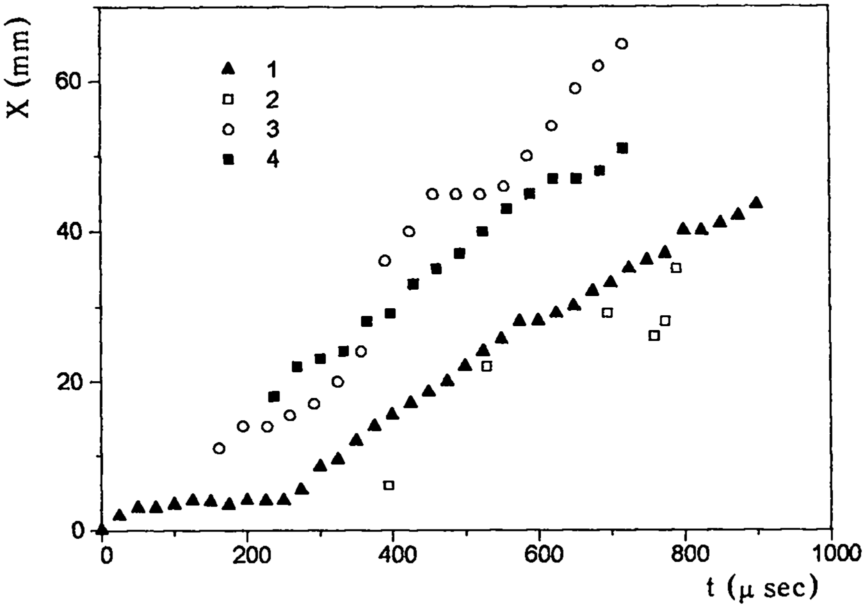

Fig.28. TMZ thickness vs. time for horizontal and vertical shock-tube experiments using different measurement techniques.

Horizontal shock-tube experiments with thin-film gas separation.

1 - data obtained by shadow technique and averaged for 9 experiments (system sensitivity is below critical);

2 - laser knife measurements (each point represents an individual experiment);

3 - shadow visualization, for sensitivity above critical value;

4 - vertical shock-tube experiment, for short time delay $t_{del} \approx 2 \div 13$ ms.

2.3.5. FILM CONTRIBUTION TO TMZ DEVELOPMENT

For the experiments of interest, a film variable in thickness used to separate gases, represents a source of additional small-scale perturbations. Homogeneous elastic film may also act as stabilizer to suppress the development of instabilities at an earlier stage, when its mass is comparable to the mixing zone gas mass. Basically, this is what may be responsible for the discrepancy between the data from experiments [40] and VNIIEF experiments.

When the first reflected shock wave has reached the interface with the mixing zone thickness then exceeding ~5-10 mm, the condition (2) is satisfied, and thus the film has virtually no effect on the flow any longer.

2.3.6. SHOCK-TUBE WALL EFFECTS ON THE OBSERVED TMZ EVOLUTION PATTERN

TMZ has its edge decelerated due to friction near the shock tube walls, thus lagging behind the whole zone to form a train which is observable in the photographs of Fig.25a. Under certain conditions, this train is likely to cause problems with the visualization of the whole zone by shadow photography, and even screen it off completely, if a shadow system is not adjusted properly.

A special study has been carried out on how shadow system sensitivity affects the TMZ thickness to be measured. The shadow system sensitivity was varied over a wide range by varying the light source size and position and knife withdrawals (see section 1.7).

As shown by these experiments, with the shadow system sensitivity being varied from minimum to some critical value, the TMZ thickness measured was almost unchanged. However, for sensitivity higher than this critical value the TMZ thickness became about twice as large.

The above-discussed data from TMZ thickness measurements were obtained for sensitivity predetermined lower than critical.

For comparison, Fig.28 shows TMZ thickness vs. time measured with the system having sensitivity above critical value, for the case where the train screens the mixing zone off.

2.4. INVESTIGATIONS OF THE PERTURBATIONS GROWTH OF GAS-GAS INTERFACE ACCELERATED BY CONVERGENT CYLINDRICAL SHOCK WAVE

2.4.1. EXPERIMENTAL GEOMETRY

Experiments to study perturbations growing at the interface between two gases (air-helium and air-freon-12) accelerated by convergent cylindrical shock wave, were conducted using electro-explosively-driven cylindrical shock tube [59].

A unperturbed interface was located at a radial distance $R_0=5.5$ cm. The interface perturbation geometry was specified as $R=R_0+\Delta_0/2\ \cos(n\varphi)$.

Initial perturbations amplitude was $\Delta_0=0.1\lambda$, or $\Delta_0=0.15\lambda$, where $\lambda_0=2\pi R_0/n$. The experiments were conducted for the values n=4,6,8.

2.4.2. NUMERICAL MODEL TO DESCRIBE GASDYNAMIC FLOWS IN THE EXPERIMENTAL SETUP

The data from test experiments (Section 2.4.3) were used to select a simple numerical model to describe adequately the dynamics of 1D flows in cylindrical shock tube within the time $t<150$ μs after the motion started.

Figure 29 is an illustration of the numerical model geometry.

To simulate the gases produced by electroexplosion, an ideal gas was taken having density $\rho_0=2.2\ 10^{-3}\ \mathrm{g/cm^3}$ and adiabatic index $\gamma=5/3$, that would fill I-region $9.75\mathrm{cm}<R<10$ cm. Initial gas pressure was specified equal to 4.56 MPa.

The other regions all were air at atmospheric pressure. The air is described by the equation of state of ideal gas having $\rho_0=1.205\ 10^{-3}\ \mathrm{g/cm^3}$ and $\gamma=1.405$.

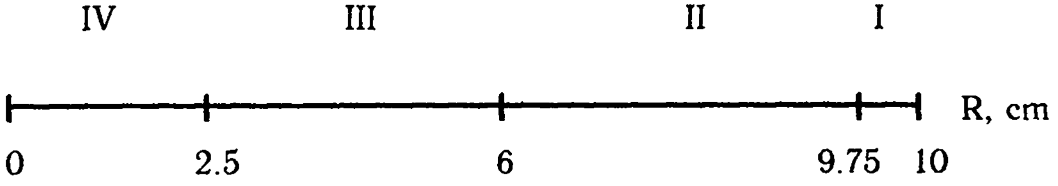

Figure 29. Geometry of the numerical model to describe flow dynamics in electroexplosive cylindrical shock-tube test experiments.
Region I - ideal gas; Regions II, III, IV - air
Interface at R=10 cm is unmoved.

2.4.3. TEST EXPERIMENTS

Figure 30 shows the calculated R-t diagram of shock front motion and R-t diagrams for Lagrangian boundaries initially located at radial distances $R_{01}=6$cm and $R_{02}=2.5$cm. For comparison, the figure also shows the respective results obtained by the test experiment. The time here and further is counted off the wire explosion.

To visualize Lagrangian boundaries in the experiment, a thin organic film was placed at the above-mentioned radii. As shown by the diagram, the numerical scheme describes rather well the flows for $t<150\mu$s.

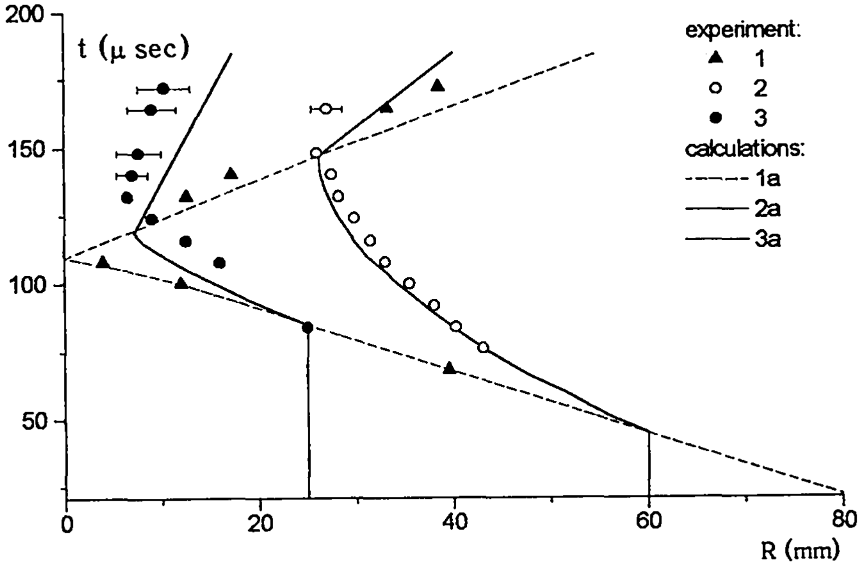

Fig.30. R-t diagram for shock wave front (1, 1a) and Lagrangian boundaries (2, 2a, 3, 3a) motions in test experiment (R_{01}=60mm and R_{02}=25mm).

2.4.4. INVESTIGATION RESULTS

Figure 31 shows photo frames for two experiments to investigate the instability development at air-helium and air-freon12 interfaces.

The imaging system field of view is shown to cover the experimental setup image only in part. The frame edge is indicated with a dashed line in the figure.

For the first case, a converging shock wave S_1 crosses interface I from heavier (air) to lighter (helium) gas. Initially, the interface perturbations amplitude changes its sign to the opposite and then increases monotonously with time. Once the shock wave S_2 reflected from the center has crossed the interface, the perturbations amplitude growth becomes more rapid. Moreover, heavier gas protuberances virtually go as far as the center to link up there.

Qualitatively, the evolution of the interface pattern is similar to that observed in the plane case (Section 2.2). Heavier gas protuberances become more narrow to transform into jets with vortex flows occurring at their boundaries.

For the other case, where the inner space is filled with freon-12, the convergent shock wave passes through the interface from lighter to heavier gas.

Initially, the perturbations amplitude decreases due to the gases being compressed by the shock wave. Following this, the amplitude increases and yet before the center-reflected shock-wave has reached the interface, again it goes down to zero to change its sign. In other words, the perturbation has time to do approximately one oscillation. The above-described process involves smearing boundaries due to the turbulent mixing associated with small-scale perturbations growth.

In first-case experiments, this mixing is the more observable.

Figure 32 shows R-t diagrams obtained in air-helium experiments, compared against the numerical data. Time reference for the calculated and experimental data was controlled by matching the points specifying the location of a convergent shock front. In this case, the interface location measurements are observed to be in good agreement with gasdynamic calculations. Like plane case, the perturbations growth observed is of asymmetric kind.

Perturbations amplitude measurements are illustrated in Figure 33 for harmonics of numbers $n=4,6,8$. Δ is the perturbations amplitude defined as the distance between the points of the interface, the most distant and the least distant from the center. As shown by the experiments, higher n perturbations have comparatively more rapid growth.

Figure 34 shows R-t diagrams of shock front and interface motions in air-freon 12 experiments. Rather good agreement between the calculated and experimental data is observed up until $t=200$ μs.

Perturbations amplitude measurement data are shown in Fig.35. Like air-helium case, the diagram has its initial portion obtained numerically. Later, the perturbations growth depends on the distribution of higher-pressure and lower-pressure regions. Shock compression of gases is followed by perturbations starting to grow as in the plane case. The initial momentum effects decrease rapidly. The acceleration direction is from heavier to lighter gas, and the interface is made stable. As a result there occur forces decelerating the perturbations growth and leading to the further decrease of its amplitude yet before the center-reflected shock wave reaches the interface.

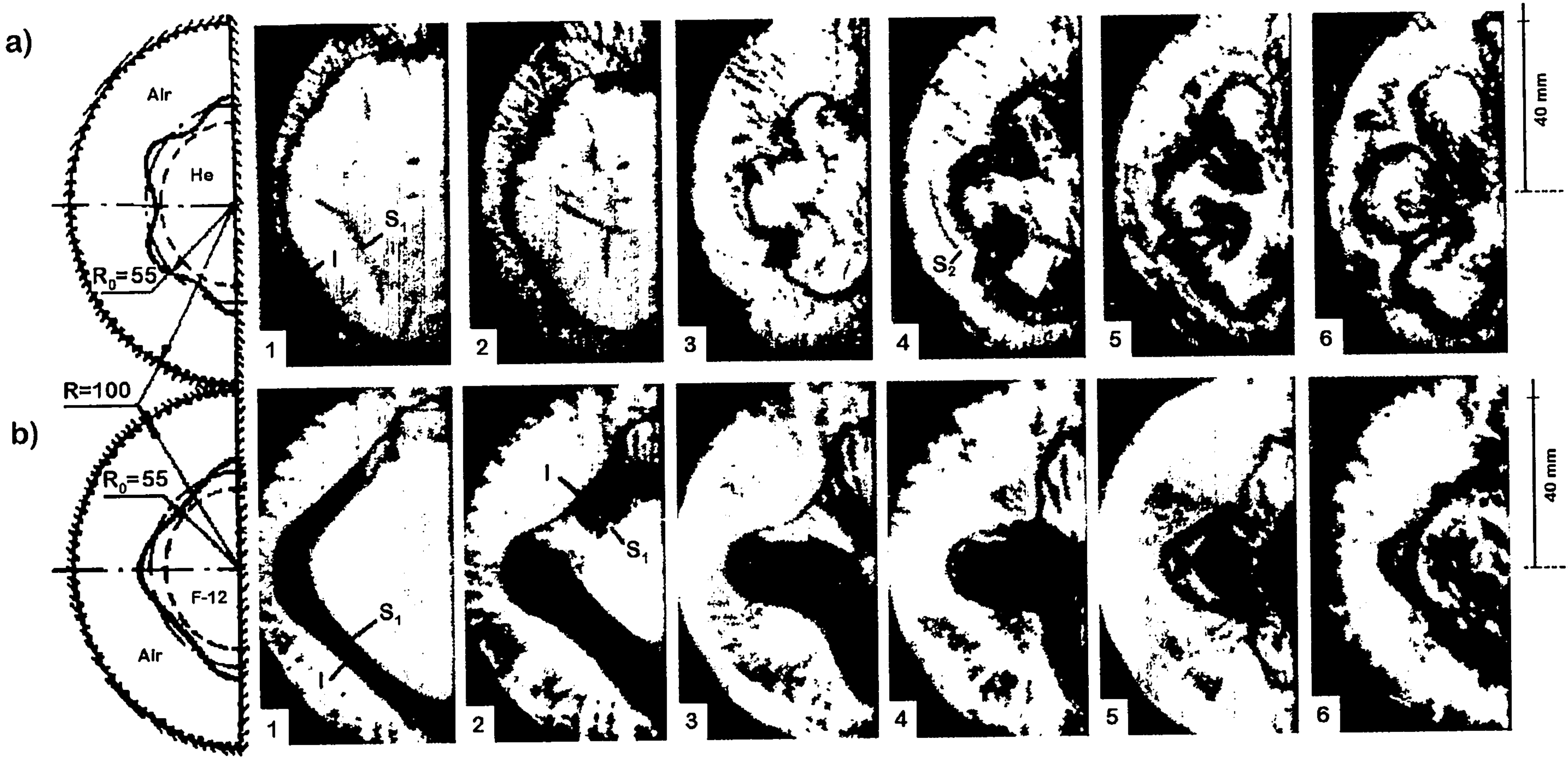

Fig. 31 Photochronogramm of the two cylindrical shock tube experiments.:
a) Air - He, n=6, Δ_0/λ=0.15, time interval between frames - $\Delta t = 12\ \mu s$;
b) Air-Freon-12, n=4, Δ_0/λ=0.1, time interval between frames - $\Delta t = 32\ \mu s$.
I - interface; S_1 - converging shock wave;
S_2 - reflected shock wave.

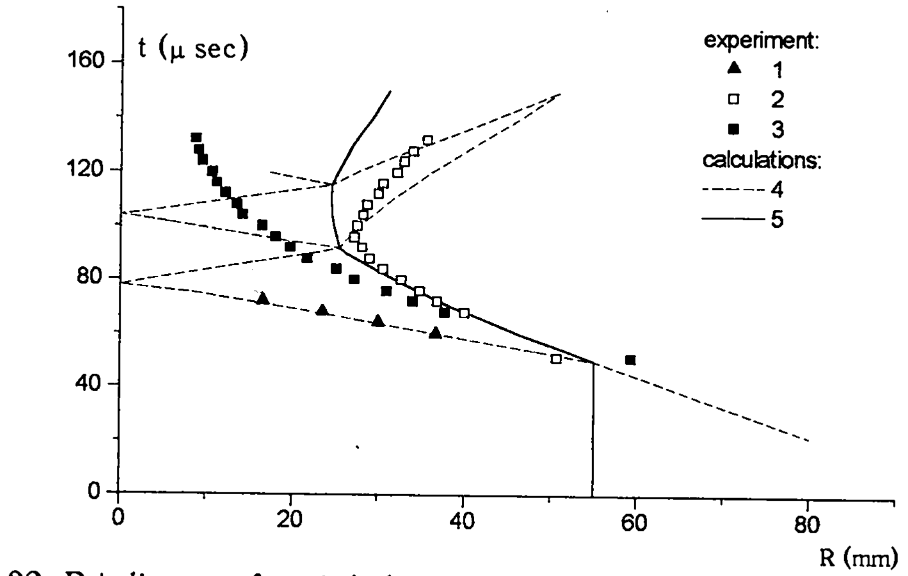

Fig.32. R-t diagram for air-helium experiment.
1 - shock wave front; 2 - bubble tops; 3 - jet ends.
Calculations done in plane geometry (see Fig.29):
4 - shock wave front; 5 - interface.

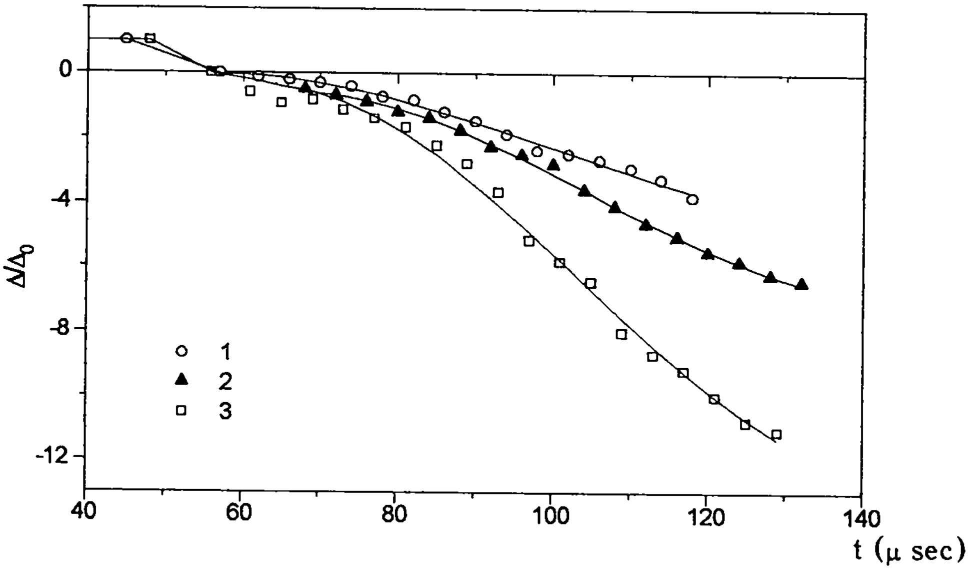

Fig.33. Interface R-t diagram for air-helium experiment.
1 - n=4, $\Delta_0/\lambda=0.1$; 2 - n=6, $\Delta_0/\lambda=0.15$; 3 - n=8, $\Delta_0/\lambda=0.1$.

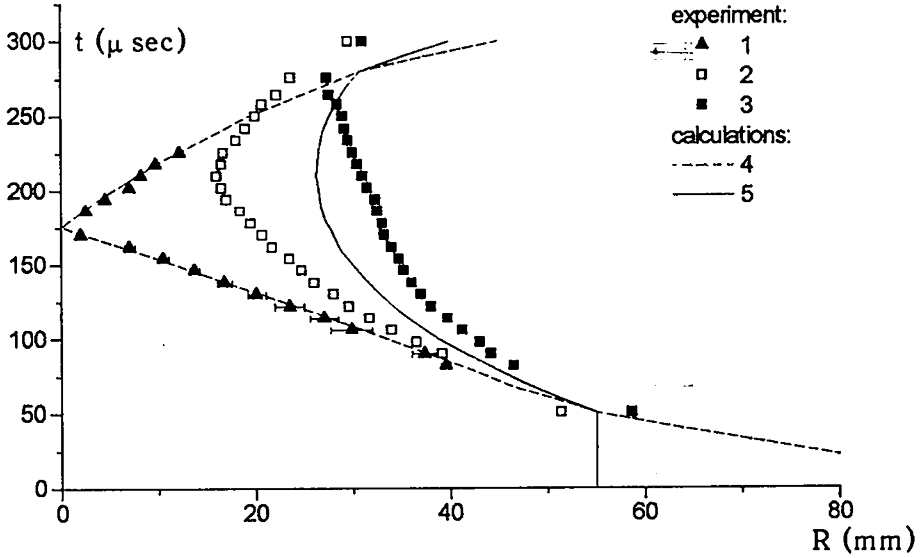

Fig.34. R-t diagrams for air and freon-12 experiments.
1 - shock wave front; 2 - bubble tops; 3 - jet ends.
Calculations done in plane geometry (see Fig.29):
4 - shock wave front; 5 - interface.

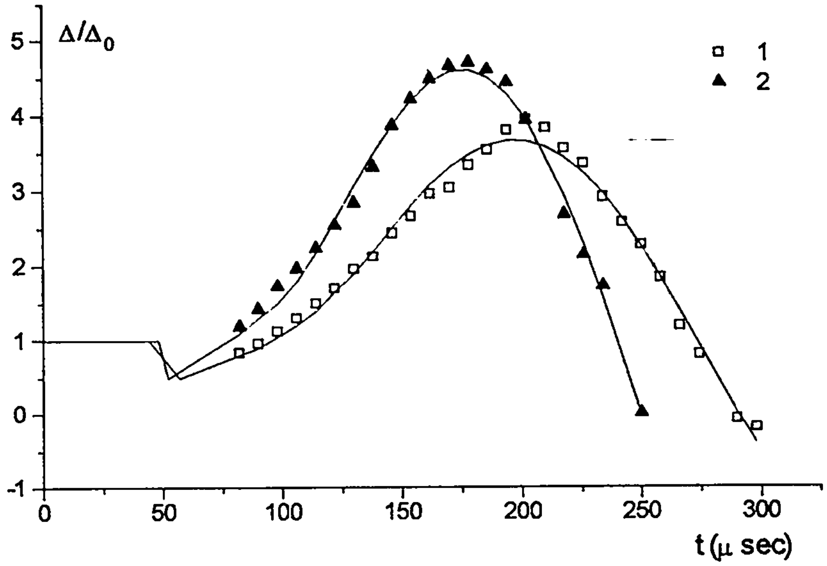

Fig.35. Perturbations amplitude vs. time for air - freon-12 experiments.
1 - n=4, $\Delta_0/\lambda=0.1$; 2 - n=8, $\Delta_0/\lambda=0.1$.

2.5. INVESTIGATION OF TURBULENT MIXING DEVELOPMENT AT GAS-GAS INTERFACE ACCELERATED BY CONVERGENT CYLINDRICAL SHOCK WAVE

2.5.1. EXPERIMENTAL GEOMETRY

The experiments were performed using an electroexplosive shock tube described in Section 1.4. TMZ development at gas-gas interface accelerated by convergent shock wave was investigated mostly in application to air-helium case [20]. There were some experiments to test the mixing at the air-hydrogen interface. All experiments had the gas interface located at a radial distance R=6cm.

2.5.2. QUALITATIVE AND QUANTITATIVE VISUALIZATION OF TMZ DEVELOPMENT

Fig.36a shows photographs for air-helium experiment. Initial perturbations are relatively regular, representing pressure fluctuations behind the convergent shock front resulting from discontinuous energy release.

The characteristic amplitude and wavelength of the TMZ boundary perturbation increase monotonously with time. At an earlier stage, the wavelength is $2\pi R/180$ (where R is the current radius of the inner TMZ boundary) and determined by the number of exploding wires (90). At times near to the highest helium compression, the characteristic wavelength increases to $\sim 2\pi R/10$ (Fig.37).

The effects of any initial perturbation types on the TMZ development pattern are illustrated by streak photographs for air-hydrogen experiment (Fig.36.b-d).

Fig.36.b shows a photographs for the experiment where wire-induced small-scale perturbations were superimposed by localized perturbations. To this end, there was a steel cylinder 0.6 cm in diameter used as rigid barrier to be placed in the way of convergent shock wave at the radius R=8.2 cm.

In this situation, the perturbed shock wave can be represented as superposition of two waves: the primary convergent wave and the divergent shock wave generating two transverse waves that move in opposite directions from the barrier location. There is a low-pressure region between the transverse waves. The front inflection is observed where these waves intersect with the primary shock front.

The boundary portion between the transverse waves moves ahead, while the portions in front of these lag behind. At subsequent times, where this perturbation was located, there develops a turbulent zone thicker than other boundary portions.

Importantly, this experiment observed no TMZ development until the center-reflected shock wave reached the interface ($t<85$ μs), this being due to the flow stability.

When $t>85$ μs, there begins the interface deceleration, this making it unstable. This is the way TMZ development proceeds.

Fig.36c shows an experimental photographs to illustrate the effects of the separation film thickness on TMZ development. This experiment used double film layer applied to three interface areas. The initial exposures show the interface somewhat lagging at these locations. With further TMZ growth, this perturbation becomes insignificant.

For the experiment illustrated by Fig.36d, initial perturbation was not specified, but it occurred accidentally as a result of secondary breakdown between

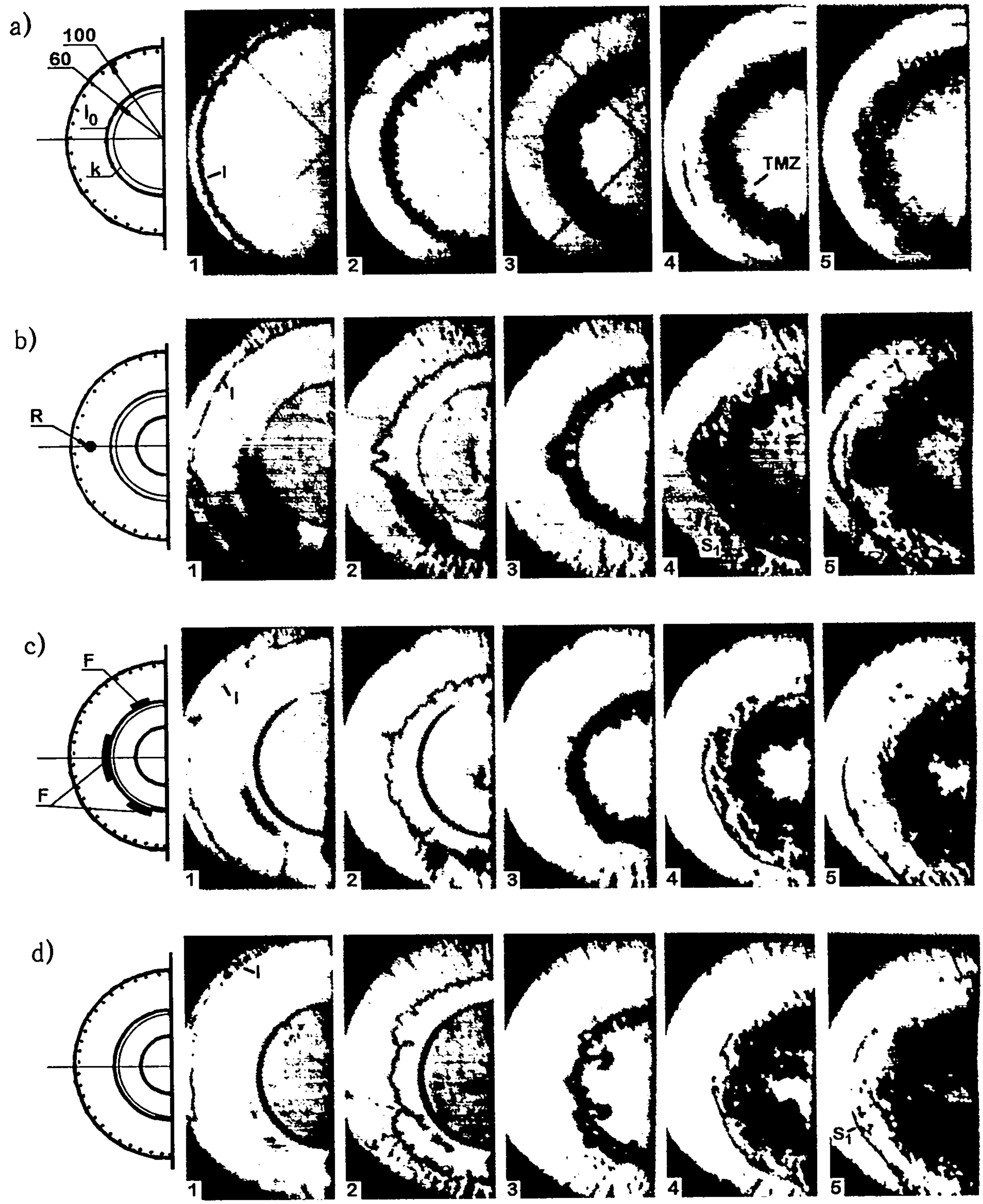

Fig. 36 The perturbation and turbulent mixing development at the cylindrical interface, accelerated by converging shock wave.

a) Air-He without initial perturbation;

b), c), d) Air-Hydrogen:

b) perturbation due to the steel rod - R; c) perturbation due to local film thickness increase - F; d) random perturbation. I_0, I - initial and current interface locations, S_1 - shock wave reflected from the center, k - frame boundary. Dimensions are in mm.

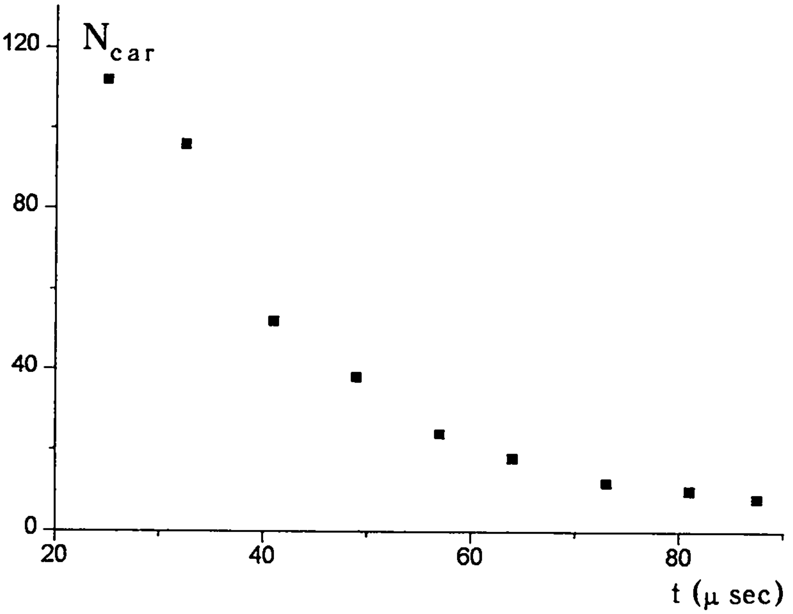

Fig.37. The number of dominant perturbation mode n* of the TMZ boundary versus time in air-helium experiment (fig.36.a).
Time counted from the shock wave arrival at the interface.

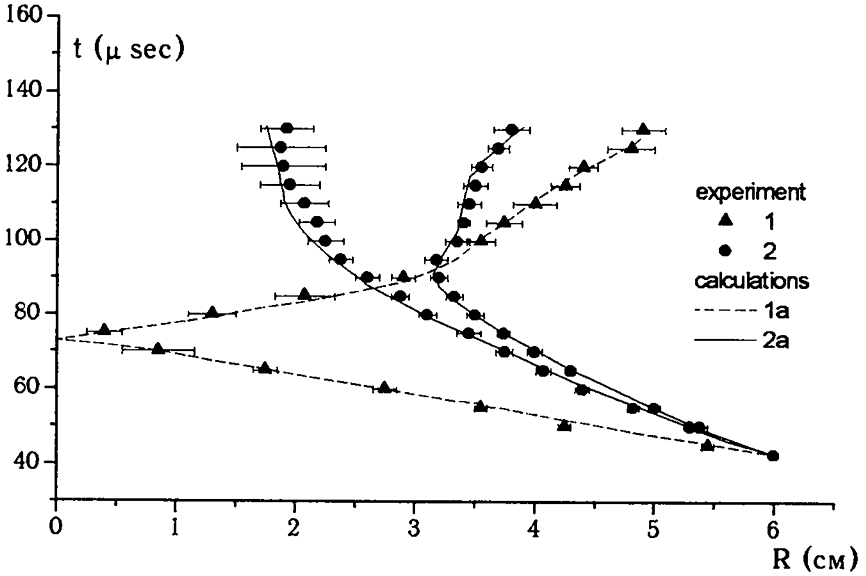

Fig.38. R-t diagram of the shock wave front (1, 1a) and TMZ boundaries (2, 2a) in air-helium experiments.
Solid and dashed lines - VIKHR code calculations.

the electrodes 3 (Fig.4) following the discharge current pause. This flow can be represented as the superposition of the primary convergent shock wave S_0 and divergent perturbation waves (transverse shock waves S_1). There is an inflection observed at the crossing point of the perturbation wave front and the primary wave front. It is these wave intersection points that cause the largest perturbations, with narrow substance jets to form subsequently in their neighborhood. The jet tips move substantially ahead of the other boundary portions. These perturbations also retain their effects with further TMZ development.

2.5.3. INVESTIGATION RESULTS

Fig.38 shows R-T diagrams of shock wave front and TMZ boundaries, obtained by averaging 9 typical air-helium experiments. For comparison, also included are VIKHR calculations for these experiments.

Shock front and TMZ boundary radii were found by averaging the measurements over 30-50 rays drawn from the center of symmetry. Root-mean-square deviation in radii is due to TMZ boundary irregularities, and determines the statistical measurement error.

Good agreement is observed between the experimental and calculated data.

2.6. INVESTIGATION OF LOCALIZED PERTURBATIONS GROWTH AT THE INTERFACES OF ACCELERATED LAYERS AND SHELLS

Experimental investigations of perturbations growing at the interfaces between liquids of different densities or liquid-gas interfaces, mostly use the technique [5]. By this technique, a vessel containing liquids is to be driven vertically downwards, and thus the initially stable interface is made unstable. This is the way the perturbations growth and turbulent mixing at the plane interface are investigated. Initial perturbations are predetermined as a standing wave generated by an oscillating object submerged into liquid [6].

More opportunities offers the technique to simulate nonstationary fluid flows using jellies [60-63, 35]. This helps investigate instabilities both in plane [61] and cylindrical case (including expanding [60] and converging shells [63]), and even for plane layers having inflected surfaces [62]. The technique may have initial perturbations of virtually any configuration predetermined at the interface. Moreover, the use of explosion gases of the gas explosive mixture (GEM) as driver allows initial perturbations to be generated as pressure nonuniformities.

2.6.1. EXPERIMENTAL DATA FOR ACCELERATED PLANE JELLY LAYERS HAVING CAVE-LIKE SURFACE PERTURBATIONS

A jelly layer 1.9 cm thick had initial perturbation predetermined on its unsteady surface as hemispherical concavity of the radius R=0.5 cm (Fig.39). The layer was driven by GEM ($C_2H_5+2.5O_2$) explosion products through the square-shaped channel of 4x4 cm^2 size. GEM layer was 3.4 cm thick. The experimental technique is described in detail in Section 1.6 (Fig.6).

Fig.40 shows photographs of the experiment. One can see the lower boundary of the layer become unstable. There occurs jelly mixing with the explosion gases, observed in the figure as darker rough-edged layer.

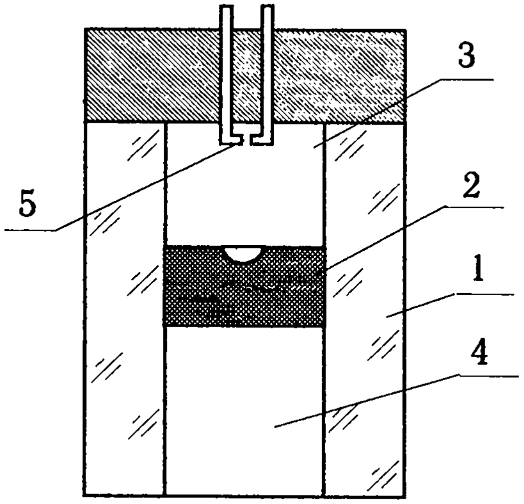

Fig.39. Experimental device to investigate cavern shape local perturbation growth at unstable jelly layer interface accelerated by gas HE products.

1 - transparent walls of the channel;
2 - jelly layer;
3 - gas HE (C_2H_2+2,5O_2);
4 - air;
5 - spark gap.

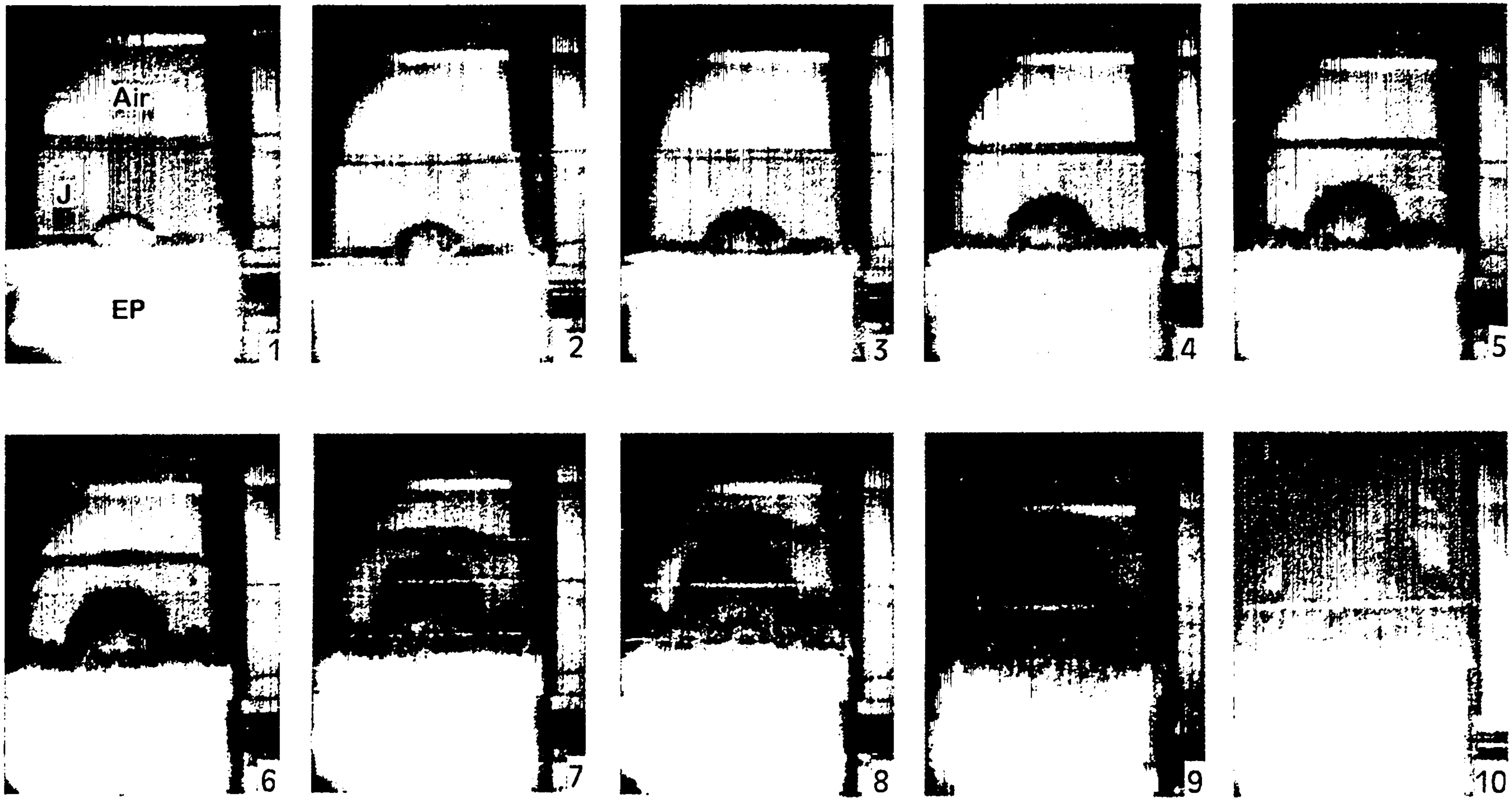

Fig. 40 Semispherical local perturbation growth at unstable jelly interface, accelerated by gas HE products.
J - jelly layer, EP - gas HE products.

The cave vertical and horizontal dimensions also increase with time. Unlike asymptotic stage in periodic perturbations growth with the bubble dome rising up at a constant velocity, the cave dome in this situation is moving at a constant acceleration. By the same law, the cave will also change its cross dimensions.

TMZ boundary perturbations grow in amplitude. However, over time its growth pattern changes. The perturbations at the plane surface continue growing, while their growth no longer proceeds where the surface is hemispherical. At latest flow stages, the cave dome is found smooth. Furthermore, no perturbations exist on its surface any more.

2.6.2. EXPERIMENTAL DATA FOR ACCELERATED PLANE JELLY LAYERS WITH SHOCK- AND DETONATION- INDUCED PERTURBATIONS

The experiments described below involved jelly surface perturbations generated by varying the number and spacing of GEM initiation points. This provided variations in the spatial interference pattern of detonation and shock waves and, consequently, in the acceleration dynamics variation for the layer earlier in its motion.

The experimental geometry is similar to that described in the previous Section except that no specific perturbations have been predetermined at the jelly surface.

The flow pattern was visualized both in transverse (through the transparent side walls) and front projections (through the jelly from the opposite to its motion).

Fig.41 shows photographs of frontally visualized GEM initiations

a) at a single point in the bottom center of the chamber;

b) with a line of 8 spark gaps positioned along the bottom of the chamber;

c) at 4 points symmetrically located in the square corners near the bottom.

The first frames show EP (explosive products) luminescence in the vicinity of the initiation points. Further frames illustrate the perturbations growth pattern at the unsteady surface showing itself as distinctive bubbles forming. Their disposition symmetry corresponds to that of the initiation points. The observed perturbations pattern is well reproducible from test to test.

Most vigorously the bubbles grow at points corresponding to intersection with the layer surface of the encounter front of detonation and secondary shock waves.

For single-point GEM initiation (Fig.41.a), there forms a central bubble on the unstable surface, having near-spherical shape, which penetrates into the jelly layer at acceleration. The bubble top moves faster than the turbulent mixing zone boundary. Together with this central bubble, smaller bubbles are observed to grow, located symmetrically in diagonals and rays directed from the surface center of the layer parallel to the chamber walls.

For GEM initiation by 8 points in a straight line, the occurrence of semi-cylindrical cave is observed (Fig.41b).

More intricate bubble arrangement is observed in Fig.41c, where GEM initiation was performed at 4 points.

Fig.42 shows the central bubble lateral dimension D as a function of the distance S covered by the layer (single initiation point experiment). It is clear, that $D \approx 0.7S$, i.e. the bubble should float up at velocity increasing in proportion with time. At later times, there will become more significant spatial limitation due to the proximity of the channel walls, and dD/dS will decrease.

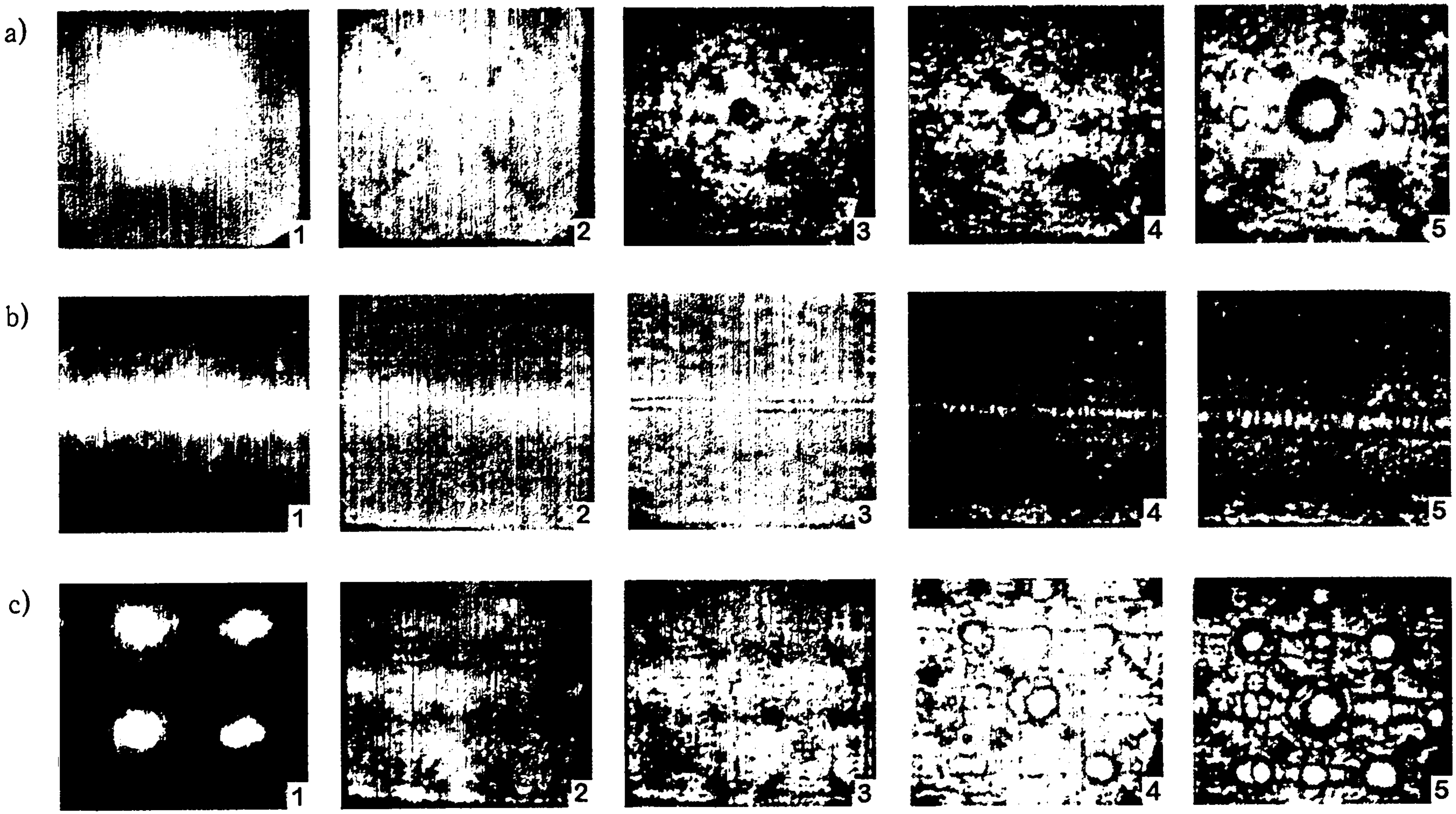

Fig. 41 Photochronogramms of the liquid layer accelerated by gas HE products (frontal projection). Perturbations grow at unstable interface.

a) HE detonation initiation at the center of the chamber bottom.
b) HE detonation initiation in 8 equal spaced points along straight line.
c) HE detonation initiation in 4 square corners.

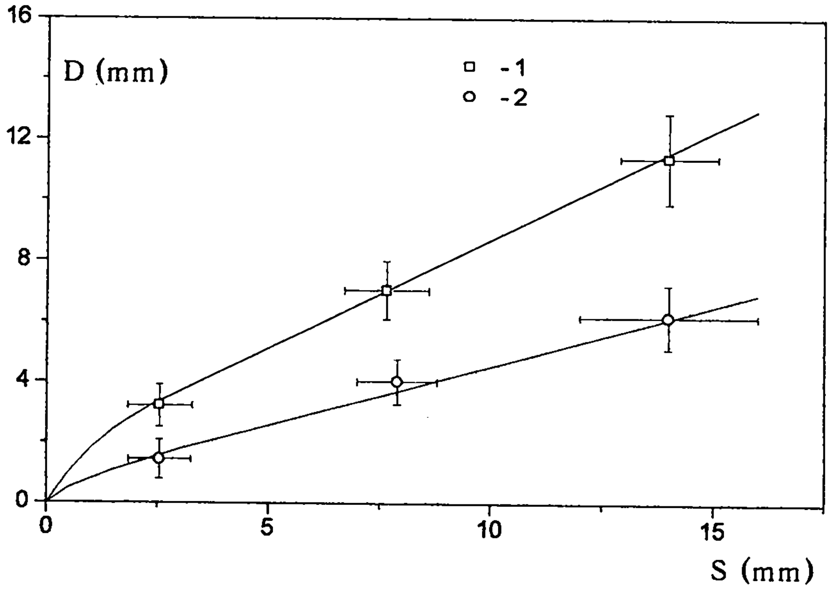

Fig.42. Central bubble diameter vs. jelly layer passage distance .
1 - one spark gap at the chamber bottom center,
2 - 8 spark gaps placed along the straight line.

Thus, localized perturbations grow in the way different from periodic perturbations evolution. For asymptotic stage of periodic perturbations growth the bubble tops move at constant velocity, and at constant acceleration for localized perturbations.

2.6.3. EXPERIMENTAL DATA FOR ACCELERATED PLANE JELLY LAYERS WITH INFLECTED SURFACE. INTERPRETATION OF RESULTS

The flow pattern qualitatively resembling the above is observed, when liquid layers having inflected surfaces [62] are driven by GEM explosion gases. There occurs a growing cave (bubble) in the vicinity of the angular peculiarity of the unstable boundary.

These flows were experimentally investigated using jelly technique (Fig.43). A plane jelly model (1) was placed in between two organic glass plates (2, 3) 20 mm thick. The distance between them was restricted by 10 mm height of side walls (4). The jelly (water-solved gelatin of C=4.4% by weight) at room temperature was poured into a former to be kept then in a refrigerator until its complete setting. The former used was the experimental setup itself with its upper plate (2) removed. The model was shaped on the inside with a tin insert placed into the setup before pouring the solution. Upon hardening, the insert was removed, and the outside profile of the model was cut out with scalpel. Either of the plates (2, 3) had a reference grid of 2 cm spacing scribed on its outer surface. Then, the setup was bolted and placed into its horizontal working position.

The inner space (5) was filled with gas explosive mixture at atmospheric pressure. GEM detonation was driven by a discharge produced in the spark gap (10). Hydrodynamic flow was visualized in transmitted light using a high-speed SFR camera.

Figs.44-46 show photographs for moving jelly layers having surface inflections at the angles $\beta=120^0$, 90^0 and $\beta<5^0$.

In the neighborhood of the inner angular point (A), there is abnormally high-rate deformation observed for the interface between the jelly (1) and explosion products (2). Thus, a cave or bubble is produced with its size growing more rapidly than the plane layer (1) at locations more distant from the angular point. Earlier in its growth, the bubble has near-cylindrical shape, to become near ellipsoidal later. At later times, there are vortical flows observed in the neighborhood of the newly generated angular points (5).

The tendency for explosion gases to disrupt the accelerated layer is as indicated by the rays directed from the apex (A) normal to the angle sides. The disruption will occur, when the layer locations distant from the apex displace to a distance smaller than its thickness.

The pattern observed in the neighborhood of the apex (B) is different. For $\beta<180^0$, the apex is virtually unmoved for a long time. The angle β increases to become equal to 180^0 over time. That is, the surface is being smoothed. For $\beta<180^0$, hydrodynamic flows show a qualitatively different pattern. There is no angle smoothing. On the contrary, a new flow detail is observed to be developing fast, which is incipient high-speed jetting (7) (Fig.46).

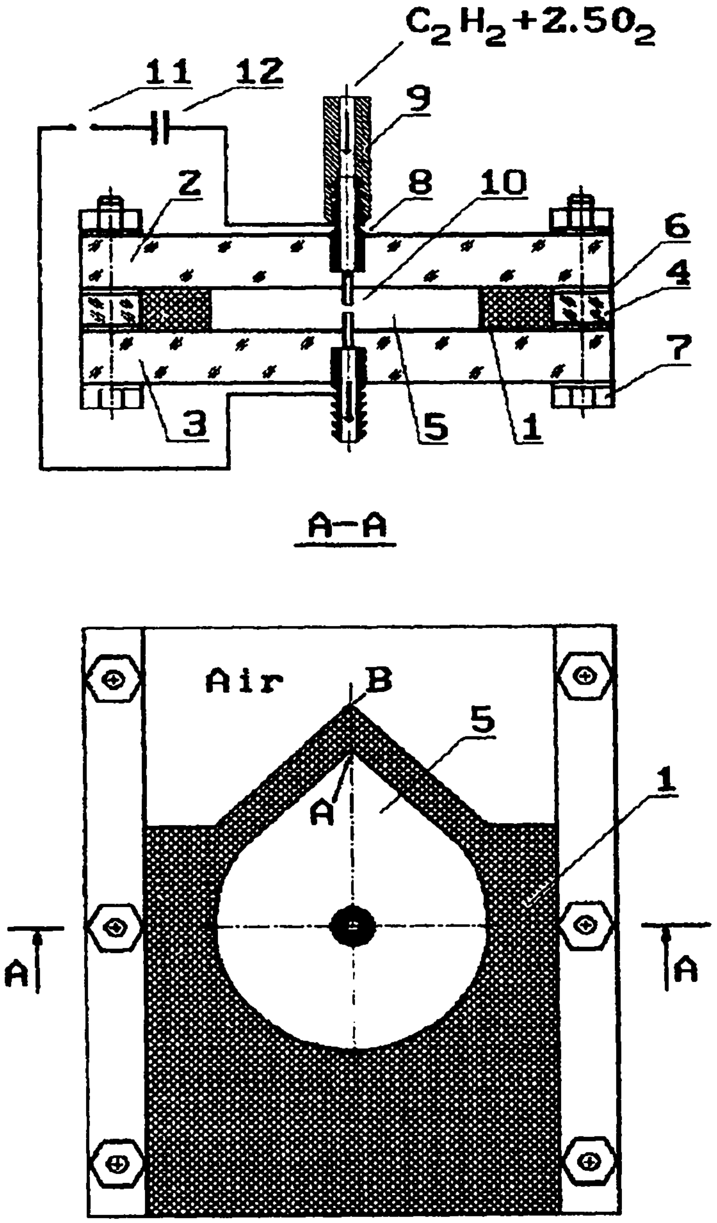

Fig.43. Experimental device .

1 - jelly operating model, 2 - upper transparent plate, 3 - lower transparent plate, 4 - side wall, 5 - the inner volume filled with gas HE, 6 - gasket, 7 - bolt, 8 - electrodes, 9 - gas inlet tube, 10 - spark gap, 11 - commutative discharger, 12 - condenser.
A, B - vertexes of the inner and outer angles of accelerated layer.

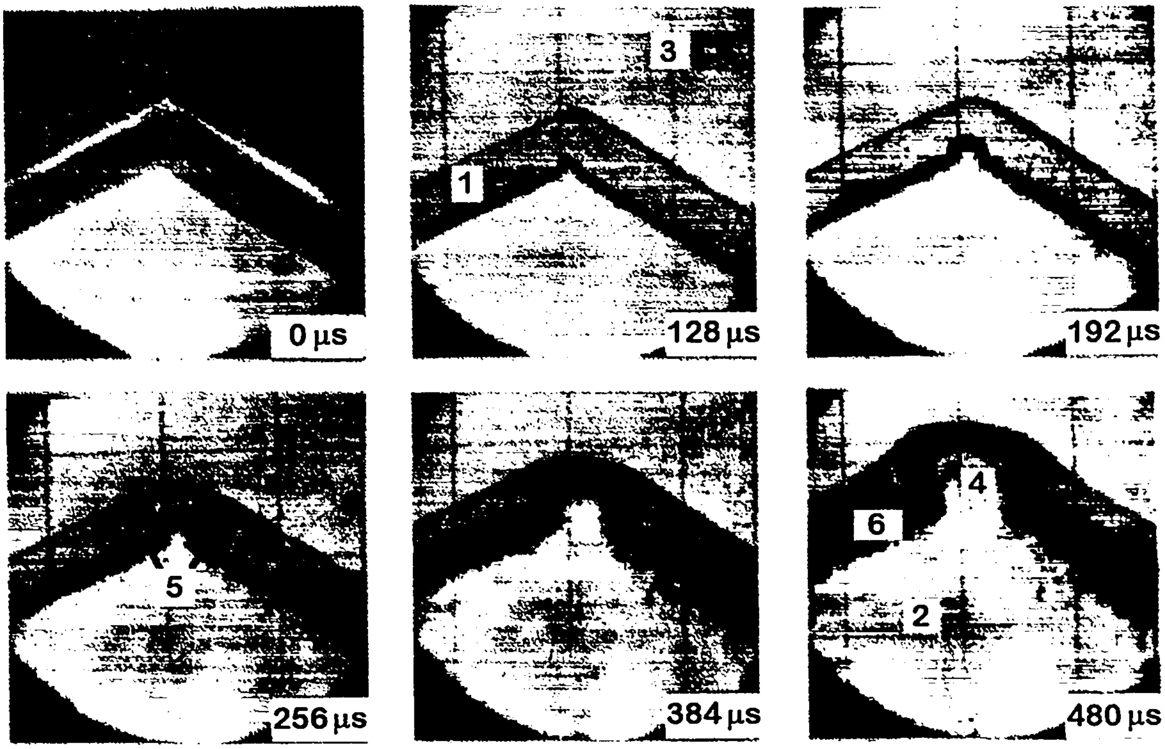

Fig.44. Photochronogramm of experiment with $\beta = 120^0$.

1 - accelerated layer;
2 - explosive products;
3 - air;
4 - cavern;
5 - -new angular peculiarities;
6 - turbulent mixing zone.

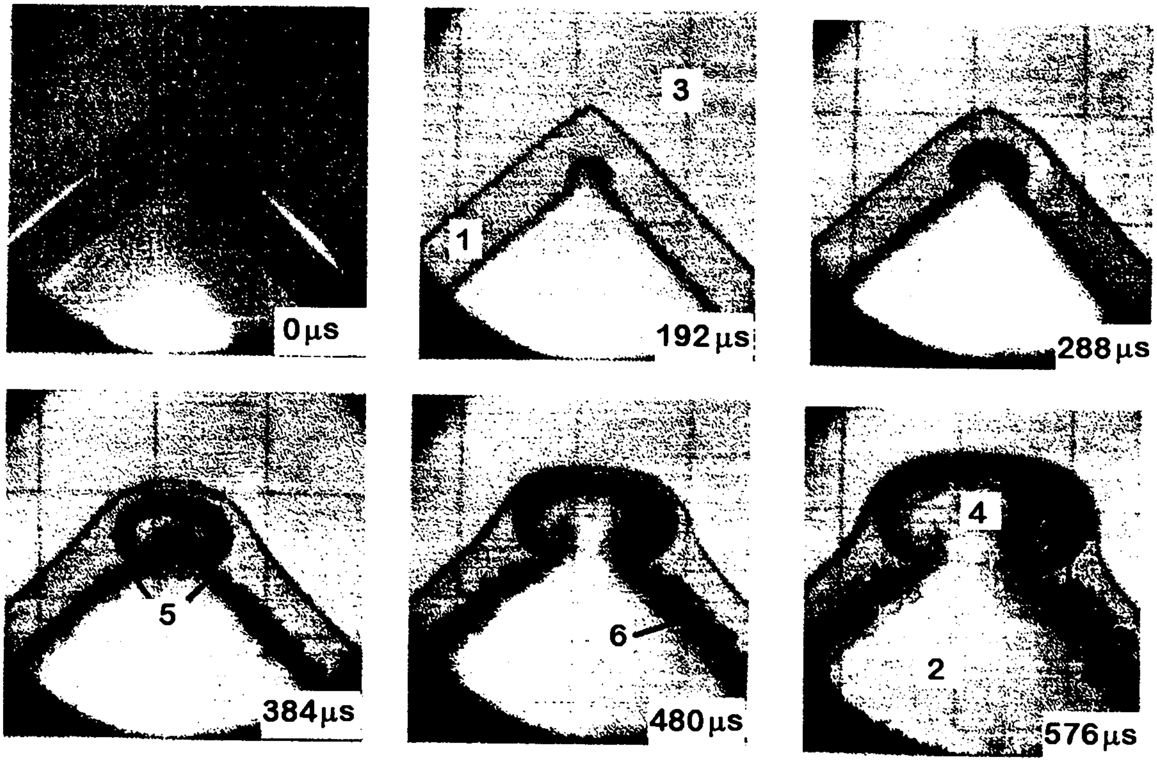

Fig.45. Photochronogramm of experiment with $\beta = 90^0$.

1 - accelerated layer;
2 - explosive products;
3 - air;
4 - cavern;
5 - -new angular peculiarities;
6 - turbulent mixing zone.

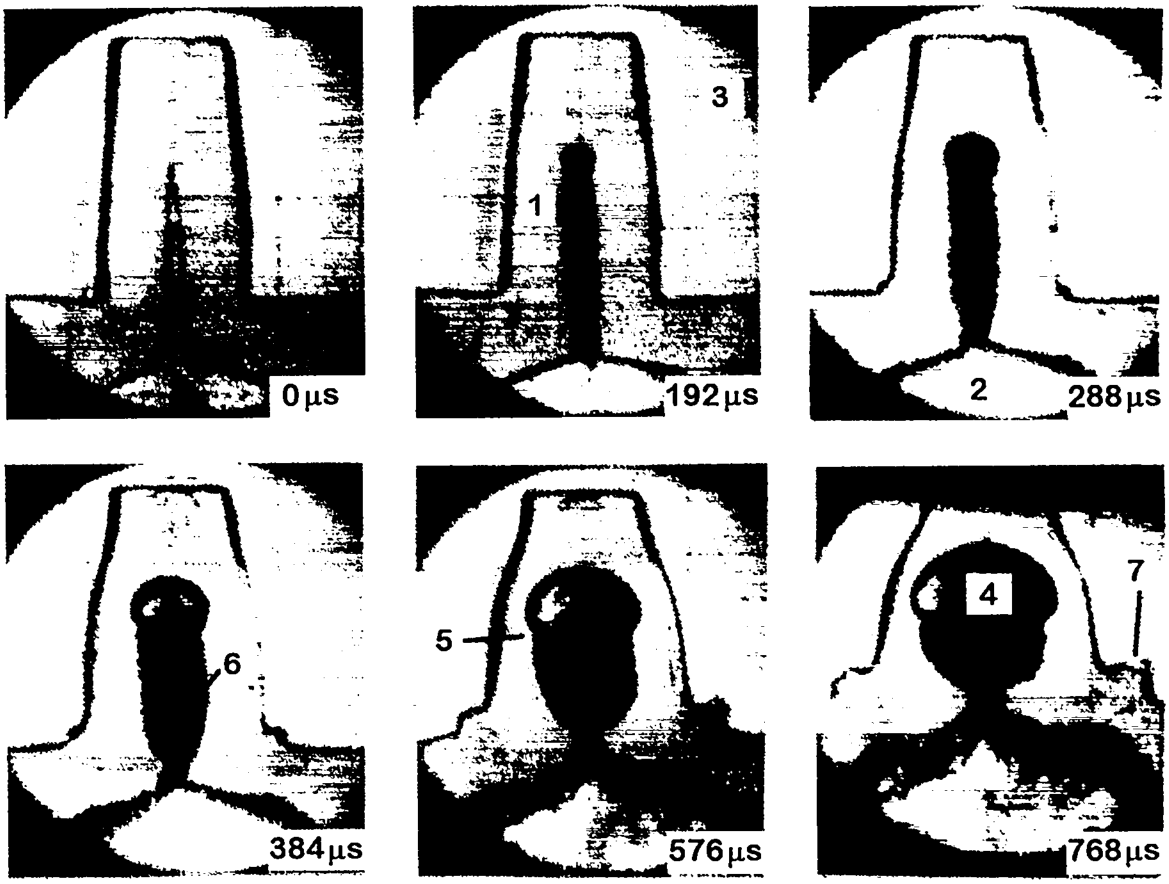

Fig.46. Photochronogramm of experiment with $\beta \approx 0^0$.

1 - accelerated layer;
2 - explosive products;
3 - air;
4 - cavern;
5 - -new angular peculiarities;
6 - turbulent mixing zone;
7 - cumulative jet embryo.

2.7. INVESTIGATION OF TURBULENT MIXING GROWTH AT THE BOUNDARIES OF CONVERGING CYLINDRICAL SHELL OF JELLY.

2.7.1. EXPERIMENTAL GEOMETRY

Fig.47 schematically shows the experiment setup [63]. The setup includes upper (1) and lower (2) plates of organic glass polished to transparency, and a mounting ring (3) of 19.5cm inner diameter and 1 cm height.

Warm gelatin solution was poured into the setup positioned horizontally with its upper plate removed. Upon hardening, a ring (4) was cut out of the bulk of jelly, concentrically on the mounting ring (3). With the upper plate (1) placed, there were two closed spaces (5) and (6) formed, the one containing air at atmospheric pressure (6), the other (5) filled with GEM which was stoichiometric mixture of acetylene and oxygen.

The ring (3) had 40 or 12 spark gaps arranged at mid-height on its inner surface. High-voltage breakdown of the spark gaps initiated a detonation wave in GEM.

The explosion gases' pressure makes the jelly ring collapse. The resulting flows were visualized using high-speed SFR camera operated in framing mode.

2.7.2. NUMERICAL MODEL

Detonation wave front has its velocity in GEM D=2450 m/s, and sound velocity through explosion gases is C $\approx$1040-1100 m/s. Experimentally, jelly shell has typical velocity as high as $\approx$50 m/s, which is much lower than detonation front velocity and sound velocity in EP, jelly and inside air. This implies that numerical interpretation of experiments may consider jelly as incompressible ideal liquid. In addition, pressure variations in the air and explosion gases can be calculated using adiabatic law, and GEM energy release considered instantaneous and uniform.

These approximations were used to do a one-dimensional calculation of jelly shell motion for the conditions equivalent to the experiment. Fig.48. illustrates the computational field geometry. The calculation considered the following parameters: air - P_0=1 atm, γ=1.4; jelly- incompressible liquid of density ρ=1 g/cm^3; GEM EP - P_0=13.5 atm, γ=1.24. The calculation was made without account for turbulent mixing effect.

Fig.49 shows calculated R-t diagram of the flow. Fig.50-52 give time histories of outer and inner boundary accelerations, inner boundary velocity, and confined air pressure.

Earlier during the cylindrical shell motion, the acceleration is directed from the periphery to the center of the system (Fig.49, 50). This is when the ring outer boundary is unstable, and inner one-stable. After the deceleration has started and the acceleration sign changed, what becomes unstable is the inner boundary, and the outer becomes stable. This is the time when the inner boundary acceleration achieved is $\sim 4 \cdot 10^6$ m/s^2.

2.7.3. INVESTIGATION RESULTS

Perturbations growth at an unstable interface depends on the nature of initial perturbations. There are the following two initial perturbation types occurring at the outer boundary:

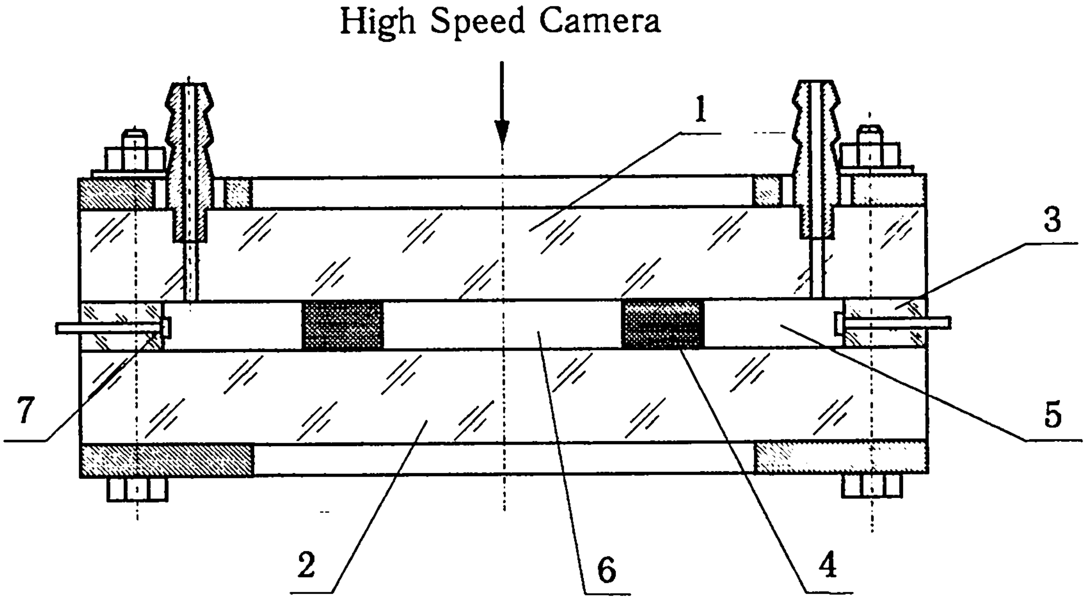

Fig.47. Schematic representation of experimental device.
1, 2 - transparent plates; 3 - casing ring; 4 - jelly ring;
5 - cavity filled with gas HE; 6 - inner cavity
filled with air (P_0=1atm.);
7 - spark dischargers.

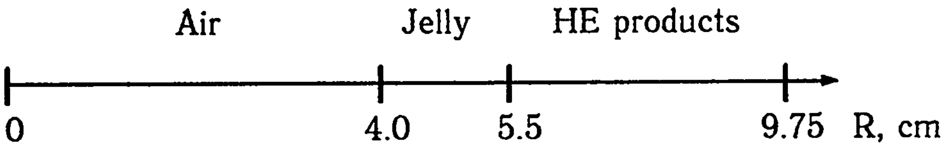

Fig.48. Computational diagramm.

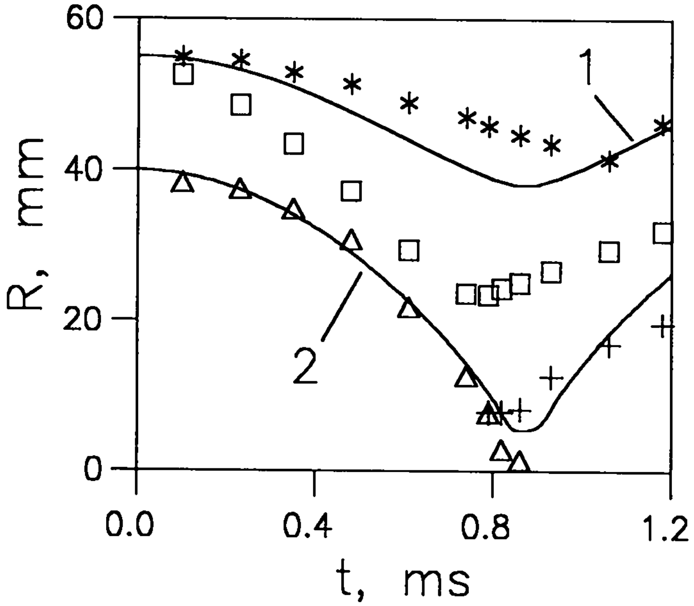

Fig. 49. R-t diagram of collapsing jelly ring.
1, 2-outer and inner ring surfaces (regular hydrodynamic calculation),
*, □ - mixing zone surfaces at outer boundary,
+, Δ - mixing zone surfaces at inner boundary of the ring (jelly ring experiment of ~0,1 kg/cm^2 strength).

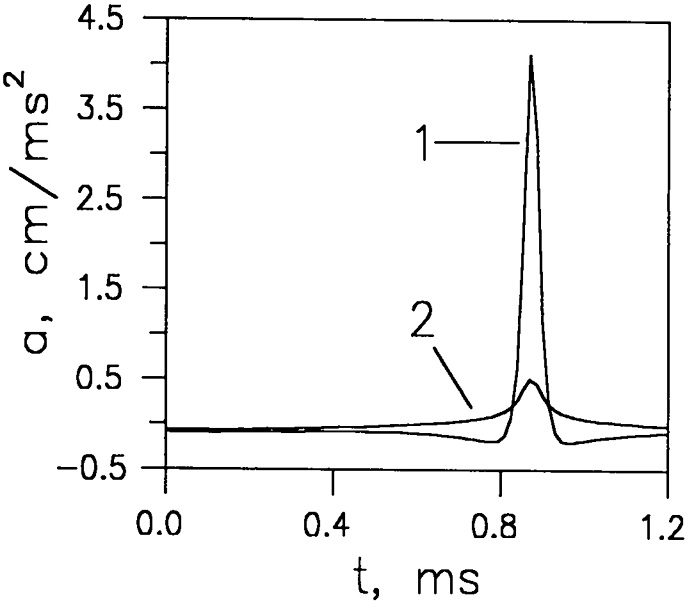

Fig. 50. Calculated time function of the 1-inner and 2-outer surface acceleration.

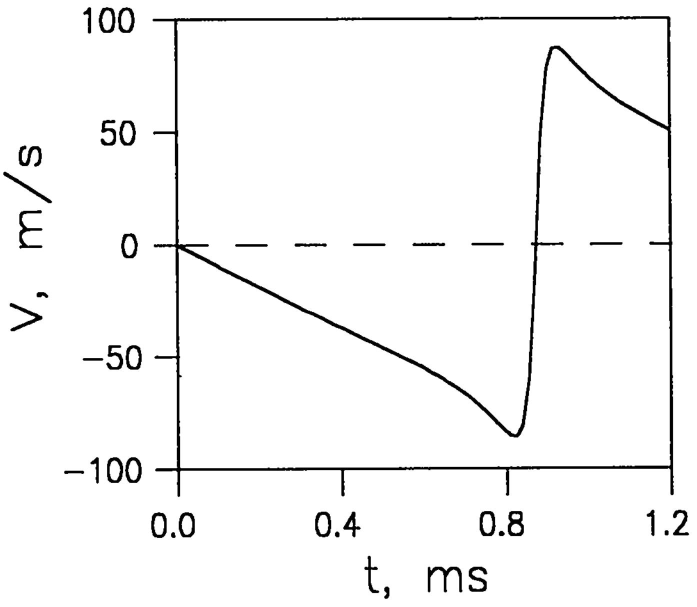

Fig. 51. Calculated time function of the inner boundary velocity V(t).

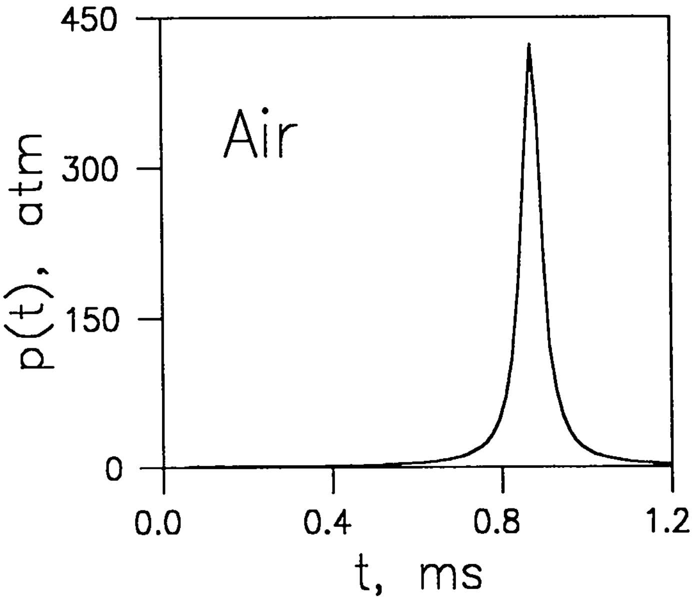

Fig. 52. Calculated time function of air pressure p(t).

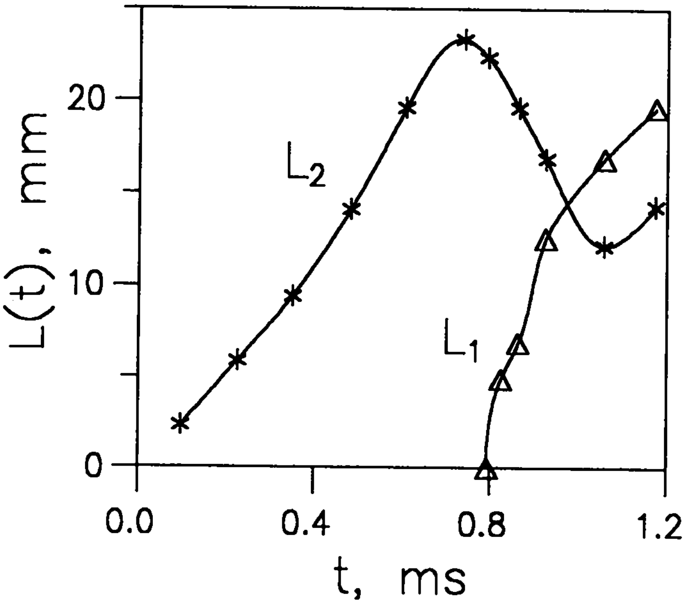

Fig. 53. Time dependence of TMZ-lengths.
$L_l(t)$ - at inner boundary;
$L_2(t)$ - at outer boundary.
Jelly strength ~ 0.1 kg/cm^2.

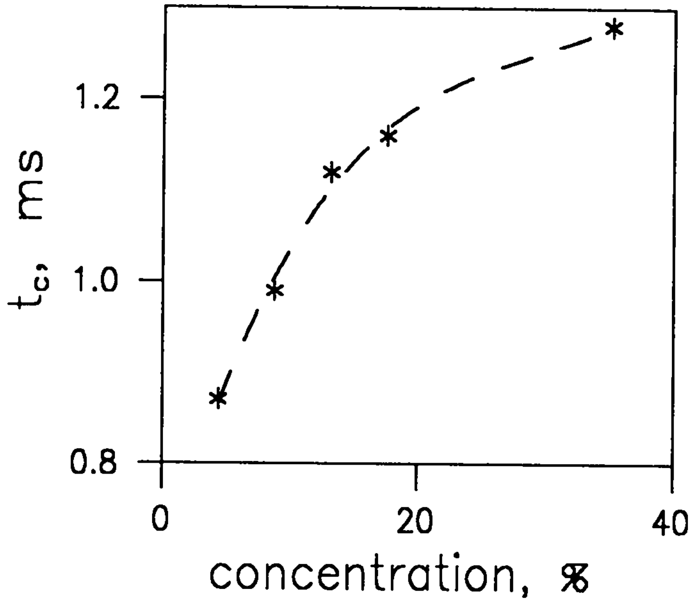

Fig. 54. Dependence of the ring collapsing time t_c on the jelly concentration.

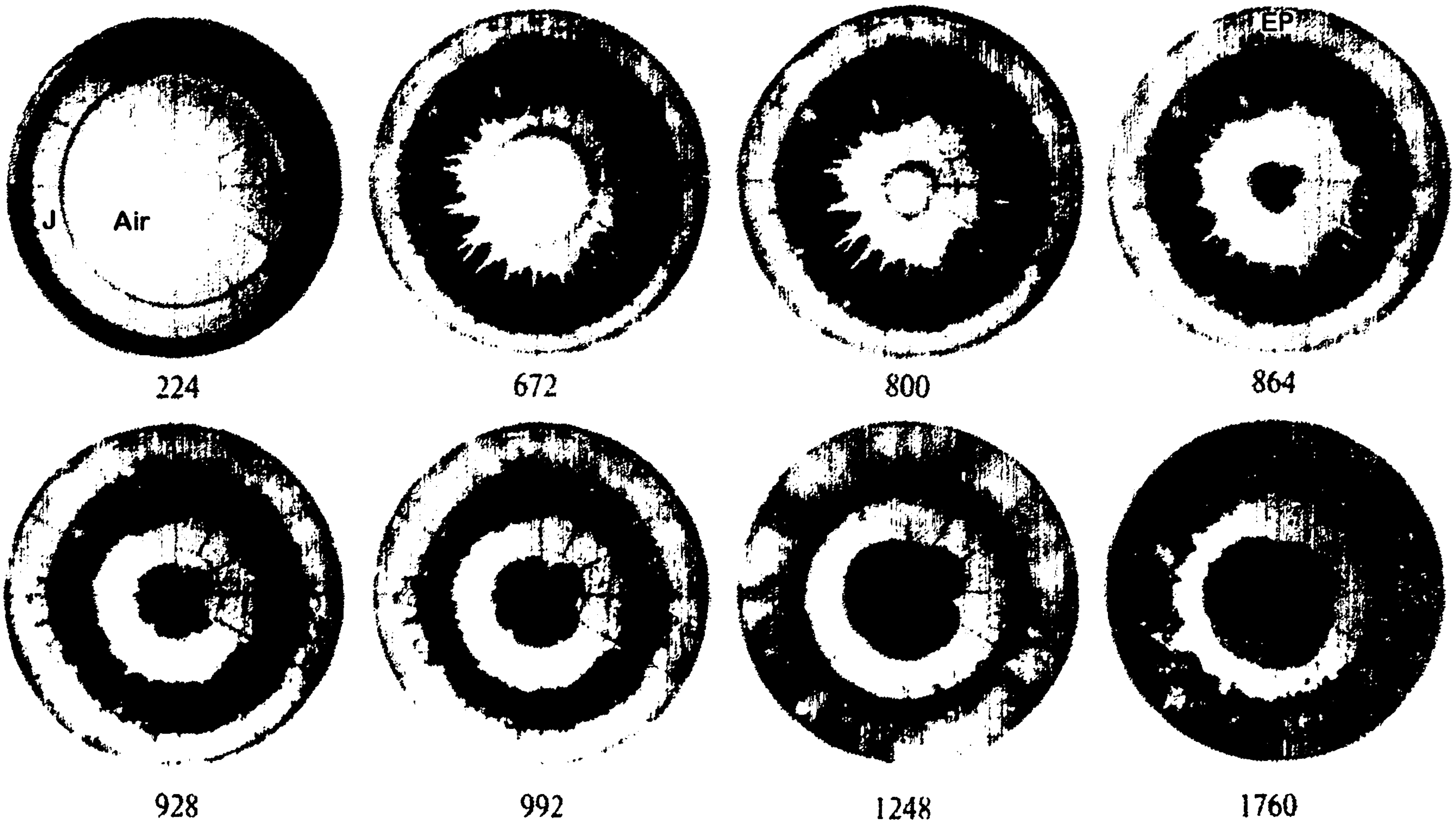

224
672
800
864
928
992
1248
1760

Fig. 55 Photochronogramm of jelly ring experiment.
J - jelly ring (strength - 0.1 kg/cm^2); EP - gas HE products.
HE detonation was initiated in 40 points. Time is in μs.

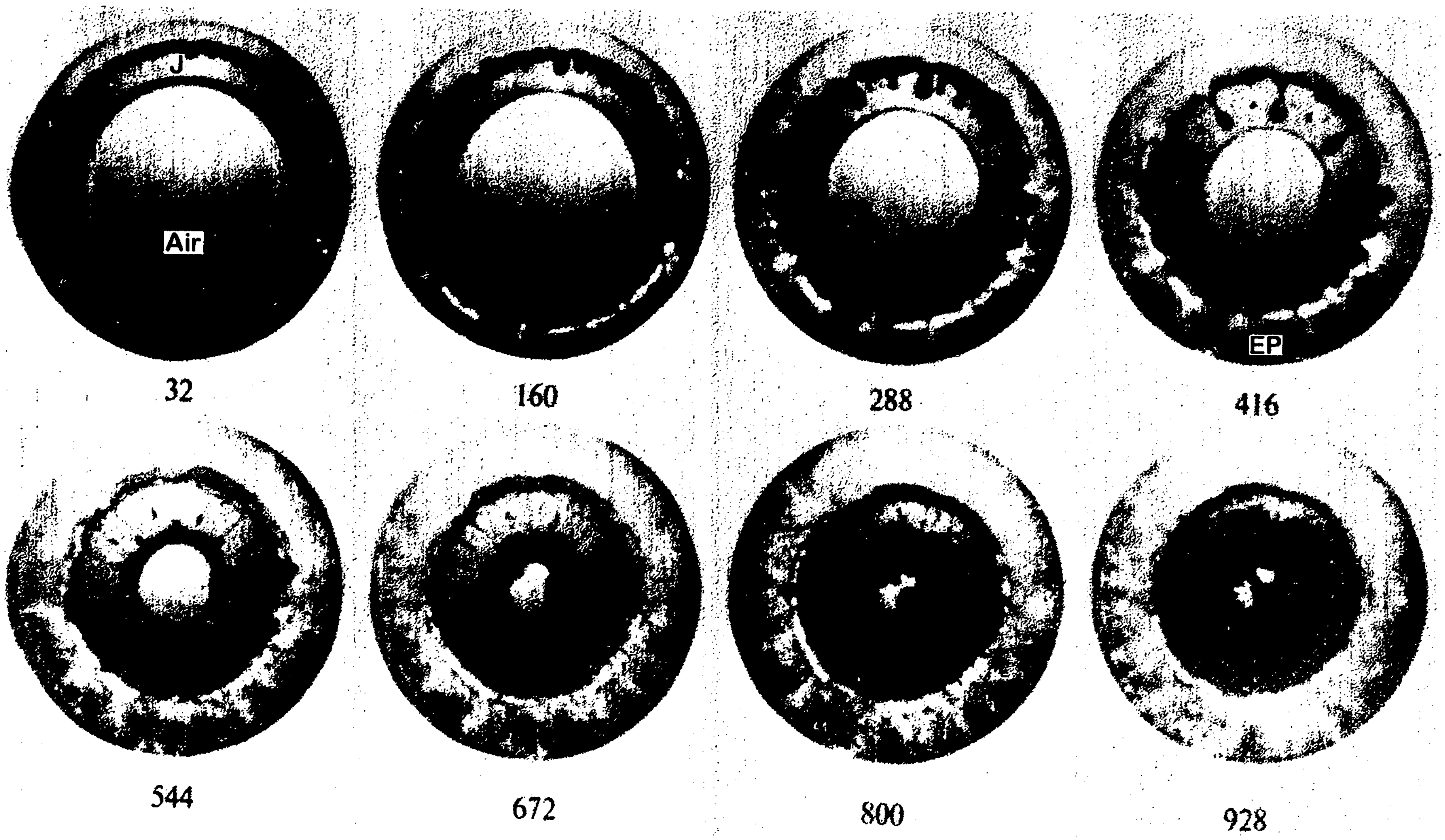

Fig. 56 Photochronogramm of jelly ring experiment.
J - jelly ring (strength - 0.4 kg/cm^2); EP - gas HE products.
HE detonation was initiated in 12 points. Time is in μs.

- surface roughness due to fabrication process. It is typically within 40-160μm;
- different acceleration of the various shell surface locations due to multipoint GEM initiation.

Fig.55 shows photographs of the experiment using jelly shell made of 4.4%-gelatin solution (jelly strength ~ 0.1 кg/cm^2). GEM was initiated at 40 points.

Just when the motion starts there develops a turbulent mixing zone at the outer jelly-EP interface. Its thickness increases with time. Bubbles are growing larger at the inner TMZ boundary (to become as large as 4-5mm lateral size). When the acceleration sign has changed (t≈800μs.), the TMZ thickness decreases until at t=1050μs it reduces to minimum. This makes the TMZ inner boundary smooth.

After deceleration has started, the inner shell boundary becomes unstable, and there also develops a turbulent mixing zone of jelly and air. While this zone has very small-scale structure, it is beyond the resolution of recording equipment optics (≅0.5 mm resolution). The turbulent zone outer boundary is found to be perturbed.

Photo negatives underwent measurements using microscope. The boundary radius was found by averaging measurements in four directions. The measurement error for radii was determined by the recording system resolution, thus being about 0.5mm.

The experimental and calculated data are given in Fig.49 Good agreement between the experiment and calculation is observed at the stage where the inner boundary is stable.

Fig.53 shows time histories of the TMZ thickness for both turbulent zones.

2.7.4. SHELL STRENGTH EFFECTS ON THE MIXING PATTERN

With jelly solution varied in concentration, there are substantial variations in the initial perturbations behavior at the boundaries.

The experiment (Fig.56) involving higher concentrated gelatin solution (with jelly strength ~ 0.4 кg/cm^2) may demonstrate that:

- there is virtually no TMZ development;
- bubbles grow vigorously where detonation waves encounter on the jelly surface (12-point GEM initiation in this experiment);
- some bubbles reach the inner shell boundary and break it even before the inside air cavity compression is the highest;
- during deceleration, some bubbles have their content (GEM explosion gases) "frozen" into the shell material.

Higher jelly strength has also significant effects on the one-dimensional shell motion. Thus, its velocity decreases, and the gas shell compression becomes more protracted in time. This is illustrated by the experimental curve for focusing time vs. gelatin concentration (Fig.54) The focusing time taken was that when the TMZ inner boundary reached the air cavity center.

2.8. TURBULENT MIXING STUDY AT GAS-ACCELERATED LIQUID LAYER INTERFACE

The majority of the published by now experimental results on turbulent mixing caused by Rayleigh-Taylor instability development under a constant or slightly varying acceleration, deal with the studies done in Russia ([17-13, 57,58]) and in Great Britain ([2,3,14-16]).

Mostly, the turbulent mixing at liquid-liquid and gas-liquid interfaces was researched with an accelerated container used [7-13,14-16]. Acceleration was specified in the range of $1.5\cdot10^2$-$2\cdot10^5$ m/s^2. It was attempted to develop the situation close to self-similar.

As a rule, the experimental data on turbulent mixing zone width, L and perturbation depth of a light substance in heavy, L_1 under a constant acceleration, are approximated by the dependencies:

$$L=\alpha At^2; \qquad L_1=\alpha_1 At^2=2\alpha_1 AS,$$

where: $A=(\rho_2-\rho_1)/(\rho_2+\rho_1)$,

S- interface path;

t- time;

ρ_1 and ρ_2 - light and heavy substance densities, respectively;

α and α_1 - empirical constants.

For liquids' mixing [2,3,10,14-16], α_1 experimental results vary in the range from 0.04 to 0.07.

VNIIEF has developed a research method for turbulent mixing at the interfaces of plane jelly [35] and liquid [64,65] layers which allows to study the mixing under various laws of acceleration changing and, in particular, under pulsed accelerations.

2.8.1. JELLY LAYER EXPERIMENTS

In ref.[35], the turbulent mixing zone evolution at the interface of the jelly layers accelerated by GEM explosion products was experimentally studied. Figure 6 displays the experiment arrangement.

Two experiment photochronograms are presented in Fig.57.

The first experiment was with one jelly layer of initial H_{J1} = 19.3mm thickness which was accelerated by GEM layer of initial H_{HE}=34mm thickness.

The second experiment was done with two jelly layers. One of them, H_{J1}=19.3mm thickness was accelerated by GEM layer initial H_{HE}=34mm thickness and through a closed volume of a compressed air layer initial 20mm thickness, accelerated the second jelly layer H_{J2}=15mm thickness.

In these experiments a jelly of low strength with 4.4% gelatin concentration was used. Under the GEM explosion product pressure, the jelly behaves as an incompressible liquid.

The acceleration was defined by differentiating the fourth power polynomial which approximates the experimental time function of the stable layer boundary shifting.

In the one-layer experiments, the acceleration based on the observed shifts was almost constant and constituted ~7 $10^4 m/s^2$.

In the second experiment, the air inter layer driven layer acceleration was of peak character. Its maximal value ~3.7 10^5 m/s^2 was achieved at ~2mm layer shift.

As the acceleration was varying, $L_1(t)$ function was presented in the form similar to the one in ref.[14]:

$$L_1=\alpha_1 A(\int g^{0.5}\, dt)^2=\alpha_1 AX$$

which is the most suitable for self-similar α_1 constant presentation.

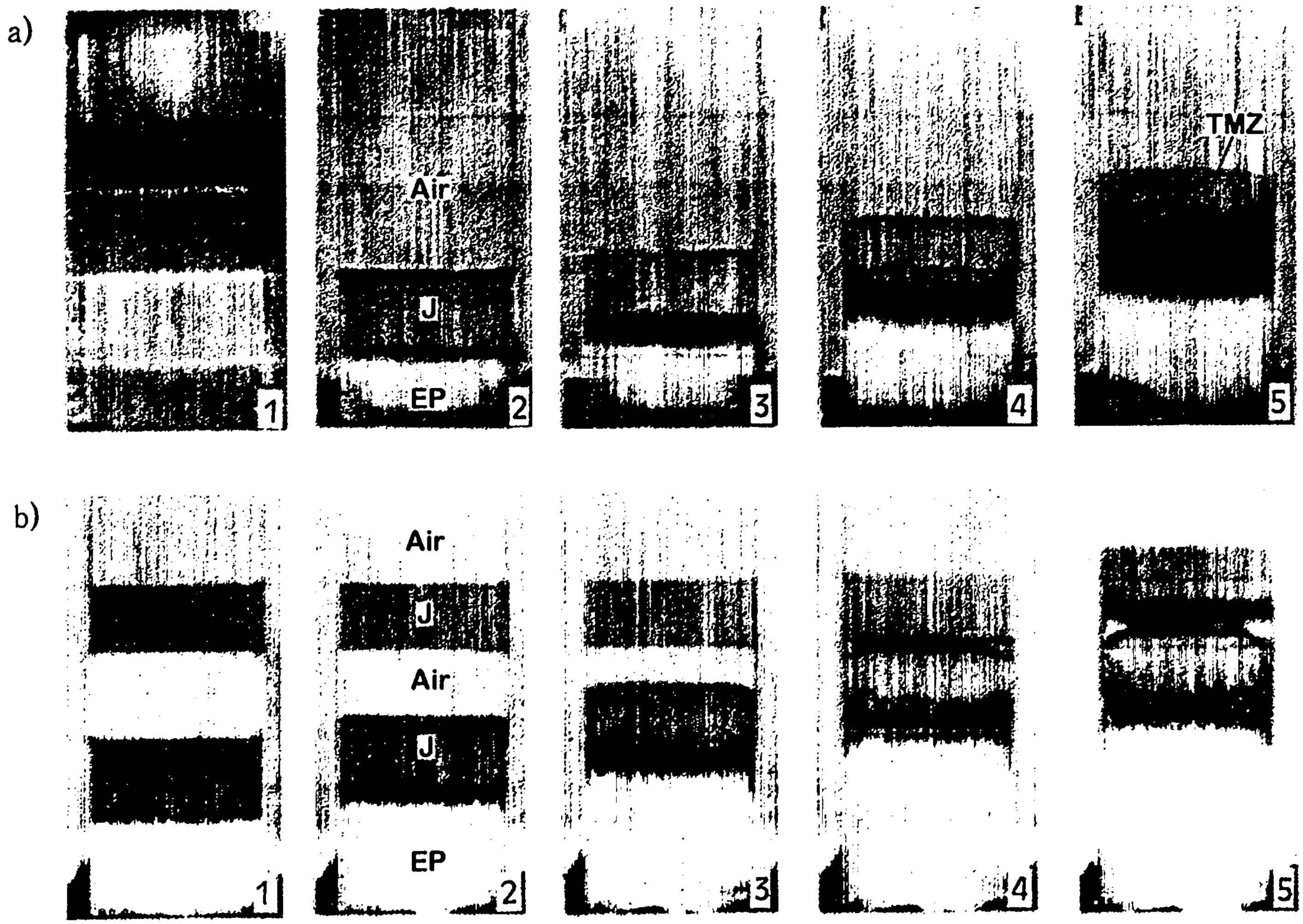

Fig. 57 Photochronogramms of experiments:
a) one jelly layer accelerated by gas HE products;
b) two jelly layers.
J - jelly layer; EP - gas HE products; TMZ - turbulent mixing zone.

Figure 58 shows dependencies $\sqrt{L_1}$ vs. $\sqrt{X}$, obtained in three experiments on jelly plane layer acceleration by GEM explosion products (1). Here, the similar data obtained in three experiments on two jelly layers' acceleration which are separated by an air interlayer. Function $\sqrt{L_1}$ vs. $\sqrt{X}$ is presented for jelly and air mixing zone (2).

These two functions differ from one another because of the difference in spectra of initial perturbations. On the jelly layer surface driven by the explosion products, there exist the dynamic perturbations caused by the discrete character of GEM initiation. On the layer surface driven by the compressing air interlayer, these perturbations are almost absent. In the first case, the pulsed boundary acceleration in the detonation wave front interaction renders an additional impact on the initial stage in TMZ evolution.

The results processed have shown that $\alpha_1 \cong 0.12$ magnitude matches most closely the experiment data, especially, for the layer driven by air interlayer. Figure 58 presents $\sqrt{L_1}$ function vs. $\sqrt{X}$ corresponding to this α_1 magnitude, in dashed lines.

2.8.2. LIQUID LAYER EXPERIMENTS

In ref. [65] the turbulent mixing zone evolution at the liquid layer boundary accelerated by the gas explosive mixture products, was experimentally studied. Section 1.6 describes the experiment arrangement (Fig.7.a).

The experiments were done at different initial GEM layer thickness H_{HE}=40-500mm and different water layer thickness H_W=25-65mm.

In some experiments, the piezoelectric gauges were used to measure the pressure in the vicinity of liquid layer stable boundary.

Experiment №689 (H_{HE}=500mm, H_W =29mm); photochronogram is given in Fig.59a.

Experiment №710 (H_{HE}=40mm, H_W=65mm); photochronogram is given in Fig.59b.

Experiment №612 (H_{HE}=120mm, H_W=25mm); photochronogram is given in Fig.59c. The photograph presents a slit sweeping of the gasdynamic flow pattern obtained by a shadow method.

Figure 59c is the experimental x-t diagram illustrating vividly the wave front motions in the liquid layer and gases.

At the detonation wave front arrival, the GEM-water interface pressure grows by a jump, and a weak shock (sound) wave starts moving into the water layer. It reflects many times against the layer boundaries and attenuates. In the explosion products, a reflected shock wave is formed. It moves from the liquid layer to the channel end, reflects against it and goes back to the EP-water interface at $t_2=t_1+180\mu s$. This wave interacting with the liquid layer, produces a new series of sound waves in the liquid. The wave amplitude is smaller than the similar wave amplitude produced by the detonation wave interaction with the layer. The subsequent shock wave fronts propagating in EP, arrive to the water surface at $t_3=t_1+400\mu s$, t_4 t_5... , thus forming similar series of attenuating waves in the water.

In this background, the layer is accelerated, the turbulent mixing zone is formed and expanded. The TMZ boundary roughness (see Fig.59.a and Fig.59.b) provides for the sound wave attenuation, additionally.

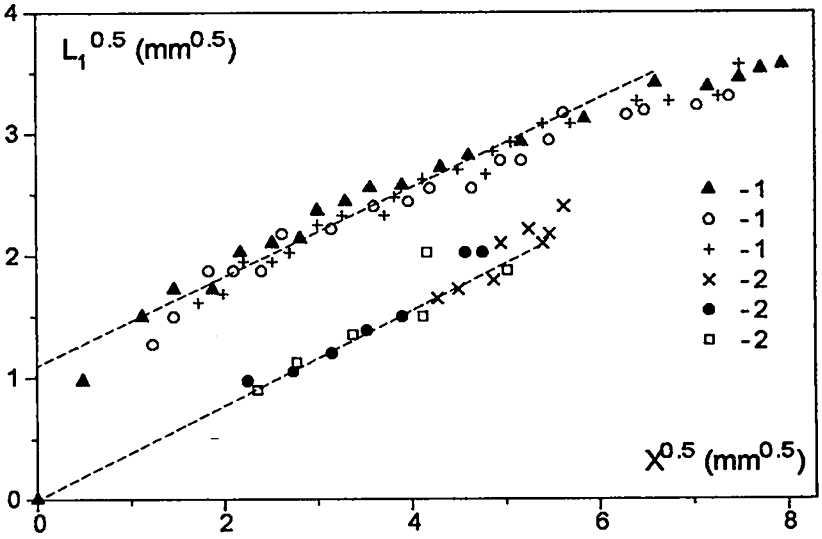

Fig. 58. $\sqrt{L_1}$ as function of $\sqrt{X}$.
1 - one layer experiments;
2 - two layer experiments; (the second layer accelerated by the compressed air).

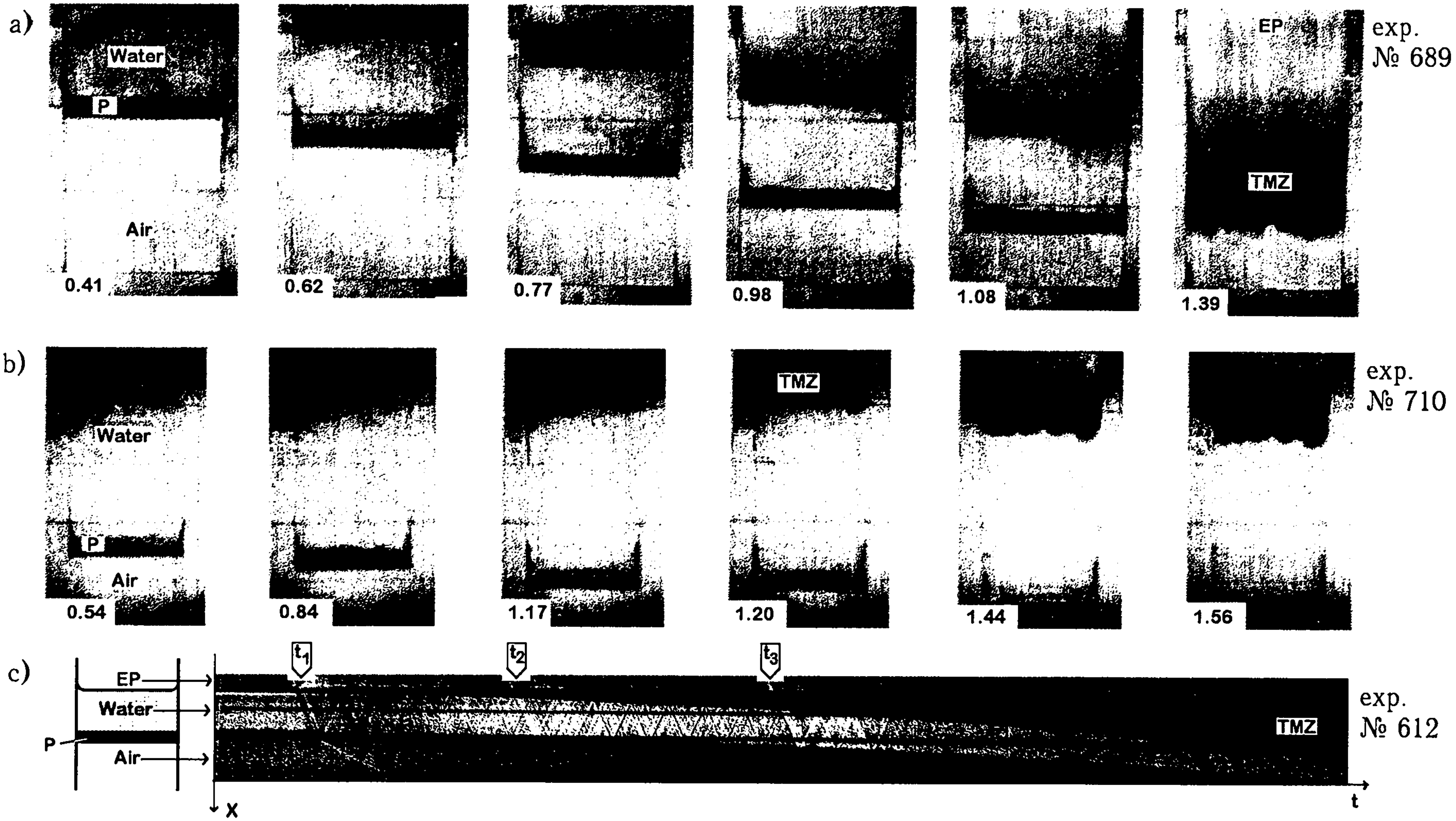

Fig.59 Turbulent mixing zone development at water layer interface, accelerated by gas HE products (EP). Time is in μs.
Photochronogramms: a) H_{HE}=500 mm, H_W=29 mm; b) H_{HE}=40 mm, H_W=65 mm.
Streak record: c) H_{HE}=120 mm, H_W=25 mm.
H_W - water layer thickness; H_{HE} - gas HE channel length; P - plate. t_1, t_2, t_3 - times of detonation front and shock wave fronts coming to the water layer interface.

Figures 60a, рис.61a, рис.62a give the time functions: S - layer path and L_l - penetration depth of gaseous EP in the liquid. The resultant S(t) measurements were approximated by the polynomial of the 4th degree. Layer acceleration, g(t), was found by a double differentiation of this polynomial. The processed experimental data are also shown in the figures.

The experiments have realized different acceleration regimes. In experiment №689 g(t) function was minimal at $t \approx 0.5$ms providing the minimal and maximal acceleration magnitudes differed by 5 times.

In experiment №559, the acceleration decreased steadily with time. It has decreased by 3 times during the recording period.

Finally, in experiment №710 the acceleration has changed only by 1.5 times. We must note that in this processing of the experimental measurements, the acceleration jumps are smoothed which are produced by shock wave impacts.

Figures 60b, 61b, 62b show $\sqrt{L_l}$ function vs. $\sqrt{X}$ built on the measurement results of these experiments.

As in the case of jelly layer acceleration driven by GEM explosive products, considered in the previous section, L_l grows abruptly at low X. This can be caused by the disturbance growths which are introduced by the GEM point initiation.

In the range of $\sqrt{X} \approx 3 \div 6$ (exper. №559, №689); $\sqrt{X} \approx 2 \div 4$ (exper. №710), the experimental function coincides approximately with linear corresponding· to $\alpha_l \cong 0.12$ constant magnitude that agrees with the experimental results of jelly layer acceleration by GEM explosion products. At high X magnitudes, dL_l/dX derivative is observed to be decreasing. The calculated estimates show that this effect can be caused by the limited transversal layer sizes. The lateral walls available result in the cut long-wave fraction of the disturbance spectrum and, consequently, in the reduced TMZ growth rate.

In ref. [64] the turbulent mixing zone evolution was experimentally studied at the liquid layer interfaces accelerated by the compressed gas under different initial pressures. Section 1.6 (Fig.7.b) describes the arrangements of these experiments.

In these experiments $\alpha_l \cong 0.05 \div 0.13$ magnitudes were obtained.

A large variation of the turbulent mixing constant magnitudes α_l and α, is observed which are obtained by different authors in the experiments of different types. This can be the result of disturbance spectra differences which are actually realized in various experiments, of the accelerated layer finite size effect, as well as of probable shock wave impact.

A series of high-accuracy experiments seem interesting to be conducted, to clarify the effects of the above mentioned factors on the turbulent mixing evolution.

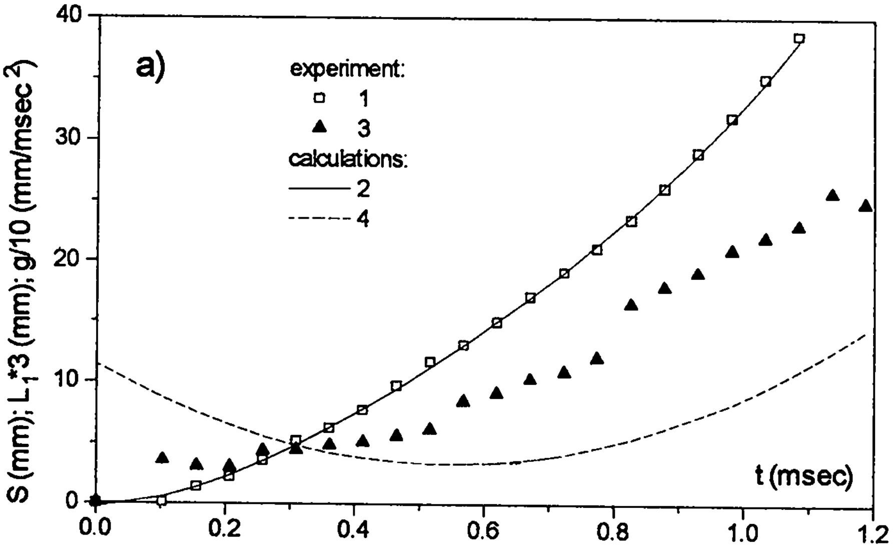

Fig.60a. Experiment №689 (H_{HE}=500 mm, H_W=29 mm).

1 - S(t);

2 - polynomial of degree 4 approximating experimental function S(t);

3 - L_1(t);

4 - g(t), calculated as polynomial time derivative

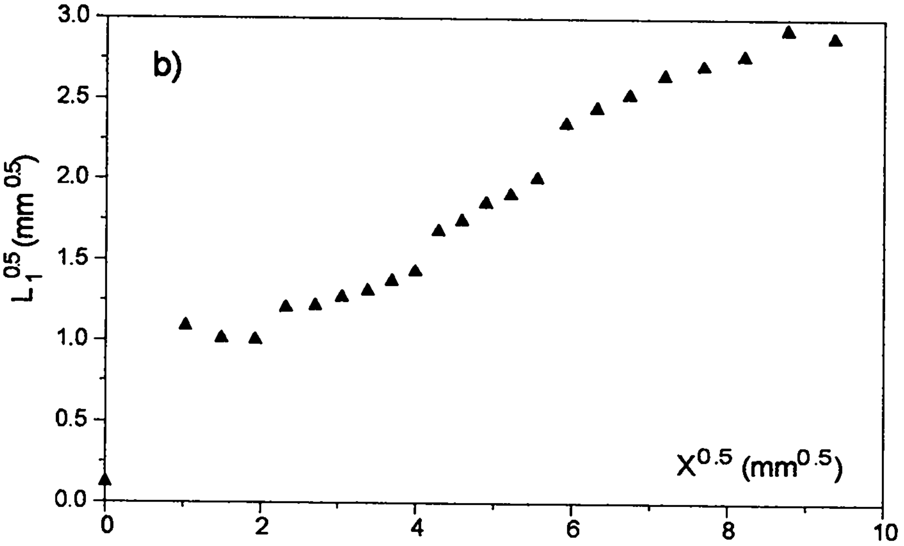

Fig. 60b. Experiment №689 (H_{HE}=500 mm, H_W=29 mm).

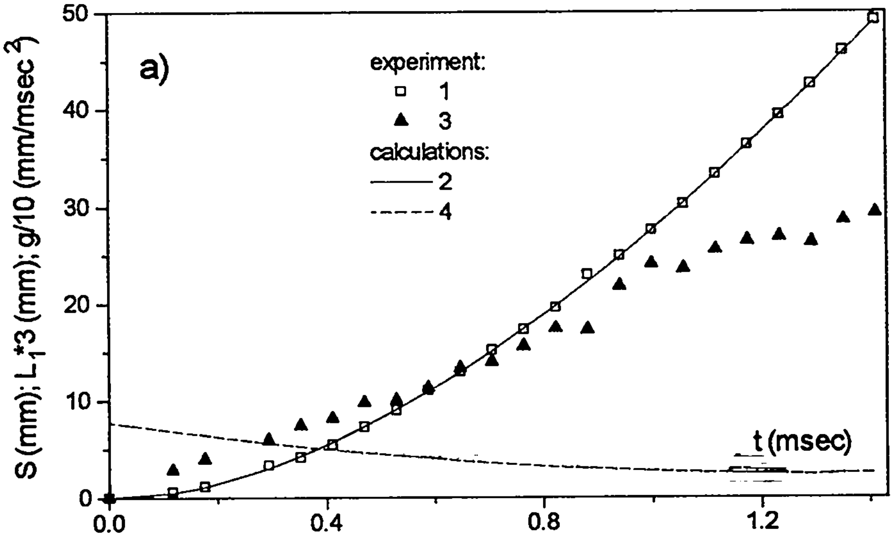

Fig.61a. Experiment №559 (H_{HE}=120 mm, H_W=25 mm).

1 - S(t);

2 - polynomial of degree 4 approximating experimental function S(t);

3 - $L_l(t)$;

4 - g(t), calculated as polynomial time derivative

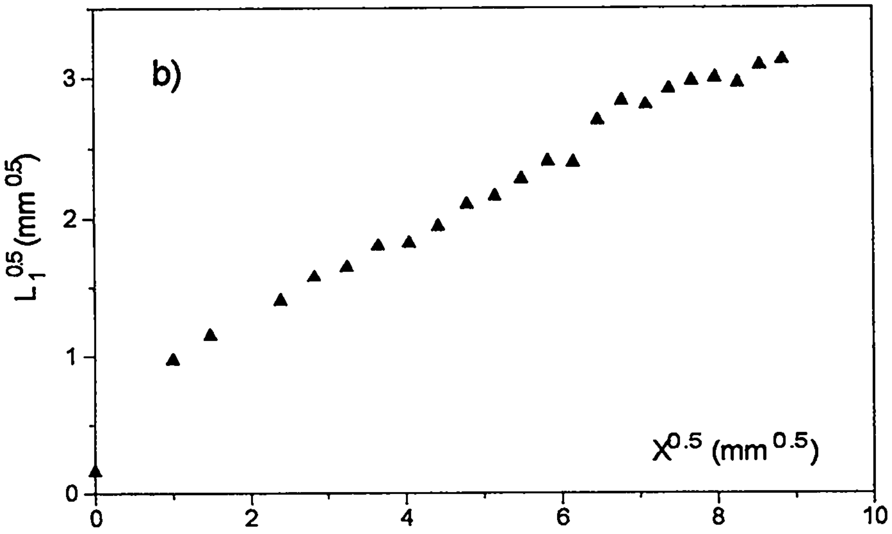

Fig. 61b. Experiment №559 (H_{HE}=120 mm, H_W=25 mm).

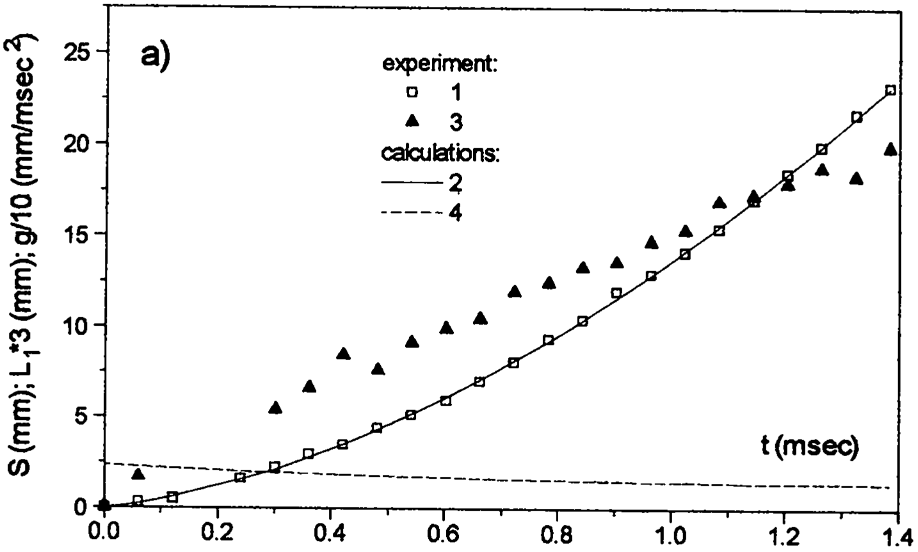

Fig.62a. Experiment №710 (H_{HE}=40 mm, H_W=65 mm).
1 - S(t);
2 - polynomial of degree 4 approximating experimental function S(t);
3 - $L_l(t)$;
4 - g(t), calculated as polynomial time derivative

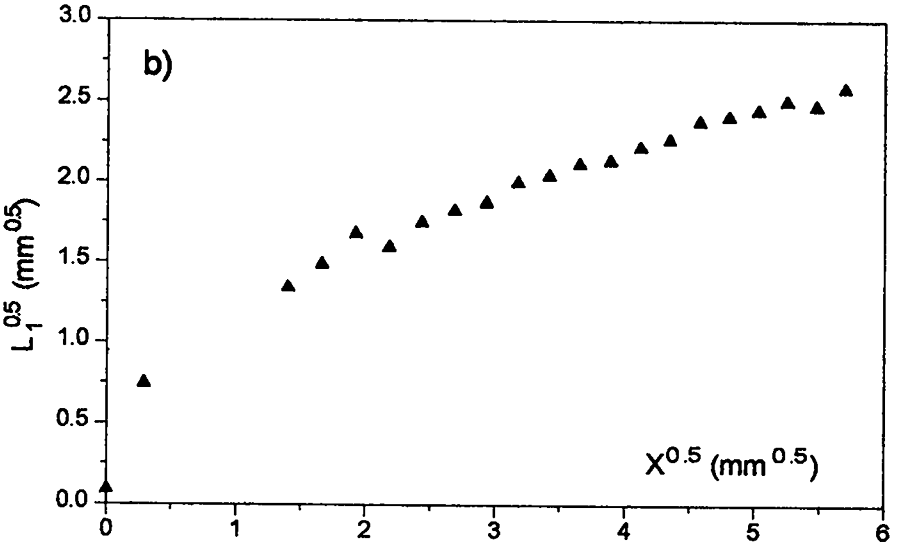

Fig. 62b. Experiment №710 (H_{HE}=40 mm, H_W=65 mm).

CONCLUSION

The VNIIEF has developed various laboratory experimental methods for hydrodynamic instabilities and turbulent mixing research. They have been applied to study various flow instabilities in plane and cylindrical geometries with gas and liquid models.

The obtained results were widely used in testing the gasdynamic instability calculation techniques and, especially, in calibration of phenomenological models of turbulent mixing.

Further development and modification of these techniques can promote the solving of the high energy density physics problems.

The interest lies in the research of:

- evolution processes in 3D, multimode initial disturbances for plane, cylindrical, spherical geometries till the stage of initial condition forgetting;
- hydrodynamic instabilities and turbulent mixing in complicated nonself-similar flows;
- turbulent mixing effect on the basic flow;
- hydrodynamic instability suppression feasibility.

REFERENCES (PART 2)

1. R.Duff, F.Harlow, C.Hirt. Effect of diffusion on interface instability between gases. Phys.Fluids 5, pp.417-425, 1962.

2. P.Linden, J.Redondo. Molecular mixing in Rayleigh-Taylor instability. Phys.Fluids A3, pp.1269-1277, 1991.

3. P.Linden, J.Redondo, D.Youngs. Molecular mixing in Rayleigh-Taylor instability. J.Fluid Mech. 265, pp.97-124, 1994.

4. G.I.Taylor. The instability of liquid surfaces when accelerated in a direction perpendicular to their planes.I. Proc.Roy.Soc., v.A201, p.192, 1950.

5. D.J.Lewis. The instability of liquid surfaces when accelerated in a direction perpendicular to their planes.II. Proc.Roy.Soc., v.A202, 1068, pp.81-96, 1950.

6. H.Emmons, C.Chang, B.Watson. Taylor instability of finite surface waves. J.of Fluid Mech., v.7, pp.177-193, 1960.

7. N.N.Anuchina, Yu.A.Kucherenko, V.E.Neuvazhaev, V.N.Ogibina, L.I.Shibarshov, V.G.Yakovlev. Turbulent mixing at the accelerated interface between two liquids. Izv. AN SSSR, MZhG, (in Russian) №6, pp.157-160, 1978

8. Yu.Kucherenko, G.Tomashov, L.Shibarshov. Experimental investigation of the gravitational turbulent mixing self-similar mode. VANT, ser.Teor.i prik. fiz.(in Russian) №1, p.13, 1988.

9. R.Ardashova, S.Balabin, N.Voloshin, Yu.Kucherenko, N.Ptitzyna, V.Chitaikin. Experimental investigation of perturbations growth within gravitationally unstable system of continuously distributed density. VANT, ser.:Teor.i prik. fiz.(in Russian) №1, p.20, 1988.

10. Yu.Kucherenko, L.Shibarshov, V.Chitaikin, S.Balabin, A.Pylaev. Experimental study of the gravitational turbulent mixing self-similar mode. 3rd Int. Workshop on the Physics of Compressible Turbulent Mixing, Abbey of Royaumont, France (1991).

11. Yu.Kucherenko, S.Balabin, A.Pylaev. Experimental study of asymptotic stage of gravitational turbulent mixing of thin liquid layers of different densities. The Proc. of the 4th Int. Workshop on the Physics of Compressible Turbulent Mixing., Cambridge, England. Ed. by P.Linden, D.Youngs & S.Dalziel. Pr. by Cambridge Univ. Press, Cambridge, England. (1993)

12. Yu.Kucherenko, V.Neuvazhaev, A.Pylaev. Behavior of gravitational turbulent mixing region under conditions leading to separation. The Proc. of the 4th Int. Workshop on the Physics of Compressible Turbulent Mixing. Cambridge , England. Ed. by P.Linden, D.Youngs & S.Dalziel. Pr. by Cambridge Univ. Press, Cambridge, England. (1993)

13. N.Ptitzyna, Yu.Kucherenko, V.Chitaikin, A.Pylaev. Experimental study into the stabilization effect in gravitational turbulent mixing development on an inclined boundary. The Proc. of the 4th Int. Workshop on the Physics of Compressible

Turbulent Mixing. Cambridge, England. Ed. by P.Linden, D.Youngs & S.Dalziel. Pr. by Cambridge Univ. Press, Cambridge, England. (1993)

14. K.Read. Experimental investigation of turbulent mixing by Rayleigh-Taylor instability. Physica 12D, pp.45-58, 1984.

15. D.Youngs. Modeling Turbulent Mixing by Rayleigh-Taylor Instability. Physica D37, pp.270-287, 1989.

16. D.Youngs. Experimental Investigation of Turbulent Mixing by Rayleigh - Taylor Instability. Advances in Compressible Turbulent Mixing. W.P.Dannevik, A.C.Buckingham, C.E.Leith Editors, pp.607-626, 1992.

17. R.D.Richtmyer. Taylor instability in shock acceleration of compressible fluids. Commun.Pure Appl.Math.,v.13, p.297, 1960.

18. E.Meshkov. Instability of shock-accelerated gas-gas interface... Izv. AN SSSR, MZhG.(in Russian), № 5, pp.151-158, 1969.

19. V.A.Andronov, S.M.Bakhrakh, E.E.Meshkov, V.N.Mokhov, V.V.Nikiforov, A.V.Pevnitskii, A.I.Tolshmiakov.Turbulent mixing at shock-accelerated interface. ZhETF (in Russian), v.71, №8, pp.806-811, 1976.

20. V.A.Andronov, S.M.Bakhrakh, E.E.Meshkov, V.V.Nikiforov, A.V.Pevnitskii, A.I.Tolshmiakov. Experimental investigation and numerical simulation of turbulent mixing in one- dimentional flows. DAN SSSR (in Russian), 1982, v.264, №1, pp.76-82.

21..S.M.Bakhrakh,.G.A.Grishina, N.P.Kovalev, E.E.Meshkov, A.И.Tolshmyakov, Yu.V.Yanilkin. Some aspects of experimental and numerical investigations of Taylor instability. Ch.MMSS.(in Russian), 1979, v.10, №1, pp.17-30.

22. E.E.Meshkov. Some experimental data on gravitational instability of the interface between media different in density. In "Hydrodynamical instabilities numerical investigations.." (in Russian) Edit. K.I.Babenko. IPM (Keldysh Institute of Applied Mathematics.) . M. 1981, pp..163-190.

23. E.E.Meshkov, V.V.Nikiforov, A.I.Tolshmyakov. On the turbulent mixing zone structure at shock-accelerated gas-gas interface.(in Russian). FGV (in Russian), № 3, pp.71-77, 1990.

24. E.Meshkov. Instability of shock-accelerated interface between two media. Proc. of the 1 Int. Workshop on the Physics of Turbulent Compressible Mixing (Prinston, 1988).

25. E.E.Meshkov, V.N.Mokhov. On the applicability of linear approximation in the problems for small perturbations growth in gasdynamics.. FGV (in Russian), №4, pp.93-96, 1982.

26. B.A.Klopov, E.E.Meshkov. On the behavior of perturbed expansion wave. FGV (in Russian), № 4, pp.96-100, 1982.

27. E.E.Meshkov Plane shock wave reflection from rigid concave wall. Izv. AN SSSR, MZhG. (in Russian), 1970, № 4, p..33

28. B.A.Klopov, E.E.Meshkov, A.I.Tolshmyakov. Cumulative effect of the shock wave reflected from spherically concave wall. PMTF(in Russian), №4, pp..33-37, 1976.

29. S.Zaytsev, E.Lazareva, V.Chernukha, V.Belyaev. Mixing growth at the interface between media different in density upon shock wave passage therethrough. DAN SSSR (in Russian), 1985, v.283, №1, p..94.

30. A.H.Aleshin, E..Gamalii, S.Zaytsev, E.Lazareva, I.Lebo, .R.Rozanov. Investigation of nonlinear and transitional phases in Richtmyer-Meskov instability. Letters to ZhTF (in Russian), v.14, №12, p.1063, 1988.

31. S.Zaytsev, A.Aleshin, E.Lasareva, E.Chebotareva, S.Titov, R.Rozanov, I.Lebo, V.Demchenko. Experimental investigation of Rayleigh-Taylor and Richtmyer - Meshkov instabilities. 3rd Int. Workshop on the Physics of Compressible Turbulent Mixing, Abbey of Royaumont, France, (1991).

32. S.Zaytsev, E.Chebotareva, S.Titov. The study of Rayleigh-Taylor instability in continuous interface. The Proc. of the 4th Int. Workshop on the Physics of Compressible Turbulent Mixing. Cambridge, England. Ed. by P.Linden, D.Youngs & S.Dalziel. Pr. by Cambridge Univ. Press, Cambridge, England.(1993).

33. E..Gamalii, S.Zaytsev, I.Lebo,.R.Rozanov, S.Titov, E.Chebotareva. Interaction shock wave and interface layer between gases having different densities.TVT (in Russian), v.26, №5, pp.960-964, 1988.

34. A.Aleshin, E.Lazareva, S.Zaytsev,.R.Rozanov, E.Gamalii, I.Lebo. Investigations of linear, nonlinear and transitional phases of Richtmyer - Meshkov instability. DAN SSSR (in Russian), v.310, №5, pp.1105-1108, 1990.

35. I.G.Zhidov, E.E.Meshkov, N.V.Nevmerzhitskii. Experimental studies of mixing dynamics on unstable interfaces of accelerated fluid layers. In: "Experimental studies of gravitational instability and turbulent mixing of stratified flows in acceleration field in terms of ICF problems" (in Russian), Preprint FIAN AN SSSR, №56, pp.52-63, 1990.

36. A.Aleshin, S.Zaytsev, E.Lazareva. The influence of the shock interaction with an interface between the two gas flows of different densities on the intensity of mixing. The Proc. of the 4th Int. Workshop on the Physics of Compressible Turbulent Mixing. Cambridge, England. Ed. by P.Linden, D.Youngs & S.Dalziel. Pr. by Cambridge Univ. Press, Cambridge, England.(1993).

37. S.Zaytsev, A.Aleshin, E.Lazareva. Richtmyer-Meshkov instability for two- and three-dimensional interfaces. The Proc. of the 4th Int. Workshop on the Physics of Compressible Turbulent Mixing. Cambridge, England. Ed. by P.Li nden, D.Youngs & S.Dalziel. Pr. by Cambridge Univ. Press, Cambridge, England.(1993).

38. S.Zaytsev, E.Chebotareva, S.Titov. The initiation and the development of Richtmyer-Meshkov instability in continuous interface. The Proc. of the 4th Int. Workshop on the Physics of Compressible Turbulent Mixing. Cambridge, England. Ed. byP.Linden, D.Youngs & S.Dalziel. Pr. by Cambridge Univ. Press, Cambridge, England. (1993).

39. B.Sturtevant. Rayleigh-taylor Instability in Compressible Fluids. Proc. of the 16th ISSWT, Aachen, 1987, edited by H.Gronig, VCH Verlagsgeselshaft, p.89, 1988.

40. M.Brouillette and B. Sturtevant. Growth Induced by Multiple shock Waves Normally Incident on Plane Gaseous Interfaces. Physica, D37, (1989), p.248.

41. R.Bonazza, B.Sturtevant. X-ray measurements of shock-induced mixing at air/xenon interface. The Proc. of the 4th Int. Workshop on the Physics of Compressible Turbulent Mixing., Cambridge, England. Ed. by P.Linden, D.Youngs & S.Dalziel. Pr. by Cambridge Univ. Press, Cambridge, England. (1993).

42. M.Brouillette, B.Sturtevant. Experiments on the Richtmyer - Meshkov instability: Small-scale perturbations on a plane interface. Phys. Fluids, A5(4), pp.916-930, 1993.

43. R.Benjamin. Shock and reshock of an unstable fluid interface. 3rd Intl. Workshop on the Physics of Compressible Turbulent Mixing, Abbey of Royaumont, France (1991).

44. Benjamin R. Experimental Observations of Shock Stability and Shock - Induced Turbulence. Advances in Compressible Turbulent Mixing. W.P.Dannevik, A.C.Buckingham, C.E.Leith Editors, pp.341-348, 1992.

45. R.Benjamin, J.Fritz. Shock loading a rippled interface between liquids of different densities. Phys. Fluids, 30, pp.331-336, 1987.

46. R.Benjamin, H.Trease, J.Shaner. Coherent density gradients in water compressed by a modulated shock wave. Phys. Fluids, 27, pp.2390 - 2393, 1984.

47. J.Jacobs. Shock - induced mixing of a light - gas cylinder. J.Fluid Mech., 234, p.629, 1992.

48. J.Jacobs, D.Jenkins, D.Klein & R.Benjamin. Experimental study of instability growth patterns of a shock-accelerated, thin fluid layer. The Proc. of the 4th Int. Workshop on the Physics of Compressible Turbulent Mixing., Cambridge, England. Ed. by P.Linden, D.Youngs & S.Dalziel. Pr. by Cambridge Univ. Press, Cambridge, England. (1993).

49. L.Houas, R.Brun, M.Hanana. Experimental investigation of shock - interface interaction. AIAA J., 24, pp.1254-1255, 1986.

50. L.Houas, A.Farhat, R.Brun. Shock induced Rayleigh-Taylor instability in the presence of a boundary layer. Phys. Fluids, 31, pp.807-812, 1988.

51. L.Houas, J.Fortes, R.Brun, J.F.Haas. Three dimensional effects in high Mach number shock-interface interaction. Proc. of the 17th Int. Symposium on Shock Waves and Shock Tubes. Yong W. Kim, Bethlehem, USA, AIP Conference Proc., pp.208-290, 1989.

52. L.Houas, I.Chemouni, A.Touat, R.Brun. Experimental investigation of Richtmyer-Meshkov induced turbulent mixing over long distances. 3rd Int. Workshop on the Physics of Compressible Turbulent Mixing, Abbey of Royaumont, France.(1991)

53. A.Touat, I.Chemouni, G.Jourdan, L.Labracherie, L.Houas. Multidirectional laser technique for Richtmyer-Meshkov mixing experiments. The Proc. of the 4th Int. Workshop on the Physics of Compressible Turbulent Mixing., Cambridge, England. Ed. by P.Linden, D.Youngs & S.Dalziel. Pr. by Cambridge Univ. Press, Cambridge, England. (1993).

54. Cavailler C., Croso H., Grandeboeuf P., Haas J.F., Rodriguez G. Results from the Vaujours Vertical Shock Tube. 3rd Int. Workshop on the Physics of Compressible Turbulent Mixing, Abbey of Royaumont, France. (1991).

55. G.Rodriguez, I.Galametz, H.Croso, J.-F.Haas. Richtmyer-Meshkov instability in a vertical shock-tube. The Proc. of the 4th Int. Workshop on the Physics of Compressible Turbulent Mixing., Cambridge, England. Ed. by P.Linden, D.Youngs & S.Dalziel. Pr. by Cambridge Univ. Press, Cambridge England. (1993).

56. D.Landeg, M.Philpott, I. Smith, A.Smith. The laser sheet as a quantitative diagnostic in shock tube experiments. The Proc. of the 4th Int. Workshop on the Physics of Compressible Turbulent Mixing. Cambridge, England. Ed. b y P.Linden, D.Youngs & S.Dalziel. Pr. by Cambridge Univ. Press, Cambridge, England. (1993).

57. A.Vasilenko, O.Buryakov, V.Olkhovskaya, V.Yakovlev. Experimental investigations of turbulent mixing of gases at the plane interface under the influence of decelerating shock wave. (in Russian), Preprint №8,. VNITF, Chelyabinsk-70, 1991.

58. A.Vasilenko, V.Olhovskaya, O.Buryakov, V.Yakovlev. Experimental investigations for turbulent mixing of gases at the plane interface under the influence of the decelerating shok wave. 3rd Int. Workshop on the Physics of Compressible Turbulent Mixing, Abbey of Royaumont, France.(1991)

59. A.Tolshmyakov, E.Meshkov. Perturbations growth at the interface accelerated by converging shock wave. Cylindrical geometry.FGV (in Russian), №3, pp.109-113, 1989.

60. O.I.Volchenko, I.G.Zhidov, B.V.Klopov, E.E.Meshkov, V.V.Popov, V.G.Rogachev, A.I.Tolshmyakov, Simulation technique for nonstationary incompressible fluid flows.. AC. 1026154, Bulletin of OIPOTZ (in Russian), №24, 1983.

61. O.I.Volchenko, I.G.Zhidov E.E.Meshkov, V.G.Rogatchev. Localized perturbations growing at the unstable boundary of accelerated liquid layer.,. Letters to ZhTF (in Russian), v.15, pp.47-51, 1989.

62. V.Rogatchev, I.Zhidov, B.Klopov, E.Meshkov, A.Tolshmyakov. Non-Stationary flows in the proximity of angular points of gas accelerated liquid layer. 3rd Int. Workshop on the Physics of Compressible Turbulent Mixing, Abbey of Royaumont, France. (1991).

63. E.Meshkov, N.Nevmerzhitsky, V.Rogatchev, I.Zhidov. Turbulent mixing development investigation with converging jelly rings. The Proc. of the 4th Int. Workshop on the Physics of Compressible Turbulent Mixing., Cambridge, England. Ed. by P.Linden, D.Youngs & S.Dalziel. Pr. by Cambridge Univ. Press, Cambridge, England. (1993).

64. E.E.Meshkov, N.V.Nevmerzhitsky. About turbulent mixing dynamics at unstable boundary of liquid layer, accelerated by compressed gas. 3rd Int. Workshop on the Physics of Compressible Turbulent Mixing, Abbey of Royaumont, France.(1991).

65. N.Nevmerzhitsky, E.Meshkov, A.Ioilev, I.Zhidov, I.Pylev, S.Sokolov. Wave processes effect on the dynamics of turbulent mixing at liquid layer surface

accelerated by compressed gas. The Proc. of the 4th Int. Workshop on the Physics of Compressible Turbulent Mixing. Cambridge, England. Ed. by P.Linden, D.Youngs & S.Dalziel. Pr. by Cambridge Univ. Press, Cambridge, England(1993)..

66. I.Glass, G.Patterson. A Theoretical and Experimental Study of Shock Tube Flows. J.Aero Sci., №2, pp.73-100 (1953).

67. R.Jahn. The refraction of shock waves at a gaseous interface. J.Fluid.Mech., 1, 457, 1956.

68. L.Harris, E.Johnson. The Production of Strong, Cellulose Acetate films. Rev. Sci. Instrum., 1933, v.4, p.454.

69. G.H.Markstein. Flow disturbances induced near a slightly wavy contact surface, or flame front, traversed by a shock vawe. J.Aero.Sci., v.24, p.238, 1957.

70. G.H.Markstein. A shock tube study of flame front-pressure wave interactions. 6th Int.Symp.Combust., pp.387-398. Reihold, 1957.

71. H.Schardin. Ein Beispiel zur Verwendung des Stosswellenzhores fur Probleme der Instationaren Gasdynamik. Z. angew. Math und Phys., 1958, 9B, No. 6/6 (Sonderband), S. 606-621.

72. A.Dubovik. Photography record of fast proceses. (in Russian) Nauka, M. 1964, p.85.

73. R.Perry, A.Kantrowitz. The production and stability of converging shock waves. J. Appl. Phys., 1951, vol.22, No.7, pp.878-886.

74. R.Knystautas, J.H.Lee. Experiments on the Stability of Converging Cylindrical Detonations, Combustion & Flame, 16, pp.61-73, 1971.

75. R.Dannen, L.Vilson. "Electrical excitations of converging shock waves". in book "Electrical explosion of conductors".(in Russian) Mir. M. 1964, pp..172-184.

76. S.Popkov. "Polymer jelly state."(in Russian) M., 1974.

77. V.Izmailova."Surface effects in protein compounds."(in Russian) M. 1988.

78. D.Holder, R.North. "Schlieren methods." London, 1963.

79. G.Dimonte, B.Remington, P.Stry, E.Burke, P.Crowley, R.Hawke, J.Morrison, A.Susoeff. Turbulent Hydrodynamic Mix Experiment. The Proc. of the 4th Int. Workshop on the Physics of Compressible Turbulent Mixing., Cambridge, Engl and. Ed. by P.Linden, D.Youngs & S.Dalziel. Pr. by Cambridge Univ. Press, Cambridge, England (1993).

80.L.Vasilyev. "Shadow techniques."(in Russian) Nauka, M., 1968.

81.O.I.Volchenko, E.E.Meshkov. A method to generate light pulse.(in Russian). AC 1531596.

82. V.Ragulsky, F.Faizulov.(in Russian) Optica and spectroscopy., XXVII, 4, 707, 1969.

83. N.Khramov.. Izv. AN SSSR, MZhG (in Russian), 4, 169, 1974.

84. A.Melling, J.Whitelaw. Disa Information, 15, 5, 1973.

85. L.I.Sedov. “Similarity and dimensional methods in mechanics.” (in Russian), Nauka, M.,1967.

86. A.Kozyrev, V.Aleksandrov, N.Popov. Fusion first for USSR. Nature, 1978, v.275, № 5680, p.476.

87. G.A.Grishina. Linear approximation method in numerical gasdynamic calculations. (in Russian). Preprint №121, IPM, M. 1980.

88. J.W.Shaner. Pattern formation by shock processes, Physica 12D , 1984, pp.154-162, North-Holland, Amsterdam.

89. K.Mayer, P.Blewett. Phys.Fluids, v.15, № 5, pp.753-759, 1972.

90. M.Lighthill. Proc.Roy.Soc.A, v.200, pp.554, 1950.

91. G.Rudinger, L.Somers. Behaviour of small regions of different gases carried in accelerated gas flows. J.Fluid Mech., v.7, pp.161-176, 1960.

92. J.Jacobs. Shock - induced mixing of a light - gas cylinder. J.Fluid Mech., v.234, p.629, 1992.

93. D.Youngs, N.Cowperthwaite, A.Smith, N.Stearman. Turbulent Mixing by Shock Induced Rayleigh - Taylor Instability. Proc. for 2nd Int Workshop on the Physics of Compressible Turbulent Mixing, Pleasanton, USA.(1989).

94..S.M.Bakhrakh, B.Klopov, E.Meshkov, A.Tolshmyakov, Yu.Yanilkin. Perturbation growth at shock-accelerated gas-gas interface. (in Russian). PMTF. 1994.

95. R.LeLevier,G.Lasher and Bjorklund. Effect of a Density Gradient on Taylor Instability. Lawrence Livermore Laboratory report. UCRL-4459, 1955.

96.Physical Quantaty Data-book. (in Russian). Under I.K.Kikoin edition. Atomizdat. M.1976.

*U.S. GOVERNMENT PRINTING OFFICE 1995-0-673-029/7066

Los Alamos
NATIONAL LABORATORY
Los Alamos, New Mexico 87545